Crystallography Reports, Vol. 50, No. 1, 2005, pp. 1–9. Translated from Kristallografiya, Vol. 50, No. 1, 2005, pp. 7–15.

CRYSTALLOGRAPHIC SYMMETRY

Dedicated to the 116th Anniversary of the Birth of Academician A.V. Shubnikov

On a Number of Some Categories of the Limiting Groups of Multidimensional Plane Crystallographic Point Groups of Symmetry

A. F. Palistrant

Moldova State University, Chisinau, Moldova

Received January 5, 2003

Abstract—Many categories of multidimensional crystallographic plane point groups of symmetry are established with the aid of two- and three-dimensional point groups of symmetry and the groups of simple and multiple antisymmetry generated by these point groups and the groups of rosette, tablet, hypertablet, crystallographic, and hypercrystallographic *P* symmetries. The numerical characteristics of all the categories of such groups are given and, for each of these groups, the numbers of the limiting groups of multidimensional symmetry (whose subgroups they are) are determined for each category based on the limiting symmetry groups of the classical point groups and the generalizing groups of *l*-tuple antisymmetry and the indicated particular cases of the *P* symmetry. © *2005 Pleiades Publishing, Inc.*

INTRODUCTION

Shubnikov's theory of antisymmetry [1] provides the basis not only for revealing physical properties of crystals, but also for solving problems in the field of multidimensional geometrical crystallography. All the antisymmetry generalizations [2–7], where the law of changing the qualities attributed to points is directly combined with the isometric transformation acting only on these points and independent of their choice, are used in the unified scheme of the *P* symmetry. The general theory of the *P* symmetry and the principles of classification of the *P* symmetries, and also the methods for deriving the groups of the *P* symmetry from the classical groups, are considered in detail elsewhere [8]. The geometrical principle of classification of the *P* symmetries proved to be especially fruitful for their multidimensional applications [8, Sect. 1.2]. This principle allows one to distinguish the following *P* symmetries: 10 rosette *P* symmetries in the case where the substitution groups of qualities *P* characterizing these *P* symmetries are isomorphic to two-dimensional point (rosette) groups G_{20} ($P \simeq G_{20}$), 31 tablet *P* symmetries at $P \simeq G_{320}$ (as the generalization of the rosette symmetries with antisymmetry), 125 first-order hypertablet *P* symmetries at $P \simeq G_{4320}$ (as the generalization of the tablet symmetries with antisymmetry or rosette symmetries with double antisymmetry [5]), 671 second-order hypertablet *P* symmetries at $P \simeq G_{54320}$ (as the generalization of the tablet *P* symmetries with double antisymmetry or rosette *P* symmetries with triple antisymmetry [5, 9]), 32 crystallographic *P* symmetries at $P \simeq G_{30}$, 122 first-order hypercrystallographic *P* symmetries at $P \simeq G_{430}$ (as the generalization of crystallographic symmetries with antisymmetry) [10], and 624 second-order hypercrystallographic symmetries at $P \simeq G_{5430}$ (as the generalization of crystallographic symmetries with double antisymmetry) [11]. The generalization of the classical rosette groups G_{20}, tablet groups G_{320}, and crystal classes G_{30} with simple and *l*-tuple antisymmetry [5], and also with the particular cases of *P* symmetry indicated above, allowed one to derive new groups of generalized symmetry, which, in turn, allowed one to determine 20 categories of *n*-dimensional plane crystallographic point groups of symmetry at $4 \le n \le 8$.

The present study is dedicated to analysis of the results thus obtained and the determination for each category of the groups of multidimensional symmetry thus determined of the number of the limiting groups whose subgroups they are.

LIMITING GROUPS AND CATEGORIES OF MULTIDIMENSIONAL SYMMETRY GROUPS

Let us consider some definitions and the list and notation of the multidimensional symmetry groups, and formulate the problem.

A symmetry group is called a plane point group if its transformations preserve invariant a certain plane and at least one point in this plane. If such a group contains rotation around axes (centers) by infinitely small angles, it is called a limiting group. Two- and three-

1063-7745/05/5001-0001$26.00 © 2005 Pleiades Publishing, Inc.

dimensional limiting point groups are well known [1, 12, 13] and, along with the point groups (whose subgroups they are), play an important role in theoretical and applied crystallography. Two-dimensional point (rosette) symmetry groups G_{20} are the subgroups of two of their limiting groups ∞ and $\infty \cdot m$, which describe the symmetry of a rotating circle and a circle at rest. Three-dimensional plane-point (tablet) symmetry groups G_{320} are the subgroups of their five limiting groups: ∞ and $\infty \cdot m$, which are the symmetry groups of rotating circular cones and right circular cones at rest; the groups $\infty : 2$ and $\infty : m$ characterizing the symmetries of differently oriented right circular cylinders; and the group $m \cdot \infty : m$, which describes the symmetry of a right circular cylinder at rest. In turn, the crystal classes G_{30} are the subgroups of their seven limiting groups represented by certain figures in [1, 12] and called the Pierre Curie groups [13]. These groups include the above symmetry transformations of right circular cones and cylinders, and also the groups ∞/∞ and $\infty/\infty \cdot m$, which characterize the symmetry of an oriented sphere and a sphere at rest. The Shubnikov notation used here for two- and three-dimensional limiting point groups is considered in detail elsewhere [1, 3, 4, 7, 12, 13].

The use of the above classical point symmetry groups and the generalizing antisymmetry groups (both of simple [1] and multiple [5] symmetry), color symmetry [2, 6], and other particular cases of the *P* symmetry [8] allowed one to reveal many categories of the basic *n*-dimensional plane point symmetry groups of the multidimensional geometrical crystallography at $n \geq 4$. Thus, it was shown [6, 8] that the use of the point groups G_{20}^{l}, G_{320}^{l}, and G_{30}^{l} of the *l*-tuple antisymmetry indicated in [5] allowed one to reveal all various symmetry groups of the categories $G_{(l+2)(l+1)\ldots 20}$, $G_{(l+3)(l+2)\ldots 320}$, and $G_{(l+3)(l+2)\ldots 30}$, where a symbol, e.g., $G_{(l+2)(l+1)\ldots 20}$, denotes the set of the groups of the $(l + 2)$-dimensional Euclidean space with invariant planes successively included into one another of dimensionalities $l + 1, l, \ldots, 2, 0$. Then, according to [6, 8], the point groups G_{20}^{P}, G_{320}^{P}, and G_{30}^{P} of the 10 rosette *P* symmetries ($P \simeq G_{20}$) fully represent the symmetry groups of the categories G_{420}, G_{5320}, and G_{530}, respectively; the groups G_{20}^{P}, G_{320}^{P}, and G_{30}^{P} of 31 table *P* symmetry ($P \simeq G_{320}$), the symmetry groups of the categories G_{5420}, G_{65320}, and G_{6530}, respectively. In a similar way, the point groups G_{20}^{P}, G_{320}^{P}, and G_{30}^{P} of 125 first-order hypertablet *P* symmetries ($P \simeq G_{4320}$)[1] fully represent all the symmetry groups of categories G_{65420}, G_{765320}, and G_{76530}, whereas 671 groups of second-order hypertablet *P* symmetry ($P \simeq G_{54320}$) with the same names allow one to determine all the symmetry groups of the categories G_{765420}, G_{876530}, and G_{876530} [9]. For example, in this case, the symbol G_{87630} indicates the set of groups of the 8-dimensional space with the invariant planes of dimensionalities 7, 6, 5, 3 and 0 (in our notation, a straight line is considered to be a 1-dimensional plane, and a point, a 0-dimensional plane). In turn, the groups G_{20}^{P}, G_{320}^{P}, and G_{30}^{P} of 32 crystallographic *P* symmetries in the geometrical classification ($P \simeq G_{30}$) allow one to interpret all the symmetry groups of the categories G_{520}, G_{6320}, and G_{630} [8]. Then, 122 groups of the first-order hypercrystallographic *P* symmetries ($P \simeq G_{430}$) with the same names fully and successively model all the symmetry groups of the categories G_{6520}, G_{76320}, and G_{7630}, and the groups of 624 second-order hypercrystallographic *P* symmetries ($P \simeq G_{5430}$) with the same names[2] model the symmetry groups of the categories G_{76520}, G_{876320}, and G_{87630} [10, 11]. This is because the groups, e.g., G_{30}^{P} at $P \simeq G_{5430}$ and the symmetry groups of the category G_{87630}, are related in the same way as the antisymmetry rosette groups G_{20}^{1} and the symmetry tablet groups G_{320} [4, 7], the two-dimensional antisymmetry groups G_{2}^{1} and the layer groups G_{32} [4, 5, 7], or the Shubnikov groups G_{3}^{1} [3, 5] and the hyperlayer groups G_{43} [6, 8].

It is clear that the problem of determining the limiting groups whose subgroups are the categories of the multidimensional plane point groups of symmetry indicated above is of great scientific interest for establishing new possible applications of the methods developed in the Zamorzaev theory of *P* symmetry, for multidimensional geometry and modern crystallography, and for solving problems associated with the generalized symmetry of crystal structures. It is impossible to solve this problem by trying to reveal a number of figures that would represent the limiting groups of symmetry as was attempted in [1, 12]. However, the methods of the theory of *P* symmetry used for the study of the above multidimensional plane crystallographic point groups may also be used to determine the number of the limiting groups of each category whose subgroups are its symmetry groups. The attempt to solve this problem first formulated in [14, 15] is made in the present study.

[1] The *P* symmetries at $P \simeq G_{4320}$ are named in such a way because the groups G_{4320} preserve a three-dimensional plane (hyperplane) in the four-dimensional space, and the difference is $4 - 3 = 1$. In a similar way, the *P* symmetries at $P \simeq G_{430}$ are called first-order hypercrystallographic symmetries.

[2] The *P* symmetries at $P \simeq G_{54320}$ are named in such a way because the groups G_{54320} preserve the hyperplane of the symmetry groups G_{4320} in the five-dimensional space, whereas the difference is $5 - 3 = 2$. Similar reasons allowed one to call the *P* symmetries at $P \simeq G_{5430}$ the second-order hypercrystallographic symmetries.

SOME STATEMENTS OF THE THEORY OF *P* SYMMETRY

We should remember some concepts of the Zamorzaev theory of *P* symmetry necessary for the solution of the formulated problem [6, 8]. In distinction from Shubnikov's antisymmetry [1, 5], Zamorzaev's theory deals with an arbitrary number *P* of qualities attributed to the points of a figure and, in distinction from Belov's *p*-color symmetry [2, 6], Zamorzaev's theory deals with an arbitrary group *P* of substitution of the qualities attributed to the points of a figure in its isometric transformations.

The set of all the *P*-symmetry transformations of the figure under consideration constitutes the group *G*. These transformations are decomposed into the symmetry transformation *s* from the group *S* of the figure *F* and the substitutions of the qualities ε from the group *P*. The set of symmetry transformation of symmetry *s* which enters the transformation of the *P* symmetry of the group *G* constitute the generating group *S*, whereas the substitutions of the qualities ε constitute the group P_1. At $P_1 = P$, the group *G* is called the group of complete *P* symmetry, and at $e \subset P_1 \subset P$, it is called the group of incomplete *P* symmetry. Using the notation $Q = G \cap P$, we arrive at the division of the *G* groups of complete *P* symmetry into senior, junior, and medium (*Q*-medium) groups, which correspond to the cases $Q = P$, $Q = e$, and $e \subset Q \subset P$. The derivation of the senior groups of the *P* symmetry is trivial. The junior groups of the given *P* symmetry are derived from a certain generating *S* group only if the latter possesses such a normal divisor *H* that the factor-group is $S/H \simeq P$. The study of the *Q*-medium groups of the *P* symmetry is associated with sorting of nontrivial normal divisors of the *P* groups of substitutions, whereas the calculation of these groups becomes possible only after the preliminary establishment of the junior groups [16]. The number of various *Q*-medium groups of the *P* symmetry in this family equals the number of various junior groups of P_0 symmetry with the same generating group if the factor-group P/Q is strongly isomorphic to P_0.

MULTIDIMENSIONAL GROUPS AND THEIR RELATION TO TWO- AND THREE-DIMENSIONAL POINT GROUPS OF *P* SYMMETRY

The signs and qualities attributed to the points of a plane or a space in the derivation of the point groups G^l_{20}, G^l_{320}, and G^l_{30} of the *l*-tuple antisymmetry at $l \geq 1$ and the point groups G^P_{20}, G^P_{320}, and G^P_{30} of the rosette, tablet, and the first- and second-order hypertablet *P* symmetries, and also first- and second-order hypercrystallographic *P* symmetries, have no geometrical sense with respect to dimensionality of the space in which these groups are considered. In additional measurements, the signs and indices attributed to the points of the given space may be interpreted geometrically, which allows one to use the established rosettes, tablet groups and crystal classes of simple and multiple antisymmetry at $l = 1$ and $l \geq 2$, as well as the particular case of the *P* symmetry mentioned above for studying certain categories of the multidimensional point symmetry groups.

The use of these methods allowed one to establish the numerical characteristics of the categories of the multidimensional point groups indicated above [8–11]. We consider these results for individual categories; the coefficient before the category symbol indicates the number of groups contained in the category.

Thus, the sets of groups of 31 G_{320}, 125 G_{4320}, 671 G_{54320}, 4885 G_{654320}, and 48907 $G_{7654320}$ are modeled (interpreted or depicted) by the groups of *l*-tuple rosette antisymmetry at $l = 1$–5[3] or by groups of $(l-1)$-tuple tablet antisymmetry at $l = 0$–4, because the groups of the *l*-tuple rosette antisymmetry G^l_{20} are used to interpret the groups of $(l-1)$-tuple tablet antisymmetry G^{l-1}_{320} [5]. In turn, the sets of groups of 122 G_{430}, 624 G_{5430}, 4362 G_{65430}, and 42292 G_{765430} are depicted by the three-dimensional point groups of the *l*-tuple antisymmetry G^l_{30} at $l = 1$–4 [5]. Further, the sets of groups of 263 G_{420}, 1274 G_{5420}, 8806 G_{65420}, and 84313 G_{765420} revealed in [6, 8, 9, 17] are interpreted successively by the rosette groups G^P_{20} of the rosette, tablet, and first- and second-order hypertablet *P*-symmetries indicated in [9]. It should be noted that the above sets of symmetry groups 1274 G_{5420}, 8806 G_{65420}, and 84313 G_{765420} are also modeled by the tablet groups G^P_{320} of the rosette, tablet, and hypertablet *P* symmetries because of the pairwise coincidence of the categories G_{5420} and G_{5320} and G_{65420} and G_{65320} [8].

It is possible to establish strongly isomorphic relation between the sets of groups of 1208 G_{520}, 7979 G_{6520}, and 73589 G_{76520} studied in [8, 18] and the sets of the rosette groups G^P_{20} of the first- and second-order hypercrystallographic *P* symmetries indicated in [10, 11]. In other words, it is possible to establish such a mutually unique mapping of one set of groups onto the other set of groups that the groups of these sets with the corresponding isomorphism would have the same structure [16]. It then follows that the notation G^P_{20} of the indicated groups gives (in the implicit form) the related multidimensional symmetry groups (as the border groups of antisymmetry in this notation mentioned above simultaneously set also the band symmetry

[3] The band symmetry groups G^1_{21} are modeled (interpreted or depicted) in the same way as the border (one-sided band) groups of antisymmetry G_{321} in Fig. 92 in [4] are represented by plane figures consisting of white and black triangles.

groups). The same sets of groups may also be interpreted by three-dimensional point groups G_{30}^{P} of the rosette, tablet, and hypertablet *P* symmetries, because the pairs of the categories G_{520} and G_{530}; G_{6520} and G_{6530}; and G_{76520} and G_{76530} coincide [8]. Finally, the sets of groups of 7311 G_{630}, 64471 G_{7630}, and 814871 G_{87630} determined in [10, 11] are modeled by the three-dimensional point groups G_{30}^{P} of the first- and second-order crystallographic and hypercrystallographic *P* symmetries.

METHODS OF SOLVING THE FORMULATED PROBLEM

Now, we proceed with the search for the method for solving the formulated problem, i.e., with finding methods for calculating the number of the limiting groups whose subgroups are multidimensional crystallographic plane point groups of the categories indicated above. It should be noted that the goal will be immediately reached as soon as we determine the number of the limiting groups whose subgroups are the groups G_{20}^{l}, G_{320}^{l}, and G_{30}^{l} of the *l*-tuple antisymmetry at $1 \le l \le 4$ and the groups G_{20}^{P}, G_{320}^{P}, and G_{30}^{P} of all the particular cases of the *P* symmetry considered in the previous section. This is because the limiting groups of each category of the groups of the generalized symmetry from the set of the groups studied, as well as the limiting groups of multidimensional symmetry groups modeled by the groups of this category, are characterized by a stongly isomorphic correspondence [16].

There are two methods for revealing the limiting groups of the generalized symmetries of the above categories: (1) the method developed by Shubnikov [19, 20] who suggested the complete systematics of the three-dimensional point groups and black-white groups generalizing the former ones, (2) and the method of using the limiting groups of rosettes and tables, 32 crystal classes, and also the groups of *l*-tuple antisymmetry and the particular cases of the *P* symmetry indicated above generalizing these classes. The first method of obtaining the limiting groups for each type of point groups of generalized symmetries considered is based on the distribution of its groups over the series including the groups of the same form with the subsequent requirement that in all the series thus formed the order of the rotation axis of the classical or generalized symmetry would tend to infinity (cf. [19, 20]). Because of a very large number of groups of any category, this method of solving the formulated problem becomes practically impracticable. The second method seems to be more realistic, because it reduces to the solution of the traditional problem: extension of the limiting groups of rosettes, tablets, and 32 crystal classes in the form of the groups of the *l*-tuple antisymmetry and the particular cases of the *P* symmetry indicated earlier. The following *theorem* substantiates the use of this method. The groups G_{20}^{l}, G_{320}^{l}, and G_{30}^{l} of the *l*-tuple antisymmetry and also the groups G_{20}^{P}, G_{320}^{P}, and G_{30}^{P} of any of concrete *P* symmetry indicated earlier are the subgroups of the analogous groups obtained by the generalization of the limiting symmetry groups of rosettes, tablets, and crystal classes with the *l*-tuple antisymmetry and also with the same *P* symmetry.

To prove the theorem, we have to perform the following: (i) to distribute all the point groups of each category over the series as was done in [19, 20]; (ii) to select different groups from the limiting groups terminating the series obtained; (iii) to generalize the limiting groups of rosettes, tablets, and 32 crystal classes with the same *l*-tuple antisymmetry and the same particular *P* symmetry; (iv) to compare the limiting groups of each category of the groups of the *l*-tuple antisymmetry or the *P* symmetry with the groups obtained in the generalization of the limiting groups of the generating groups of this category with the same *l*-tuple antisymmetry or the *P* symmetry.

Thus, the systematization performed in a way similar to that in [19] allows one to distribute the discrete groups of one-sided rosettes G_{20} over four infinite series:

$$\left.\begin{array}{l}(1)\ 1, 3, 5, \ldots, \infty\\ (2)\ 2, 4, 6, \ldots, \infty\end{array}\right\} \text{and} \left.\begin{array}{l}(3)\ 1\cdot m, 3\cdot m, 5\cdot m, \ldots, \infty\cdot m\\ (4)\ 2\cdot m, 4\cdot m, 6\cdot m, \ldots, \infty\cdot m\end{array}\right\}.$$

These series are terminated with two limiting groups ∞ and $\infty \cdot m$, whereas the groups of two-sided rosettes G_{320} form 14 series, including four series written for one-sided rosettes and 10 new series:

$$\left.\begin{array}{l}(5)\ 1:2, 3:2, 5:2, \ldots, \infty:2\\ (6)\ 2:2, 4:2, 6:2, \ldots, \infty:2\end{array}\right\},$$

$$\left.\begin{array}{l}(7)\ \tilde{2}, \tilde{6}, \tilde{10}, \ldots, \infty:m\\ (8)\ \tilde{4}, \tilde{8}, \tilde{12}, \ldots, \infty:m\end{array}\right\},$$

$$\left.\begin{array}{l}(9)\ 1:m, 3:m, 5:m, \ldots, \infty:m\\ (10)\ 2:m, 4:m, 6:m, \ldots, \infty:m\end{array}\right\},$$

$$\left.\begin{array}{l}(11)\ m\cdot 1:m, m\cdot 3:m, m\cdot 5:m, \ldots, m\cdot\infty:m\\ (12)\ m\cdot 2:m, m\cdot 4:m, m\cdot 6:m, \ldots, m\cdot\infty:m\end{array}\right\},$$

$$\left.\begin{array}{l}(13)\ \tilde{2}\cdot m, \tilde{6}\cdot m, \tilde{10}\cdot m, \ldots, m\cdot\infty:m\\ (14)\ \tilde{4}\cdot m, \tilde{8}\cdot m, \tilde{12}\cdot m, \ldots, m\cdot\infty:m\end{array}\right\},$$ which are terminated with five different limiting groups ∞, $\infty \cdot m$, $\infty : 2$, $\infty : m$, and $m \cdot \infty : m$ (cf. with table in [19]).

Extending the limiting groups of rosettes to the antisymmetry groups, we arrive, according to [1, 5], at two generating groups ∞ and $\infty \cdot m$, two senior groups $\boldsymbol{\infty} = \infty \times \mathbf{1}$ and $\boldsymbol{\infty} \cdot m = (\infty \cdot m) \times \mathbf{1}$, and one junior (black–

white) group $\infty \cdot \mathbf{m}$, i.e., altogether, five limiting groups. The same result is obtained if, following [19, 20], we also distribute over the series the antisymmetry groups of rosettes G_{20}^1. Indeed, the systematics of the generating groups of this category repeats the systematics of the symmetry groups of one-sided rosettes and leads to two limiting groups ∞ and $\infty \cdot m$.[4] The systematics of the senior groups of rosette antisymmetry results in four series $\left.\begin{matrix} 1 \times \mathbf{1}, 3 \times \mathbf{1}, 5 \times \mathbf{1}, \ldots, \infty \times \mathbf{1} \\ 2 \times \mathbf{1}, 4 \times \mathbf{1}, 6 \times \mathbf{1}, \ldots, \infty \times \mathbf{1} \end{matrix}\right\}$, $\left.\begin{matrix} (1 \cdot m) \times \mathbf{1}, (3 \cdot m) \times \mathbf{1}, \ldots, (\infty \cdot m) \times \mathbf{1} \\ (2 \cdot m) \times \mathbf{1}, (4 \cdot m) \times \mathbf{1}, \ldots, (\infty \cdot m) \times \mathbf{1} \end{matrix}\right\}$ with the terminal limiting groups $\infty \times 1$ and $(\infty \cdot m) \times \mathbf{1}$. The systematic of junior groups leads to four series $\mathbf{2}$, $\mathbf{4}$, $\mathbf{6}$, …, $\boldsymbol{\infty}$, $\left.\begin{matrix} 1 \cdot \mathbf{m}, 3 \cdot \mathbf{m}, 5 \cdot \mathbf{m}, \ldots, \infty \cdot \mathbf{m} \\ 2 \cdot \mathbf{m}, 4 \cdot \mathbf{m}, 6 \cdot \mathbf{m}, \ldots, \infty \cdot \mathbf{m} \end{matrix}\right\}$ and $\mathbf{2} \cdot m, \mathbf{4} \cdot m, \mathbf{6} \cdot m$, …, $\boldsymbol{\infty} \cdot m$ with the terminal limiting groups $\boldsymbol{\infty} \times \mathbf{1}$, $(\infty \cdot m) \times 1 = \boldsymbol{\infty} \cdot m$, and $\infty \cdot \mathbf{m}$. Thus, the groups of the category G_{20}^1 are the subgroups of the five limiting groups derived from the limiting rosette groups in the process of their generalization with antisymmetry. However, the groups G_{20}^1 interpret the symmetry groups of the category G_{320}. Therefore, the number of the limiting groups of tablets coincides with the number of the limiting groups of rosette antisymmetry, which was to be proved.

Generalizing the limiting groups of tablets with antisymmetry, we arrive at five generating groups of this category coinciding with the limiting groups, five senior groups obtained in a trivial way, and 6 junior groups $\infty : \mathbf{2}$, $\infty \cdot m$, $\infty : \mathbf{m}$, $\mathbf{m} \cdot \infty : m$, $m \cdot \infty : \mathbf{m}$, and $\mathbf{m} \cdot \infty : \mathbf{m}$, i.e., 16 limiting groups altogether. The same result is also obtained if we distribute over the series the groups of symmetry and antisymmetry of tablets G_{320}^1, because the systematics of the generating and senior groups of this category yield five limiting groups each, whereas the systematics of the junior groups lead to six limiting groups, as follows from the table of black–white point groups [20] if one neglects the systematics of the cubic groups. Thus, the groups of the category G_{320}^1 are also the subgroups of 16 limiting groups obtained from the limiting tablet groups in their generalization with antisymmetry.

It follows from the systematic of three-dimensional point groups of symmetry and antisymmetry performed in [19, 20] that the groups of the category G_{30}^1 are the subgroups of 21 limiting groups obtained from seven limiting point symmetry groups (Pierre Curie symmetry groups [13]) in their generalization with antisymmetry; of these groups 7 are generating groups, 7 are senior groups, and 7 are junior groups, which are exhausted by the 6 junior limiting groups of tablets and the group $\infty/\infty \cdot \mathbf{m}$.

Similar to the case in [19, 20], the distribution of the point groups of the *l*-tuple symmetry over the series at $l \geq 2$ terminating with the limiting groups becomes too cumbersome. Thus, the systematics with the fulfillment of the conditions indicated in [19, 20] distributes the three-dimensional point groups of double antisymmetry G_{30}^2 over 320 series which converge to 83 different limiting groups. Indeed, according to the general theory of double antisymmetry [5, p. 84], the following types of the groups are distinguished among the groups of the category G_{30}^2: generating groups, senior groups of order 1, senior groups of order 2, senior groups of order (1, 2), and senior groups of two different orders (i.e., Π, C_1, C_2, C_{12}, and C_1C_2, respectively); senior groups of order 1, junior groups of order 2, and senior groups of order (1, 2) (i.e., M_1, M_2, and M_{12}, respectively); senior groups of order 1, junior groups of order 2, senior groups of order 2, junior groups of order 1, senior groups of order (1, 2), and junior groups of order 1 (C_1M_2, C_2M_1, and $C_{12}M_1$, respectively); and junior groups of two different orders (M_1M_2). All the groups of each type are of the following five types: Π, C_1, C_2, C_{12}, and C_1C_2 of the category G_{30}^2 are distributed, in accordance with the table in [19], over 16 series and converge to 7 different limiting groups; all the groups of each of the following six types: M_1, M_2, M_{12}, C_1M_2, C_2M_1, and $C_{12}M_2$ of the same category are distributed, according to the table in [20], over 30 series and converge to 7 different limiting groups. Thus, the groups of the category G_{30}^2 of the 11 types indicated above are the subgroups of $7 \times 5 + 7 \times 6 = 77$ limiting groups of the same 11 types. The remaining groups of the type M_1M_2 of the three-dimensional point groups of double antisymmetry are distributed, as is shown in [5, 21], over the 60 series converging to 27 different limiting groups. Of these 27 limiting groups, 7 are of the type C_1M_2; 7 are of the type C_2M_1; 7 are of the type $C_{12}M_1$, which repeat the limiting groups obtained earlier; and 6 are new junior groups of the independent types $\mathbf{m} \cdot \infty : m'$, $\mathbf{m} \cdot \infty : \mathbf{m}'$, $m' \cdot \infty : \mathbf{m}$, $m' \cdot \infty : \mathbf{m}'$, $\mathbf{m}' \cdot \infty : \mathbf{m}$, and $\mathbf{m}' \cdot \infty : m'$, generated by the group $m \cdot \infty : m$ (cf. p. 166 in [5]). The result obtained confirms that the groups of the category G_{30}^2 are the subgroups of 83 different limiting groups.

Since the groups of the category G_{30}^2 model all the different groups of the category G_{5430}, it follows that the five-dimensional discrete symmetry groups of this category are the subgroups of 83 limiting groups repeating the groups obtained from 7 limiting groups of

[4] In other words, it completely reproduces the systematics of the rosette symmetry groups written above.

32 crystal classes in their generalization with the double antisymmetry, etc.

The proof of the theorem for the groups of the categories G_{20}^{P}, G_{320}^{P}, and G_{30}^{P} is somewhat more complicated, but the scheme of the proof is the same.

SOLUTION OF THE PROBLEM

Now, let us conclude the solution of the problem which was begun in the proof of the theorem. With this aim, we establish, first, the numbers of various groups generated by the limiting symmetry groups of rosettes, tablets, and crystal classes in their generalization with the l-tuple antisymmetry and the particular cases of the P symmetry indicated above.

In order to find the total number of the groups of l-tuple antisymmetry with the generating limiting groups of the of the categories G_{20}, G_{320}, and G_{30}, we invoke the formulas from the monograph in [5, p. 96] in which P_l denotes the number of all the groups of the l-tuple antisymmetry of a certain category and N_l indicates the number of junior l independent groups among them. For all the group categories, $P_0 = N_0$ is the number of various groups of the classical symmetry.

For the limiting rosette groups, $N_0 = 2$, $N_1 = 1$, and $N_l = 0$ at $l \geq 2$. Thus, we obtain for the limiting symmetry groups of the category G_{20} the following: $P_1 = 2 \times 2 + 1 = 5$; $P_2 = 5 \times 2 + 6 \times 1 = 16$; $P_3 = 16 \times 2 + 35 \times 1 = 67$; $P_4 = 67 \times 2 + 240 \times 1 = 374$; and $P_5 = 374 \times 2 + 2077 \times 1 = 2825$. According to the theorem proven above, these are the numbers of the limiting groups of the category G_{20}^{l} at l = 1–5. Taking into account the relation of the multi-dimensional symmetry groups $G_{(l+2)(l+1)\ldots 20}$ with the groups of the category G_{20}^{l} at the l values given above, we obtain that the symmetry groups of the categories G_{320}, G_{4320}, G_{54320}, G_{654320}, and $G_{7654320}$ are the subgroups of 5, 16, 67, 374, and 2825 limiting groups, respectively.

Since in the case of the limiting groups of tablets $N_0 = 5$, $N_1 = 6$, $N_2 = 6$, and $N_l = 0$ at $l \geq 2$, using the same formulas from [5], we find that $P_1 = 2 \times 5 + 6 = 16$, $P_2 = 5 \times 5 + 6 \times 6 + 6 = 67$, $P_3 = 16 \times 5 + 35 \times 6 + 14 \times 6 = 374$, $P_4 = 67 \times 5 + 240 \times 6 + 175 \times 6 = 2825$. These are the numbers of the limiting groups of the categories G_{320}^{l} at l = 1–4. However, since the groups G_{320}^{l} model the symmetry groups of the categories $G_{(l+3)(l+2)\ldots 320}$, this also establishes that the symmetry groups of the categories G_{4320}, G_{54320}, G_{654320}, and $G_{7654320}$ corresponding to the l values indicated above are successively the subgroups of 16, 67, 374, and 2825 limiting groups.

The coincident numbers of the limiting groups of the l-tuple antisymmetry with the generating limiting groups of rosettes and of the groups of $(l-1)$-tuple antisymmetry with the generating limiting groups of tablets confirm the correctness of the performed calculations, because the limiting groups of the rosettes and tablets of multiple antisymmetries are related in the same way as the groups of the categories G_{20}^{l} and G_{320}^{l-1} [5].

In turn, it follows from [5, 19, 20] and the previous section that, for the limiting groups of three-dimensional point groups, $N_0 = 7$, $N_1 = 7$, $N_2 = 2$, and $N_l = 0$ at $l \geq 3$. Thus, according to the formulas from [5, p. 96] with seven generating limiting groups and the above N_l values, the numbers of the limiting groups of the l-tuple antisymmetry at l = 1–4 are $P_1 = 2 \times 7 + 7 = 21$, $P_2 = 5 \times 7 + 6 \times 7 + 6 = 83$, $P_3 = 16 \times 7 + 35 \times 7 + 14 \times 6 = 441$, $P_4 = 67 \times 7 + 240 \times 7 + 175 \times 6 = 3199$. According to the theorem, the number of the limiting groups whose subgroups are the groups G_{30}^{l} coincides with the number P_l. Since the groups G_{30}^{l} model the symmetry groups $G_{(l+3)(l+2)\ldots 30}$, the groups of the categories G_{430}, G_{5430}, G_{65430}, and G_{765430} corresponding to l = 1–4 are the subgroups of 21, 83, 441, and 3199 limiting groups, respectively.

Now, let us establish the number of the limiting groups whose subgroups are the groups G_{20}^{P}, G_{320}^{P}, and G_{30}^{P} considered earlier for some particular cases of the P symmetry. In accordance with the theorem, we first have to determine the numbers of various groups generated by the limiting symmetry groups of categories G_{20}, G_{320}, and G_{30} during their generalization with all the first-order groups of rosette, tablet, and hypertablet P symmetries and all the second-order hypertablet in [9] and first-order crystallographic, hypercrystallographic, and second-order hypercrystallographic P symmetries listed in [10, 11].

In order to obtain the numbers of the limiting groups sought, one may use the formulas from [9–11], which allow one to calculate the complete numbers of the groups of P symmetry of an arbitrary category via the number of the initial symmetry groups and the number of the junior groups that may be derived from the symmetry groups of the given category during their generalization with the indicated P symmetries, because the corresponding numerical data for the limiting groups of the rosettes, tablets, and crystal classes are known [5].

Thus, for the limiting groups of rosettes, the number of the generating groups is $K = 2$, the number of the junior groups of 2-symmetry is $M_2 = 1$, and the numbers of the junior groups at the remaining P symmetries that enter the formulas from [9] are $M_P = 0$. Therefore, in the generalization of two limiting groups of the category G_{20} with 10 rosette P symmetries, we have $10 \times 2 + 11 \times 1 = 31$ groups whose subgroups are the groups G_{20}^{P} of the rosette P symmetries and the symmetry groups G_{420} modeled by the former groups. Generaliz-

ing the same 2 limiting groups, ∞ and $\infty \cdot m$, with 31 tablet P symmetry, we obtain $31 \times 2 + 63 \times 1 = 125$ groups whose subgroups are the groups G_{20}^{P} of the rosette P symmetries and the symmetry groups G_{5420} modeled by the former groups. The generalization of the same two limiting groups with 125 first-order hypertablet P symmetry groups yields, according to the formula from [9], $125 \times 2 + 421 \times 1 = 671$ groups whose subgroups are the groups G_{20}^{P} of the first-order hypertablet P symmetries and the symmetry groups G_{654320} modeled by these groups. Finally, generalizing the same two limiting rosette groups with 671 hypertablet second-order P symmetry and using the formula from [9], we establish the number of the groups of these P symmetries as $671 \times 1 + 3543 \times 1 = 4885$ limiting groups whose subgroups are the G_{20}^{P} groups of second-order hypertablet P symmetries and the symmetry groups G_{765420} modeled by these groups.

Let us now proceed to the number of the limiting groups whose subgroups are the G_{20}^{P} groups of the crystallographic and hypercrystallographic P symmetries of the first and second order. In accordance with the theorem, these numbers coincide with the numbers of groups generated by two limiting groups of the symmetry groups G_{20} during their generalization with these P symmetries and can readily be determined using the formulas from [10, 11], because for the groups ∞ and $\infty \cdot m$ we are interested in, we possess all the numerical data necessary for the use of the formulas mentioned above. Thus, substituting $K = 2$, $M_2 = 1$, and $M_P = 0$ into the formula for the calculation of the number of groups of 32 crystallographic P symmetries, we obtain for the remaining P symmetries in this formula $32 \times 2 + 58 \times 1 = 122$ limiting groups whose subgroups are the groups G_{20}^{P} of the crystallographic P symmetries and the symmetry groups G_{520} modeled by the former ones. Using the formula from [10] for calculating the number of 122 hypercrystallographic P symmetries of the first order, we have $122 \times 2 + 380 \times 1 = 624$ limiting groups whose subgroups are the groups G_{20}^{P} of the first-order hypercrystallographic P symmetries and the symmetry groups G_{6520} modeled by these groups. Substituting the above K, M_2, and M_P values into the formula from [11], we determine the number of the limiting groups of 624 hypercrystallographic second-order P symmetries $624 \times 2 + 3114 \times 1 = 4362$ whose subgroups are the groups G_{20}^{P} of these P symmetries and the symmetry groups G_{76520} modeled by these groups.

The numbers of the limiting subgroups whose subgroups are the groups G_{320}^{P} of the P symmetries mentioned above are determined in the similar way, because we have for limiting groups of category G_{320} all the numerical data necessary for the use of the formulas from [9, 11]: $K = 5$, $M_2 = M_{21} = 6$, $M_{2'} = M_{22} = 3$, and $N_P = 0$ at the remaining P symmetries that enter these formulas [5, 6, 8].

Substituting the symbol values into the formula from [9] for calculating the number of groups of the 10 rosette P symmetries, we have $10 \times 5 + 11 \times 6 + 3 \times 3 = 125$ limiting groups whose subgroups are the groups G_{320}^{P} of these 10 P symmetries and the groups G_{5320} modeled by these groups and coinciding with the symmetry groups G_{5420} [6, 8]. In a similar way, using the formula from [9] for calculating the number of groups of 31 tablet P symmetry, we obtain $31 \times 5 + 63 \times 6 + 17 \times 6 + 12 \times 3 = 671$ limiting groups whose subgroups are the groups G_{320}^{P} of this 31 P symmetry and the groups G_{65320} modeled by these groups and coinciding with the symmetry groups G_{65420}. At the same values of the unknowns, the formula from [9] for calculating the groups of 125 hypertablet P symmetries of the first order yields $125 \times 5 + 421 \times 6 + 259 \times 6 + 60 \times 3 = 4885$ limiting groups whose subgroups are the groups G_{320}^{P} of these 125 P symmetries and the groups G_{765320} modeled by these group and coinciding with the symmetry groups G_{765420}. In a similar way, using the formulas from [9] for establishing the number of groups of the 671 hypertablet P symmetry of the second order and substituting the values of the unknowns, we obtain $671 \times 5 + 354 \times 6 + 3857 \times 6 + 384 \times 3 = 48907$ limiting groups whose subgroups are the G_{320}^{P} groups of this 671 P symmetry and the groups $G_{8765320}$ modeled by these groups and coinciding with the symmetry groups $G_{8765420}$.

Now, substituting the values of the unknowns and $M_{22} = 1$ into the formula from [10] for calculating the groups of 32 crystallographic P symmetries, we have $32 \times 5 + 58 \times 6 + 14 \times 6 + 2 \times 1 + 10 \times 3 = 624$ limiting groups whose subgroups are the groups G_{320}^{P} of these 32 P symmetries and the groups F_{6320} modeled by these groups and coinciding with the symmetry groups G_{6520}. The formula from [10] for calculating the groups of the 122 hypercrystallographic P symmetries of the first order allows us to calculate at the same values of the unknowns the number $122 \times 5 + 380 \times 6 + 217 \times 6 + 5 \times 1 + 55 \times 3 = 4362$ of the limiting groups whose subgroups are the groups G_{320}^{P} of these 122 P symmetries and the groups G_{76320} modeled by these groups and coinciding with the symmetry groups G_{76520}. Finally, substituting the values of the unknowns into the formula from [11] for calculating the number of groups of the 624 hypercrystallographic P symmetries of the second order, we obtain $624 \times 5 + 3114 \times 6 + 3220 \times 6 + 16 \times 1 + 384 \times 3 = 42292$ limiting groups whose subgroups are the groups G_{320}^{P} of these 624 P symmetries

and the groups G_{876320} modeled by these groups and coinciding with the symmetry groups G_{876520}. The same numbers of the limiting groups whose subgroups are the coinciding categories of the multidimensional symmetry groups confirm the correctness of the above calculations.

For the remaining limiting groups of the category G_{30}, the values of the unknowns that enter the formulas from [9–11] which we already used twice are, $K = M_2 = 7$, $M_{2_1} = 6$, $M_{2'} = M_{22} = 3$, $M_{22} = 1$, and $M_P = 0$ for the other P symmetries used in these formulas. Substituting these numerical data into the formulas from [9], we obtain the following: (1) $10 \times 7 + 11 \times 7 + 3 \times 3 = 156$ limiting groups whose subgroups are the groups G_{30}^P of the 10 rosette P symmetries and the groups G_{530} modeled by these groups and coinciding with the symmetry groups G_{520}; (2) $31 \times 7 + 63 \times 7 + 17 \times 6 + 12 \times 3 = 796$ limiting groups whose subgroups are the G_{30}^P groups of the 31 tablet P symmetry and the groups G_{6530} modeled by these groups and coinciding with the symmetry groups G_{6520}; (3) $125 \times 7 + 421 \times 7 + 259 \times 6 + 60 \times 3 = 5556$ limiting groups whose subgroups are the groups G_{30}^P of the 125 hypertablet P symmetries of the first order and the groups G_{6530} modeled by these groups and coinciding with the symmetry groups G_{6520}; and (4) $671 \times 7 + 3543 \times 7 + 3857 \times 6 + 384 \times 3 = 53792$ limiting groups whose subgroups are the groups G_{30}^P of the 671 hypertablet P symmetry of the second order and the groups G_{76530} modeled by these groups and coinciding with the symmetry groups G_{76520}.

Then, knowing the values of the unknowns in formulas from [10, 11], we obtain: (1) $32 \times 7 + 58 \times 7 + 2 \times 1 + 10 \times 3 + 14 \times 6 = 746$ limiting groups whose subgroups are the groups G_{30}^P of 32 crystallographic P symmetries and the groups G_{630} modeled by these groups; (2) $122 \times 7 + 380 \times 7 + 5 \times 1 + 55 \times 3 + 217 \times 6 = 4986$ limiting groups whose subgroups are the groups G_{30}^P of the 122 hypercrystallographic P symmetries of the first order and the groups G_{7630} modeled by these groups; and (3) $624 \times 7 + 3114 \times 7 + 16 \times 1 + 368 \times 3 + 3220 \times 6 = 46606$ limiting groups whose subgroups are the groups G_{30}^P of hypercrystallographic P symmetries of the second order and the groups G_{87630} modeled by these groups. The latter calculation completes the solution of the formulated problem, which was started in [14].

In the course of the problem solution it became clear that the pairs of the coinciding categories G_{5420}, G_{5320} and G_{65420}, G_{65320} are the subgroups of equal numbers of the limiting groups, which is quite natural. However the limiting groups of the pairs of the coinciding categories G_{520}, G_{530}; G_{6520}, G_{6530}; and G_{76520}, G_{76530} are not equal because of the specific feature of the systematics of the groups G_{30}, G_{30}^l, and G_{30}^P. It should be remembered that the systematics of the groups G_{20}, G_{20}^l, G_{20}^P, G_{320}, G_{320}^l, and G_{320}^P, similar to that in [19, 20], lead to the limiting groups that terminate only the infinite series of discrete groups of these categories, whereas the systematics of groups G_{30}, G_{30}^l, and G_{30}^P lead not only to the infinite series but also to infinite series containing discrete groups, which do not allow one to obtain the limiting groups sought by tending to infinity the order of the rotation axis of the classical or generalized symmetry in the symbols of the generating elements (see tables in [19, 20]). This specific feature of the systematics of three-dimensional point groups and their generalizations is unimportant for establishing the number of the limiting groups of the category G_{30}^l by calculating the number of the groups generated by the Curie symmetry groups in their generalization with the l-tuple antisymmetry, but it is very important for establishing in a similar way the number of the limiting groups of the category G_{30}^P. It follows from this that the symmetry groups of the categories G_{530}, G_{6530}, and G_{76530} are successively the subgroups not of 156, 796, and 5556 limiting groups but of 122, 624, and 4362 limiting groups.

NUMERICAL RESULTS

The numerical results of the study performed with the indication of the numbers of various discrete crystallographic symmetry groups and their limiting groups in the form of the coefficients before the category symbols are represented as follows. 10(2) G_{20}, 31(5) G_{320}, 125(16) G_{4320}, 671(67) G_{54320}, 4885(374) G_{654320}, 48907(2825) $G_{7654320}$, 263(31) G_{420}, 1274(125) G_{5420} (=G_{5320}), 8806(671) G_{65420} (=G_{65320}), 84313(4885) G_{765420} (=G_{765320}), 1208(122) G_{520} (=G_{530}), 7979(624) G_{6520} (=G_{6530}), 73589(4362) G_{76520} (=G_{76530}, G_{76320}); 1129572(48907) $G_{8765320}$ (=$G_{8765420}$), 789691(42244) G_{876320} (=G_{876520}, G_{876530}); 32(7) G_{30}, 122 (21) G_{430}, 624(83) G_{5430}, 4362(441) G_{65430}, 42292(3199) G_{765430}, 7311(746) G_{630}, 64471(4986) G_{7630}, 814871(46606) G_{87630} (cf. [14, 15]).

ACKNOWLEDGMENTS

I would like to express my deep gratitude to V.A. Koptsik for the discussion of the results obtained and his valuable remarks.

REFERENCES

1. A. V. Shubnikov, *Symmetry and Antisymmetry of Finite Figures* (Akad. Nauk SSSR, Moscow, 1951) [in Russian].
2. N. V. Belov and T. N. Tarkhova, Kristallografiya **1** (1), 4 (1956) [Sov. Phys. Crystallogr. **1**, 5 (1956)].
3. V. A. Koptsik, *The Shubnikov Groups* (Mosk. Gos. Univ., Moscow, 1966) [in Russian].
4. A. V. Shubnikov and V. A. Koptsik, *Symmetry in Science and Art* (Nauka, Moscow, 1972; Plenum, New York, 1974).
5. A. M. Zamorzaev, *The Theory of Simple and Multiple Antisymmetry* (Shtiintsa, Chisinau, 1976) [in Russian].
6. A. M. Zamorzaev, É. I. Galyarskiĭ, and A. F. Palistrant, *Color Symmetry, Its Generalizations and Applications* (Shtiintsa, Chisinau, 1978) [in Russian].
7. B. K. Vaĭnshteĭn, *Crystal Symmetry. Methods of Structural Crystallography* (Nauka, Moscow, 1979) [in Russian].
8. A. M. Zamorzaev, Yu. S. Karpova, A. P. Lungu, and A. F. Palistrant, *P-Symmetry and Its Further Development* (Shtiintsa, Chisinau, 1986) [in Russian].
9. A. F. Palistrant, Kristallografiya **45** (6), 967 (2000) [Crystallogr. Rep. **45**, 887 (2000)].
10. A. M. Zamorzaev and A. F. Palistrant, Kristallografiya **44** (6), 976 (1999) [Crystallogr. Rep. **44**, 909 (1999)].
11. A. F. Palistrant and A. M. Zamorzaev, Kristallografiya **45** (1), 7 (2000) [Crystallogr. Rep. **45**, 1 (2000)].
12. A. V. Shubnikov, Tr. Lab. Kristallogr. Akad. Nauk SSSR, No. 2, 7 (1940).
13. A. V. Shubnikov, Usp. Fiz. Nauk **59** (4), 591 (1956).
14. A. F. Palistrant and S. V. Jablan, Filomat (Nis) **8**, 41 (1994).
15. A. F. Palistrant, in *Abstracts of International Conference on Geometry "As a Whole"* (Cherkassy, 1997), p. 74.
16. A. M. Zamorzaev, Izv. Akad. Nauk Resp. Mold., Mat., No. 1, 75 (1994).
17. A. F. Palistrant, Izv. Akad. Nauk Resp. Mold., Mat., No. 1, 21 (1994).
18. A. M. Zamorzaev, Izv. Akad. Nauk Resp. Mold., Mat., No. 2, 22 (1995).
19. A. V. Shubnikov, Kristallografiya **4** (3), 286 (1959) [Sov. Phys. Crystallogr. **4**, 267 (1960)].
20. A. V. Shubnikov, Kristallografiya **6** (4), 490 (1961) [Sov. Phys. Crystallogr. **6**, 394 (1962)].
21. L. A. Shuvalov, Kristallografiya **7** (6), 822 (1962) [Sov. Phys. Crystallogr. **7**, 669 (1963)].

Translated by L. Man

Crystallography Reports, Vol. 50, No. 1, 2005, pp. 10–12. Translated from Kristallografiya, Vol. 50, No. 1, 2005, pp. 16–18.

THEORY OF CRYSTAL STRUCTURES

On the Modeling of Crystal Structures and the Growth of Crystals

N. L. Smirnova

Moscow State University, Vorob'evy gory, Moscow, 119992 Russia

Received February 26, 2003

Abstract—It is demonstrated that the universal laws of system organization govern the growth of crystals and the construction of models of crystal structures. It is established that there is an interrelation between the growth of crystals of chemical compounds and the modeling of their crystal structures. © *2005 Pleiades Publishing, Inc.*

Differentiation–integration is one of the universal principles of the organization and the development of various systems [1–3]. Upon transition from a single-component system to a binary system, there arises a heterogeneity that leads to a polarity of the interaction and the diversity as a universal property of the systems. As a consequence of the bond polarity in the medium, atoms of one type in a crystal at the growth front tend to be surrounded by atoms of another type (the principle of nonindifference) [4], which, for particular compositions, results in ordering. The physical reason for the atomic ordering lies in the fact that, in the alloys able to undergo ordering, the structure in which atoms of a particular type are surrounded by atoms of another type appears to be more energetically favorable [5]. At high temperatures, this arrangement of atoms leads to the formation of a structure with a short-range order. For the same reason, a decrease in the temperature is accompanied by an order–disorder phase transition and brings about the formation of an ordered structure with a long-range order. Energetically, the configurations in which atoms of one component are surrounded by atoms of another component are characterized by lower energies [6]. According to [7], the ordering axiom implies the formation of the same environment of identical particles at a specific concentration.

None of the theories elaborated thus far allows one to construct any possible ordered structures [6]. For example, within the framework of the Gorsky–Bragg–Williams approach and other theories, the structure of an ordered phase is assumed to be known in advance. Therefore, the investigation into the processes of ordering, in essence, is reduced to a thermodynamic analysis of a particular phase transition between two phases with known structures.

Another universal law that governs the organization of systems is the law of small numbers. This law was established in different areas of knowledge by many scientists, such as Empedocles, Dalton, Häuy, Bogdanov, Goldschmidt, and Pauling. More recently, the law of small numbers was formulated as a universal law for all systems: upon the formation of organized (ordered) systems, the number of different types of objects should be small (from 1 to 4). A more complex object is built up of 1 to 4 simpler different subunits [8, 9]. The generalized law of small numbers states that the binary ratios occurring in nature and composed of numerals that are larger than several units (1–4) are nonuniformly distributed and form arithmetic progressions of binary ratios in which not only the initial ratios (for example, 1 : 1) but also the ratios added term by term (for example, 0 : 1) consist of small numerals [10].

The rigorous law of small numbers restricts the diversity and requires a uniformity of elements and their local coordination. The single-type short-range order uniquely determines the long-range order, the small number of parent structures, and their composition [8]. The nonrigorous law of small numbers admits the formation of series of structures with constant or variable compositions [8, 11]. An ordered polymorphism and isomorphism in spaces of different dimensions are treated as the constructive laws of system organization [12].

Manifestations of an ordered polymorphism and isomorphism in polytypic mixed-layered structures have been known since the early 20th century. In [13], the following law was formulated: superstructures are built up of two different structural fragments (layers of polyhedra, structural minals, modules) according to the law of ordered microepitaxy, i.e., according to one of the basic laws of structure formation. Owing to the difference between the structural fragments, in the general case, there exists a two-dimensional (in one direction) heteropolytypism, which has the form of polytypism if a combination of two different structural minals is treated as a single layer.

Series of structural minals and other fragments can be dominant: *c*'*c*", *c*'*c*"*c*", *c*'*c*"*c*"*c*", *c*'*c*"*c*'*c*", *c*'*c*"*c*'*c*"*c*", *c*'*c*"*c*"*c*'*c*"*c*", and *c*'*c*"*c*'*c*"' [14]. An increase in the sequences composed of *c*" structural

1063-7745/05/5001-0010$26.00

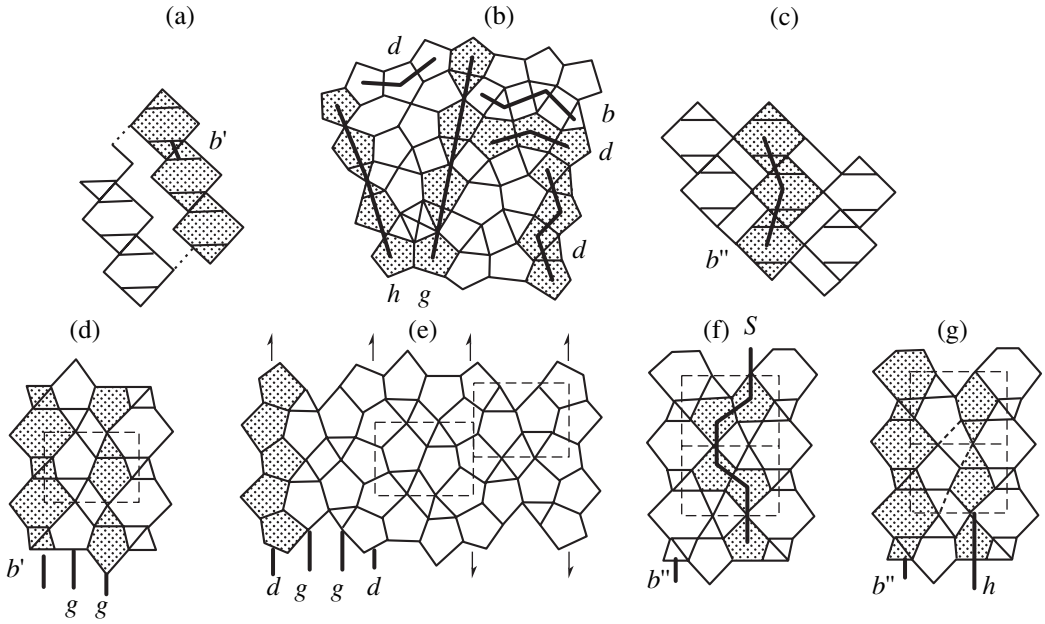

Fig. 1. Coatings of the plane with triangles, tetragons, pentagons, hexagons, and ribbons formed by these polygons. For explanation, see the text.

minals leads to the formation of lamellas and segregation. Upon ordering, defects of different types (including twinning planes that break the structural periodicity) form nuclei and then aggregates, twins, or new structures of real or hypothetical substances. Layers have a tendency either toward segregation or toward ordering. The boundary between quasi-homogeneous real crystals and crystalline (including epitaxial and syntaxial) aggregates is smeared [15, 16]. Supramolecular nonequilibrium phenomena in spatially modulated crystals [17] and the formation of suprastructures and superstructures can take place.

In the course of crystal growth, a small number of radicals (from 1 to 4) formed by different atoms, rather than a large number of these atoms themselves, are incorporated into the structure. The crystal is a matrix into which atoms, molecules, and their groupings are incorporated. Atoms and their ensembles can be embedded in a small number of positions. Symmetry is considered as a system controlling the crystal growth. After this system nucleates, there occurs an intensive ordered precipitation of atoms and their ensembles along the directions of the symmetrical greatest common divisors.

The growth of crystals of chemical compounds and the modeling of their crystal structures are governed by similar principles; i.e., the principles of modeling of crystal structures are closely related to the principles of crystal growth.

The first models of structural types of crystalline compounds were constructed on the basis of the nonindifference principle and the law of small numbers [8, 13]. The proposed models and the corresponding compositions were confirmed by using the example of hundreds of structural types considered in [12], models and structural types analyzed in [6, 18–20], etc. The "wave" character of the structure of solids stems from these two basic principles of the constructive-minal concept.

Let us consider novel structures that are described by the models developed previously with the use of the nonindifference principle and the law of small numbers. The genetics of coatings of the plane with different structural elements, such as triangles, tetragons, pentagons, and hexagons (hereafter, these elements will be denoted by numerals 3, 4, 5, and 6, respectively), which form ribbons and then coatings upon monotypic joining, was analyzed earlier in [21]. The coatings of the plane with polygons are described either in terms of sharing of their edges (*e*) and vertices (*v*) or in terms of the absence of sharing (*i*–isolated).

The structures of α-uranophane and other minerals can also be described in the framework of the constructive-minal concept. For this purpose, the projections of the structures of the aforementioned minerals are compared with the coating 25 [21], which consists of triangles 3, tetragons 4, and pentagons 5 (Fig. 1b). Pentagons form a ribbon *d* (5*e*1), and triangles and tetragons make up a ribbon *b* (34). A fragment of coating 25 composed of these alternating ribbons forms a coating *db* (5*e*1.34) depicted at the right of Fig. 1b. Ribbon 5*e*1 corresponds to pentagonal bipyramids shared by edges, whereas ribbon 34 corresponds to tetrahedra (triangles) and tetragons. In this coating, one more ribbon, is worthy of notice, namely, *g* (5*i*1 or 53). The sharing of this ribbon by edges leads to the formation of the same coat-

ing but with a new configuration, namely, 53-*e*1. Ribbons 53 in the structures considered in [22] are topologically different due to the rotation of tetrahedra: 53(1) and 53(2). Apart from the coating composed of a ribbon 53(1), to the aforementioned structures there correspond heteropolytypes consisting of structural minals of the initial coatings 53(1).53(2) in ratios of 1 : 1 and 2 : 2. With due regard for the distortions, ribbons 5*e*1 also differ from each other. The first structure corresponds to the coating formed by ribbons 5*e*11, the second structure is associated with the coating consisting of ribbons 5*e*12, and the third structure is represented by the heteropolytype composed of ribbons 5*e*11.5*e*12 in a ratio of 1 : 1. Therefore, more than ten structures correspond to coatings of the type 5. These structures were considered in greater detail in [22].

The analysis of the structures of the glaserite–olgite (Fig. 1d), β-K_2SO_4 (Fig. 1e), $NaBa_3Si_2O_7(OH)$ (Fig. 1f), and $Ba_3NaGe_2[GeO_4]_2(OH)_6H_2(O,OH)_2$ (Fig. 1g) minerals revealed structural minals related by the symmetry elements [23]. However, the ribbons formed by the structural elements (pentagons 5) were not considered in [23]. In the structure shown in Fig. 1e, two ribbons *g* (5*i*1) corresponding to coating 25 [21] alternate with ribbons *d* (5*e*1) and form a new coating, namely, the heteropolytype consisting of ribbons 5*e*1.2.5*i*1 (*dgg*). In the structure depicted in Fig. 1d, two ribbons *g* (5*i*1) alternate with a ribbon *b*' (6*i*1) of coating 24 (type 6); i.e., this is a heteropolytype *b*"*gg* (6*i*1.2.5*i*1) of two coatings 25 (type 5) and 24 (type 6). Finally, the structures represented in Figs. 1f and 1g consist of ribbons *b*"*hh* (2.5*vi*.6*i*2) and *b*"*hh* (2.5*vi*.6*i*2). A ribbon *h* can also be referred to as ribbon 2.5*v*4 or 2.5*v*3. Pentagons in double ribbons form structural elements 5*e* joined together into a ribbon 5*ev*. This *S*-shaped ribbon can be seen in the coatings shown in Figs. 1b and 1g. Ribbon *S* (5*ev*) alternates with a ribbon *b*" (6*i*2) of coating 17 (type 6). Therefore, the small number of triangles, tetragons, pentagons, and hexagons and their combinations form numerous real structures and also defect structures, segregates, and lamellas in accordance with the constructive laws of two-dimensional ordered isomorphism.

Making allowance for the aforementioned nonindifference principle and the law of small numbers, it is possible to reduce considerably the variety of structure formation models and to predict a small number of possible variants.

REFERENCES

1. A. A. Bogdanov, *Tectology* (Ékonomika, Moscow, 1989), Vols. 1, 2 [in Russian].
2. V. F. Turchin, *Phenomenon of Science: A Cybernetic Approach to the Evolution* (ÉTS, Moscow, 2000) [in Russian].
3. *Great Soviet Encyclopedia* (Sovetskaya Éntsiklopediya, Moscow, 1972), Vol. 9, p. 305 [in Russian].
4. N. L. Smirnova, Vestn. Mosk. Univ., Ser. Geol., No. 8, 181 (1952).
5. M. A. Krivoglaz and A. A. Smirnov, *Theory of Ordered Alloys* (Fizmatlit, Moscow, 1958), p. 13 [in Russian].
6. A. G. Khachaturyan, *Theory of Phase Transformations and the Structure of Solid Solutions* (Nauka, Moscow, 1974), pp. 14, 102 [in Russian].
7. R. V. Galiulin, Usp. Fiz. Nauk **172** (2), 229 (2002).
8. N. L. Smirnova, Kristallografiya **1** (2), 165 (1956) [Sov. Phys. Crystallogr. **1**, 128 (1956)].
9. N. L. Smirnova, in *Proceedings of All-Union Conference on Crystal Chemistry of Inorganic Compounds* (L'vov. Gos. Univ., L'vov, 1971), p. 5.
10. N. L. Smirnova and N. V. Belov, Dokl. Akad. Nauk SSSR **279** (3), 633 (1984) [Sov. Phys. Dokl. **29**, 866 (1984)].
11. N. L. Smirnova, Kristallografiya **46** (1), 10 (2001) [Crystallogr. Rep. **46**, 4 (2001)].
12. N. L. Smirnova, Kristallografiya **4** (1), 20 (1959) [Sov. Phys. Crystallogr. **4**, 17 (1960)]; Kristallografiya **4** (5), 778 (1959) [Sov. Phys. Crystallogr. **4**, 734 (1960)].
13. N. L. Smirnova and R. N. Sheftal', Vestn. Mosk. Univ., Ser. Geol., No. 6, 85 (1968).
14. N. L. Smirnova, Vestn. Mosk. Univ., Ser. Geol., No. 3, 53 (1974).
15. A. G. Bulakh, *General Mineralogy* (S.-Peterb. Gos. Univ., St. Petersburg, 1999) [in Russian].
16. N. L. Smirnova, Kristallografiya **9** (2), 265 (1964) [Sov. Phys. Crystallogr. **9**, 206 (1964)].
17. V. A. Koptsik, *Regularities in the Development of Complex Systems: Evolution and Supramolecular Nonequilibrium Phenomena* (Nauka, Leningrad, 1980), p. 179 [in Russian].
18. V. S. Urusov, N. A. Dubrovinskaya, and L. S. Dubrovinskiĭ, *Design of Probable Crystal Structures of Minerals* (Mosk. Gos. Univ., Moscow, 1990) [in Russian].
19. N. L. Smirnova, *Problems in Crystallology* (Mosk. Gos. Univ., Moscow, 1976), p. 63 [in Russian].
20. S. V. Borisov, Kristallografiya **45** (5), 779 (2000) [Crystallogr. Rep. **45**, 709 (2000)].
21. N. L. Smirnova, Kristallografiya **21**, 822 (1976) [Sov. Phys. Crystallogr. **21**, 468 (1976)].
22. R. K. Rastsvetaeva, A. V. Arakcheeva, and A. V. Barinova, Vestn. Nizhegorod. Univ. im. N. I. Lobachevskogo, Ser.: Fiz. Tverd. Tela, No. 1 (4), 38 (2001).
23. Yu. K. Egorov-Tismenko, E. V. Sokolova, N. L. Smirnova, and N. A. Yamnova, Mineral. Zh. **6** (6), 3 (1984).

Translated by O. Borovik-Romanova

Crystallography Reports, Vol. 50, No. 1, 2005, pp. 102–107. Translated from Kristallografiya, Vol. 50, No. 1, 2005, pp. 109–114.

LATTICE DYNAMICS AND PHASE TRANSITIONS

Ferroelastic Domain Walls in $BiVO_4$

V. A. Nepochatenko* and E. F. Dudnik**

** Bila Tserkva State Agrarian University, Sobornaya pl. 8/1, Bila Tserkva, Kiev oblast, 09117 Ukraine*

e-mail: aaa@btsau.kiev.ua

*** Dnepropetrovsk State University, Dnepropetrovsk, 49050 Ukraine*

Received January 27, 2003

Abstract—Analysis of the domain structure is performed using the method of matching strains at the interface and the model of thin domain walls. Equations describing the matching interlayers for crystal lattices are derived and the interlayer parameters are obtained for all possible types of domain walls in $BiVO_4$. It is shown that the matching interlayers have monoclinic symmetry. A difference between the elastic energy of a domain wall and the parameters of adjacent orientation states is revealed. © *2005 Pleiades Publishing, Inc.*

INTRODUCTION

A model of a ferroelastic domain wall consisting of an induced phase (interlayer) was proposed in [1]. This interlayer performs matching of the crystal lattices of two adjacent orientational states via two thin interfaces. It is shown by an example of lead orthophosphate that two kinds of interlayers are possible: one with the symmetry of the paraelectric phase (*P* twinning) and the other with the symmetry of the ferroelectric phase (*F* twinning). In the case of the *P* twinning, all components of the spontaneous strain of the interlayer are zero, which results in the symmetry appropriate for the lattices of two adjacent domains. For the *F* twinning, only the main components of the spontaneous strain are zero, whereas the shear component is nonzero. In this case, the interlayers related to the first and second domains should be matched. To compensate the shear strain, each domain should be rotated along with its interlayer around the corresponding axis, which gives rise to a symmetry element that is necessary to match the interlayers. This kind of twinning leads to a change in the form of the crystal.

In terms of this model, the induced phase (interlayer) is matched with the ferroelastic phase through two thin parallel interfaces. A model of a thin planar interface for the low-temperature monoclinic phase was proposed in [2]. The equation for the interface is obtained from the condition that the interface surface is common for the two lattices. Upon formation of the interface, rotation of the crystallographic axes at a small angle ψ is observed. We will refer to this angle as the phase-matching angle.

According to the above model, the elastic energy of a domain wall is localized in the interlayer. Since the elastic energy is proportional to the interlayer thickness, in order to minimize it, the domain-wall thickness was assumed to be equal to the smallest distance at which lattice parameters make sense; i.e., the distance between the parallel interfaces should be large enough to contain, at least, one cell of the induced phase.

It is of interest to apply this approach to the analysis of the structure of domain walls in $BiVO_4$, the orientation of which is not determined by the symmetry elements of the high-temperature phase.

Bismuth vanadate belongs to the class of pure proper ferroelastics [3]. At 225°C, a second-order transition from the tetragonal β phase (sp. gr. $I4/a$) to the monoclinic α phase ($I2/b$) is observed in this crystal [4, 5]. Two types of domain walls, W_1' and W_2', which are almost perpendicular to each other (~91°), are observed in the ferroelastic α phase [6]. Orientation of the domain walls depends on the spontaneous-strain components [7]. The angle between a domain wall and the [100] direction is 37.4° (according to [6], ~32°) and the domain-wall width is smaller than 200 Å. It was found that each orientation state can take two similar orientations (with a difference of ~1°) [8].

Since there is a significant spread of experimental data on the domain-wall orientation (~5°), in this study, in contrast to [1], the initial equation for a domain wall is considered unknown and a more general approach is used to solve this problem.

We will use the following orthogonal coordinate system: the *X* and *Z* axes are parallel to the *a* and *c* axes, respectively, and the *Y* axis makes an angle $\varphi = \gamma - 90°$ with the *b* axis. Let us introduce the following designations. Parameters of the β phase are a_0 and c_0; parameters of the α phase are a_1, b_1, c_1, and $\varphi_1 = \gamma_1 - 90°$; interlayer parameters are a_2, b_2, c_2, and $\varphi_2 = \gamma_2 - 90°$; orientation states are C_1 and C_2; coordinate systems are x_1, y_1, and z_1 for C_1; x_2, y_2, and z_2 for C_2; x_3, y_3, and z_3 for

the interlayer from the side of C_1; and x_4, y_4, and z_4 for the interlayer from the side of C_2; and (IFs) : IF1 and IF2 are thin interfaces from the side of C_1 and C_2, respectively.

STRUCTURE OF DOMAIN WALLS

A domain wall consists of an interlayer and two parallel interfaces, the orientation of which should coincide with the orientation of the domain wall. According to [2], the equation for a thin interface matching two monoclinic cells with the parameters a_1, b_1, c_1, $\varphi_1 = \gamma_1 - 90°$ and a_2, b_2, c_2, $\varphi_2 = \gamma_2 - 90°$ has the following form in the coordinate system of the first cell:

$$X_1^2 A_{11} + Y_1^2 A_{22} + Z_1^2 A_{33} + 2X_1 Y_1 A_{12} = 0, \quad (1)$$

where

$$A_{11} = 1 - \left(\frac{a_2}{a_1}\right)^2,$$

$$A_{22} = 1 - \frac{1}{\cos^2\varphi_1}\left(\left(\frac{b_2}{b_1}\right)^2 \cos^2\varphi_2 + \left(\frac{a_2}{a_1}\sin\varphi_1 - \frac{b_2}{b_1}\sin\varphi_2\right)^2\right),$$

$$A_{33} = 1 - \left(\frac{c_2}{c_1}\right)^2,$$

$$A_{12} = -\frac{a_2}{a_1\cos\varphi_1}\left(\frac{a_2}{a_1}\sin\varphi_1 - \frac{b_2}{b_1}\sin\varphi_2\right).$$

In the coordinate system of the second cell, this equation can be written as

$$X_2^2 B_{11} + Y_2^2 B_{22} + Z_2^2 B_{33} + 2X_2 Y_2 B_{12} = 0, \quad (2)$$

where

$$B_{11} = 1 - \left(\frac{a_1}{a_2}\right)^2,$$

$$B_{22} = 1 - \frac{1}{\cos^2\varphi_2}\left(\left(\frac{b_1}{b_2}\right)^2 \cos^2\varphi_1 + \left(\frac{a_1}{a_2}\sin\varphi_2 - \frac{b_1}{b_2}\sin\varphi_1\right)^2\right),$$

$$B_{33} = 1 - \left(\frac{c_1}{c_2}\right)^2,$$

$$B_{12} = -\frac{a_1}{a_2\cos\varphi_2}\left(\frac{a_1}{a_2}\sin\varphi_2 - \frac{b_1}{b_2}\sin\varphi_1\right).$$

Under the condition

$$\det|A_{ij}| = 0 \quad (3)$$

Eq. (1) corresponds to the equation of two intersecting planes. From (3), we obtain

$$A_{33}(A_{11}A_{22} - A_{12}^2) = 0.$$

Two situations are possible:

$$A_{33} = 0, \quad (4)$$

$$A_{11}A_{22} - A_{12}^2 = 0. \quad (5)$$

As will be shown below, situation (4) is implemented in $BiVO_4$. Hence,

$$c_2 = c_1 \quad (6)$$

and (1) corresponds to the following equations for interfaces:

$$X_1 + BY_1 = 0, \quad (7)$$

$$X_1 + NY_1 = 0, \quad (8)$$

where $B = D_{12} - \sqrt{D_{12}^2 - D_{22}}$, $N = -1/B = D_{12} + \sqrt{D_{12}^2 - D_{22}}$, $D_{12} = A_{12}/A_{11}$, and $D_{22} = A_{22}/A_{11}$.

We will find the domain-wall equation from the condition for matching the thermal-expansion tensor at the interface in the coordinate system of C_1. Let the angle between adjacent orientation states be α. Then, according to [9], we obtain the following domain-wall equations:

$$X_1 + KY_1 = 0, \quad (9)$$

$$X_1 - \frac{1}{K}Y_1 = 0, \quad (10)$$

where

$$K = \frac{2e_{12}\sin\alpha - (e_{11} - e_{22})\cos\alpha + \sqrt{4e_{12}^2 + (e_{11} - e_{22})^2}}{(e_{11} - e_{22})\sin\alpha + 2e_{11}\cos\alpha},$$

and e_{ij} are the components of the thermal-expansion tensor.

We will denote the domain walls described by Eqs. (9) and (10) as W_1' and W_2', respectively. Let us consider whether F twinning is possible upon the formation of W_1'. Since the equation for the interface coincides with the domain-wall equation, we derive from (7)–(9) that

$$K = D_{12} \pm \sqrt{D_{12}^2 - D_{22}}. \quad (11)$$

For this type of twinning, only the main spontaneous-strain components of the matching interlayer are zero [1]. Therefore,

$$a_2 = b_2, \quad (12)$$

$$\varphi_2 \neq 0. \quad (13)$$

Thus, a monoclinic cell with a rhombic base corresponds to the interlayer from the side of C_1. The parameters of this cell are determined by Eqs. (6) and (11)–(13).

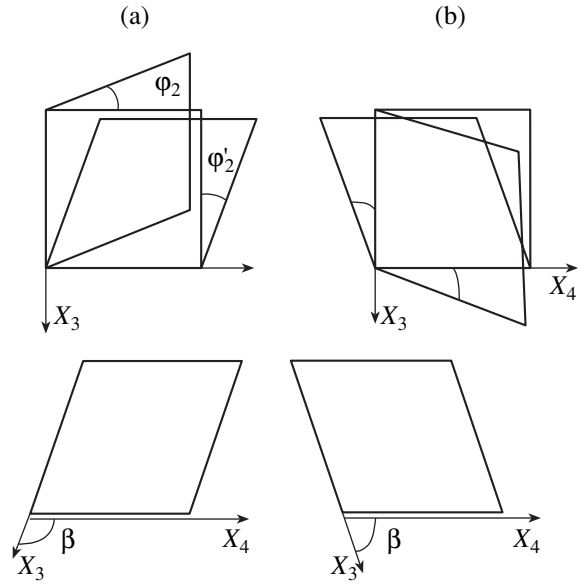

$\varphi_2 > 0, \varphi_2' < 0, \beta = \pi/2 + \varphi_2 \quad \varphi_2 < 0, \varphi_2' > 0, \beta = \pi/2 + \varphi_2$

Fig. 1. Schematic representaion of the matching conditions for interlayer cells (case of the *F* twinning): (a) $\varphi_2 > 0$, $\varphi_2' < 0$, and $\beta = \frac{\pi}{2} + \varphi_2$ and (b) $\varphi_2 < 0$, $\varphi_2' > 0$, and $\beta = \frac{\pi}{2} + \varphi_2$.

Figure 1 shows schematically two possible variants of matching the interlayer lattices for the *F* twinning (bases of the interlayers are shown). As can be seen, the angles φ_2 and φ_2' should have different signs and equal magnitudes. To match the lattices, the coordinate systems of the interlayers should be rotated with respect to each other at the angle φ_2.

The parameters of the interlayer from the side of C_2 are determined similarly (changing the sign of φ_2 in (1)). The equation for W_1' in the coordinate system of C_2 is derived from (9) derived by rotating the coordinate system by the angle α around the z_1 axis:

$$X_2 + MY_2 = 0, \tag{14}$$

where $M = (K\cos\alpha - \sin\alpha)/(\cos\alpha + K\sin\alpha)$.

Taking into account the above conditions, we obtain the system of equations determining the parameters of the interlayer from the side of C_2:

$$\begin{cases} c_2 = c_1 \\ a_2 = b_2 \\ M = D_{12}' \pm \sqrt{D_{12}'^2 - D_{22}'}, \end{cases} \tag{15}$$

where $D_{12}' = A_{12}'/A_{11}$ and $D_{22}' = A_{22}'/A_{11}$; the coefficients A_{12}' and A_{22}' differ from A_{12} and A_{22} by the sign of the angle φ_2.

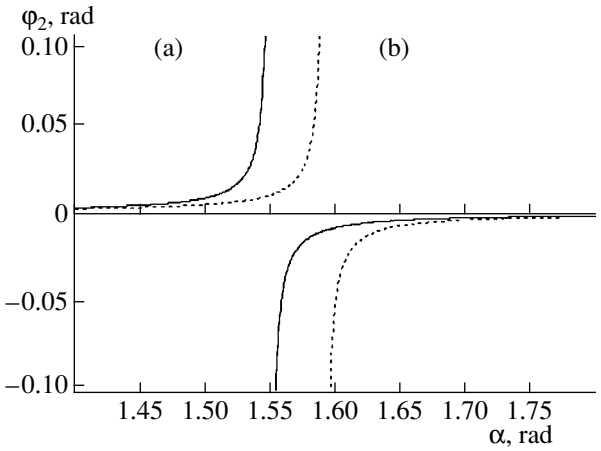

Fig. 2. Dependence of the parameter φ_2 on the angle α for the domain walls (a) W_1' and (b) W_2'.

Joint solution of (15) and (11) yields the dependences of φ_2 and a_2 on the angle α:

$$\varphi_2 = \arcsin L, \tag{16}$$

$$a_2 = a_1\sqrt{\frac{1+K^2}{K^2 - E/\cos\varphi_1}}, \tag{17}$$

where

$$L = \frac{U}{Q}, \quad Q = 2\frac{a_1}{b_1\cos\varphi_1}[P(K - \tan\varphi_1) - M - \tan\varphi_1],$$

$$P = \frac{1+M^2}{1+K^2},$$

$$U = M^2 - K^2P + 2\tan\varphi_1(KP - M) + \tan^2\varphi_1(1-P) - \left(\frac{a_1}{b_1\cos\varphi_1}\right)^2(P-1),$$

$$E = 2K\left(\sin\varphi_1 - \frac{a_1\sin\varphi_2}{b_1}\right) - \frac{1}{\cos\varphi_1}\left[\left(\frac{a_1}{b_1}\cos\varphi_2\right)^2 + \left(\sin\varphi_1 - \frac{a_1\sin\varphi_2}{b_1}\right)^2\right].$$

These dependences are shown in Figs. 2a and 3a. Such behavior of the interlayer parameters is due to the existence of the singularity $\alpha = 1.55$ rad, near which $Q \longrightarrow 0$. Discontinuities of the functions are observed at the interval $\alpha \in (1.5495, 1.55034)$.

Let us now determine the value of α that is implemented in the crystal. From Eq. (2), we obtain (in the same way as for Eqs. (6)–(8)) the equations for the

interfaces (and, therefore, for the domain wall) in the coordinate systems of the interlayers from C_1 and C_2:

$$X_3 + K_1 Y_3 = 0, \quad (18)$$

$$X_4 + M_1 Y_4 = 0, \quad (19)$$

where $K_1 = C_{12} \pm \sqrt{C_{12}^2 - C_{22}}$, $M_1 = C'_{12} \pm \sqrt{C'^2_{12} - C'_{22}}$, $C_{12} = B_{12}/B_{11}$, $C_{22} = B_{22}/B_{11}$, $C'_{12} = B'_{12}/B_{11}$, and $C'_{22} = B'_{22}/B_{11}$; the coefficients B'_{12} and B'_{22} differ from the corresponding coefficients B_{12} and B_{22} by the sign of the angle φ_2.

Analysis of the conditions for matching the interlayer crystal lattices (Fig. 1) shows that the angle between the planes determined by (18) and (19) should be equal to

$$\beta = \pi/2 - \varphi_2. \quad (20)$$

Numerical solution of (16)–(20) using the parameters of the β and α phases [4, 5] shows that two structures, W'_{11} and W'_{12}, correspond to the domain wall. The corresponding interlayer parameters are listed in the table, where D is the strain tensor with respect to the parameters of the ferroelastic phase; α is the angle between adjacent orientation states; ψ_1 and ψ_2 are the angles of rotation of the interlayer coordinate system with respect to C_1 and C_2, respectively (Fig. 4); and E_1 and E_2 are the surface densities of the elastic energy of the domain wall with respect to the parameters of C_1 and C_2, respectively. The energy of the domain walls was determined by the formula

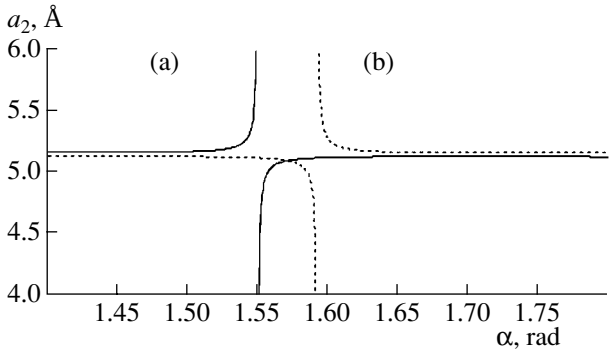

Fig. 3. Dependence of the parameter a_2 on the angle α for the domain walls (a) W'_1 and (b) W'_2.

$$E = \frac{d}{2} C_{ijkl} e_{ij} e_{kl}, \quad (21)$$

where C_{ijkl} are the elastic constants [10], e_{ij} are the components of the tensor D, and d is the domain-wall thickness (7 Å).

The structure of W'_2 was determined in the same way, except for condition (20), which was transformed

Parameters of the W'_1 and W'_2 structures of domain walls

	W'_1			W'_2		
	W'_{11}		W'_{12}	W'_{21}		W'_{22}
α, rad	1.5432		1.5559	1.5857		1.5984
K	–1.4303		–1.411	0.7313		0.7411
M	0.7411		0.7313	–1.411		–1.4303
φ_2, rad	0.06191		–0.07015	0.07015		–0.06191
a_2, Å	5.2997		4.9791	4.9791		5.2997
ψ_1, rad	0.03449		0.017	–0.03826		0.05506
ψ_2, rad	0.05506		–0.03826	0.017		–0.03449
$D \times 10^{-2}$	2.055 –2.762 0		–4.119 3.851 0	–4.119 –3.176 0		2.055 3.437 0
	4.141 0		–2.159 0	–2.1159 0		4.141 0
	0		0	0		0
E_1, J/m^2	0.1796		0.2247	0.1409		0.2041
E_2, J/m^2	0.2041		0.1409	0.2247		0.1796

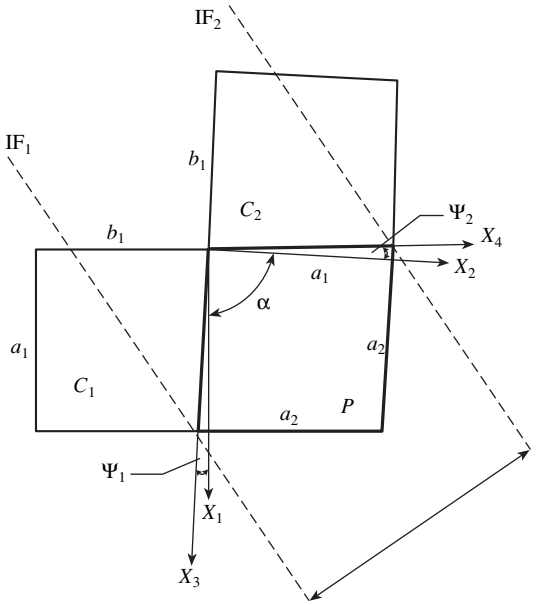

Fig. 4. Matching of the cells of the adjacent orientation states C_1 and C_2 by the interlayer P; α is the angle between the orientation states, IF_1 and IF_2 are the interfaces, ψ_1 and ψ_2 are the matching angles for the interfaces, and d is the domain-wall thickness.

as

$$\beta = \pi/2 + \varphi_2. \quad (22)$$

Figures 2b and 3b show the dependences of the parameters φ_2 and a_2 on the angle α. As can be seen, the singularity $\alpha = 1.5926$ rad and the curves are shifted to larger angles in comparison with the dependence for W_1'. Two structures (W_{21}' and W_{22}', see table) also correspond to this domain wall.

Since the P twinning is a particular case of the F twinning at $\varphi_2 = 0$, while this solution is absent, interlayers with the symmetry of the paraelectric phase are not formed in the crystal.

DISCUSSION OF THE RESULTS AND CONCLUSIONS

It can be seen from the results obtained that two structures are possible for each domain wall in $BiVO_4$. Four orientation states correspond to these structures. The angle between the domain wall and the [100] direction for these states takes values of 35°, 35.3°, 36.1°, and 36.5°. The latter value only slightly differs from the experimental one (37.4° [8]). The angle between adjacent orientation states is determined from the equation

$$\alpha = \pi/2 + \varphi_2 + \psi_1 - \psi_2, \quad (23)$$

where φ_2 is the matching angle for interlayer lattices, ψ_1 is the matching angle for the interface IF_1 between the ferroelastic phase C_1 and the induced phase P (interlayer), and ψ_2 is the matching angle for the interface IF_2 between C_2 and P (Fig. 4).

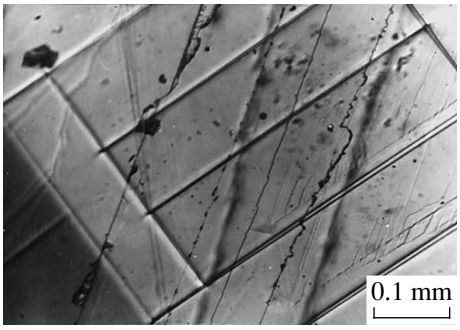

Fig. 5. Domain structure of $BiVO_4$.

The angle between the domain walls W_1' and W_2', depending on the structures involved in their formation, may have the following values: 91.2°, 91.58°, and 90.85°. Figure 5 shows the domain structure of $BiVO_4$ obtained during a short-term strain of a single-domain crystal. The angle between W_1' and W_2' is $91.4° \pm 0.5°$. Splitting of some domain walls into two similar walls is observed. The angle between these walls is $0.8° \pm 0.5°$. It is possible that this splitting corresponds to two structures of the domain wall (the difference in their orientations is 0.37°).

Since the angles φ_2 and φ_2' have different signs (Fig. 1), there is a difference in the shear component of the strain tensor D (determined with respect to the parameters of C_1 and C_2) and, therefore, in the domain-wall energy. We will refer to this difference as the anisotropy of the elastic energy of the domain wall:

$$\Delta E = E_1 - E_2. \quad (24)$$

Note that the two possible structures of the domain wall have different signs of ΔE.

Since the motion of a domain wall should be accompanied by a decrease in its energy, the multidomain state should be "pushed out" from the crystal. $BiVO_4$ single crystals (grown by the Czochralski method) are single-domain, which, apparently, is due to the joint action of the noted anisotropy and the second-order phase transition.

Thus, based on the domain-wall model proposed, we can conclude that (i) domain walls are thin in bismuth vanadate, (ii) matching interlayers for crystal lattices have the symmetry of the ferroelastic phase, and (iii) the elastic domain-wall energy differs slightly from the corresponding parameters of adjacent orientation states.

ACKNOWLEDGMENTS

We are grateful to A.Yu. Kudzin for his helpful participation in the discussion of the results.

REFERENCES

1. V. A. Nepochatenko, Kristallografiya **48** (2), 324 (2003) [Crystallogr. Rep. **48**, 290 (2003)].
2. E. F. Dudnik and V. A. Nepochatenko, Kristallografiya **25**, 984 (1980) [Sov. Phys. Crystallogr. **25**, 564 (1980)].
3. L. A. Shuvalov, Izv. Akad. Nauk SSSR, Ser. Fiz. **43** (8), 1554 (1979).
4. A. W. Sleight and H. Y. Chen, Mater. Res. Bull. **14** (12), 1571 (1979).
5. W. J. F. David, A. M. Glazer, and A. W. Hewat, Phase Transit. **1** (4), 155 (1979).
6. C. Manolikas and S. Amelinckx, Phys. Status Solidi A **60**, 167 (1980).
7. J. Sapriel, Ferroelectrics **13** (1–4), 459 (1976).
8. L. S. Wainer, R. F. Baggio, and H. L. Dussel, Ferroelectrics **31**, 121 (1981).
9. V. A. Nepochatenko, Kristallografiya **49**, 917 (2004) [Crystallogr. Rep. **49**, 828 (2004)].
10. L. P. Avakyants, A. M. Antonenko, E. F. Dudnik, *et al.*, Fiz. Tverd. Tela (Leningrad) **24** (8), 2486 (1982) [Sov. Phys. Solid State **24**, 1411 (1982)].

Translated by Yu. Sin'kov

Crystallography Reports, Vol. 50, No. 1, 2005, pp. 108–114. Translated from Kristallografiya, Vol. 50, No. 1, 2005, pp. 115–121.

LATTICE DYNAMICS AND PHASE TRANSITIONS

Characteristic Features of the Change of Domain Structure in Mixed $[(NH_4)_{1-x}Rb_x]_3H(SO_4)_2$ Crystals in the Vicinity of Superprotonic Phase Transition

L. F. Kirpichnikova*, M. Polomska, A. Pietraszko***, V. S. Shakhmatov****, and B. Hilczer****

** Shubnikov Institute of Crystallography, Russian Academy of Sciences, Leninskiĭ pr. 59, Moscow, 119333 Russia*
e-mail: luba@ns.crys.ras.ru
*** Institute of Molecular Physics, Polish Academy of Sciences, Poznan, 60-179 Poland*
**** Institute of Low Temperature and Structure Research, Polish Academy of Sciences, Wroclaw, 50-959 Poland*
e-mail: adam@int.pan.wroc.pl
***** Joint Institute for Nuclear Research, Moscow oblast, Dubna, 141980 Russia*
Received May 27, 2004

Abstract—X-ray diffraction measurements of mixed $[(NH_4)_{1-x}Rb_x]_3H(SO_4)_2$ crystals of different compositions are performed. The characteristics of the change of the domain structure in the vicinity of the supeprotonic–ferroelastic phase transition in crystals of different compositions are studied and compared with the variations of the crystal structure in the course of gradual substitution of ammonium by rubidium. This phase transition is theoretically described based on the phenomenological theory of a high-temperature phase transition.

INTRODUCTION

Mixed $[(NH_4)_{1-x}Rb_x]_3H(SO_4)_2$ (TARHS) crystals belong to the family of protonic conductors described by the general formula $M_3H(XO_4)_2$, where M = NH_4, Rb, and Cs and X = S and Se [1–5]. The structure of the high-temperature supeprotonic $(NH_4)_3H(SO_4)_2$ (TAHS) phase is trigonal, sp. gr. $R\bar{3}m$. The ferroelastic monoclinic phase (sp. gr. $A2/a$) of this compound is formed below T_S = 413 K [4, 6, 7]. Moreover, ammonium crystals at low temperature undergo four more phase transitions [4, 6]. TAHS crystals have three types of hydrogen bonds of which two link nitrogen atoms and oxygen atoms of sulfate tetrahedra. The third short symmetric hydrogen bond (2.54 Å) links two neighboring sulfate ions via the so-called apical proton [7]. It is important that $Rb_3H(SO_4)_2$ (TRHS) crystals undergo only one irreversible phase transition at T_S = 486 K, whereas the phase formed below T_S is not ferroelastic. Below T_S, the $Rb_3H(SO_4)_2$ crystals are monoclinic, sp. gr. $C2/c$ [8], and, according to [5, 9], they are transformed into the superprotonic cubic phase at T_S. The length of the apical hydrogen bond in rubidium-containing crystals is slightly shorter than in ammonium-containing ones [3, 5, 10]. The mixed $[(NH_4)_{1-x}Rb_x]_3H(SO_4)_2$ crystals exhibit supeprotonic properties; the temperature of the superprotonic phase transition increases with the gradual substitution of rubidium by ammonium. The compounds with $x > 0.5$ have two superprotonic phases [5, 9, 11].

Recently, we discovered an anomalous change of the ferroelastic domain structure in the vicinity of the superprotonic transition in the crystals of the $M_3H(XO_4)_2$ family [12, 13]. The unusual change of the domain structure in the vicinity of the superprotonic transition is of special interest, because the establishment of the cause of such behavior is important for more clear understanding of the characteristics of the microscopic mechanism of the transition into the phase with high conductivity. Moreover, the mixed crystals in the $[(NH_4)_{1-x}Rb_x]_3H(SO_4)_2$ system attract attention because TAHS crystals below the point of the superprotonic phase transition show ferroelastic properties, whereas TRHS crystals do not possess such properties.

Thus, it is important to study the mixed $[(NH_4)_{1-x}Rb_x]_3H(SO_4)_2$ crystals in more detail. Below, we describe our further study of the ferroelastic domain structure of mixed TARHS crystals, the X-ray diffraction studies of the crystals of various compositions, and the theoretical consideration of the superprotonic–ferroelastic phase transition in one of the mixed crystals with a high rubidium content.

EXPERIMENTAL

The study of the temperature variations of the ferroelastic domain structure of mixed $[(NH_4)_{1-x}Rb_x]_3H(SO_4)_2$ crystals with $x < 0.5$ showed that being cooled below T_S in a narrow (~2 K) temperature interval results in the appearance of a large num-

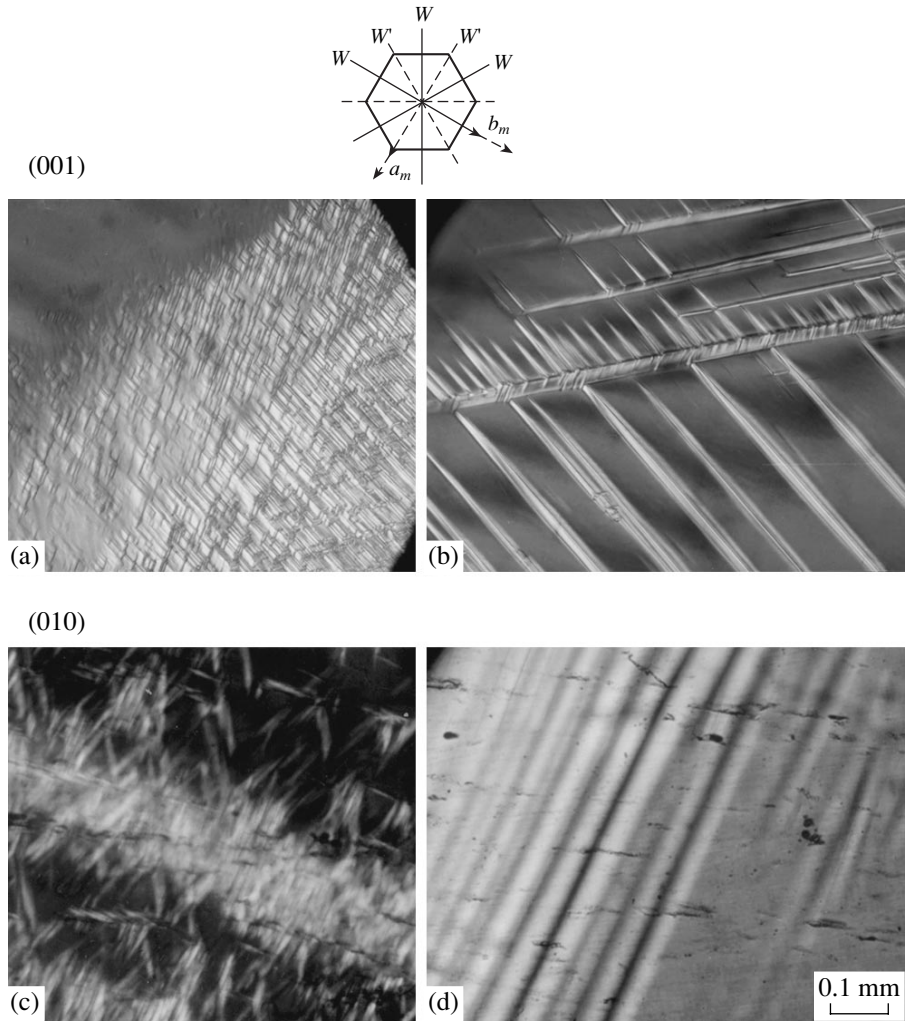

Fig. 1. Domain structure in the (001) cut of $[(NH_4)_{0.97}Rb_{0.03}]_3H(SO_4)_2$ crystals during their heating from the temperature of the superprotonic phase to the temperatures (a) (T_S – 1 K), (b) (T_S – 5.8 K) and in the (010) cut of these crystals to the temperatures (c) (T_S – 1 K) and (d) (T_S – 5 K).

ber of small lenslike domains (Figs. 1a and 1c). The domains are so small and distorted that it is difficult to establish how many orientational states can exist in this narrow temperature range. With further lowering of the temperature, large domains are also formed (Figs. 1b and 1d). We observed the domain walls of the *W* and *W*' type (Sapriel classification [15]) corresponding to the change of the symmetry from trigonal, $\bar{3}m$, to monoclinic, 2/*m*. In the superprotonic phase, the crystals are transparent and optically uniaxial. In the transition to the superprotonic phase, both TRHS crystals and also mixed crystals with $x > 0.9$ are disintegrated into small pieces. Below the first superprotonic phase transition, the crystals with high rubidium content also consist of very small domains, but no formation of large domains with further lowering of the temperature is observed. Below the temperatures (~T_S – 2 K), small domains are transformed into defect regions; the sample looses its transparency and becomes turbid. As is seen from Fig. 2a, in the superprotonic phase, the polydomain (001) cut of a $[(NH_4)_{0.3}Rb_{0.7}]_3H(SO_4)_2$ crystal becomes transparent (Fig. 2b). With a further increase in the temperature, the second supeprotonic phase is formed at T_{S2}, which is accompanied by the formation of brightly colored regions (Fig. 2c). The lowering of the temperature below T_{S2} made the sample polycrystalline and nontransparent. However, not by heating the crystal up to T_{S2}, but by first heating it only up to the temperature of the first superprotonic state and then decreasing it, small domains are formed at the temperatures lower than T_{S1}. These domains are transformed into defect regions (Fig. 2d) at the temperature (~T_{S1} – 2 K). The X-ray diffraction studies showed that the first superprotonic phase of mixed crystals is trigonal and is described by the sp. gr. $R\bar{3}m$, whereas the second superprotonic phase consists of a crystal in the polycrystalline state. The superprotonic phase of TRHS

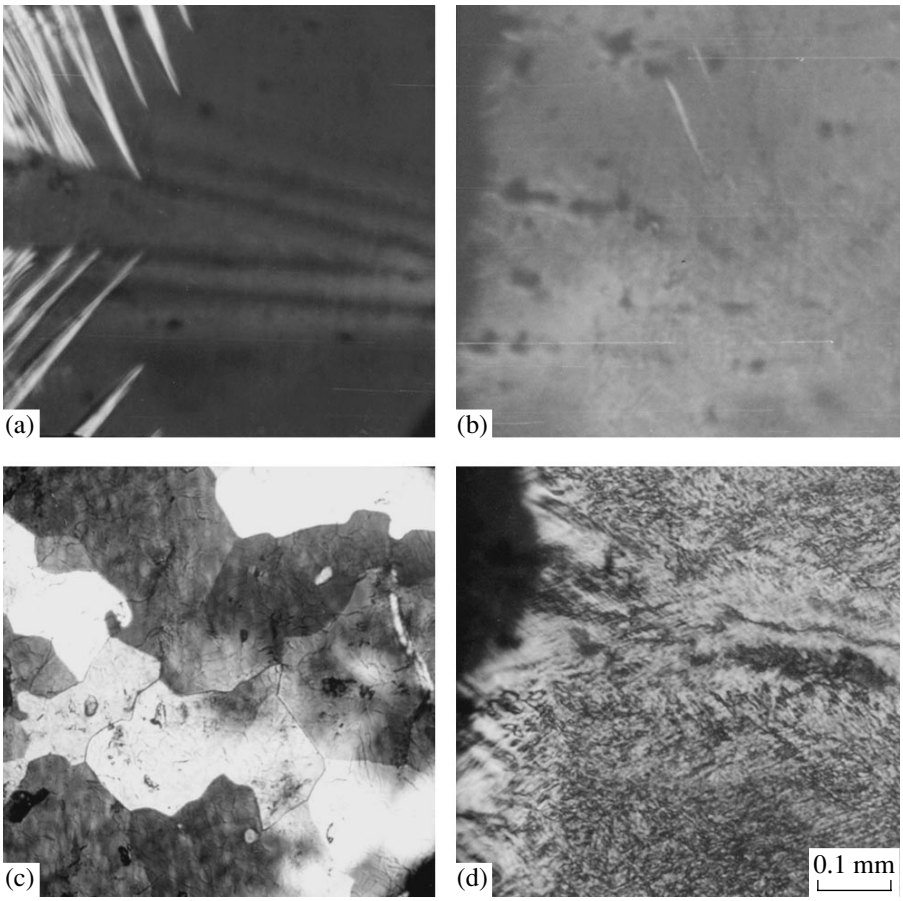

Fig. 2. Surfaces of the (001) cut of $[(NH_4)_{0.3}Rb_{0.7}]_3H(SO_4)_2$ crystals at (a) 300 K, (b) T_{S1}, (c) T_{S2}, and (d) after cooling below the temperature of the first superprotonic phase transition at ($T_S - 2$ K).

crystals is trigonal and is described by the sp. gr. $R\bar{3}m$ like all the other crystals of the $M_3H(XO_4)_2$ family.

The change of the unit-cell parameters of the crystals of the TARHS system at room temperature depends on the Rb concentration (Table 1). It is clearly seen from Table 1 that with the substitution of ammonium by rubidium, the unit-cell parameters, the monoclinicity angle, and the unit-cell volume remain almost unchanged.

Hydrogen bonds are of special importance and strongly effect the physical properties and thermodynamic stability of the crystalline state. The existence of isolated dimers is characteristic of the monoclinic crystal structure of mixed TARHS crystals: each two neighboring SO_4 ions are bonded via an apical proton and form a dimer. The parameters of the apical hydrogen O–H···O bond at room temperature in the monoclinic phase of different mixed TARHS crystals are indicated in Table 2. The measurements show that mixed crystals

Table 1. Unit-cell parameter of $[(NH_4)_{1-x}Rb_x]_3H(SO_4)_2$ crystals

x	a, nm	b, nm	c, nm	β, deg	V, nm^3
0					
0.03	1.5443	0.5870	1.0181	101.84	0.90328
0.05	1.5443	0.5870	1.0181	101.84	0.9033
0.70	1.5312	0.5877	1.0163	102.19	0.89409
0.86	1.5219	0.5889	1.0157	102.30	0.99842
1	1.5177	0.5901	1.0172	102.57	0.8892

Table 2. Donor–acceptor distance d_{D-A}, donor–hydrogen distance d_{D-H}, and hydrogen–acceptor distance $d_{H\ldots A}$ in hydrogen bonds in the (001) plane that link SO_4 tetrahedra into dimers in $[(NH_4)_{1-x}Rb_x]_3H(SO_4)_2$ crystals at room temperature

x	d_{D-A}, nm	d_{D-H}, nm	$d_{H\ldots A}$, nm
0			
0.03	0.2550	0.1275	0.1275
0.7	0.2543	0.0638	0.1928
0.86	0.2521	0.0686	0.1839
1	0.2503	0.0600	0.1920

with a high rubidium content and TRHS crystals have only slightly varying hydrogen bonds, but, what is very important, these hydrogen bonds become asymmetric. Figure 3 shows the temperature curves of the lattice parameters of the $[(NH_4)_{0.03}Rb_{0.97}]_3H(SO_4)_2$ crystals; Fig. 4, the temperature curves of the unit-cell volume of this compound.

The temperature dependences of the unit-cell parameters of the $[(NH_4)_{0.3}Rb_{0.7}]_3H(SO_4)_2$ crystal in the $D_{3d}^5(R\bar{3}m)$ and $C_{2h}^6(C2/c)$ phases may be described based on the phenomenological theory, because the $D_{3d}^5(R\bar{3}m) \longrightarrow C_{2h}^6(C2/c)$ transition is the subgroup phase transition. Figure 5 illustrates the relation between the monoclinic and trigonal the unit cells in the $D_{3d}^5(R\bar{3}m) \longrightarrow C_{2h}^6(C2/c)$ phase transition. In the low-temperature $C_{2h}^6(C2/c)$ phase, three domains (D_1, D_2, and D_3) are observed. The parameters of the crystal lattice of the domain at room temperature are as follows: $a_m = 10.16$ Å, $h_m = 5.88$ Å, and $c_m = 15.31$ Å, the monoclinicity angle is $\beta = 102.16°$. The main translation vectors of the crystal lattice in the $D_{3d}^5(R\bar{3}m)$ phase at $T \sim 475$ K are $|\mathbf{a}_1| \equiv a_{rh} = 8.23$ Å; $i = 1, 2, 3$; and the angle formed by vectors $\mathbf{a}_i$ and $\mathbf{a}_j$ equals $\alpha_{rh} = 42.2°$.

The expansion of the free energy, which describes the $D_{3d}^5(R\bar{3}m) \longrightarrow C_{2h}^6(C2/c)$ phase transition, has the form

$$F = F_\varphi + F_e + F_{\varphi e}. \quad (1)$$

The term F_φ dependent on the components of the order parameter $(\varphi_1, \varphi_2, \varphi_3)$ is written as

$$\begin{aligned} F_\varphi = {} & \frac{1}{2}r(\varphi_1^2 + \varphi_2^2 + \varphi_3^2) + \frac{1}{4}u_0'(\varphi_1^2 + \varphi_2^2 + \varphi_3^2)^2 \\ & + \frac{1}{4}u_1'(\varphi_1^4 + \varphi_2^4 + \varphi_3^4) \\ & + \frac{1}{4}u_2'[(2\varphi_1^2 - \varphi_2^2 - \varphi_3^2)^2 + 3(\varphi_2^2 - \varphi_3^2)^2] \\ & + \frac{1}{6}\nu(\varphi_1^2 + \varphi_2^2 + \varphi_3^2)^3, \end{aligned} \quad (2)$$

where $r = \alpha(T - T_c)$, T_c is the temperature of the phase transition; the constants $\alpha > 0$, u_i', and ν do not depend on the temperature; and the component of the order parameter φ_i is characterized by the wave vector $\frac{\mathbf{b}_i}{2}$. The second term F_e in Eq. (1) is the elastic energy,

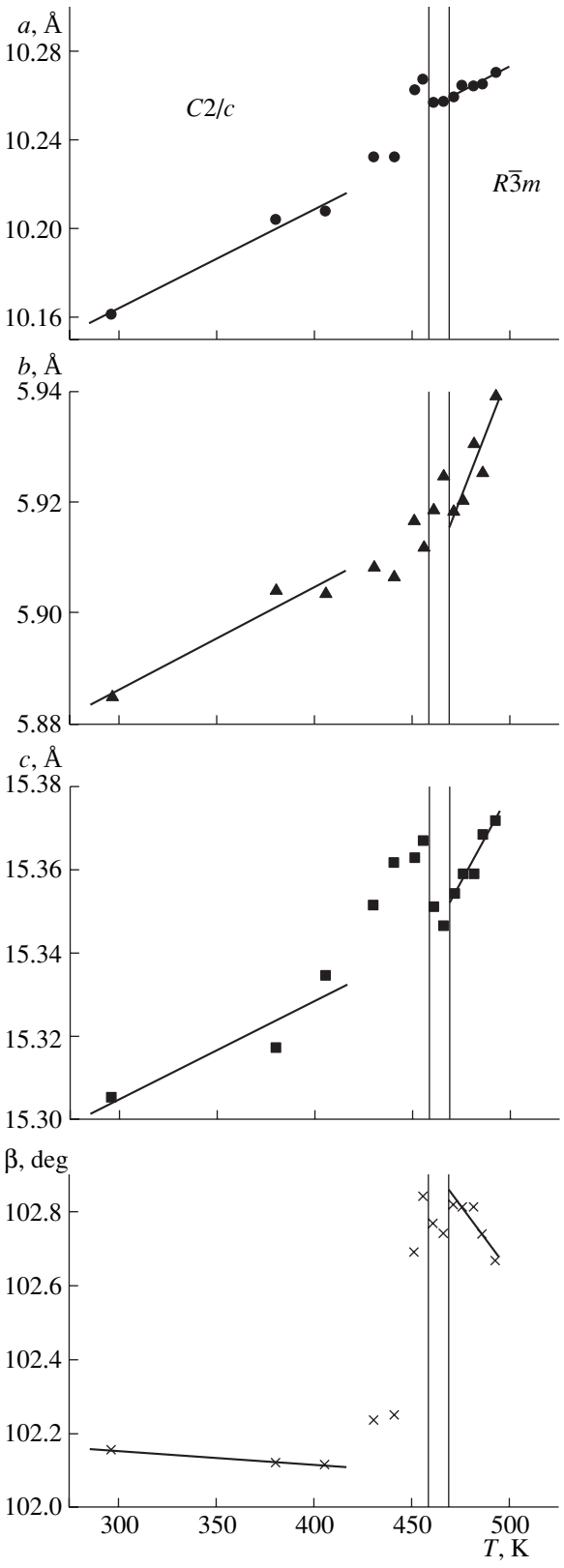

Fig. 3. Temperature curves of the lattice parameters in a $[(NH_4)_{0.3}Rb_{0.7}]_3H(SO_4)_2$ crystal in the $C_{2h}^6(C2/c)$ and $D_{3d}^5(R\bar{3}m)$ phases in the monoclinic setting.

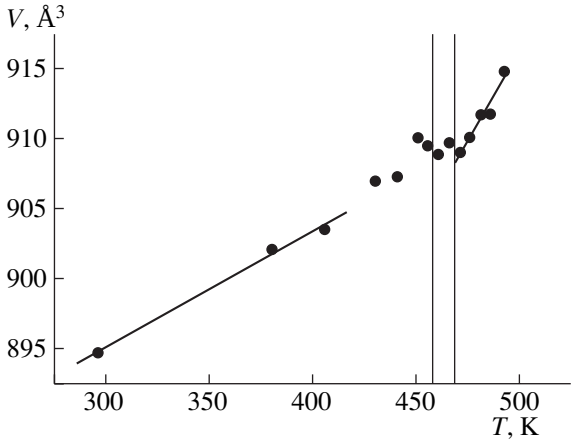

Fig. 4. Temperature dependence of the unit-cell volume of a $[(NH_4)_{0.3}Rb_{0.7}]_3H(SO_4)_2$ crystal in the monoclinic setting.

which may be written in the form

$$F_e = \frac{1}{2}C_{11}(e_1^2 + e_2^2) + \frac{1}{2}C_{33}e_3^2 + \frac{1}{2}C_{44}(e_4^2 + e_5^2) + C_{13}e_3(e_1 + e_2) + C_{14}[(e_1 - e_2)e_5 - 2e_4e_6] + \frac{1}{2}C_{16}[(e_1 - e_2)^2 + 4e_6^2], \quad (3)$$

where C_{ij} are the elasticity moduli and e_i are the components of the strain tensor. The last term in Eq. (1) describes the interaction of the order parameter with strains,

$$F_{\varphi e} = (\varphi_1^2 + \varphi_2^2 + \varphi_3^2)[\beta_1(e_1 + e_2) + \beta_3 e_3] + \beta_2[(2\varphi_1^2 - \varphi_2^2 - \varphi_3^2)(e_1 - e_2) - 2\sqrt{3}(\varphi_2^2 - \varphi_3^2)e_6] + \beta_5[(2\varphi_1^2 - \varphi_2^2 - \varphi_3^2)e_5 + \sqrt{3}(\varphi_2^2 - \varphi_3^2)e_4]. \quad (4)$$

The effective potential at $\varphi \equiv \varphi_1 \neq 0$ and $\varphi_2 = \varphi_3 = 0$ describes the phase transition into one of three single-domain states (D_1 in Fig. 5):

$$F_{\text{eff}} = \frac{1}{2}r\varphi^2 + \frac{1}{4}u\varphi^4 + \frac{1}{6}\nu\varphi^6 + [\beta_1(e_1 + e_2) + \beta_3 e_3]\varphi^2 + 2\beta_2(e_1 - e_2)\varphi^2 + 2\beta_5 e_5\varphi^2 + F_e, \quad (5)$$

where $u \equiv u_0' + u_1' + 4u_2'$.

The temperature dependence of the squared order parameter (at $T < T_c$) in the case of a second-order phase transition ($\tilde{u} > 0$) is determined by the formula

$$\varphi^2 = \frac{\alpha(T_c - T)}{\tilde{u}} \quad (6)$$

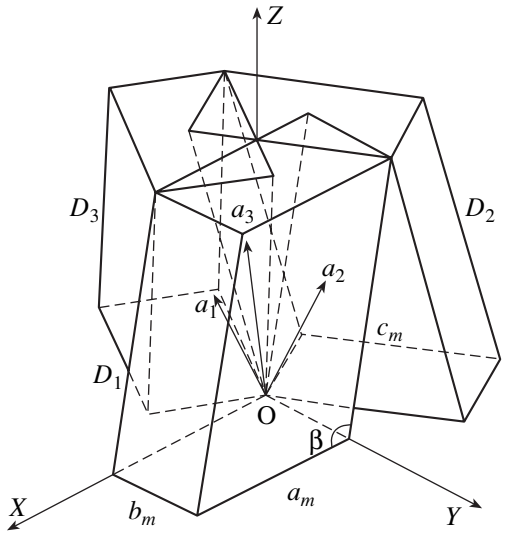

Fig. 5. Relation between the monoclinic (a_m, b_m, c_m) and trigonal (a_1, a_2, a_3) unit cells and the orientation of the ferroelastic D_1, D_2, and D_3 domains.

or the formula

$$\varphi^2 = \frac{|\tilde{u}| + \sqrt{\tilde{u}^2 + 4\nu\alpha(T_c - T)}}{2\nu} \quad (7)$$

in the first-order phase transition ($\tilde{u} < 0$ and $\nu > 0$). Here $\tilde{u} \equiv u + 4\sum_{i=1, i\neq 4}^{5}\beta_i B_i$ and the constants B_i are

$$B_1 + B_2 = \frac{2C_{13}\beta_3 - 2C_{33}\beta_1}{C_{11}C_{33} - 2C_{13}^2},$$
$$B_1 - B_2 = \frac{-2C_{44}\beta_2 + 2C_{14}\beta_5}{C_{44}C_{16} - C_{14}^2}, \quad (8)$$
$$B_3 = \frac{2C_{13}\beta_1 - C_{11}\beta_3}{C_{11}C_{33} - 2C_{13}^2}, \quad B_5 = \frac{-2C_{16}\beta_5 + 2C_{14}\beta_2}{C_{44}C_{16} - C_{14}^2}.$$

The components of the strain tensor depend on the squared order parameter as

$$e_1 = B_1\varphi^2, \quad e_2 = B_2\varphi^2, \quad e_3 = B_3\varphi^2, \quad e_5 = B_5\varphi^2. \quad (9)$$

The tensor components were calculated by the formulas

$$e_1(T) = \frac{a_m(T) - a(475\text{ K})}{a(475\text{ K})},$$
$$e_2(T) = \frac{b_m(T) - b(475\text{ K})}{b(475\text{ K})}, \quad (10)$$
$$e_3(T) = \frac{c_m(T) - c(475\text{ K})}{c(475\text{ K})},$$
$$e_5(T) = -\frac{c_m(T)\cos[\beta(T)] - c(475\text{ K})\cos[\beta(475\text{ K})]}{2c(475\text{ K})\sin[\beta(475\text{ K})]}.$$

Then, the linear temperature dependence was subtracted from the calculated components. This temperature dependence is the consequence of the thermal expansion of the crystal in the C_{2h}^6 ($C2/c$) phase and is not related to the phase transition. The tensor of spontaneous strain is

$$\begin{pmatrix} -\varepsilon_1^{sp} & 0 & \varepsilon_2^{sp} \\ 0 & \varepsilon_1^{sp} & 0 \\ \varepsilon_2^{sp} & 0 & 0 \end{pmatrix}, \quad (11)$$

where $\varepsilon_1^{sp} \equiv \frac{e_2 - e_1}{2}$ and $\varepsilon_2^{sp} \equiv e_5$.

Figure 6 shows the temperature curves of the components of spontaneous deformation.

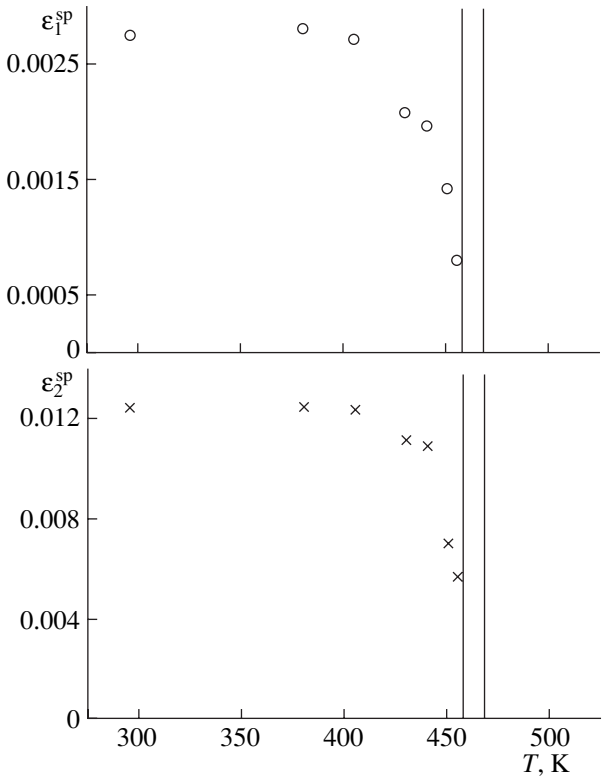

Fig. 6. Temperature dependences of the components of the tensor of spontaneous deformation.

DISCUSSION OF RESULTS

The X-ray studies showed that $Rb_3H(SO_4)_2$ crystals and also mixed TARHS crystals are isomorphous at room temperature. In the superprotonic phase above T_{S1} they belong to the trigonal system as all the other crystals of the $M_3H(XO_4)_2$ family [2–4, 6–8, 14].

The study of the domain-structure evolution with the temperature of mixed $[(NH_4)_{1-x}Rb_x]_3H(SO_4)_2$ crystals with $x < 0.5$ shows that small domains exist in the ferroelastic phase only in the narrow temperature range in the vicinity of the superprotonic transition. With lowering of the temperature, these small domains are replaced by large ones. Small domains also arise in the vicinity of T_{S1} in mixed crystals with a high rubidium content ($0.5 < x < 0.9$). The crystals with $x > 0.9$ showed no domain structure; these disintegrated in the superprotonic transition. The temperature of the appearance of small domains coincides with the temperature of an increase in conductivity. This is a very important fact. Below T_S, oxygen atoms in the neighboring SO_4 tetrahedra in mixed TARHS crystals are linked by short hydrogen bonds in the (001) plane. The positions of hydrogen bonds in the crystal are fixed by the crystal symmetry. With heating of the crystal above T_S, the crystal is transformed into the ($R\bar{3}m$) phase in which the apical proton is distributed over six equivalent positions in the (001) plane with the probability 1/6, which results in the appearance of protonic conductivity [16]. Along with other factors, high conductivity follows from the symmetric characteristics of the trigonal phase and results in delocalization of hydrogen bonds. The disordered net of hydrogen bonds is formed in the structures where the number of hydrogen atoms per unit cell is less than the total multiplicity of the positions energetically favorable for hydrogen bonding [9]. Below T_S, hydrogen bonds are localized. An increase in protonic conductivity in the vicinity of the phase transition is favored by the formation of small ferroelastic domains. The main part in the twinning processes is played by reorientation of sulfate tetrahedra rotated in the neighboring domains. In this case, the multiplicity of the structurally equivalent protonic positions is changed. The NMR study of the proton dynamics showed [17] that at higher temperatures, the velocity and amplitude of vibrations of sulfate tetrahedra increase. In the vicinity of T_S, one observes anomalously high growth of internal vibrations of sulfate tetrahedra and their reorientation. In the low-temperature phase, protons are ordered, but in the vicinity of T_S more pronounced vibrations of HSO_4 groups give rise to internal stresses and domain formation (if a crystal possesses ferroelastic properties). Thus, the appearance of the additional (satellite) domain walls below T_S is associated with the formation of internal stresses due to proton delocalization. A nonferroelastic crystal may be destroyed under the action of the internal stresses in this temperature range.

We also established that an increase in the rubidium content in mixed crystals results in a considerable change of the hydrogen-bond symmetry, which makes hydrogen bonds unstable in the transition to the superprotonic state. The asymmetry of the apical hydrogen bond observed for crystals with a high rubidium content and also for TRHS crystals seems to be one of the

factors changing the domain-structure dynamics in the vicinity of the superprotonic transition.

ACKNOWLEDGMENTS

The authors are grateful to V.V. Dolbinina and A.I. Baranov for supplying us with the necessary crystals. The study was supported by the Russian Foundation for Basic Research, project no. 02-03-67485.

REFERENCES

1. A. Pawlowski, Cz. Pawlaczyk, and B. Hilczer, Solid State Ionics **44**, 17 (1965).
2. K. Gesi, J. Phys. Soc. Jpn. **42**, 1785 (1977).
3. K. Gesi, J. Phys. Soc. Jpn. **48**, 886 (1980).
4. M. Kamoun, M. Ben Ghozlen, and A. Daoud, Phase Transit. **9**, 247 (1987).
5. A. I. Baranov, V. V. Dolbinina, E. D. Yakushkin, *et al.*, Ferroelectrics **217**, 285 (1998).
6. K. Gesi and K. Ozawa, J. Phys. Soc. Jpn. **43**, 570 (1977).
7. S. Suzuki and Y. Y. Makita, Acta Crystallogr., Sect. B: Struct. Crystallogr. Cryst. Chem. **34**, 355 (1978).
8. S. Fortier, M. E. Frazer, and D. Hyding, Acta Crystallogr., Sect. C: Cryst. Struct. Commun. **41**, 1139 (1985).
9. A. I. Baranov, Kristallografiya **48** (6), 1081 (2003) [Crystallogr. Rep. **48**, 1012 (2003)].
10. L. S. Smirnov, A. I. Baranov, L. A. Shuvalov, *et al.*, Fiz. Tverd. Tela (St. Petersburg) **43** (1), 115 (2001) [Phys. Solid State **43**, 117 (2001)].
11. E. D. Yakushkin, A. I. Baranov, and V. N. Anisimova, Kristallografiya **44** (1), 123 (1999) [Crystallogr. Rep. **44**, 116 (1999)].
12. L. Kirpichnikova, B. Hilczer, M. Polomska, *et al.*, Solid State Ionics **45**, 191 (2001).
13. L. Kirpichnikova, M. Polomska, A. Pietraszko, *et al.*, Ferroelectrics **290**, 61 (2003).
14. D. V. Merinov, Solid State Ionics **84**, 89 (1996).
15. J. Sapriel, Phys. Rev. B **12**, 5128 (1975).
16. A. Pietraszko, B. Hilczer, and A. Pawlowski, Solid State Ionics **119**, 281 (1999).
17. J. Dolinsek, U. Mikas, J. E. Javorsek, *et al.*, Phys. Rev. B **58** (13), 8445 (1998).

Translated by L. Man

Crystallography Reports, Vol. 50, No. 1, 2005, pp. 115–119. Translated from Kristallografiya, Vol. 50, No. 1, 2005, pp. 122–126.

LATTICE DYNAMICS AND PHASE TRANSITIONS

X-ray Diffraction Study of Phase Transitions in $Na_3Sc_2(PO_4)_3$ and $Ag_3Sc_2(PO_4)_3$ Single Crystals in Temperature Range from 160 to 500 K

G. V. Shilov, L. O. Atovmyan, and V. I. Kovalenko

Institute of Problems of Chemical Physics, Russian Academy of Sciences, Institutskiĭ pr. 18, Chernogolovka, Moscow oblast, 142432 Russia

e-mail: gshilov@icp.ac.ru

Received August 11, 2003

Abstract—Two phase transitions are revealed for the first time in $Ag_3Sc_2(PO_4)_3$ single crystals in the vicinity of the temperatures 303 and 165–180 K. It is established that the phase transition at 303 K corresponds to the well-known phase transition to the superionic state in $Na_3Sc_2(PO_4)_3$ single crystals in the temperature range 423–433 K, whereas the phase transition observed in the temperature range 170–180 K corresponds to the phase transition from the rhombohedral to monoclinic phase at about 320 K in the monoclinic $Na_3Sc_2(PO_4)_3$ single crystals. It is also established that rhombohedral $Na_3Sc_2(PO_4)_3$ single crystals undergo the second phase transition. © *2005 Pleiades Publishing, Inc.*

INTRODUCTION

The $Na_3Sc_2(PO_4)_3$ compound possesses superionic properties at temperatures $T > 440$ K and the conductivity value at the level of the best superionic conductors. Various properties of this compound were studied in a large number of X-ray diffraction, conductivity, and calorimetric measurements [1–11]. It is established that, at room temperature, the crystals of this compound form two polymorphous modifications—monoclinic (α phase) and rhombohedral (β phase). The crystals of the α phase possess ferroelectric properties and, upon being heated, acquire the nonpolar state (β phase) with the structure usually described by the sp. gr. $R\bar{3}c$. According to [1–10], the temperature of this phase transition lies within 313–337 K. The $\alpha \longrightarrow \beta$ transformation is considered to be a first-order phase transition with the hysteresis at about 13° and a feebly marked thermal effect. The characteristic feature of the crystal of the β phase is its ionic conductivity and the presence of superstructural reflections on its X-ray diffraction patterns. The second phase transition from the rhombohedral β to superionic γ phase is observed at a temperature about 430 K. It is accompanied by a thermal effect and shows no hysteresis. At temperatures above the latter phase transition, the respective X-ray diffraction patterns have no superstructural reflection.

In terms of the crystal structure, the $\alpha \longrightarrow \beta$ transition is explained by redistribution of Na atoms over the structure framework whose symmetrization is accompanied by atomic displacements not exceeding 0.8 Å [1–4] and the appearance of superstructural reflections due to the ordered redistribution of Na atoms over the structure positions with multiplicities 6 and 18. According to the X-ray diffraction data obtained in a wide temperature range, the occupancies of the positions with multiplicities 6 and 18 in both the β and γ phases are the same.

Since the superstructural reflections were ignored in the structure determination of the β phase, all the opinions on the cause of their appearance are of a purely speculative character. Moreover, all the X-ray diffraction experiments were performed in the range of small θ angles. Therefore, the absence of high-angle reflections in the experimental data set did not allow one to study possible splitting of the positions with multiplicities 6 and 12 despite the fact that high values of the thermal parameters of Na atoms in the γ phase clearly indicate such splitting [3].

Based on the detailed calorimetric studies performed on polycrystal $Na_3Sc_2(PO_4)_3$ samples on a scanning Kalvet calorimeter, Gusakovskaya and Pirumova established that the main cause of the discrepancy of the data obtained in different experiments is the thermodynamically nonequilibrium state of the complex sodium–scandium system in which slight variations in the growth conditions gave rise to the formation of either monoclinic or rhombohedral phases or their mixtures in various percentage ratios [9, 10].

1063-7745/05/5001-0115$26.00 © 2005 Pleiades Publishing, Inc.

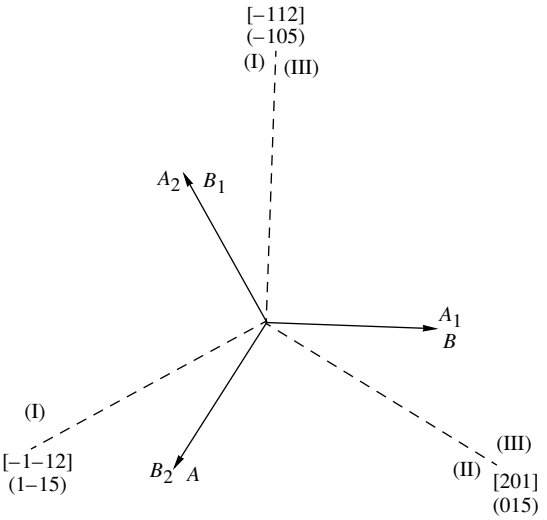

Fig. 1. The schematic which allows one to determine the crystal state (twinned, nontwinned) after a cycle of phase transitions ($\alpha \longrightarrow \beta \longrightarrow \gamma, \gamma \longrightarrow \beta \longrightarrow \alpha$). Reflection indices in the hexagonal setting (*ABC*) are indicated in parentheses; indices of these reflections in the monoclinic setting are indicated in square brackets. Symbols (I), (II), and (III) indicate the numbers of twin components.

Taking into account the fact that X-ray analysis is usually performed on one single crystal whose quality and phase composition may be controlled, we studied the phase transitions in $Na_3Sc_2(PO_4)_3$ (α, β) and $Ag_3Sc_2(PO_4)_3$ single crystals on a single crystal diffractometer. The focus was made on the study of the phenomena accompanying the phase transitions at the macroscopic level.

EXPERIMENTAL AND DISCUSSION OF RESULTS

Both monoclinic and rhombohedral single crystals of the $Na_3Sc_2(PO_4)_3$ compound were synthesized by growth from flux at 1100°C. The crystals of the α phase were grown on seeds of this phase. The $Ag_3Sc_2(PO_4)_3$ crystals were obtained by replacement of sodium by silver in monoclinic $Na_3Sc_2(PO_4)_3$ crystals. The substitution was performed in an aqueous $AgNO_3$ solution. The solution concentrations which provided growth of crystals not deteriorating during replacement of sodium by silver were determined empirically. The studies were performed on a single crystal KM-4 diffractometer produced by KUMA DIFFRACTION (Poland) with the use of the monochromatic MoK_α radiation.

The α phase of $Na_3Sc_2(PO_4)_3$ is crystallized in the monoclinic system with the lattice parameters a = 15.378 Å, b = 8.907 Å, c = 9.083 Å, β = 123.50°, sp. gr. *Cc*. Since the phase transformations were studied at the macroscopic level, the macroscopic single-crystal parameters were recorded, namely, unit-cell parameters and sensitive X-ray diffraction reflection characteristics of a certain phase state of the single crystal. During the study, we managed to record such X-ray diffraction reflections; in particular, for the monoclinic state, we used the (–1 1 2) and (–1 –1 2) reflections (monoclinic unit cell), and for the rhombohedral β state, we recorded the (1 –0.5 7) reflection (hexagonal unit cell). The sample was a 0.1 × 0.1 × 0.15-mm single crystal. Heating of the crystal up to 48°C resulted in disappearance of the (–1 1 2) reflection and appearance of the (1 –0.5 7) reflection, which indicated the transition of the single crystal from the monoclinic to rhombohedral phase. In the reverse $\beta \longrightarrow \alpha$ transition, the reflection attained the maximum intensity at about 40°C; i.e., two phases, β and α, may coexist in the reverse transition in the temperature interval of about 10°C. We studied this transition on several single crystals and established that the $\alpha \longrightarrow \beta$ transition took place at about 48°C in a narrow temperature interval equal to about 2 K, the reverse $\beta \longrightarrow \alpha$ phase transition may have a temperature delay of about 10°C. It should also be indicated that, in all the experiments, no matter how many times the $\alpha \longrightarrow \beta$ and $\beta \longrightarrow \alpha$ phase transitions took place, the crystal always returned to the initial monoclinic state unless we passed through the $\beta \longrightarrow \gamma$ phase transition. The situation changed if the single crystal was heated above the temperature of the second phase transition, which took place at about 150°C. After the transition of the single crystal from the β to the γ state (which was accompanied by disappearance of the superstructural reflections) and its subsequent cooling (transformation of the crystal into the α phase), we saw that, in some instances, the crystal returned to the initial monoclinic phase, although in some other instances, it lost its quality and the peak profiles split into two. In one of such cycles, $\alpha \longrightarrow \beta \longrightarrow \gamma, \gamma \longrightarrow \beta \longrightarrow \alpha$, we obtained a new monoclinic state of the single crystal with the monoclinic unit cell related to the initial one by a threefold axis. This led us to the assumption that single crystals may disintegrate into blocks related by a threefold axis. Based on this assumption, we suggested the scheme which allowed us to control the state of the crystalline sample. This scheme is shown in Fig. 1, where *A* and *B* (I), A_1 and B_1 (II), and A_2 and B_2 (III) are the axes of the hexagonal unit cells related by a threefold axis and the *C* axes pass through the point O normally to the drawing plane. Dashed lines show the projections of three reciprocal-lattice vectors with their indices in the hexagonal axes being indicated in parentheses and their axes in the monoclinic axes being indicated in square brackets. Each pair of such reflections determines three possible types of blocks: (–1 0 5) and (1 –1 5) (type I), (1 –1 5) and (0 1 5) (type II), and (0 1 5) and (–1 0 5) (type III). The simultaneous appearance in the diffraction field of these three types of reflections indicates twinning. This scheme is very convenient since, in the transition to the monoclinic phase, it allows one to determine a new state of the crystal still in the hexagonal setting.

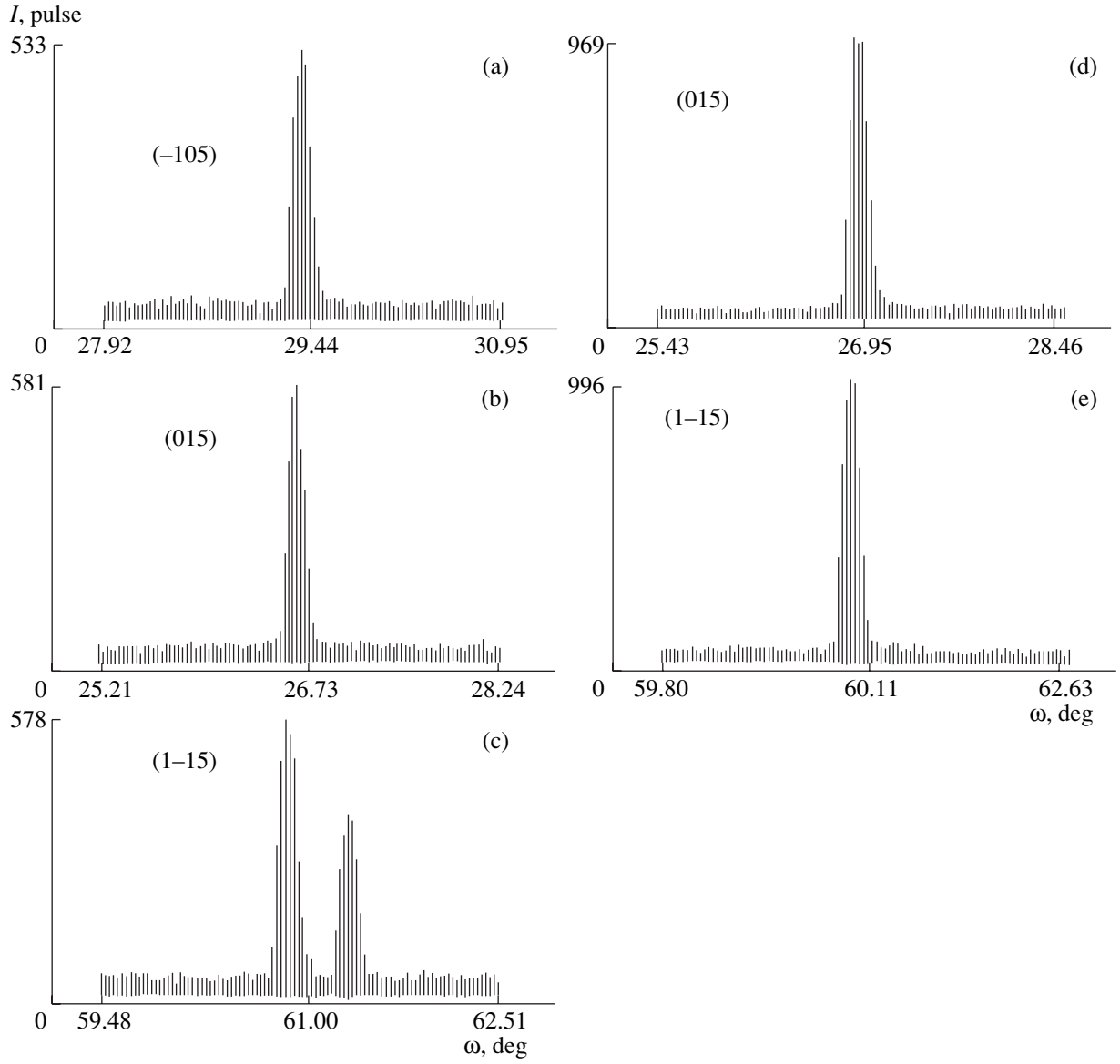

Fig. 2. (a–c) X-ray reflection profiles of (a–c) twinned and (d, e) untwinned crystals obtained by ω scanning of the points. Along the abscissa, the scanning interval is indicated (in deg); along the ordinate, the reflection intensities are indicated (in pulses).

Analyzing the profiles of these three reflections, one may determine how many twin components are possessed by the crystalline sample. Figures 2a and 2c show the profiles of these reflections, which indicate the two-component [(I) and (III)] state of the crystal acquired by it in one of the cycles ($\alpha \longrightarrow \beta \longrightarrow \gamma$, $\gamma \longrightarrow \beta \longrightarrow \alpha$), whereas the second pair of the reflection profiles in Figs. 2d and 2e shows that the crystal has acquired again the single crystal state (I) during the repeated cycles $\alpha \longrightarrow \beta \longrightarrow \gamma, \gamma \longrightarrow \beta \longrightarrow \alpha$. The fact that the 1–15 peak in Fig. 2c is split is explained by the fact that it has two components and, in the $\beta \longrightarrow \alpha$ transition, the monoclinic unit cell becomes strongly distorted in comparison with the monoclinic unit cell calculated from the hexagonal in the β state. The analysis of a large number of crystals of the α phase showed that they may be both nontwinned (used for further studies and called high-quality single crystals) and twinned crystals, which, in terms of single crystal diffractometry, are crystals of poor quality. All these facts are consistent with the Curie principle, which, in application to our case, reads as follows. If a threefold axis is not preserved in the $\gamma \longrightarrow \beta$ transition in one crystalline sample, it is still preserved for the whole mass of crystals. Summarizing the results obtained, we should like to emphasize the following:

—In the transition from the rhombohedral to monoclinic phase ($\beta \longrightarrow \alpha$), a certain temperature delay is observed in the interval of about 10°C; in other words, in this region, two phases, monoclinic and rhombohe-

dral, may coexist. We believe that this may be associated with the characteristics of the single crystal structure and that the β ⟶ α transition results in an increase in the unit-cell volume. Indeed, any ideal mosaic crystal consists of slightly misoriented coherent ~10^{-4}–10^{-5} cm blocks. During cooling, first the blocks lying on the crystal surface are cooled and transit into the β phase, which is accompanied by an increase in their volume and creation of unfavorable conditions for other blocks in the single crystal bulk.

—We also established that, after the α ⟶ β and β ⟶ α transitions, the crystal always returned to its initial state, no matter how many cycles of these transitions took place. Thus, it is possible to conclude that no redistribution of Na atoms over the cavities of the structure framework occurred in the transition from the monoclinic to rhombohedral phase. In the α ⟶ β transition, the $Sc_2(PO_4)_3$ framework of the crystal structure is symmetrized and Na atoms are displaced toward the twelve- and sixfold positions characteristic of the rhombohedral phase, thus creating certain modulations in the arrangement around these ideal positions. This results in the appearance of diffuse superstructural reflections in the diffraction field of the β phase of the single crystal. The fact that not all the Na atoms in the β phase are displaced to the special positions explains the reversibility in the α ⟶ β and β ⟶ α cycles. The indirect confirmation of the fact that not all the sodium atoms are displaced to the special positions is their large thermal parameters.

—It is also established that, when passing the cycle α ⟶ β ⟶ γ, γ ⟶ β ⟶ α, the crystal may acquire a state different from the initial one. If the crystal is in the γ phase, the superstructural reflections in the diffraction field disappear, which is associated with the transition of Na atoms in the structure into the state of dynamic disorder around their special positions. In the γ ⟶ β transition, a new configuration of Na atoms may be formed, which is accompanied by the appearance of superstructural reflections, whereas in the β ⟶ α transition, one of three possible nontwinned states or several twinned states (combinations of nontwinned states) of the crystal may be observed. Thus, the crystal of the β phase may be twins, but since the framework is symmetrized and the Na atoms are statistically disordered over their special positions by a value of the order of their thermal vibrations, the structure is well described within the hexagonal unit cell.

We also studied single crystals of the rhombohedral $Na_3Sc_2(PO_4)_3$ phase ($a = b = 8.914$ Å, $c = 22.293$ Å, γ = 120°, sp. gr. $R\bar{3}c$). With an increase in the temperature, this crystal undergoes the β ⟶ γ transition at 160°C, i.e., at a temperature 10°C higher than in the monoclinic phase. This transition was established from disappearance of the superstructural reflections. We also revealed for the first time the second phase transition in this system at about 260 K, which was accompanied by disappearance of superstructural reflections and a small jumpwise decrease in the parameter *c* of the hexagonal unit cell. Possibly, this is the transition to the centrosymmetric monoclinic group *C*2/*c*. It is most probable that the rhombohedral phase is a twinned crystal consisting of three components which equally scatter X-ray radiation and are related by a threefold axis.

As was indicated, $Ag_3Sc_2(PO_4)_3$ single crystals were obtained by replacing Na with Ag. As is well known from the published data [12] and is also confirmed by our studies, the silver-containig crystals are hexagonal with the unit-cell parameters $a = b = 8.964$ Å, $c = 22.582$ Å, sp. gr. $R\bar{3}c$. Thus, in terms of the symmetry change, the replacement of Na with Ag in $Na_3Sc_2(PO_4)_3$ single crystals remind one of the α ⟶ β phase transition in these crystals. Indeed, we established that replacement of Na with Ag at room temperature results in the disappearance of diffraction reflections inherent in the monoclinic phase (in particular, the reflection with the (–1 1 2) indices) and the formation of superstructural (–1 0.5 7) reflections.

We also studied single crystals of the silver-containing phase over a wide temperature range and established that heating of a single crystal above 30°C results in disappearance of the superstructural reflections, but no jumps in the unit-cell parameters were observed. In cooling below 30°C, superstructural reflections are formed, which are preserved up to 180 K. In the temperature range 180–170 K, the superstructural reflections in the X-ray diffraction spectrum disappear and the reflections characteristics of the monoclinic phase are formed. The transition is completed at 170 K. The reverse transition starts at 170 K and is completed at 180 K. Thus, we established two phase transitions in the $Ag_3Sc_2(PO_4)_3$ crystals. Their characteristics correspond to the characteristics of two phase transitions in the monoclinic $Na_3Sc_2(PO_4)_3$ single crystal. At 30°C, the β ⟶ γ phase transition takes place, and at 180–170°C, the β ⟶ α transition takes place. Thus, the $Ag_3Sc_2(PO_4)_3$ crystals already undergo the transition to the superionic phase at a temperature above 30°C. It should be indicated that, after the replacement of Na with Ag, the crystals of the new silver-containing phase behave in a similar way irrespective of the fact in which of the single crystals—monoclinic or rhombohedral—sodium was replaced with silver.

REFERENCES

1. V. A. Efremov and V. B. Kalinin, Kristallografiya **23**, 703 (1978) [Sov. Phys. Crystallogr. **23**, 393 (1978)].
2. B. M. Lazoryak, V. B. Kalinin, S. Yu. Stefanovich, *et al.*, Dokl. Akad. Nauk SSSR **250**, 861 (1980) [Sov. Phys. Dokl. **25**, 67 (1980)].

3. L. O. Atovmyan, V. V. Tkachev, V. I. Ponomarev, *et al.*, Zh. Strukt. Khim. **20**, 940 (1979).
4. S. Yu. Stefanovich and V. B. Kalinin, Fiz. Tverd. Tela (Leningrad) **23** (11), 3509 (1981) [Sov. Phys. Solid State **23**, 2043 (1981)].
5. L. O. Atovmyan, N. G. Bukun, V. I. Kovalenko, *et al.*, Élektrokhimiya **19**, 933 (1983).
6. D. Tran Qui, J. J. Capponi, M. Condrand, *et al.*, Solid State Ionics, No. 5, 305 (1981).
7. L. Boehm, C. J. Delbecq, E. Hutchinson, *et al.*, Solid State Ionics, No. 5, 311 (1981).
8. G. Collin, R. Comes, J. P. Boilot, *et al.*, J. Phys. Chem. Solids **47** (9), 843 (1986).
9. I. G. Gusakovskaya and S. I. Pirumova, Zh. Neorg. Khim. **39** (8), 1281 (1994).
10. I. G. Gusakovskaya, S. I. Pirumova, and V. I. Kovalenko, Zh. Obshch. Khim. **67** (4), 592 (1997).
11. H. Y.-P. Hong, in *Abstracts of International Conference on Fast Ion Transport in Solids, Electrodes, and Electrolytes* (Wisc., 1978), p. 431.
12. L. O. Atovmyan and V. V. Tkachev, Koord. Khim. **21** (7), 585 (1995).

Translated by L. Man

Crystallography Reports, Vol. 50, No. 1, 2005, pp. 120–123. Translated from Kristallografiya, Vol. 50, No. 1, 2005, pp. 127–131.

LATTICE DYNAMICS AND PHASE TRANSITIONS

To the Phenomenological Theory of Ferroelectric Phase Transitions

D. G. Sannikov

Shubnikov Institute of Crystallography, Russian Academy of Sciences, Leninskiĭ pr. 59, Moscow, 119333 Russia

e-mail: sannikov@ns.crys.ras.ru

Received February 25, 2004

Abstract—Some insufficiently studied aspects of proper ferroelectric phase transitions are considered. These are the role played by higher-degree terms of the expansion of a thermodynamic potential in polarization, the universal temperature dependences of physical quantities represented in terms of dimensionless variables, the soft mode (which, along with other modes, gives the contribution to polarization) and the polarization considered as an order parameter, and also the phase transition from piezoelectric phases. © *2005 Pleiades Publishing, Inc.*

THERMODYNAMIC POTENTIAL

The subject indicated in the title of this paper has long been developed and considered in numerous articles and monographs (see, e.g., the first review [1] and recent monograph [2] and the references there). However, some problems were not considered in sufficient detail in these publications and are still not quite clear. It is these problems, important first and foremost in processing of the experimental data, that are considered in the present article without comments to the well-known statements. Consider for the sake of definiteness and simplicity a one-component order parameter (many of the statements that will be made below are also applicable to two- and three-component order parameters). The density of the thermodynamic potential may be represented in the form

$$\Phi = 1/2\alpha P^2 + 1/4\beta P^4 + 1/6\gamma P^6 - PE, \quad (1)$$

where P and E are the components of the polarization and electric-field strength vectors, which are transformed according to the one-dimensional representation of the point symmetry group of the initial phase of the crystal. Thus, we obtain the equation $\partial\Phi/\partial P = 0$ which, under the condition that $\partial^2\Phi/\partial P^2 \geq 0$, determines the equilibrium P values at the given value of E,

$$\alpha P + \beta P^3 + \gamma P^5 - E = 0 \quad (2)$$

(the numerical coefficients in Eq. (1) are selected in a way to give the simplest form of Eq. (2)). Differentiating Eq. (2) in P, we obtain the reciprocal electric susceptibility χ^{-1} (also at the given E value),

$$\chi^{-1} = \alpha + 3\beta P^2 + 5\gamma P^4. \quad (3)$$

We limit our consideration only to these two quantities—P and χ^{-1}.

The coefficients of thermodynamic potential (1) are assumed to depend on the temperature T, pressure, and other parameters, e.g., the chemical composition of the crystal. We limit our consideration to the temperature dependence alone. The occurrence of a phase transition signifies that the coefficient α passes through the zero value (the initial phase should lose its stability) and, therefore, it is possible to assume that, in a small vicinity of the phase transition, we have

$$\alpha = \alpha_T(T - \theta), \quad \beta, \gamma = \text{const}. \quad (4)$$

SECOND-ORDER PHASE TRANSITION

Consider first a second-order phase transition in which $\beta > 0$ so that the invariant with the coefficient γ may be ignored. Then, Eqs. (2)–(4) yield the solutions (at $E = 0$)

$$\begin{aligned} P &= 0, \quad \chi^{-1} = \alpha_T(T - \theta); \\ P^2 &= \alpha_T(\theta - T)/\beta, \quad \chi^{-1} = 2\alpha_T(\theta - T) \end{aligned} \quad (5)$$

for the initial ($\alpha > 0$) and polar ($\alpha < 0$) phases (θ is the phase-transition temperature). Note also that the crystal is assumed to be a single domain one.

Thus, it is rather tempting to try to refine these relationships by taking into account the additional terms of the Φ expansion in P^2 with the coefficient γ. Then, considering the expansion in terms of $(\theta - T)$ for a polar phase, we have

$$\begin{aligned} P^2 &= (\alpha_T/\beta)(\theta - T) \\ &\times [1 - (\alpha_{TT}/\alpha_T - \beta_T/\beta - \alpha_T\gamma/\beta^2)(\theta - T)], \\ \chi^{-1} &= 2\alpha_T(\theta - T)[1 - (\alpha_{TT}/\alpha_T - \alpha_T\gamma/\beta^2)(\theta - T)]. \end{aligned} \quad (6)$$

1063-7745/05/5001-0120$26.00

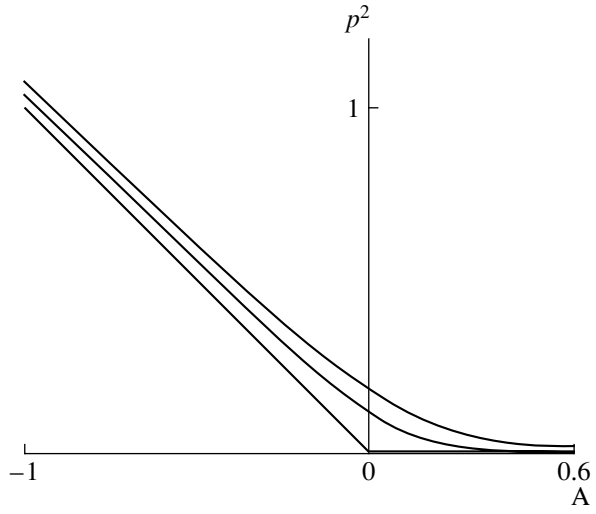

Fig. 1. Dependence of p^2 on A for a second-order phase transition.

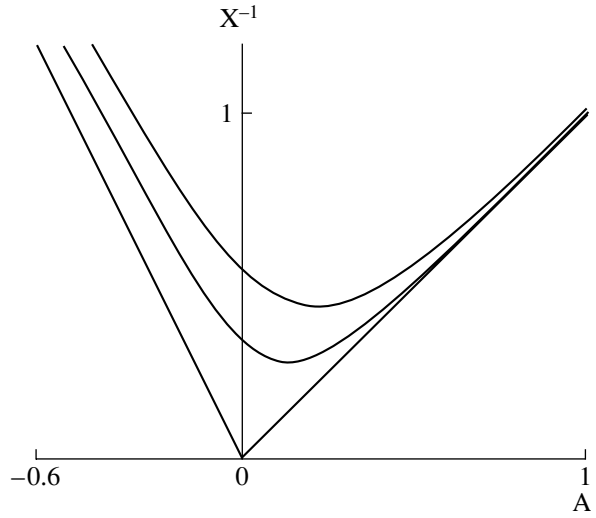

Fig. 2. Dependence of X^{-1} on A for a second-order phase transition.

The above equations also take into account the expansions of the coefficients themselves in $(T - \theta)$,

$$\alpha = \alpha_T(T - \theta) + \alpha_{TT}(T - \theta)^2, \quad \beta = \beta + \beta_T(T - \theta), \quad \gamma = \gamma. \tag{7}$$

It is seen from Eq. (6) that, taking into account the term of the Φ expansion with the coefficient γ, one has also to take into account the following term of the expansions (7) of the coefficients α and β in $(T - \theta)$. Instead of two coefficients α_T and β, we obtain five coefficients α_T, β, γ, α_{TT}, and β_T. To determine α_T and β, it is sufficient to know the experimental data for $P^2(T)$ and $\chi^{-1}(T)$ (see Eq. (5)), whereas to determine all five coefficients, we also need three additional experimental dependences, which makes the theory less attractive. Thus, it is not justified to take into account the coefficient γ for refining the experimental dependences for a second-order phase transition. Note also that, for a second-order phase transition close to the first-order transition for which the coefficient β is anomalously low, the allowance for γ may be quite justified because the terms α_{TT}/α_T and β_T/β may be negligible in comparison with the term $\alpha_T\gamma/\beta^2$.

UNIVERSAL DEPENDENCES

Represent the dependences $P^2(T)$ and $\chi^{-1}(T)$ in graphical form. It is convenient to pass to the dimensionless variables p, e, ϕ, A, and X (second-order phase transition)

$$P = p\beta^{1/2}, \quad E = e\beta^{5/2}, \quad \Phi = \phi\beta^3, \quad \alpha = A\beta^2, \quad \chi^{-1} = X^{-1}\beta^2. \tag{8}$$

The $p^2(A)$ and $\chi^{-1}(A)$ dependences in these variables (as well as the dependences of other physical quantities, e.g., heat capacity, determined from Eq. (1) under the conditions that $\gamma = 0$) acquire a universal character—they are valid for any crystal which undergoes a proper second-order ferroelectric phase transition. These dependences may be called universal and, therefore, it is useful to represent these dependences in graphical form. Figures 1 and 2 show these dependences at $e = 0$, 0.04, and 0.08 (the scales along the A axis and the p^2 and X^{-1} axes are selected to be the same). In particular, it follows from Figs. 1 and 2 that the experimental data should be given for $P^2(T)$ and $\chi^{-1}(T)$ rather than for $P(T)$ and $\chi(T)$, which is well known, especially with respect to χ.

The experimental $\chi^{-1}(T)$ dependence allows one to determine the phase-transition temperature $T = \theta$ at $E = 0$ and the coefficients $\alpha_T = \chi^{-1}/(T - \theta)$ at $T > \theta$ and $\alpha_T = \chi^{-1}/2(T - \theta)$ at $T < \theta$, and the coefficient $\beta = (\chi^{-1}/3)^3/E^2$ at $E \neq 0$, where χ^{-1} is taken at $T = \theta$. The experimental dependence $P^2(T)$ allows one to determine the phase transition temperature $T = \theta$ at $E = 0$, the coefficient ratio $\alpha_T/\beta = P^2/(\theta - T)$ at $T < \theta$, and the coefficient $\beta = E^2/P^3$ at $E \neq 0$, where P is taken at $T = \theta$. Obviously, the dependences in Figs. 1 and 2 are valid in a relatively small vicinity of the phase-transition point $T = \theta$, where the following inequalities are valid (see Eq. (7)):

$$\theta - T \ll \theta, \quad \alpha_{TT}(\theta - T) \ll \alpha_T, \quad \beta_T(\theta - T) \ll \beta, \quad \gamma(\theta - T) \ll \beta^2/\alpha_T. \tag{9}$$

It should be emphasized that the experimental dependences, in particular, $P^2(T)$ and $\chi^{-1}(T)$ in dimensionless variables (which requires the knowledge of the θ, α_T, and β values), should coincide with the universal

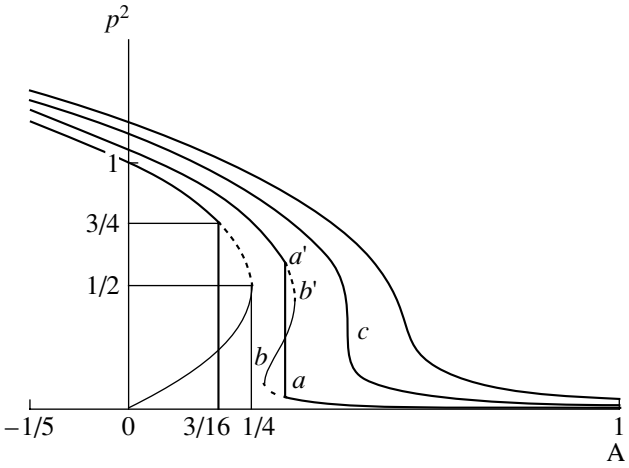

Fig. 3. Dependence of p^2 on A for a first-order phase transition (the coordinates of the points are $A_b = 0.279$, $A_{a,a'} = 0.314$, $A_{b'} = 0.337$, $p^2_{a'} = 0.611$, $p^2_{b'} = 0.450$, $p^2_b = 0.115$, and $p^2_a = 0.051$).

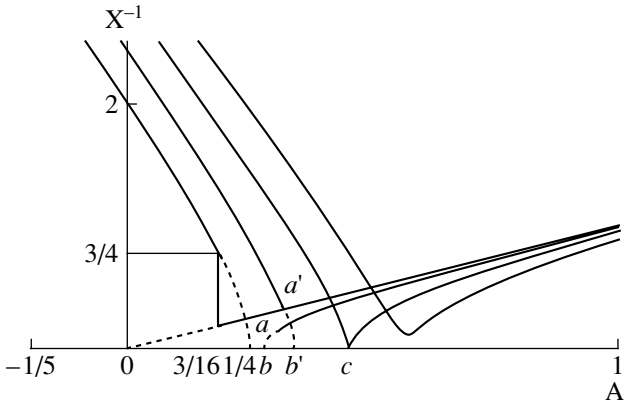

Fig. 4. Dependence of p^2 on A for a first-order phase transition (the coordinates of the points are A as in Fig. 3, $X^{-1}_{a'} = 0.348$, and $X^{-1}_a = 0.175$).

dependences in Figs. 1 and 2. This coincidence is an additional criterion of the correctness of the experimental dependences obtained and the values of the coefficients determined from these dependences and also of the fulfillment of conditions (9) (at least within a certain temperature range).

FIRST-ORDER PHASE TRANSITION

Now consider a first-order phase transition in which $\beta < 0$ and it is necessary to take into account the invariant with the coefficient γ in Eq. (1). From Eqs. (2)–(4), the following expressions for the initial and polar phases follow at $E = 0$:

$$P = 0, \quad \chi^{-1} = \alpha_T(T - \theta);$$
$$P^2 = (1/2\gamma)(|\beta| + B), \quad \chi^{-1} = (1/\gamma)B(|\beta| + B), \quad (10)$$
$$B \equiv [\beta^2 - 4\gamma\alpha_T(T - \theta)]^{1/2}.$$

The point of the loss of stability of the initial phase is $\alpha = 0$, and the polar phase loses stability at the point $\alpha = \beta^2/4\gamma$. The phase-transition point (the point of equality of the thermodynamic potentials of two phases) is $\alpha = 3\beta^2/16\gamma$. Note also that, since the expressions under the root sign in Eq. (10) cannot be expanded, the latter inequality (9) need not be necessarily fulfilled.

Now, the dimensionless variables acquire the form

$$P = p(|\beta|/\gamma)^{1/2}, \quad E = e(|\beta|^5/\gamma^3)^{1/2},$$
$$\Phi = \phi|\beta|^3/\gamma^2, \quad \alpha = A\beta^2/\gamma, \quad \chi^{-1} = X^{-1}\beta^2/\gamma. \quad (11)$$

Setting $\gamma = 1$ in Eq. (10) and replacing $|\beta|$ with β, we arrive at the dimensionless variables given by Eq. (8). In variables given by Eq. (11), the dependences $p^2(A)$ and $X^{-1}(A)$ are of universal nature—they are valid for any crystal which undergoes a proper first-order ferroelectric phase transition. These dependences may be called universal and, therefore, should be represented in a convenient graphical form. In Figs. 3 and 4, these dependences are given at $e = 0$, 0.06, e_c, and 0.2, where $e_c = 0.24(0.3)^{1/2} \sim 0.13145$ is the critical field in which jump in P^2 disappears in the transition, so that the transition is smeared as in the case of any field in a second-order phase transition. The inflection point on the $p^2(A)$ curve at $e = e_C$ has the coordinates $A_C = 0.45$ and $p^2_c = 0.3$. The dashed lines in Figs. 3 and 4 indicate the metastable states, and the thin lines indicate unstable states. The scale along the A axis is two times larger than along the P^2 axis and four times larger than along the X^{-1} axis.

POLARIZATION AS AN ORDER PARAMETER

Consider also a problem which seems to give no rise to any doubt whether it is possible to consider polarization as an order parameter in a proper ferroelectric phase transition. It is assumed that the coefficient α before P^2, which may be called the coefficient of polarization elasticity (see Eq. (1)), goes to zero at $T = \theta$. However, in displacive transitions (their consideration is more illustrative than the consideration of order–disorder transitions), the elasticity of one of the normal vibrations, the so-called soft mode, goes to zero, whereas the contributions to polarization may come from several modes having the same symmetry, i.e., transforming by the same representation of the point

symmetry group of the initial phase of the crystal (according to which the component P is also transformed)

$$P = a_1\eta + a_2\xi, \tag{12}$$

where only η is the soft mode (it is sufficient to consider only two modes, i.e., two normal vibrations, η and ξ).

The density of the thermodynamic potential may be represented in the form

$$\Phi = 1/2\alpha_1\eta^2 + 1/2\alpha_2\xi^2 + 1/4\beta_1\eta^4 + \beta_2\eta^3\xi + \ldots + 1/6\gamma_1\eta^6 - \ldots - (a_1\eta + a_2\xi)E, \tag{13}$$

where only the coefficient α_1 depends on T in the same way as in Eq. (4). The three dots indicate that some invariants of higher orders with respect to η are rejected (see below). It is important that, since η and ξ are the normal coordinates, there is no mixed invariant $\sim\eta\xi$ in Eq. (13) (in accordance with the definition of normal coordinates). Varying Φ with respect to ξ, we obtain (within the accuracy of the degrees of η taken into account in Eq. (13)) $\xi = -(\beta_2/\alpha_2)\eta^3 + \ldots$. Substituting this result into Eq. (13), we have

$$\Phi = 1/2\alpha_1\eta^2 + 1/4\beta_1\eta^4 + 1/6(\gamma_1 - \beta_2^2/\alpha_2)\eta^6 - \ldots - a_1\eta E. \tag{14}$$

Comparing Eqs. (1) and (14), we see that the use of the polarization P given by Eq. (1) instead of the soft mode η given by Eq. (14) is reduced to the change of the coefficients of the potential, which is not important in the phenomenological approach. A particular case may arise if, for some reasons, the coefficient a_1 has an anomalously low value, i.e., the contribution of the soft mode to polarization is small. Then potential (1) may lead to erroneous results, and one has to use potential (13). This is the case of the so-called weak ferroelectricity first considered in [3, 4].

INITIAL PIEZOELECTRIC PHASE

Consider the case where the initial phase is piezoelectric. Then the thermodynamic potential may be represented as

$$\Phi = 1/2\alpha P^2 - \lambda Pu + 1/2cu^2 + 1/4[\beta P^4 + \beta_1 P^3 u + \beta_2 P^2 u^2 + \beta_3 P u^3 + \beta_4 u^4] - PE - \sigma u, \tag{15}$$

where u is the component of the strain tensor and σ is the conjugated component of the mechanical-stress tensor. As is seen from Eq. (15), the potential is symmetric with respect to the variables P and u, each of which may be considered as an order parameter depending on which of the coefficients goes to zero at the transition point. If the coefficient $(\alpha - \lambda^2/c)$ (see below) goes to zero, then it is P, and if the coefficient $(c - \lambda^2/\alpha)$ goes to zero, it is u. We limit our consideration to the case where the order parameter is P.

Varying the potential given by Eq. (15) with respect to u and substituting the result obtained into Eq. (15), we obtain (under the condition that $\sigma = 0$)

$$\Phi = 1/2\bar{\alpha}P^2 + 1/4\bar{\beta}P^4 - PE,$$
$$\bar{\alpha} = \alpha - \lambda^2/c, \tag{16}$$
$$\bar{\beta} = \beta + \beta_1\lambda/c + \beta_2(\lambda/c)^2 + \beta_3(\lambda/c)^3 + \beta_4(\lambda/c)^4.$$

Note also that the coefficient c at $\bar{\alpha} > 0$ does not vanish.

The phase transition in a free crystal ($\sigma = 0$) takes place at $\bar{\alpha} = 0$, i.e., $\alpha = \lambda^2/c$. In the initial ($\bar{\alpha} > 0$) and polar ($\bar{\alpha} < 0$) phases, we obtain the dependences on T similar to Eqs. (5) at $E = 0$:

$$P = 0, \quad \chi_\sigma^{-1} = \bar{\alpha}_T(T - \theta);$$
$$P_\sigma^2 = \bar{\alpha}_T(\theta - T)/\beta, \quad \chi_\sigma^{-1} = 2\bar{\alpha}_T(T - \theta), \tag{17}$$

where the subscript σ indicates that the dependences $P_\sigma(T)$ and $\chi_\sigma^{-1}(T)$ are written for a free crystal.

It is impossible to satisfy the conditions which would have provided the phase transitions not at $\sigma = 0$ but at $u = 0$ (clamped crystal). Of course, a crystalline sample may be clamped mechanically; i.e., it is possible to fulfill the condition $u = 0$ at its surface. However, a phase transition would have given rise to mechanical stresses and the related excessive energy. As a result, the crystal would decompose into domains in which the condition $u = 0$ would not be fulfilled. It is possible to measure susceptibility χ under the condition $u = 0$. Then, in particular, we obtain for the initial phase

$$\chi_u^{-1} = \alpha, \tag{18}$$

where the subscript u indicates that this dependence is written for a clamped crystal.

ACKNOWLEDGMENTS

The author is grateful to G.A. Kessenikh for his help in the computer preparation of the figures. This study is supported by the Russian Foundation for Basic Research, project no. 03-02-16104.

REFERENCES

1. V. L. Ginzburg, Usp. Fiz. Nauk **38**, 355 (1949).
2. B. A. Strukov and A. P. Livanyuk, *Physical Principles of Ferroelectric Phenomena in Crystals* (Nauka, Moscow, 1995), p. 302 [in Russian].
3. V. Kopski, Solid State Commun. **19**, 417 (1976).
4. A. K. Tagantsev, I. G. Siniĭ, and S. D. Prokhorova, Izv. Akad. Nauk SSSR, Ser. Fiz. **51**, 2082 (1987).

Translated by L. Man

Crystallography Reports, Vol. 50, No. 1, 2005, pp. 124–126. Translated from Kristallografiya, Vol. 50, No. 1, 2005, pp. 132–134.

PHYSICAL PROPERTIES OF CRYSTALS

Relationship between the Optical Inhomogeneity and Microdomain Structure of Lithium Niobate

A. B. Smirnov and B. B. Ped'ko

Tver State University, Sadovyi per. 35, Tver, 170002 Russia

e-mail: Boris.Pedko@tversu.ru

Received March 3, 2003

Abstract—A model for the occurrence of optical inhomogeneity in lithium niobate single crystals in the regions of localization of microdomains with charged walls is considered. © *2005 Pleiades Publishing, Inc.*

In the absence of external actions, a perfect lithium niobate crystal (the symmetry group 3*m*) should exhibit no birefringence for a ray propagating along the *z* axis (coincident with the 3-fold symmetry axis). However, birefringence was observed experimentally in some regions of lithium niobate crystals. Traditionally, optical inhomogeneity of $LiNbO_3$ is attributed to the real structure of the crystal, including the domain structure [1, 2].

It is believed that lithium niobate crystals are characterized by similar optical properties of adjacent domains of opposite orientation. Nevertheless, it was shown experimentally that two adjacent 180° domains can be visualized by the polarization-optical method. The objective of this study was to investigate the relationship between the local optical inhomogeneity of lithium niobate and its microdomain structure.

A visually revealed structure was observed by the polarization-optical method on MPSU-1 and MIN-8 polarization microscopes and by etching [3].

Using etching, we revealed areas with a microdomain structure, which manifested itself as regular etching patterns up to 10 μm in size (Figs. 1, 2). Charged inclined domain walls were also visualized (Fig. 2). The microdomain structure in lithium niobate crystals was observed by the polarization-optical method in the form of bright areas about 10 μm in size. At higher magnification, they are visualized in the form of two adjacent bright areas, the shape of which is similar to the sign of infinity ∞ (Fig. 3).

A simple model for visualization of a wedge-shaped domain (in the form of a cone of revolution) by the polarization-optical method was considered. For a domain emerging at the surface (Figs. 4, 5), there exist charged domain walls, at which the field component changes its direction (remaining perpendicular to the polar axis) according to the symmetry of the domain in the form of a cone of revolution. Namely, when passing along the domain perimeter, the field component circulates following the scheme $E_2 \Rightarrow -E_1 \Rightarrow -E_2 \Rightarrow E_1$.

The distribution of birefringence was calculated for the regions located along the domain perimeter. In this calculation, the indicatrix equation $\sum_{i, j = 1, 2, 3} a_{i, j} x_i x_j = 1$ was used and the presence of the fields $\mathbf{E}_1$ and $\mathbf{E}_2$, perpendicular to the optical axis, was taken into account [4].

For light propagating in a lithium niobate crystal along the *z* axis, the birefringence is $\Delta n = n_o' - n_e' = n_o^3 r_{22} E_2$. The presence of the fields $\mathbf{E}_1$ and $\mathbf{E}_2$ corresponds to different types of distortion of the indicatrix section $z = 0$. In the first case, the indicatrix section is only distorted without rotation around the polar axis. In the second case, rotation by 45° occurs. Here, different domain regions exhibit different birefringence and, hence, the extinction positions will differ for different regions of the domain wall localization. This leads to the domain visualization between crossed polarizers in the form of two adjacent symmetric regions, which is confirmed experimentally (Fig. 3).

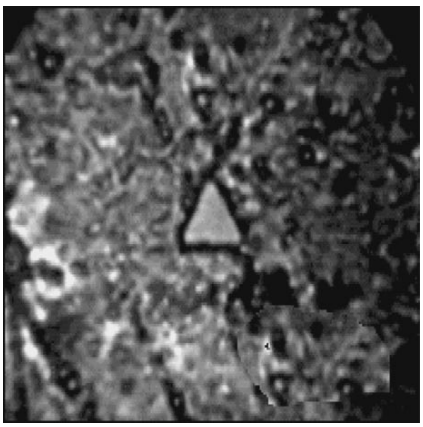

Fig. 1. Etching patterns (domains) revealed on the *z*-cut surface of an LN crystal in the form of regular trihedra. The observation in reflected light. The field of observation is 50×50 μm^2 in size.

1063-7745/05/5001-0124$26.00 © 2005 Pleiades Publishing, Inc.

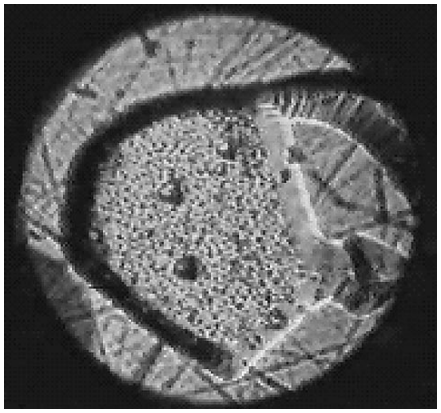

Fig. 2. Domain structure with inclined (with respect to the polar axis) walls revealed on the surface of a lithium niobate crystal by etching. The field of observation is 30×30 μm^2 in size.

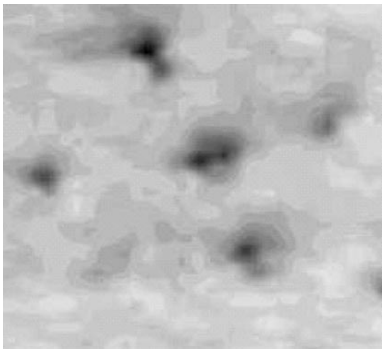

Fig. 3. Inverted photograph of the microdomain structure revealed by the polarization-optical method. The field of observation is 100×100 μm^2 in size.

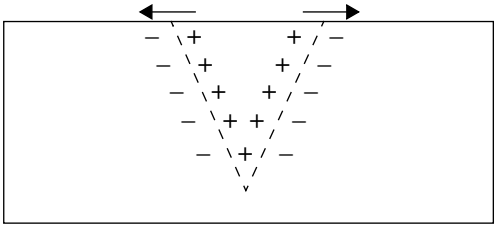

Fig. 4. A schematic diagram of a wedge-shaped microdomain. The plane is parallel to the polar axis.

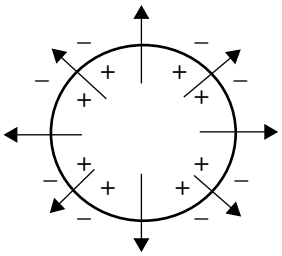

Fig. 5. A schematic diagram of a wedge-shaped microdomain. The polar cut.

The calculated diagram of light transmission along the *z* axis of the polarization-optical system (the crystal is placed between crossed polarizers and an external switching electric field responsible for the electro-optical effect is applied to it—see Fig. 6) is in good agreement with the experimental pattern (Fig. 3).

The second possible reason for the domain visualization by the polarization-optical method is a refractive index gradient occurring along the domain boundary. This gradient can be due to pyroelectric fields generated upon crystal heating. We estimated the value of the refractive-index gradient appearing with changing temperature in the regions of the domain wall localization for a domain that is antiparallel to the matrix of the principal domain. The variation in the refractive index at the interface between two adjacent domains with opposite directions of pyroelectric fields within the domain wall is $\delta n = n_o^3 r_{13} \dfrac{\gamma \Delta T(t) d}{\varepsilon_o \varepsilon_{33}}$, where n_o is the ordinary refractive index, γ is the pyroelectric coefficient, r_{13} is the electrooptic coefficient, d is the crystal plate thickness, ε_{33} is the dielectric permittivity, and ΔT is the change in temperature. For a crystal plate with thickness $d = 0.1 \times 10^{-2}$ m, $\lambda = 5085.8$ nm, $n_o^3 = 2.3356$, $r_{13} = 8.6 \times 10^{-12}$ V/m, and $\varepsilon_{33} = 38.5$, the value of the birefringence at an "instantaneous" change in temperature by 10 K was 0.005. To obtain the refractive-index gradient, the found value should be divided by the domain wall width. The presence of this gradient makes possible the polarization-optical observation of domain walls in lithium niobate. The electric fields with opposite directions in adjacent domains can be considered as fields that arise due to the pyroelectric effect upon crystal heating and reach significant values [5].

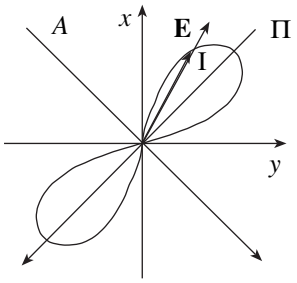

Fig. 6. Light transmission diagram for the polarization-optical system (the crystal is between crossed polarizers) under varying direction of an external electric field. Light propagates along the *z* axis.

Thus, in lithium niobate crystals (exhibiting no difference in the optical properties of adjacent domains of antiparallel orientation), a refractive-index gradient in the domain wall region, due to the presence of pyroelectric fields, may arise upon heating. This makes it possible to observe domain boundaries by the polarization-optical method. In turn, the occurrence of optical inhomogeneity in lithium niobate crystals may be due to the existence of wedge-shaped microdomains with charged domain walls.

ACKNOWLEDGMENTS

We are grateful to N.Yu. Franko for the help in etching experiments. This study was supported by NWO, project no. 16-04-1999, and the Russian Foundation for Basic Research, project no. 01-02-16511.

REFERENCES

1. V. P. Yarunichev and G. S. Berezovskaya, Izv. Akad. Nauk BSSR, Ser. Fiz.–Mat. Nauk **5**, 126 (1979).
2. E. I. Bratishchenko, B. B. Ped'ko, V. M. Rudyak, and V. P. Yarunichev, Izv. Akad. Nauk SSSR, Ser. Fiz. **48** (6), 1213 (1984).
3. N. Yu. Franko, B. B. Ped'ko, I. I. Sorokina, and N. A. Khokhonina, Izv. Ross. Akad. Nauk, Ser. Fiz. **64** (4), 1140 (2000).
4. A. S. Sonin and A. S. Vasilevskaya, *Electrooptical Crystals* (Nauka, Moscow, 1971) [in Russian].
5. K. G. Belabaev, V. T. Gabriélyan, and V. Kh. Sarkisov, in *Piezoelectric and Ferroelectric Materials and Their Application* (MDNTP, Moscow, 1971), p. 33 [in Russian].

Translated by A. Zolot'ko

Crystallography Reports, Vol. 50, No. 1, 2005, pp. 127–136. Translated from Kristallografiya, Vol. 50, No. 1, 2005, pp. 135–144.

PHYSICAL PROPERTIES OF CRYSTALS

Vibrational Spectra of Crystals of Bismuth Borates

A. V. Egorysheva*, V. I. Burkov, Yu. F. Kargin*, V. G. Plotnichenko***, and V. V. Koltashev*****

** Kurnakov Institute of General and Inorganic Chemistry, Russian Academy of Sciences, Leninskiĭ pr. 31, Moscow, 119991 Russia*

e-mail: yu.kargin@rambler.ru

*** Moscow Institute of Physics and Technology, Institutskiĭ per. 9, Dolgoprudnyĭ, Moscow oblast, 141700 Russia*

**** Fiber Optics Center, Institute of General Physics, Russian Academy of Sciences, ul. Vavilova 38, Moscow, 117942 Russia*

Received April 16, 2003

Abstract—The vibrational spectra of crystals of bismuth borates $Bi_{24}B_2O_{39}$, $Bi_4B_2O_9$, $BiBO_3$, and $Bi_2B_8O_{15}$ were obtained for the first time, and the spectra of $Bi_3B_5O_{12}$ and BiB_3O_6 crystals measured in the range 30–1600 cm^{-1} at room temperature were refined. The lines observed were assigned to the corresponding vibrational transitions on the basis of the theoretical group analysis and comparison of the obtained results with the vibrational spectra of borates of different composition. The complication of the structure of bismuth borates with increasing content of B_2O_3 was traced by the example of vibrational spectra. © *2005 Pleiades Publishing, Inc.*

INTRODUCTION

Under stable equilibrium conditions, five compounds are formed in the Bi_2O_3–B_2O_3 system [1]: $Bi_{24}B_2O_{39}$, $Bi_4B_2O_9$, $Bi_3B_5O_{12}$, BiB_3O_6, and $Bi_2B_8O_{15}$. The structures of these compounds were studied in [2–6]. In the crystal lattices of $Bi_{24}B_2O_{39}$ and $Bi_4B_2O_9$, boron is located in $[BO_3]^{3-}$ groups that are unbound with each other (isolated). The lattices of the compounds with a higher boron concentration ($Bi_3B_5O_{12}$, BiB_3O_6) contain polyborate anions formed by $[BO_3]^{3-}$ and $[BO_4]^{5-}$ groups. There are also metastable compounds $BiBO_3$ and $Bi_5B_3O_{12}$ [7], the structures of which have not been investigated.

There are fragmentary data in the literature on the vibrational spectra of some bismuth borates. The Raman spectra of $Bi_3B_5O_{12}$ single crystals were considered by us previously [8]. In some studies, the vibrational spectra of BiB_3O_6 crystals were analyzed (see, for example, [9]). The IR spectra of polycrystalline samples of some bismuth borates were reported in [10]. The vibrational spectra of single crystals of most bismuth borates have not been analyzed.

In this paper, we report the results of studying the vibrational spectra of borates formed in the Bi_2O_3–B_2O_3 system.

CRYSTAL GROWTH

$Bi_{24}B_2O_{39}$ single crystals were grown by conventional high-temperature flux method (TSSG). The charge composition corresponded to 16 mol % of B_2O_3. Single crystals of congruently melting bismuth borates $Bi_4B_2O_9$ (T_m = 948 K), $Bi_3B_5O_{12}$ (T_m = 995 K), BiB_3O_6 (T_m = 981 K), and $Bi_2B_8O_{15}$ (T_m = 988 K) were grown by the Czochralski method from a charge corresponding to a stoichiometric composition. Initially, a block crystal was grown on a platinum wire and one of the blocks was then used as a seed. The crystals were grown in a resistance furnace in a platinum crucible 90 cm^3 in volume. To ensure the homogeneity of the

Table 1. Positions of the lines (cm^{-1}) observed in the IR and Raman spectra of $Bi_{24}B_2O_{39}$ crystals

Raman spectrum	Raman spectrum	IR spectrum	Assignment
54		480	
63	522		
83	532	528	
97	553		
129		576	
141	624		
206	696	698	$\gamma(B_{(3)}–O)$
232	723	722	
275	853		$\nu_s(B_{(3)}–O)$
341	1121	1116	
372	1201		$\nu_{as}(B_{(3)}–O)$
458	1280	1276	
	1398	1406	2γ
	1443		

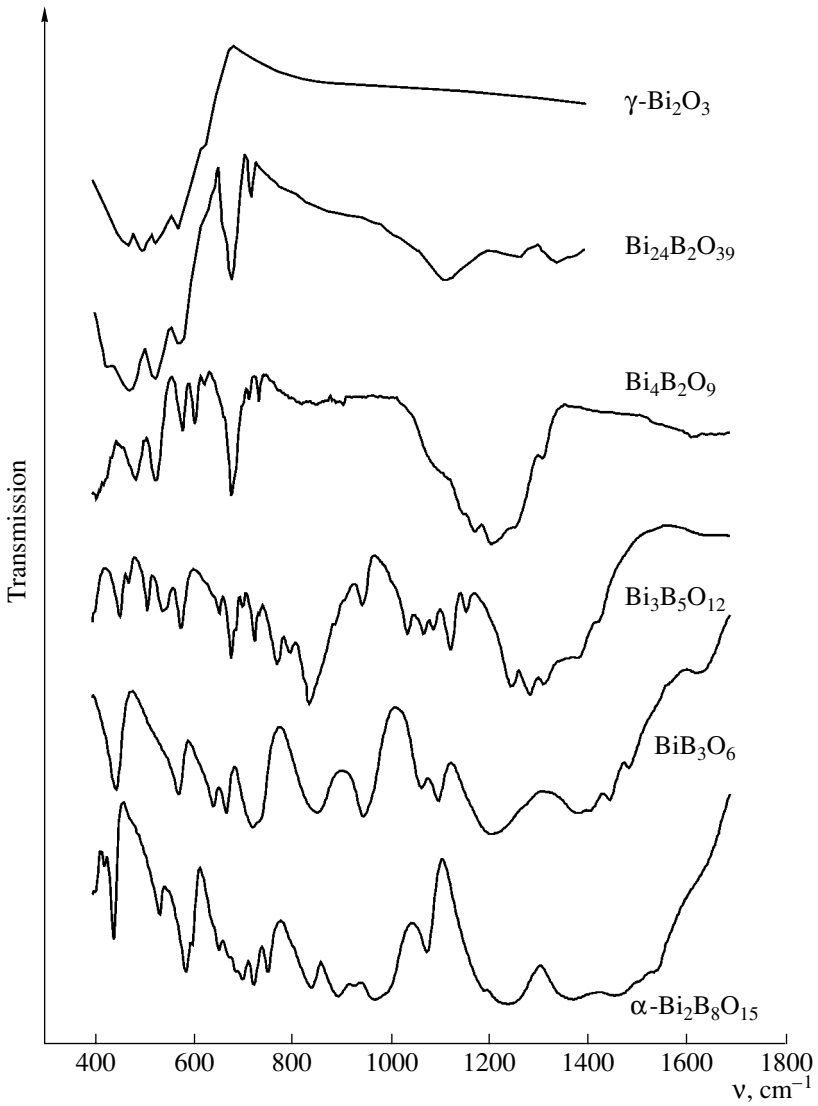

Fig. 1. IR transmission spectra of bismuth borates.

melt, a powdered compound previously obtained by solid-phase synthesis was loaded into the crucible. Bi_2O_3 of high-purity grade (13-3) and H_3BO_3 of high-purity grade (12-3) were used as the initial components. The growth of single crystals of bismuth borates from melt is characterized by the following features: the liquidus curve of the $Bi_{24}B_2O_{39}$ compound lies in narrow concentration (14–18 mol % of B_2O_3) and temperature (622–628 K) ranges; melts of the $Bi_3B_5O_{12}$, BiB_3O_6, and $Bi_2B_8O_{15}$ compounds have high viscosity and tend to glass formation; and the $Bi_2B_8O_{15}$ compound is characterized by a polymorphic transition (T = 969 K). The growth of BiB_3O_6 and $Bi_2B_8O_{15}$ crystals is complicated by tendency to immiscibility.

The above features determined the conditions for crystal growth. The pulling rate was 0–0.2 mm/h, the rotation velocity was 1.5–6 rpm, and the supercooling temperature was in the range 2–4°C (20°C for α-$Bi_2B_8O_{15}$). BiB_3O_6 and $Bi_2B_8O_{15}$ crystals were grown at a constant temperature. The cooling rate during the growth of $Bi_4B_2O_9$ and $Bi_3B_5O_{12}$ did not exceed 0.1 K/h. The axial temperature gradient above the melt was 0.8 K/cm. All grown crystals of bismuth borates were colorless. The crystal sizes varied from 5 to 10 mm in diameter and from 15 to 30 mm in length.

Polycrystals of the metastable compound $BiBO_3$ were obtained from a stoichiometric charge. The melt was heated to 800°C and then cooled at a rate of 5 K/h. The phase composition of the compound obtained was monitored by X-ray diffraction analysis.

The Raman spectra of single-crystalline samples were measured on a T 64000 (Jobin Yvon) triple spectrograph in the range 20–1600 cm^{-1}. The spectra were excited by an Ar laser (Spectra Physics) at a wavelength

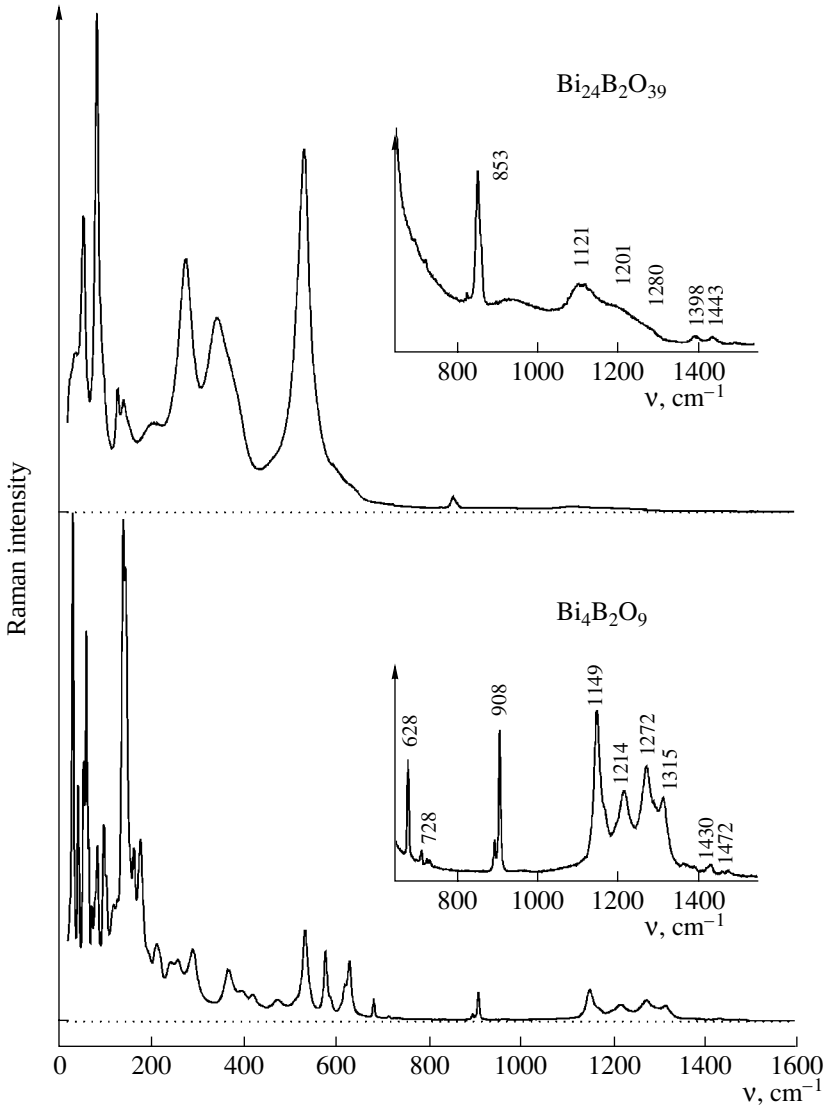

Fig. 2. Raman spectra of $Bi_{24}B_2O_{39}$ and $Bi_4B_2O_9$ crystals.

of 5145 Å. The spectral resolution was 1 cm^{-1}. The IR spectra of bismuth borates in the range 400–1600 cm^{-1} were measured on a NICOLET NEXUS FT-IR spectrometer with a spectral resolution of 4 cm^{-1}. The investigations were performed with powders pressed into KBr pellets.

RESULTS AND DISCUSSION

The vibrational spectra of bismuth borates are determined by vibrations of bismuth–oxygen and boron–oxygen structural units. On the basis of the results of [10–15], characteristic spectral regions can be selected in which bands due to vibrations along the Bi–O and B–O bonds are observed. The vibrational bands in the range 0–150 cm^{-1} in the Raman spectrum of α-Bi_2O_3 are due to external vibrations of Bi atoms [11, 12]. Internal vibrations along the Bi–O bonds have higher frequencies; their main contribution to the vibrational spectrum is in the range $150 < \nu < 500$ cm^{-1}. It is known [10, 13, 14] that four normal vibrations with frequencies $\nu_s \sim 740$–890 cm^{-1}, $\gamma \sim 400$–600 cm^{-1}, $\nu_{as} \sim 1000$–1150 cm^{-1}, and $\delta \sim 600$ cm^{-1} correspond to the $[BO_4]^{5-}$ tetrahedron. The frequencies of normal vibrations of $[BO_3]^{3-}$ groups lie in the ranges $\nu_s \sim 850$–960 cm^{-1}, $\gamma \sim 650$–800 cm^{-1}, $\nu_{as} \sim 1100$–1450 cm^{-1}, and $\delta \sim 500$–600 cm^{-1} [10, 13–15].

$Bi_{24}B_2O_{39}$. $Bi_{24}B_2O_{39}$ crystals belong to the cubic system, sp. gr. $I23$, $Z = 2$ [2]. $Bi_{24}B_2O_{39}$ crystals have sillenite structure, which is characterized by five sets of equivalent points with the types of positional symmetry $T(1)$, $D_2(3)$, $C_3(4)$, $2C_2(6)$, and $C_1(12)$. Theoretical group analysis gives the following set of modes of

Table 2. Positions of the lines (cm^{-1}) observed in the IR and Raman spectra of $Bi_4B_2O_9$ crystals

Raman spectrum	Raman spectrum	IR spectrum	Assignment
31		407	
43	419	422	
56	474	459	
61	534	488	
65	578	528	
72	588	582	
80	620	607	
84	630	627	
98	682	681	
103	715	717	$\gamma(B_{(3)}–O)$
120	728	737	
128		885	
140	896	893	$\nu_s(B_{(3)}–O)$
146	908	908	
154		1107	
164	1149	1149	
178	1168	1173	
212	1214	1207	$\nu_{as}(B_{(3)}–O)$
244	1272	1254	
259	1315	1309	
291	1430		
368	1472		2γ
395			

vibrations: $\Gamma = 8A + 8E + 25T$. Triply degenerate vibrations (T) are active in Raman and IR spectra, and nondegenerate (A) and doubly degenerate (E) vibrations are active in Raman spectra. In terms of the polyhedral description of the $Bi_{24}B_2O_{39}$ lattice, B atoms are located in isolated $[BO_3]^{3-}$ groups, which link BiO_x coordination polyhedra. Therefore, the positional symmetry of B atoms is reduced from T to C_3.

The shape of the vibrational spectra of $Bi_{24}B_2O_{39}$ (Figs. 1, 2) is determined by vibrations of the Bi–O framework constructed from $[Bi_2O_8]$ dimers. The positions and intensities of the bands observed in the spectra of $Bi_{24}B_2O_{39}$ (Table 1) are in good agreement with the known data for other compounds with sillenite structure [16]. Comparison of the vibrational spectra of $Bi_{24}B_2O_{39}$ and γ-Bi_2O_3 crystals, which also have sillenite structure, shows that the vibrations along the B–O bonds are responsible for the weak bands at 698, 722, and 1100–1300 cm^{-1} in the IR spectrum and the bands peaked at 853, 1121, 1201, and 1280 cm^{-1} in the Raman spectrum. The positions of these bands are in good agreement with the known experimental data on the frequencies of the fundamental modes of vibrations of $[BO_3]^{3-}$ groups. The bands at 698 and 722 cm^{-1} are due to the symmetric bending vibration γ, which is not active in the Raman spectra within the C_3 symmetry. The appearance of weak bands in the Raman spectrum at 696 and 723 cm^{-1} indicates violation of the planarity of the $[BO_3]^{3-}$ anion. The totally symmetric stretching vibration ν_s, which is active only in the Raman spectrum, is responsible for the band at 853 cm^{-1}—the strongest band in this spectral region. The wide band in the range 1100–1300 cm^{-1} should be assigned to the doubly degenerate vibration ν_{as}. Some red shift of this band is, obviously, related to the effect of bismuth on the character of the B–O bond. A similar effect in other sillenites, for example, P or V sillenites, leads to a significant red shift of the frequencies of stretching vibrations of the $[PO_4]^{3-}$ and $[VO_4]^{3-}$ groups (960 and 765 cm^{-1}, respectively [16]) with respect to the frequencies of stretching vibrations of these groups in different phosphates (ν_3 for $[PO_4]^{3-}$ is 1100 cm^{-1}) [13, 15] and vanadates (ν_3 for $[VO_4]^{3-}$ is 790–850 cm^{-1}) [13, 17]. It is almost impossible to select the bands corresponding to δ vibrations of $[BO_3]^{3-}$ groups against the background of vibrations of the Bi–O framework of the $Bi_{24}B_2O_{39}$ lattice. The γ vibration is forbidden in the first-order Raman spectrum; however, the forbiddenness is removed for overtones with doubled frequency $2\nu_\gamma$. This fact accounts for the bands at 1398 and 1443 cm^{-1} observed in the Raman spectrum.

$Bi_4B_2O_9$. In the structure of $Bi_4B_2O_9$ (sp. gr. $P2_1/c$, $Z = 4$ [3]), as well as $Bi_{24}B_2O_{39}$, boron atoms are trigonally coordinated by oxygen. In this case, there exist two nonequivalent isolated $[BO_3]^{3-}$ groups. All atoms in the unit cell occupy positions with the symmetry C_1. Analysis predicts the appearance of $\Gamma_{vbn}^{opt} = (45A_g + 45B_g) + (44A_u + 43B_u)$ vibrations in the spectra of $Bi_4B_2O_9$. Ninety vibrations of A_g and B_g symmetry will be active in the Raman spectrum and 87 vibrations (A_u and B_u) will be active in the IR spectrum.

The increase in the boron content in $Bi_4B_2O_9$ in comparison with $Bi_{24}B_2O_{39}$ leads to a significant increase in the intensity of the bands corresponding to boron–oxygen vibrations (Figs. 1, 2). The positions of the bands in the vibrational spectra of $Bi_4B_2O_9$ at $\nu >$ 600 cm^{-1} are in the frequency range in which fundamental vibrations of the $[BO_3]^{3-}$ anion are observed in the spectra of $Bi_{24}B_2O_{39}$ (Table 2). The presence of two nonequivalent $[BO_3]^{3-}$ groups in the crystal structure and their low positional symmetry, which removes the degeneracy of the ν_{as} and δ vibrations, are responsible for the increase in the number of observed spectral bands.

$Bi_3B_5O_{12}$. In the structure of $Bi_3B_5O_{12}$ (sp. gr. *Pnma*, $Z = 4$ [4]), the pentaborate anion $[B_5O_{11}]^{7-}$ is formed of two six-member rings lying in perpendicular planes,

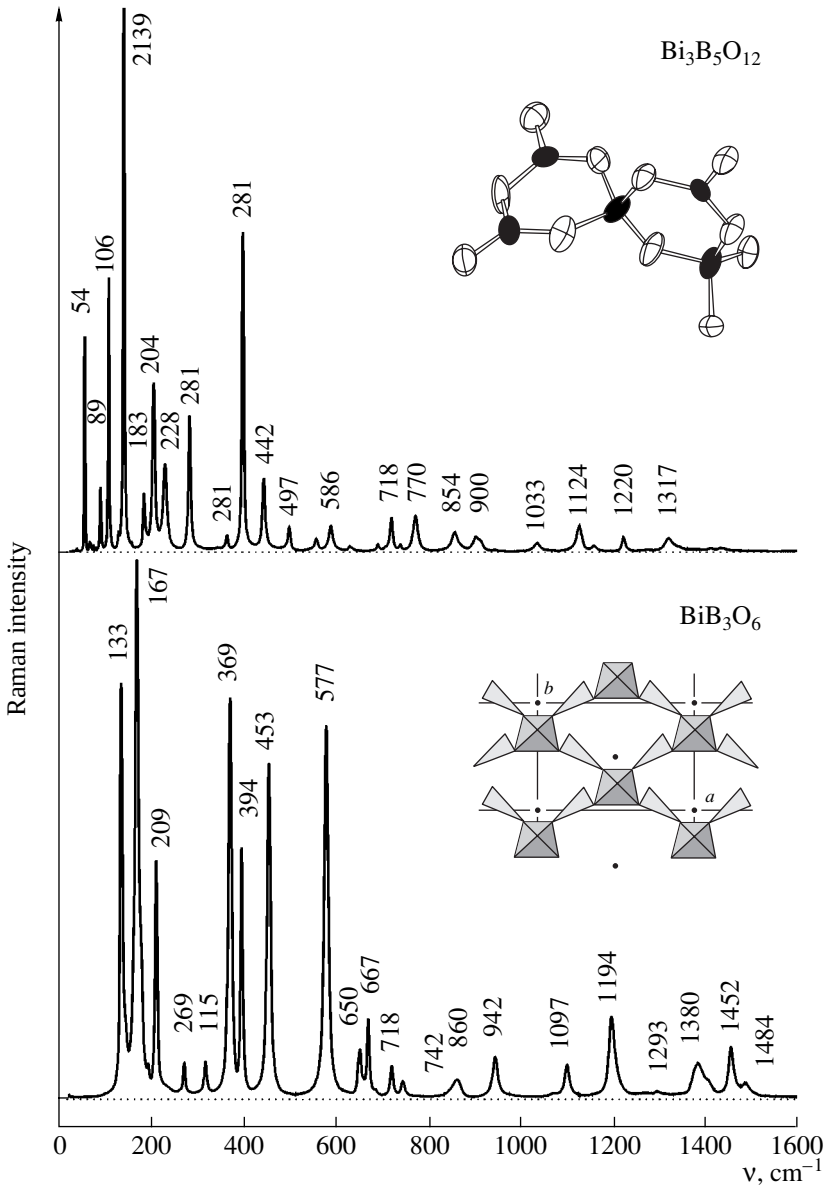

Fig. 3. Raman spectra of $Bi_3B_5O_{12}$ and BiB_3O_6 crystals. The insets show the structures of the $[B_5O_{11}]^{7-}$ and $[B_3O_6]_{\infty\infty}$ anions, respectively [4, 5].

one of which consists of two $[BO_3]^{3-}$ triangles and one $[BO_4]^{5-}$ tetrahedron. The other ring consists of one $[BO_3]^{3-}$ triangle and two $[BO_4]^{5-}$ tetrahedra. In the unit cell of $Bi_3B_5O_{12}$, Bi(1), B(1), B(2), B(3), O(1), O(2), O(5), O(6), O(7), and O(8) atoms occupy C_s symmetry positions. The positional symmetry of other atoms (Bi(2), B(4), O(3), O(4), O(9)) is C_1. Analysis of the symmetry of normal vibrations with the wave vector $k = 0$ shows that the distribution of 237 optical lattice vibrations of $Bi_3B_5O_{12}$ over irreducible representations has the form

$$\Gamma_{\text{vbn}}^{\text{opt}} = (35A_g + 25B_{1g} + 35B_{2g} + 25B_{3g}) + (25A_u + 34B_{1u} + 24B_{2u} + 34B_{3u}).$$

Due to the central symmetry of the crystal lattice of $Bi_3B_5O_{12}$, one should expect the appearance of vibrations of A_g, B_{1g}, B_{2g}, and B_{3g} symmetries in the Raman spectrum of this compound, 120 vibrations in total. The IR spectrum should contain 117 vibrations of A_u, B_{1u}, B_{2u}, and B_{3u} symmetries.

The Raman and IR spectra of $Bi_3B_5O_{12}$ contain a large number of mutually overlapping bands (Figs. 1, 3). In total, 38 lines can be distinguished in the spectra of $Bi_3B_5O_{12}$ at room temperature (Table 3), among which the lines due to vibrations of $[BO_3]^{3-}$ and $[BO_4]^{5-}$ groups can be selected. The low positional symmetry of the $[BO_4]^{5-}$ and $[BO_3]^{3-}$ groups in the $Bi_3B_5O_{12}$ lattice leads to the splitting of the vibrational bands. There-

Table 3. Positions of the lines (cm^{-1}) observed in the IR and Raman spectra of $Bi_3B_5O_{12}$ crystals

Raman spectrum	Raman spectrum	IR spectrum	Assignment
54		427	$\delta(B_{(4)}–O)$
66	442	435	
80	452	455	
86	469	473	
89	497	494	δ(pentaborate anion)
106		509	
111		523	$\delta(B_{(3)}–O)/\delta(B_{(4)}–O)$
119		538	
139	553	550	
147	586	578	
160	616	611	$\delta(B_{(4)}–O)$
167	629	625	
183	638	638	
204		657	
213	683	681	$\gamma(B_{(3)}–O)$
228		690	
281	699	704	
339	718	728	
362	734	739	
396	770	773	$\nu_s(B_{(4)}–O)$
413		800	
	823	827	$\nu_s(B_{(3)}–O)$
	838	839	
	854	863	
	900	891	
	909	910	
	943	946	ν_s(pentaborate anion)
	1004	1006	$\nu_{as}(B_{(4)}–O)$
	1033	1037	
	1067	1071	
		1090	
	1124	1126	
	1155	1157	
	1220	1248	$\nu_{as}(B_{(3)}–O)$
	1271	1284	
	1317	1316	
	1380	1385	
	1432	1438	ν_{as}(pentaborate anion)
	1466	1460	$2\gamma(B_{(3)}–O)$

Table 4. Positions of the lines (cm^{-1}) observed in the IR and Raman spectra of BiB_3O_6 crystals

Raman spectrum	Raman spectrum	IR spectrum	Assignment
	453	447	$\delta(B_{(4)}–O)$
133	577	574	$\delta(B_{(3)}–O)$
167	650	645	$\delta(B_{(4)}–O)$
192	667	671	$\gamma(B_{(3)}–O)$
209	685		
269	718	725	
315	742	738	
369	860	855	$\nu_s(B_{(3)}–O)/\nu_s(B_{(4)}–O)$
394	942	949	ν(polyanion)
	1065	1066	$\nu_{as}(B_{(4)}–O)$
	1097	1101	
	1194	1209	$\nu_{as}(B_{(3)}–O)$
	1293		
	1380	1389	
	1401	1406	
	1452	1448	ν(polyanion)
	1484	1487	$2\gamma(B_{(3)}–O)$

fore, the Raman and IR spectra of $Bi_3B_5O_{12}$ (Figs. 1, 3) in the frequency range of vibrations of these groups (450–1500 cm^{-1}) demonstrate a large number of asymmetric bands—superpositions of different vibrations of the B–O framework, which are spectrally unresolved at room temperature.

The IR and Raman spectra of $Bi_3B_5O_{12}$ are similar in shape with the spectra of alkali-metal pentaborates [14, 18]. The pentaborate anion $[B_5O_{10}]^{5-}$ in these compounds ($[B_5O_6(OH)_4]^-$ in hydrated borates) is formed by two rings lying in perpendicular planes. Each ring consists of two $[BO_3]^{3-}$ triangles and one $[BO_4]^{5-}$ tetrahedron, which completely corresponds to the structure of one of the rings of the $[B_5O_{11}]^{7-}$ anion in $Bi_3B_5O_{12}$ (Fig. 2). Calculation of the normal vibrations of the $[B_5O_{10}]^{5-}$ ion in terms of the D_{2d} symmetry [19] showed that the frequency of bending vibrations of this pentaborate anion is in the vicinity of $\delta \sim 500$ cm^{-1}. The values of ν_s in the range ~950–1025 cm^{-1} and near 1350 cm^{-1} correspond to the totally symmetric and asymmetric vibrations, respectively. The range of $\nu <$ 150 cm^{-1} corresponds to the vibrations related to the rotational motion of the rings. However, it is difficult to select the band corresponding to these vibrations in the vibrational spectra of $Bi_3B_5O_{12}$ against the strong bands due to external vibrations of Bi atoms. The presence of additional oxygen in the $[B_5O_{11}]^{7-}$ anion in the crystal structure of $Bi_3B_5O_{12}$ reduces the symmetry of the polyborate anion to D_{2h}, which leads to the splitting of vibrational bands. It can be evidenced by the IR and Raman spectra of ulexite ($NaCaB_5O_{10} \cdot 8H_2O$) [14]. The pentaborate anion $[B_5O_6(OH)_6]^{3-}$ of this compound is formed by two six-member rings containing one

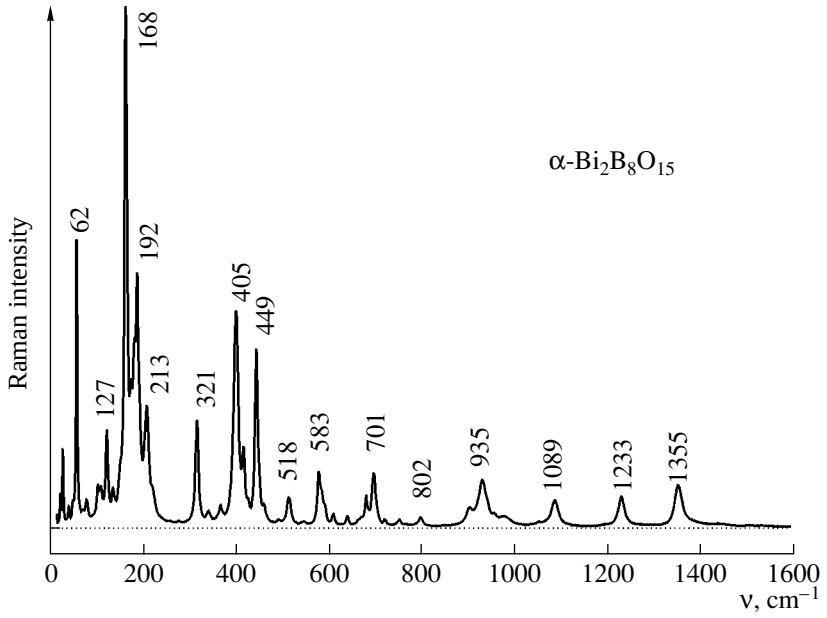

Fig. 4. Raman spectra of α-$Bi_2B_8O_{15}$ crystals.

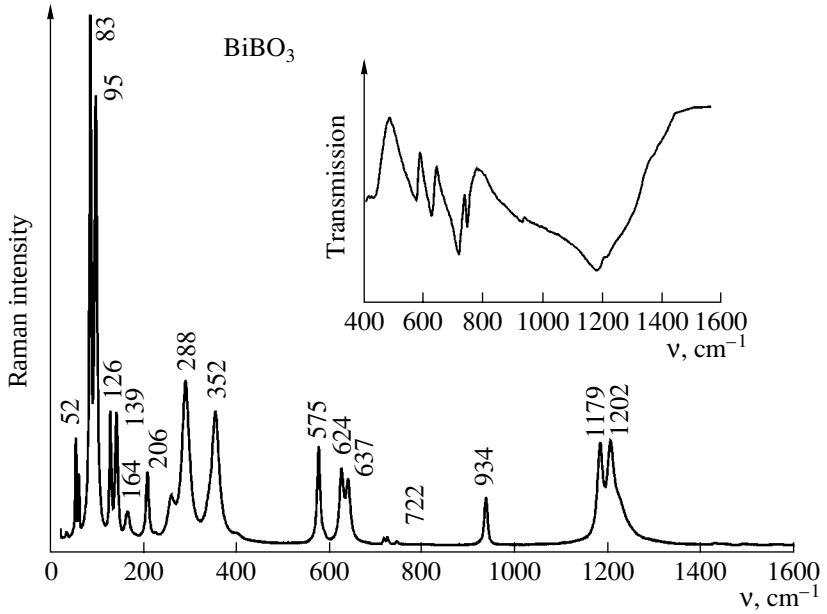

Fig. 5. Raman and IR (inset) spectra of $BiBO_3$ crystals.

$[BO_3]^{3-}$ and two $[BO_4]^{5-}$ groups, which corresponds to the second ring of the pentaborate anion in $Bi_3B_5O_{12}$. According to the data of [14, 18, 19], the most likely interpretation of the bands in the vibrational spectrum of $Bi_3B_5O_{12}$ is given in Table 3.

BiB_3O_6. The structure of BiB_3O_6 (sp. gr. C_2, $Z = 2$) is layered. It is formed by alternating $[BO_3]^{3-}$ and $[BO_4]^{5-}$ boron–oxygen anions (in the ratio 2 : 1) and Bi atoms [5]. Bi and B(1) atoms occupy positions with symmetry C_2 in the unit cell of BiB_3O_6. The positional symmetry of other atoms (B(2), O(11), O(12), and O(2)) is C_1. Analysis of the vibrations shows that $\Gamma_{vbn}^{opt} = 13A + 14B$. All 27 vibrations are active in the IR and Raman spectra.

Twenty-five bands were detected in the vibrational spectrum of BiB_3O_6 (Figs. 1, 3). Their positions are listed in Table 4. Vibrations of the B–O framework in

Table 5. Positions of the lines (cm^{-1}) observed in the IR and Raman spectra of α-$Bi_2B_8O_{15}$ crystals

Raman spectrum	Raman spectrum	IR spectrum
28	405	405
32	421	424
45	430	
54	449	444
62	465	471
76	496	498
84	518	535
108	551	548
114	583	588
127	596	602
140	614	
156	644	640
168		656
179	673	673
187	685	687
192	701	704
213	725	727
225	756	756
282	802	799
321		843
346	908	899
372	935	928
	960	972
	983	990
	1056	1078
	1089	
		1194
	1233	1240
	1355	1349
		1375
		1467
		1511
		1547

BiB_3O_6 can be considered as vibrations of an infinite two-dimensional (2D) grid $[B_3O_6]_{\infty\infty}$ located parallel to the (001) plane. A fragment composed of $[BO_3]^{3-}$, $[BO_4]^{5-}$, and $[BO_3]^{3-}$ groups connected in series can be regarded as a structural unit of this grid (Fig. 3). The grid is formed by linking free vertices of $[BO_3]^{3-}$ and $[BO_4]^{5-}$ groups belonging to neighboring fragments of $[B_3O_6]_{\infty\infty}$. $[BO_4]^{5-}$ tetrahedra share all their oxygen vertices with $[BO_3]^{3-}$ triangles, whereas each triangle has one vertex that is not linked in the grid. The structural features characteristic of the $[B_3O_6]_{\infty\infty}$ grid in the BiB_3O_6 lattice are also observed in corrugated metachains $[B_6O_{12}]_\infty$ forming the B–O framework of rare-earth borates $Ln(BO_2)_3$, where Ln = La–Tb [20]. Therefore, the vibrational spectra of BiB_3O_6 are similar in many respects to the spectra of rare-earth borates but are not identical to them [20, 21]. Among the known layered borate polyanions, the structure of the $[B_9O_{15}]_{\infty\infty}$ polyanion, which is characteristic of α-$Na_2O : 3B_2O_3$, is most similar to that of $[B_3O_6]_{\infty\infty}$ [20]. The main difference is that all $[BO_3]$ groups in $[B_3O_6]_{\infty\infty}$ are not directly linked to each other. Thus, a new type of polyborate anion is observed in BiB_3O_6.

In the IR and Raman spectra of BiB_3O_6, along with the bands due to vibrations of the $[BO_3]^{3-}$ and $[BO_4]^{5-}$ groups, bands near 942–949 and 1065–1100 cm^{-1} are observed. It is accepted [22–25] to attribute these bands to vibrations of complexes containing both $[BO_3]^{3-}$ and $[BO_4]^{5-}$ groups. The bands at 1450 and 1480 cm^{-1} could be interpreted as overtones at the doubled frequency of out-of-plane bending vibrations of the B atom in the $[BO_3]^{3-}$ group (725 and 738 cm^{-1}, respectively). However, the significant intensity of the band at 1452 cm^{-1} (Fig. 3) indicates that this band can be assigned to first-order vibrations of the $[B_3O_6]_{\infty\infty}$ polyanion. According to [25], this spectral region shows a band that is present in all spectra of melts, glasses, and crystals containing linked $[BO_3]^{3-}$ triangles, one of the vertices of which is not involved in the formation of a polyborate anion. The presence of a free vertex makes it possible to select the local symmetric bond vibration of the B–O middle group, which manifests itself in the Raman spectra as a high-frequency polarized line in the vicinity of ~1460 cm^{-1}. The band in the range 660–670 cm^{-1} is also assigned to vibrations of the B–O middle group [26].

$Bi_2B_8O_{15}$. In the complex framework structure of α-$Bi_2B_8O_{15}$ (sp. gr. $P2_1$, Z = 2 [6]), several different infinite chains can be selected. The boron–oxygen chain is formed by B–O rings composed of three $[BO_3]^{3-}$ groups. The rings are linked with each other by a $[BO_3]^{3-}$ group. The two other chains are formed by different groups ($[BO_3]^{3-}$, $[BiO_6]^{9-}$, $[BO_4]^{5-}$) linked in series. The α-$Bi_2B_8O_{15}$ structure contains 4-, 6-, 8-, 12-, and 24-member rings. All atoms in the unit cell of this compound occupy general positions with C_1 symmetry. In the vibrational spectra, one should expect the appearance of $\Gamma_{vbn}^{opt} = 74A + 73B$ vibrations, which are active in both IR and Raman spectra.

Due to the low symmetry of the crystal lattice of α-$Bi_2B_8O_{15}$, the vibrational spectra of this compound contain a large number of bands (Figs. 1, 4; Table 5). Among the main groups of bands, one can select the bands characteristic of vibrations of the metaborate ring. The lines at about 590, 700, 760, 808, 960, 1360, and 1490 cm^{-1} are attributed to vibrations of this anion

Table 6. Positions of the lines (cm^{-1}) observed in the IR and Raman spectra of $BiBO_3$ crystals

Raman spectrum	Raman spectrum	IR spectrum	Assignment
32			
52	399	426	
58	575	574	
83	624	625	
95	637		
126	714	716	
139	722		$\gamma(B_{(3)}–O)$
164	742	744	
206	934	928	$\nu_s(B_{(3)}–O)$
223	1179	1178	
257	1202	1208	$\nu_{as}(B_{(3)}–O)$
228	1221		
352			

[26–29]. Along with these lines, the spectra show a large number of bands, identification of which is difficult due to the large structural variety of polyborate anions forming the $Bi_2B_8O_{15}$ lattice.

$BiBO_3$. The positions of the bands and their insignificant splitting in the vibrational spectra of $BiBO_3$ (Fig. 5, Table 6), the structure of which has not been studied yet, indicate that B atoms are located in isolated $[BO_3]^{3-}$ triangles in this compound. These data confirm the preliminary results of powder X-ray diffraction analysis, according to which $BiBO_3$ can be assigned to calcite structures (sp. gr. $R\bar{3}c$). The low-temperature modification $InBO_3$ [30], the IR spectrum of which is similar to the spectrum of $BiBO_3$, belongs to this structural type [10]. In the $InBO_3$ lattice, B atoms occupy identical positions and are located in isolated $[BO_3]^{3-}$ groups.

CONCLUSIONS

The vibrational spectra of crystals of bismuth borates of different composition (including the compounds containing polyborate anions $[B_5O_{11}]^{7-}$ and $[B_3O_6]_{\infty\infty}$, which are not present in crystals of other borates) are considered. In the crystals containing less than 50 mol % of B_2O_3 ($Bi_{24}B_2O_{39}$, $Bi_4B_2O_9$, $BiBO_3$), in which boron is located in isolated $[BO_3]^{3-}$ triangles, the effect of bismuth on the character of boron–oxygen bonds leads to the red shift of a number of bands corresponding to fundamental vibrations of the $[BO_3]^{3-}$ group. With an increase in the B_2O_3 content, the B–O framework of the lattice becomes more complex. The formation of $[B_5O_{11}]^{7-}$ polyborate anions ($Bi_3B_5O_{12}$) or 2D $[B_3O_6]_{\infty\infty}$ grids (BiB_3O_6) leads to the appearance of bands in the spectral ranges 920–980 and 1420–1500 cm^{-1}, which are characteristic of polyborate anions containing both $[BO_3]^{3-}$ and $[BO_4]^{5-}$ groups. The vibrational spectra of these crystals contain bands due to vibrations of polyborate anions of different structure, including the $[B_3O_6]^{3-}$ metaborate ring.

When going from the $Bi_{24}B_2O_{39}$, $Bi_4B_2O_9$, and $BiBO_3$ compounds (in the structure of which boron is in isolated $[BO_3]^{3-}$ groups) to the compounds with condensed $[BO_3]^{3-}$ groups, the strongest bands in the absorption spectra, observed at 1100–1300 cm^{-1} (ν_{as}), are shifted to a higher frequency region. A similar result was obtained in [21, 31–35], where cyclic and chain metaborates, pyroborates, and borosilicates were studied.

REFERENCES

1. E. M. Levin and C. L. McDaniel, J. Am. Ceram. Soc. **45** (8), 355 (1962).
2. Yu. F. Kargin and A. V. Egorysheva, Neorg. Mater. **34** (7), 859 (1998).
3. A. Hyman and A. Perloff, Acta Crystallogr., Sect. A: Cryst. Phys., Diffr., Theor. Gen. Crystallogr. **28**, 2007 (1972).
4. A. Vegas, F. H. Cano, and S. Garsia-Blanco, J. Solid State Chem. **17**, 151 (1976).
5. P. von Fröhlich, L. Bohaty, and J. Lieberitz, Acta Crystallogr., Sect. C: Cryst. Struct. Commun. **40**, 343 (1984).
6. A. V. Egorysheva, A. S. Kanishcheva, Yu. F. Kargin, *et al.*, Zh. Neorg. Khim. **47** (12), 1961 (2002).
7. Yu. F. Kargin, V. P. Zhereb, and A. V. Egorysheva, Zh. Neorg. Khim. **47** (8), 1362 (2002).
8. A. V. Egorysheva, V. I. Burkov, V. S. Gorelik, *et al.*, Fiz. Tverd. Tela (St. Petersburg) **43** (9), 1590 (2001) [Phys. Solid State **43**, 1655 (2001)].
9. A. A. Kaminskii, P. Becker, L. Bohaty, *et al.*, Opt. Commun. **206**, 179 (2002).
10. C. E. Weir and R. A. Schroeder, J. Res. Natl. Bur. Stand., Sect. A **68** (5), 465 (1964).
11. S. N. Narang, N. D. Patel, and V. B. Kartha, J. Mol. Struct. **327**, 221 (1994).
12. V. N. Denisov, A. N. Ivlev, A. S. Lipin, *et al.*, J. Phys.: Condens. Matter **9**, 4967 (1997).
13. K. Nakamoto, *Infrared and Raman Spectra of Inorganic and Coordination Compounds*, 4th ed. (Wiley, New York, 1986; Mir, Moscow, 1991).
14. J. Li, S. Xia, and S. Gao, Spectrochim. Acta A **51** (4), 519 (1995).
15. *Vibrations of Oxide Lattices*, Ed. by A. N. Lazarev and M. O. Bulanin (Nauka, Leningrad, 1980) [in Russian].
16. V. I. Burkov, V. S. Gorelik, A. V. Egorysheva, and Yu. F. Kargin, J. Russ. Laser Res. **22** (3), 243 (2001).
17. L. V. Kristallov, M. Ya. Khodos, and L. L. Perelyaeva, Zh. Neorg. Khim. **34** (9), 2358 (1989).
18. R. Janda and G. Heller, Spectrochim. Acta, Part A **36** (11), 997 (1980).

19. V. Devaragan, E. Grafe, and E. Funck, Spectrochim. Acta, Part A **32** (5), 1225 (1976).
20. N. I. Leonyuk and L. I. Leonyuk, *Crystal Chemistry of Anhydrous Borates* (Mosk. Gos. Univ., Moscow, 1983) [in Russian].
21. B. F. Dzhurinskiĭ, Doctoral Dissertation in Chemistry (Inst. of General and Inorganic Chemistry, USSR Academy of Sciences, Moscow, 1972).
22. T. W. Bril, Philips Res. Rep. Suppl. **2**, 114 (1976).
23. W. L. Konijnendijk, Philips Res. Rep. Suppl. **1**, 243 (1975).
24. E. I. Kamitsos and M. A. Karakassides, Phys. Chem. Glasses **30** (1), 19 (1989).
25. Yu. K. Voron'ko, A. V. Gorbachev, A. B. Kudryavtsev, and A. A. Sobol', Neorg. Mater. **28** (8), 1707 (1992).
26. B. N. Meera and J. Ramakrishna, J. Non-Cryst. Solids **159** (1), 1 (1993).
27. Yu. K. Voron'ko, A. V. Gorbachev, A. B. Kudryavtsev, *et al.*, Neorg. Mater. **28** (8), 1713 (1992).
28. Yu. K. Voron'ko, A. V. Gorbachev, A. A. Sobol', and L. I. Tsymbal, Neorg. Mater. **30** (5), 646 (1994).
29. V. Moryc and W. S. Ptak, J. Mol. Struct. **511–512**, 241 (1999).
30. E. M. Levin, R. S. Roth, and J. B. Martin, Am. Mineral. **46**, 1030 (1961).
31. P. Broadhead and G. A. Newman, J. Mol. Struct. **10**, 157 (1971).
32. A. N. Lazarev, *Vibrational Spectra and Structure of Silicates* (Nauka, Leningrad, 1968), p. 216 [in Russian].
33. I. I. Plyusnina and Yu. Ya. Kharitonov, Zh. Strukt. Khim. **4** (4), 555 (1963).
34. L. I. Al'shinskaya, N. I. Leonyuk, A. V. Pashkova, *et al.*, Vestn. Mosk. Univ., Ser. 4: Geol., No. 3, 107 (1978).
35. I. R. Magunov, S. V. Voevudskaya, A. P. Zhernova, *et al.*, Izv. Akad. Nauk SSSR, Neorg. Mater. **21** (9), 1532 (1985).

Translated by Yu. Sin'kov

Crystallography Reports, Vol. 50, No. 1, 2005, pp. 13–19. Translated from Kristallografiya, Vol. 50, No. 1, 2005, pp. 19–26.

CRYSTAL CHEMISTRY

Symmetry and Topological Analysis of the OD Nenadkevichite–Labuntsovite–Zorite Family

E. L. Belokoneva

Faculty of Geology, Moscow State University, Vorob'evy gory, Moscow, 119992 Russia

e-mail: elbel@geol.msu.ru

Received November 14, 2003

Abstract—The symmetry and topology of the structures of nenadkevichite, labuntsovite, and zorite minerals are analyzed within the Dornberger-Schiff OD theory. The common "layers," their symmetry, and the symmetry variants of their stacking determining their diversity and close structural characteristics are considered, which allowed us to relate these minerals to one family. According to the fundamental theorem of the OD theory, the number *Z* of possible combinations of aperiodic blocks inserted between the layers in zorite equals two simultaneously along two axes of the structure, which explains the structural disorder. Some hypothetical structures are also considered. © *2005 Pleiades Publishing, Inc.*

Labuntsovite [1], nenadkevichite [2], and zorite [3] were discovered by different researchers in the same Lovozero alkali massif at the Kola Peninsula in the Khibiny Mountains in 1926, 1955, and 1973, respectively. All these minerals are titanium–niobium silicates and have rather complicated compositions. In 1926, a newly discovered mineral was named titanium elpidite, but in 1955, after its parallel study with nenadkevichite and establishment of many similar properties and isomorphous miscibility with the latter, titanium elpidite was renamed labuntsovite. These two minerals were considered as individual species because of the prevalent content of Ti and K in labuntsovite in comparison with prevalent content of Nb and Na in nenadkevichite and their different symmetries: labuntsovite has a monoclinic unit cell, whereas nenadkevichite has an orthorhombic one. The crystal structure of labuntsovite, $(K,Ba,Na,Ca)_4(Ti,Nb)_{4.5}(Si_4O_{12})_2(O,OH)_5 \cdot nH_2O$, was first studied using single crystal data in [4] and recently was refined for the composition $Na_{2.15}K_{1.85}Ba_{1.05}(Ti_4Mn_{0.3}Mg_{0.1}Fe_{0.05}(Si_4O_{12})_2O_3(OH) \cdot 5.2H_2O$ in [5]. Practically simultaneously with the labuntsovite structure determination [4], the nenadkevichite structure $(Na_{3.76}K_{0.24}Ca_{0.11}Mn_{0.03}) \cdot (Nb_{2.76}Ti_{1.18})(Si_4O_{12})_2(O_{2.80}OH_{1.20}) \cdot 8H_2O$ was studied in [6]. It was established that the two minerals really have different symmetries described by the sp. grs. *I*2/*m* (*C*2/*m*) and *Pbam*, respectively. The X-ray precession patterns of labuntsovite [4] had diffuse reflections which indicated doubling of the parameter along one of the unit-cell axes. Despite the fact that it was impossible to record odd reflections, only the final structural model that took into account such reflections provided the interpretation of the structural disorder. The structure of zorite, $Na_6[Ti(Ti_{0.9}Nb_{0.1})_4(Si_6O_{17})_2(O,OH)_5] \cdot 11H_2O$, was solved in [7]. The rotation and precession X-ray diffraction patterns of this mineral showed diffuse reflections indicating doubling of one of the unit-cell parameters and also some reflections violating the periodicity along two other axes. Similar to the case of labuntsovite, the final structural model was created with due allowance for doubling of one of the lattice parameters because of diffuse reflections. The structural relation of this mineral to orthorhombic nenadkevichite was also established. The nenadkevichite structure was solved in a diffraction experiment (Picker diffractometer) [6] with a rather high value of the final reliability factor, $R_{hkl} = 8.4\%$ ($F_{hkl} > 3\sigma$), which leads to an assumption of the presence of additional diffuse reflections not taken into account and possible disorder in nenadkevichite.

The present study was undertaken with the aim to give new topological and symmetric description of the close structures of the family consisting of the three above minerals and establish their similar and different features, the cause of their structural disorder, and possible structural variants.

According to the Dornberger-Schiff theory of OD structures first suggested in [8], the structures contain common building units (structural blocks) with different periodicities: aperiodic, one-dimensionally periodic, and two-dimensionally periodic units. This theory was applied to some concrete structures with two-dimensionally periodic units, i.e., layers. It was also suggested to accompany analysis of the layer symmetry with the analysis of the symmetry methods of layer conjugation into pairs in real structures. The most important point in the analysis of the symmetry and topology is the consideration of the ratio of the symmetry multiplicities of an individual layer and a pair of such layers. If a difference is revealed, i.e., the order *N* of the symmetry group of one layer is higher than the

Main crystallographic characteristics of labuntsovite, nenadkevichite, and zorite

	Labuntsovite [1]	Labuntsovite [5]	Nenadkevichite [2]	Zorite [3]
a, Å	14.18	14.216	7.408	23.9
b, Å	7.74 (×2)	13.755	14.198	7.23
c, Å	13.70	7.767	7.148	6.955 (×2)
γ(β), deg	117.0	116.7		
Sp. gr.	$B11\frac{2}{m}$	$C1\frac{2}{m}1$	*Pbam*	*Cmmm*

order of the symmetry group *F* of the pair of such layers, then the second layer may be located with respect to the first by several methods. The number of the variants of its location is determined by the ratio of the symmetry multiplicities *Z* = *N*/*F*. The layer symmetry does not characterize the structure as a whole; it characterizes only the layer symmetry or the partial symmetry operation. In other words, a higher symmetry (pseudosymmetry) of individual layers in comparison with the symmetry of their combination forms the basis of the structural diversity. The simplest and clearest examples of analysis of *OD* structures [8] are discussed in [9]. The important fact is that the individual layer element (two-dimensionally periodic block) is not necessarily a layer in terms of crystal chemistry.

Similarity of labuntsovite, nenadkevichite, and zorite structures is most clearly seen from the comparison of their projections along the axis with the common parameter ~13.7 Å corresponding to the monoclinicity axes of labuntsovites, *c* [1] or *b* [5], and the *c* axis of nenadkevichite [2] and zorite [3] (see table). Consider a common structural fragment in nenadkevichite (Fig. 1). The framework of the structure has layers parallel to the *ac* plane denoted as *L*(1). They are formed as a result of the condensation of the $(Nb,Ti)_2[SiO_4]_4O_2 = 2[(Nb,Ti)OSi_2O_8]$ rods elongated in the direction of the *a* axis (Figs. 1a and 1b). The rods are composed of (Nb,Ti) octahedra sharing the vertices and form an oscillating zigzag chain and Si tetrahedra attached simultaneously to two octahedra of the chain because of their mutual rotation toward one another. The alternation of the rotations and attachment of the tetrahedra proceeds in accordance with the law of a glide plane *g*(*a*). The local symmetry of the rod, λ-*PO*, may be described by the group *Pmam* in which the only glide element is directed along the one-dimensional rod periodicity. The connection of these rods along the *c* axis into a two-dimensionally periodic layered unit proceeds via the vertices of Si tetrahedra and the action of the mirror reflection planes *m* normal to the *c* axis. This results in the formation of diortho groups of Si tetrahedra (Fig. 1b), which, finally, form the anionic silicon-oxygen radical: a four-membered ring. The structure-forming layer $L(1)(Nb,Ti)OSi_2O_6$ (Figs. 1a and 1b) is characterized by a higher orthorhombic pseudosymmetry described by the sp. gr. *Pmam* in comparison with the structure symmetry described by the sp. gr. *Pbam* (table). This symmetry is the partial symmetry operation λ-*PO*, the local symmetry of the layer not inherent in the structure as a whole, or, using the terminology suggested in [8], the symmetry having no continuation. The connection of the layers into the framework may also be achieved with the aid of the symmetry operation *m* and, if there were no Na atoms, the symmetry thus obtained would have been described by the sp. gr. *Cmmm*. The existence of the pseudosymmetry described by the sp. gr. *Cmmm* follows from the analysis of atomic coordinates and is indicated in [6]. In fact, this pseudosymmetry which follows from the presence of λ-*PO* layers is characteristic of the frameworks of all three structures and, not being the true symmetry of any of the three minerals, it is nevertheless one of their most important characteristics determining structural diversity.

Both nenadkevichite and labuntsovite are described by the symmetry groups which are the subgroups of the sp. gr. *Cmmm*. In nenadkevichite (sp. gr. *Pbam*), the supergroup preserves the mirror plane *m* in the third position in its notation and the glide *b* and *a* planes, whereas the main symmetry element, lattice *C*, is violated by the Na atoms. A number of other symmetry elements of the supergroup are also lost. In the nenadkevichite structure, a layered two-dimensional block with the symmetry λ,ρ-*PO* in the notation of [8] (in brackets, the direction of layer multiplication is indicated; the symbol ρ indicates the nonpolarity of the layer along the direction of its multiplication) is multiplied by the σ,ρ-*PO* *Pmm*2 symmetry operations to form a mixed framework of tetrahedra and octahedra. The layer topology is such that its combination with another layer into a framework is possible only by one way: via sharing the vertices of Si tetrahedra; in other words, there are no possibilities for the displacement of one layer with respect to another one. Analysis of the symmetry and topology allows one to predict the formation of the layered structures form the initial layer but not framework structures. The end vertices of Si tetrahedra are dangling and the charges of O atoms may be compensated, e.g., by the entrance of alkali or alkali earth metals into the interlayer space. For layered variants, there are numerous variants of the layer positions in the pairs provided by the ratio of the symmetry mul-

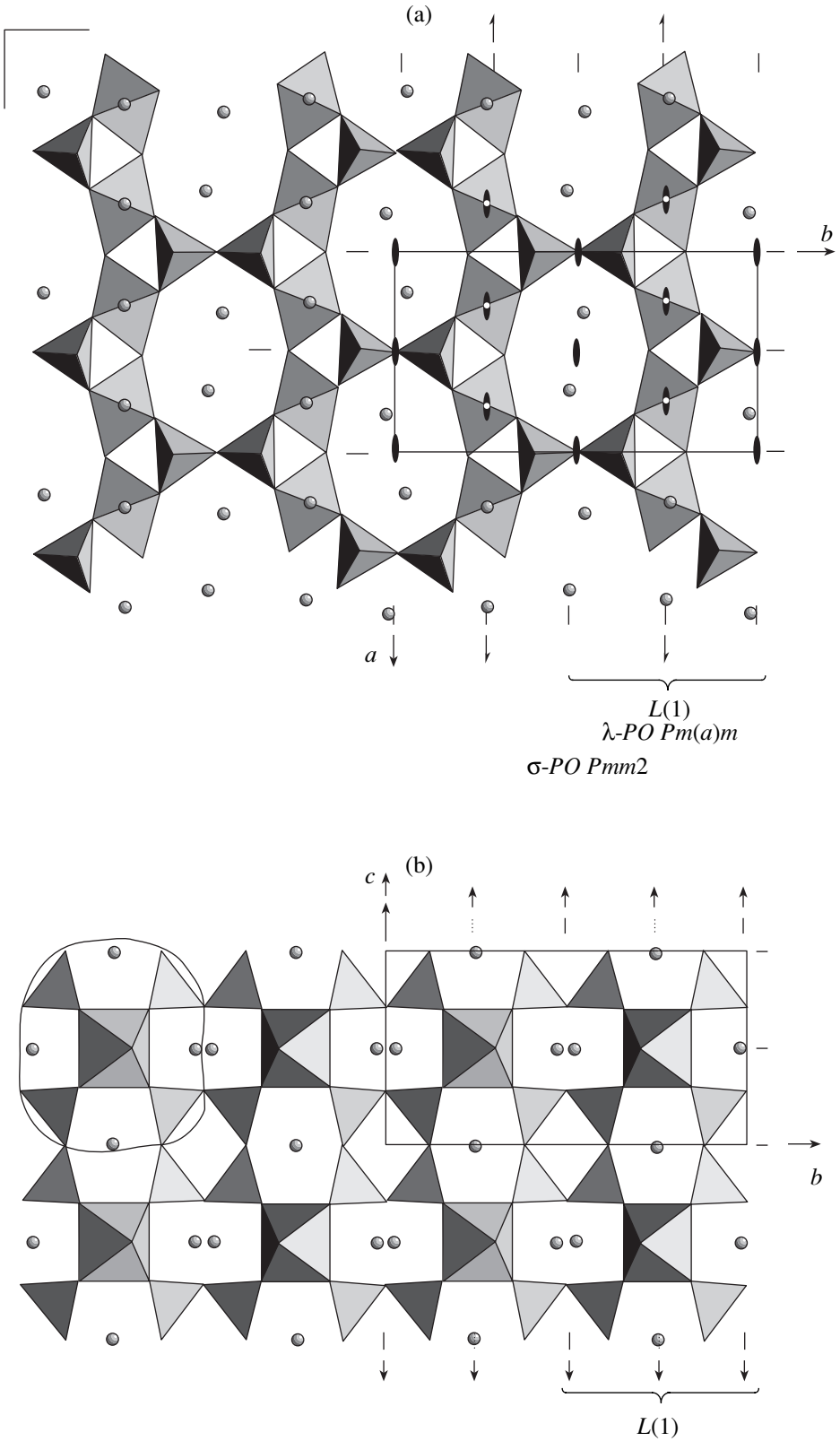

Fig. 1. Mixed framework consisting of octahedra and tetrahedra in nenadkevichite. Na atoms are depicted by circles. One may see the *L*(1) layers and their symmetry elements λ-*PO*, and also the multiplying symmetry elements σ-*PO*. (a) *ab* projection; (b) *bc* projection, one of the rod ends is encircled.

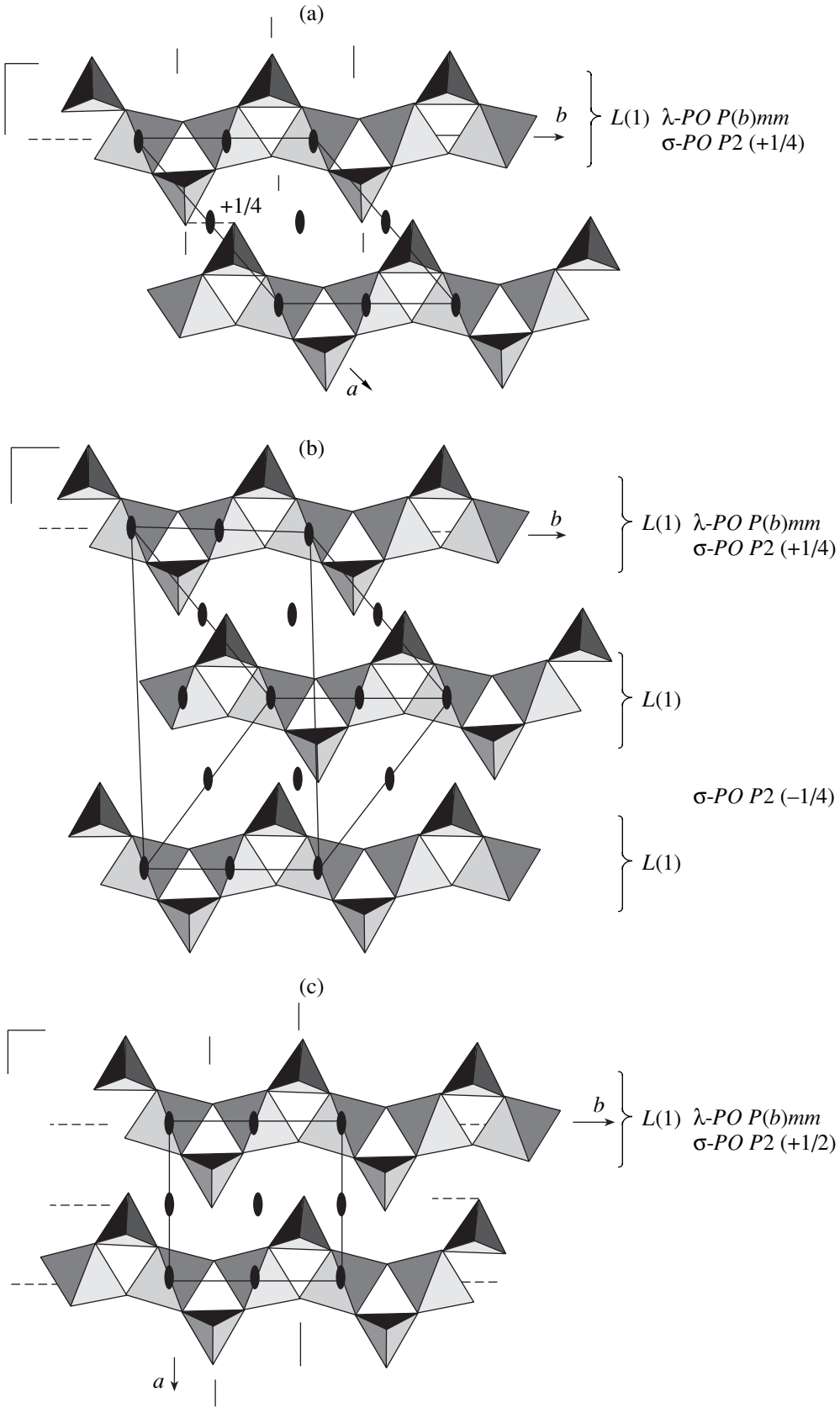

Fig. 2. Hypothetical layered structures based on nenadkevichite layers $L(1)$, (a) monoclinic unit cell, sp. gr. $P11\frac{2}{m}$. (b) Twin structure, (c) orthorhombic unit cell, sp. gr. *Pbmm*.

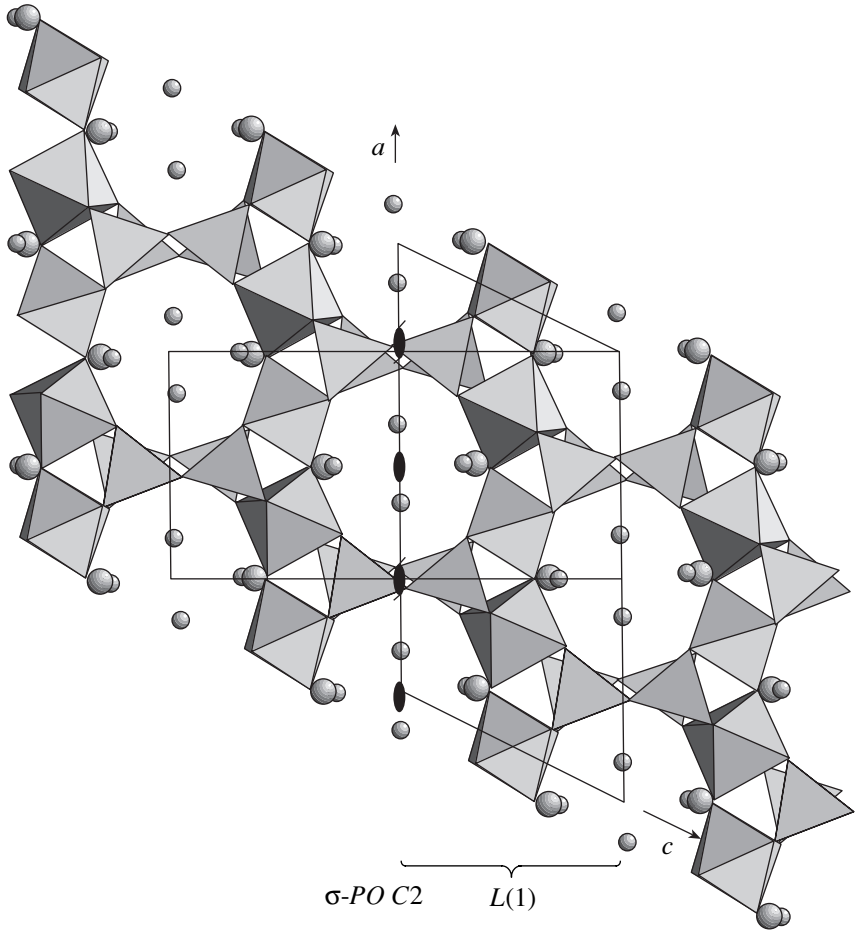

Fig. 3. Mixed framework of octahedra and tetrahedra in labuntsovite. The Ba and K atoms are depicted by large and small circles. One can see the labuntsovite unit-cell, the *L*(1) layers, and the multiplying symmetry σ-*PO* elements; *ac* projection.

tiplicity λ,ρ-*PO Pm*(*a*)*m*, which gives rise to the formation of various hypothetical structures and twins (Fig. 2). The principles of construction of the whole group of the framework and layered structures are similar to that of the hexaborate group [10]. Possibly, there exist structures with the maximum degree order (MDO), more complicated periodic structures, and also aperiodic disordered structures. None of the known Ti,Nb,Zr silicate minerals and synthetic phases have a layered structure, which indicates the instability of the silicate structures with dangling tetrahedron vertices. At the same time, in hexaborates, the layered structures are rather widespread, whereas the condensation into the framework via the vertices of the B triangles is encountered in only one synthetic borate [10]. This shows that the occurrence of various structural variants depends on the influence of the electrostatic principles of valence compensation.

For labuntsovite described by the sp. gr. $C1\frac{2}{m}1$ [5] (or $B11\frac{2}{m}$ in the setting used in [4]) the group–subgroup relation with respect to the supergroup *Cmmm* is also valid. The mirror reflection plane in the second position of the group notation [5] is preserved, whereas the short translation of the oblique monoclinic unit cell $c \sim 7.8$ Å corresponds to the *C* lattice of the supergroup (Fig. 3). Lowering of the symmetry from orthorhombic to monoclinic is associated with the loss of the mirror plane passing through the Si tetrahedra in the first position of the supergroup. This is explained by the entrance of large Ba^{+2} and K^{+} ions in labuntsovites (Fig. 3) and the distortion of the framework for the creation of their necessary coordination, whereas in nenadkevichites, these are smaller Na^{+} ions. The entrance of rather small Mn^{+2} ions into the labuntsovite structure only slightly distorts the framework and may hardly cause lowering of the symmetry to monoclinic [5] with respect to orthorhombic nenadkevichite, where this position is occupied by a somewhat larger Na^{+} ion. A layer with the symmetry (pseudosymmetry) λ,ρ-*PO Pm*(*g*)*m*, where *g* is the general notation of a glide symmetry plane irrespective of the selection of the axes, is transformed into the next layer not by σ,ρ-*PO Pmm*2 but by σ,ρ-*PO C*2(2_1). In other words, it is transformed

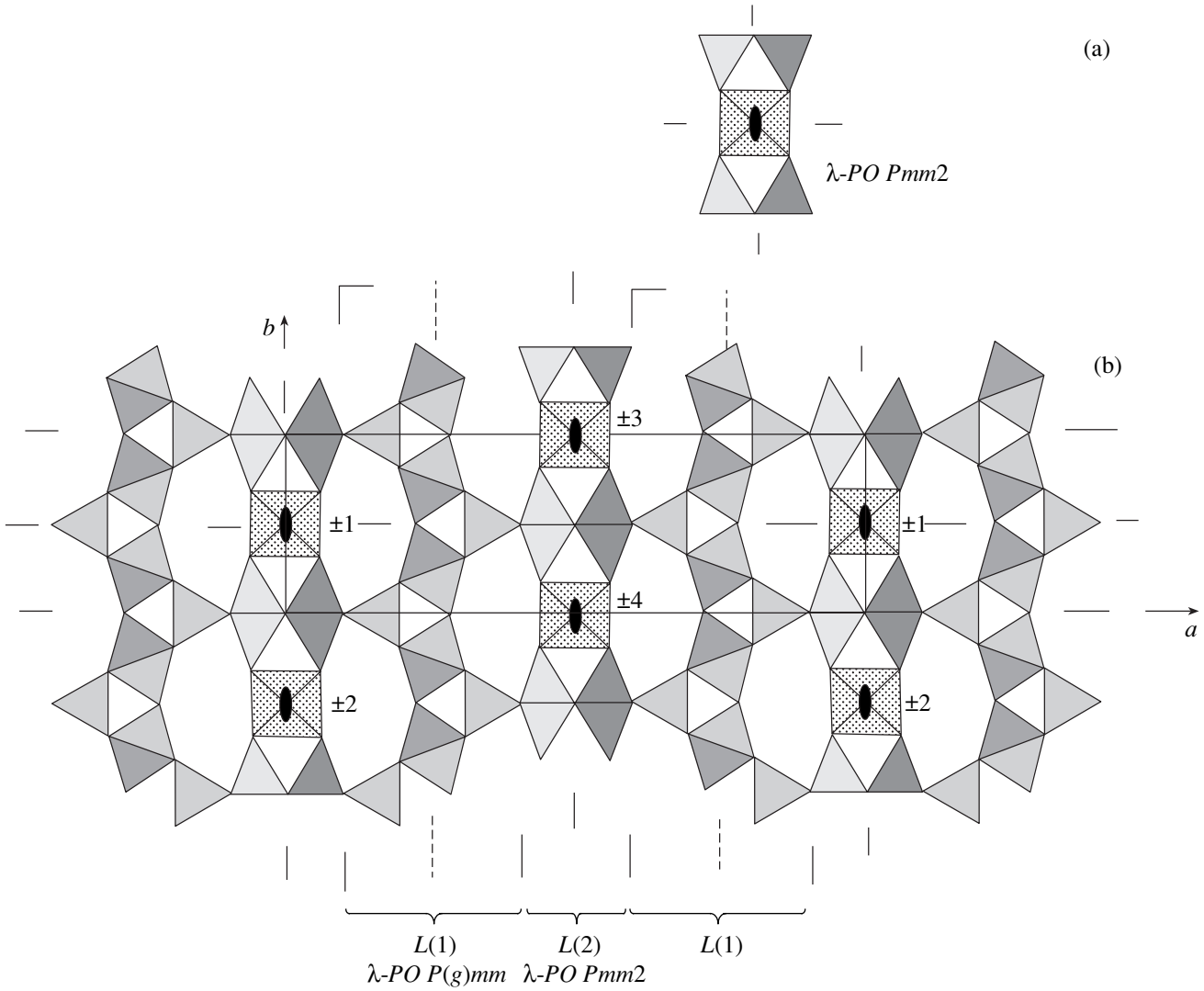

Fig. 4. (a, b) Mixed framework of octahedra, hemioctahedra, and tetrahedra in the zorite structure. (a) The inserted $[TiSi_4O_{15}]$ block and its symmetry. (b) The averaged structure in the *ab* projection. One may see the *L*(1) and *L*(2) layers and numbered voids occupied by blocks.

by the symmetry elements not of the orthorhombic but of the monoclinic group (Fig. 3).

Dornberger-Schiff suggested description of such structures forming the *OD* family in a general form with the aid of the symmetry groupoid in which the first line indicates the group of the partial symmetry operations of the λ-*PO* layers and the second line indicates the multiplying σ-*PO* operations. For the two given structures built by the same type of layers, this is written as

$$Pm(g)m \quad \lambda,\rho\text{-}PO$$
$$\{Pmm2 \,//\, C121\} \quad \sigma,\rho\text{-}PO.$$

The generalized *OD* approach to the symmetric description in which the structural blocks have dimensionality lower than two (indicated as a possible variant in [8]) may also be applied to the zorite structure. Despite the use of the notation of the *OD* theory in the study of the zorite structure [7], no main symmetric cause of the structural disorder was established. The fragment, which is additional in comparison with the nenadkevichite, is in fact not a rod (as was indicated in [7], i.e., one-dimensionally periodic unit) but a block (aperiodic unit). This requires the change of the structure description in terms of the *OD* theory given in [7], which, we believe, is too complicated and difficult to understand.

The zorite structure is composed of the already mentioned nenadkevichite–labuntsovite *L*(1) layers alternating along the *a* axis with the *L*(2) layers containing aperiodic blocks [3]. Each such block is formed by the central Ti-hemioctahedron and two Si diortho groups attached to the opposite edges of its square basis. Its formula may be written as $[TiSi_4O_{15}]$, and its symmetry or pseudosymmetry corresponds to the group *Pmm*2.

The *ab* projection shows that the distance from the end tetrahedra surrounding the zeolite cavity of the framework of the nenadkevichite-labuntsovite type coincides with the block size (Figs. 4a and 4b, where the pseudoaxis 2 of the block is directed toward the reader, i.e., is aligned in the *c* direction). This provides the conjugation (hybridization) of two different units. In other words, a block may enter any cavity of the nenadkevichite framework by pushing away its *L*(1) layers for a width of the diortho group and form a new ribbon-like anionic radical [7]. Here, the symmetry is very important: each cavity and the block in this cavity have common mirror planes *m* at the boundary and in the middle which divide them into two equal parts. The presence of *m* at the cavity boundaries provide the equal probability of the attachment of blocks above and below the plane along the *b* axis (Fig. 4b). Therefore, in the averaged structure with the parameter $b \sim 7.2$ Å [7], two Si tetrahedra share the face. Under the assumption that blocks are incorporated only in cavities 1 and not 2, and in cavities 3 and not 4 (Fig. 4b), the Si tetrahedra in the structural model with doubled *b* parameter cannot share faces. Diffuse additional reflections indicating doubling of the *b* axis also indicate the structure disorder along this direction. The most important fact here is that the layers and blocks have different symmetry multiplicities. Symmetry multiplicity of the *L*(1) layer (*P*(*g*)*mm*) equals 8, and symmetry multiplicities of the block (*Pmm*2) and the "layer + block" pair equal 4. At the same time, the existence of the second horizontal plane *m* at the third position of the group notation and the absence of such a plane for a block makes possible its two orientations also along the *c* axis: upward and downward (±1, ±2, …). These determine the structural disorder along the *c* axis and give rise to reflections violating the periodicity of the *c* axis. According to the basic theorem of the *OD* theory, the ratio *Z* of the order of the symmetry group of the layer *L*(1) to the order of the symmetry group of the block in the layer *L*(2) (and the "layer + block" pair) is $Z = N/F = 8/4 = 2$, which corresponds to two variants of location of the block from *L*(2) with respect to the layer *L*(1) along two axes of the structure. It is characteristic of the structure with two types of layers, that the position of the layer (block) with a lower symmetry λ-*PO* is determined by the symmetry of the layer with a higher symmetry λ-*PO*. The symmetry groupoid may be described as

$$L(1)\ (\mathrm{Nb,Ti})\mathrm{OSi_2O_6} \quad L(2)\ [\mathrm{TiSi_4O_{15}}],$$

$$\lambda\text{-}PO\ \{P(g)mm\} \quad L\text{-}PO\ \{Pmm2\}$$

$$[(1) \pm b \pm c].$$

The symmetry variants and the corresponding disorder result in the fact that the period along the *a* axis may also be doubled (alternation of blocks in cavities 1, 3, 1, 3, … in Fig. 3a is changed to the alternation of blocks in cavities 1, 3, 1, 4, 1), tripled, or even become aperiodic if the block alternation is violated, especially if one takes into account block signs.

Possibly, there also exist the structures in which the nenadkevichite–labuntsovite layers *L*(1) are directly adjacent to one another and, thus, form double, triple, and larger framework fragments, whereas the number of the blocks of layers *L*(2) would decrease. This would be reflected in the chemical composition of similar hypothetical minerals or synthetic compounds containing the decreasing amount of the $[\mathrm{TiSi_4O_{15}}]$ component. The series of the *OD* structures consisting of two types of layers were recently called polysomes, and the end members of these series were considered. However, because of the aperiodicity of the $[\mathrm{TiSi_4O_{15}}]$ block, this *OD* family has only one end member.

Thus, analysis of the symmetry and topology within the Dornberger-Schiff *OD* theory and the use of the basic theorem $Z = N/F$ allow one to establish the similarity and the causes of the structural diversity for three minerals, predict possible structures, and describe in the simple form the *OD* family. The occurrence of all the three minerals in one deposit confirms their structural and genetic relation. It is well known that more complicated layer combinations in polytypes correlate with a higher temperature of their formation. In this case, an important factor for the formation of each variety is the chemical composition of the medium in an unusual alkali pegmatite process in the Lovosero massif. The prevailing Ba, K, and Nb content in comparison with Na and Ti content results in the prevalent formation of labuntsovite in comparison with nenadkevichite. The additional amount of Ti and Si results in the formation of an additional block and its incorporation into the structure and formation of zorite and its hypothetical varieties.

REFERENCES

1. E. I. Semenov and T. A. Burova, Dokl. Akad. Nauk SSSR **101** (6), 1113 (1955).
2. M. V. Kuz'menko and M. E. Kazakova, Dokl. Akad. Nauk SSSR **100** (6), 1159 (1955).
3. A. N. Mer'kov, I. V. Bussen, E. A. Goĭko, *et al.*, Zap. Vses. Mineral. O–va **102**, 54 (1973).
4. N. I. Golovastikov, Kristallografiya **18** (5), 950 (1973) [Sov. Phys. Crystallogr. **18**, 596 (1973)].
5. R. K. Rastsvetaeva, N. V. Chukanov, and I. V. Pekov, Dokl. Akad. Nauk **357** (1), 64 (1997).
6. P. G. Perrault, C. Boucher, J. Vicat, *et al.*, Acta Crystallogr., Sect. B: Struct. Crystallogr. Cryst. Chem. **29**, 1432 (1973).
7. P. A. Sandomirskiĭ and N. V. Belov, Kristallografiya **24** (6), 1198 (1979) [Sov. Phys. Crystallogr. **24**, 686 (1979)].
8. K. Dornberger-Schiff, Abh. Dtsch. Akad. Wiss. Berlin **3**, 1 (1964).
9. E. L. Belokoneva, Kristallografiya **48** (2), 256 (2003) [Crystallogr. Rep. **48**, 222 (2003)].
10. E. L. Belokoneva, Zh. Neorg. Khim. **49** (6), 967 (2004).

Translated by L. Man

Crystallography Reports, Vol. 50, No. 1, 2005, pp. 137–141. Translated from Kristallografiya, Vol. 50, No. 1, 2005, pp. 145–149.

PHYSICAL PROPERTIES OF CRYSTALS

Synthesis, Physical Properties, and Atomic Structure of Niobium-Doped $RbTiOPO_4$ Crystals

V. I. Voronkova*, V. K. Yanovskiĭ*, E. P. Kharitonova*, S. Yu. Stefanovich*, N. I. Sorokina, O. D. Krotova**, and N. I. Kononkova*****

** Moscow State University, Vorob'evy gory, Moscow, 119992 Russia*
e-mail: voronk@crysc24.phys.msu.ru
*** Shubnikov Institute of Crystallography, Russian Academy of Sciences, Leninskiĭ pr. 59, Moscow, 119333 Russia*
**** Vernadsky Institute of Geochemistry and Analytical Chemistry, Russian Academy of Sciences, ul. Kosygina 19, Moscow, 119991 Russia*
Received January 26, 2004

Abstract—Single crystals of solid solutions $Rb_{1-x}Ti_{1-x}Nb_xOPO_4$ (RTP : Nb) were grown and the temperature dependences of their dielectric and nonlinear optical properties and electric conductivity were studied. The maximum possible niobium content in these crystals is close to $x = 0.1$. The niobium impurities decelerate growth of {100} faces, and crystals take a plate-like habit. With increasing doping level, ferroelectric phase transitions diffuse and their temperature decreases. A specific feature of the dielectric properties of RTP : Nb crystals is the appearance of a broad relaxation maximum ε_{33} in the temperature range 200–600°C caused by the formation of vacancies in the rubidium cation sublattice. The intensity of second-harmonic generation under laser irradiation decreases with increasing niobium content. The atomic structure of a crystal with $x = 0.01$ is studied and it is established that niobium substitutes for titanium only in Ti(1) positions. © *2005 Pleiades Publishing, Inc.*

INTRODUCTION

Rubidium titanyl phosphate $RbTiOPO_4$ (RTP) belongs to a vast family of compounds with $KTiOPO_4$ (KTP) structure [1, 2], which are promising materials for application in nonlinear optics and are of scientific interest due to the combination of ferroelectric properties and high ionic conductivity [3]. The nonlinear optical properties of RTP crystals are similar to those of well-known KTP crystals, but RTP crystals are more preferable as electro-optical modulators due to lower conductivity. Recently, a number of publications have appeared which deal with the growth of RTP crystals and their properties [4–6]. In particular, it was revealed [4] that crystallization fields of both the low-temperature orthorhombic RTP phase and the high-temperature cubic phase are present in the ternary system Rb_2O–TiO_2–P_2O_5. Perfect RTP crystals were prepared from a less viscous melt with rubidium fluoride [6]. A higher stability to laser radiation in comparison to KTP crystals was noted in [4, 6]. Niobium-doped rubidium titanyl phosphate crystals were prepared and studied, and it was ascertained that they are characterized by higher birefringence and intensity of second-harmonic generation [7, 8]. It was noted [9] that impurities of pentavalent elements Nb and Sb have a strong influence on the ferroelectric properties and electric conductivity of KTP crystals, but there are no similar data for RTP crystals. In this study, a series of $Rb_{1-x}Ti_{1-x}Nb_xOPO_4$ (RTP:Nb) crystals with various niobium contents were grown and the specific features of their electrical and nonlinear optical properties were analyzed. Specific features of the atomic structure of $Rb_{0.98}Ti_{0.99}Nb_{0.01}OPO_4$ single crystals were also investigated.

EXPERIMENTAL

RTP : Nb single crystals were grown by spontaneous flux crystallization in the quaternary system Rb_2O–TiO_2–Nb_2O_5–P_2O_5. Mixtures of high-purity-grade reagents $RbNO_3$, TiO_2, $NH_4H_2PO_4$, and Nb_2O_5 were heated to 600°C to decompose rubidium nitrate and ammonium salt, and then they were mixed in an agate mill and sealed in 50-ml platinum crucibles. Homogenization of melts was performed at 1000–1030°C, depending on their composition, for 24 h. Then the melts were cooled to 800°C at a rate of 1 K/h, after which the melt was poured off, and the crystals formed were washed out in water to remove the remaining solvent.

The chemical composition of the crystals was determined on a Camebax SX-50 microanalyser at an accelerating voltage of 15 kV and a probe current of 30 nA. $RbNbSiO_5$, $MnTiO_3$, and apatite were used as references for elemental analysis. The growth forms of crystals were studied on a ZRG-3 two-circle goniometer.

Table 1. Composition of the starting melts, Nb content (x), Nb-distribution coefficient (K_{Nb}), and specific features of the morphology of $Rb_{1-x}Ti_{1-x}Nb_xOPO_4$ crystals

Composition of starting melts, mol %				x	K_{Nb}	Most developed faces
TiO_2	Nb_2O_5	P_2O_5	Rb_2O			
25	0	32	43	0	–	{201}, {011}
24.8	0.2	32	43	0.013	0.81	{201}, {011}, {100}
24.6	0.4	32	43	0.021	0.66	{201}, {100}, {011}, {110}
24	1	32	43	0.046	0.61	{100}, {201}, {011}, {110}
23	2	32	43	0.078	0.53	{100}, {201}, {011}
22	3	32	43	0.10	0.47	{100}, {201}, {011}

The crystal structure was studied on a CAD-4F Enraf-Nonius diffractometer. The temperature dependences of the dielectric constant and electric conductivity were measured in the temperature range from 20 to 900°C on samples with silver electrodes using a Tesla BM 431E bridge at a frequency of 1 MHz. To study the temperature dependences of the intensity of second-harmonic generation of a YAG:Nd laser, we used a powder technique similar to the Kurtz–Perry method.

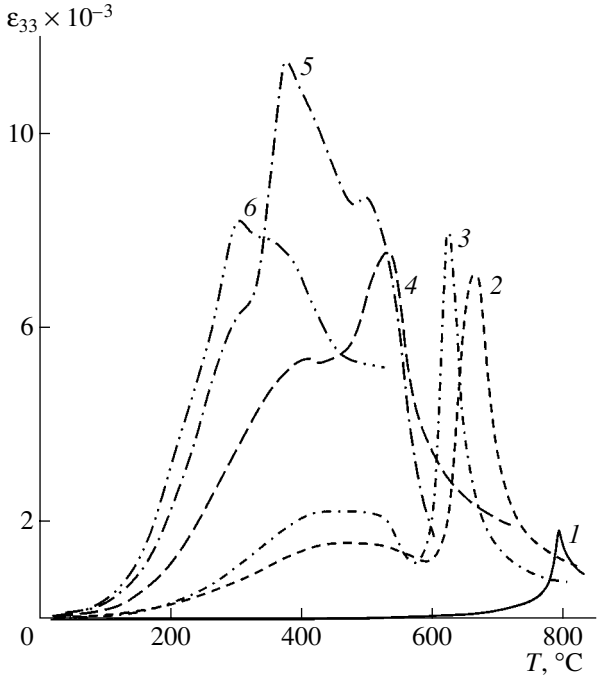

Fig. 1. Temperature dependence of the dielectric constant ε_{33} of $Rb_{1-x}Ti_{1-x}Nb_xOPO_4$ single crystals with x = (*1*) 0; (*2*) 0.013; (*3*) 0.021; (*4*) 0.046; (*5*) 0.078; and (*6*) 0.10.

RESULTS AND DISCUSSION

The compositions of the starting melts, the degree of substitution of titanium by niobium (x) in $Rb_{1-x}Ti_{1-x}Nb_xOPO_4$ crystals, the corresponding distribution coefficients, and the indices of the most developed faces are given in Table 1. The niobium distribution coefficient depends strongly on the composition of the starting melts—it decreases from 0.8 to 0.5 with decreasing niobium content. On average, this value exceeds the corresponding parameter for KTP : Nb crystals grown under nearly the same conditions by more than a factor of two [9]. The maximum degree of substitution of titanium by niobium in RTP proved to be about 10% (x = 0.1), which is close to the value found previously in [8]. The chemical analysis showed that the mechanism of niobium incorporation can be represented by the formula $Rb_{1-x}Ti_{1-x}Nb_xOPO_4$. The average unit-cell parameters of the crystals are a = 12.96 Å, b = 6.50 Å, and c = 10.57 Å, increasing by about 0.3% with increasing Nb content. From the starting melts with more than 3 mol % of niobium, a high-temperature cubic phase of rubidium titanate–phosphate $RbTiPO_5$ of very light violet color was crystallized.

The RTP : Nb single crystals obtained (3–10 mm in size) were transparent and colorless, but their quality decreased noticeably with increasing Nb content due to the formation of solvent inclusions and cracks. A specific feature of the morphology of pure RTP crystals is the absence or a slight development of the {100} faces and the complete absence of the {110} faces. However, these faces arise even at a low Nb content. At high Nb contents, the {100} faces are strongly developed and the crystals become plate-like.

The temperature dependences of the dielectric constant ε_{33} of the crystals with different niobium contents measured at a frequency of 1 MHz are shown in Fig. 1. The main specific feature of these dependences is the significant (by about 400°C) shift of the anomaly due to the ferroelectric phase transition to low temperatures with increasing niobium content. In this case, the intensity and width of this anomaly significantly increase. The second feature of these dependences is the occurrence of a broad anomaly in the temperature range 100–600°C, which has a relaxation nature. This anomaly is absent in the temperature dependence of the dielectric constant of pure RTP crystals measured at a frequency of 1 MHz [3] but is observed in the frequency range 50–500 kHz [10]. The intensity of this anomaly increases with increasing niobium content and can be as high as 7000–8000.

Niobium impurities also affect significantly the conductivity of RTP crystals (Fig. 2). The conductivity σ_{33} increases by more than an order of magnitude even when 1% of Ti is substituted by Nb. However, with a

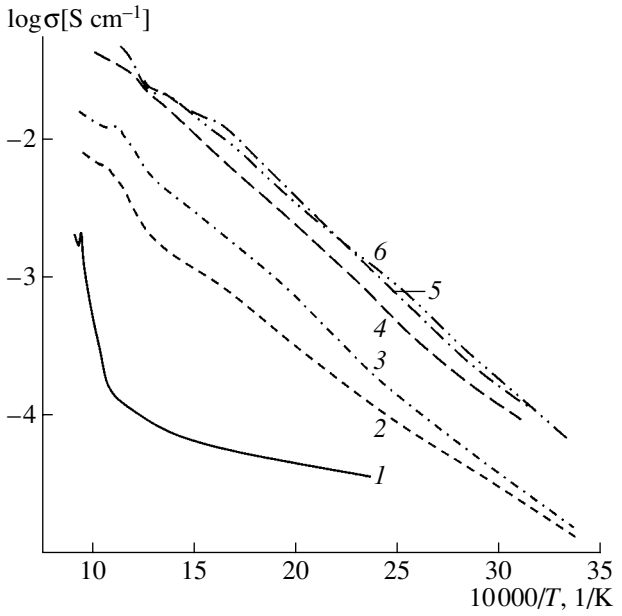

Fig. 2. Temperature dependence of the conductivity σ_{33} of $Rb_{1-x}Ti_{1-x}Nb_xOPO_4$ single crystals with x = (*1*) 0; (*2*) 0.013; (*3*) 0.021; (*4*) 0.046; (*5*) 0.078; and (*6*) 0.01.

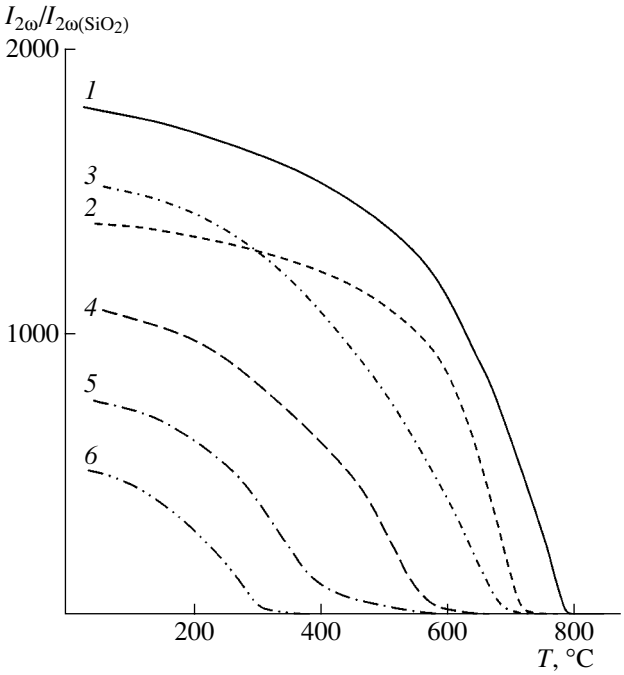

Fig. 3. Temperature dependence of the second-harmonic generation under laser irradiation of $Rb_{1-x}Ti_{1-x}Nb_xOPO_4$ single crystals with x = (*1*) 0; (*2*) 0.013; (*3*) 0.021; (*4*) 0.046; (*5*) 0.078; and (*6*) 0.01.

further increase in the Nb content, the conductivity increases more slowly, and, at x = 0.05–0.10, the conductivity remains nearly constant. In this case, the activation energy changes from 0.2 eV for pure RTP crystals to 0.5 eV for doped ones.

Figure 3 shows the temperature dependence of the intensity $I_{2\omega}$ of the second-harmonic generation of laser radiation measured on $Rb_{1-x}Ti_{1-x}Nb_xOPO_4$ crystals with various niobium contents, ground to 8–10 μm. As can be seen, with an increase in the doping level, the intensity $I_{2\omega}$ decreases, excluding some increase in the range 20–250°C at x = 0.02–0.04, and its change in the range of the ferroelectric phase transition becomes more diffuse. The concentration dependences of the Curie temperature T_C, determined from the dielectric and nonlinear optical data, are shown in Fig. 4. The nonlinearity of these dependences, which is strongly pronounced for KTP crystals doped with Nb and Sb [9], proved to be insignificant for RTP:Nb crystals.

To reveal the interrelationship between the atomic structure and physical properties of $Rb_{1-x}Ti_{1-x}Nb_xOPO_4$ crystals, we studied the structure of one of them. The experimental conditions are listed in Table 2 (the correction to X-ray absorption was not considered. The measured unit-cell parameters were a = 12.955(3) Å, b = 6.500(4) Å, and c = 10.552(3) Å. The atomic coordinates, position occupancies, and thermal parameters are listed in Table 3, and the interatomic distances are given in Table 4. It is found that niobium is incorporated into

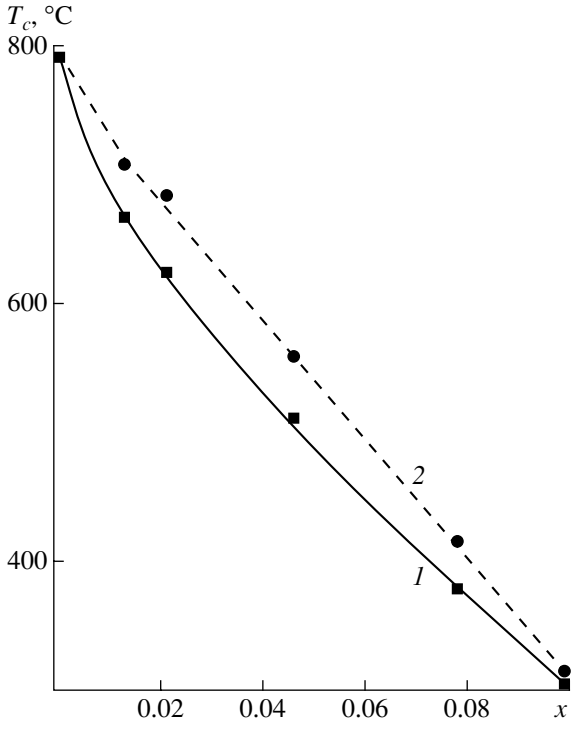

Fig. 4. Dependences of the phase-transition temperature T_C on rubidium content in $Rb_{1-x}Ti_{1-x}Nb_xOPO_4$ single crystals according to the data of (*1*) dielectric measurements and (*2*) measurements of the second-harmonic generation.

Table 2. Conditions of the X-ray experiment and refinement parameters

Chemical composition	$Rb_{0.98}Ti_{0.99}Nb_{0.01}OPO_4$
μ, cm^{-1}	129.15
Diffractometer	CAD-4F Enraf-Nonius
Radiation	MoK_α
Monochromator	Graphite
Scanning technique	ω/2θ
Space group	$Pna2_1$
Ranges of *h*, *k*, *l*	$-25 \le h \le 25$
	$-12 \le k \le 12$
	$0 \le l \le 21$
θ_{max}	45°
Total number of measured reflections, $\|F\|_{hkl}$	12169
Number of independent reflections, $\|F\|_{hkl} > 3\sigma_{\|F\|_{hkl}}$	3310
Structure type	$KTiOPO_4$
Calculation program	JANA 2000
Weighting scheme	$1/\sigma^2$
Number of parameters in refinement	169
Reliability factors R/R_w	0.052/0.072

Table 3. Atomic coordinates, occupancies (q_i), and equivalent thermal parameters for $Rb_{0.98}Ti_{0.99}Nb_{0.01}OPO_4$ crystals

Atom	*x*/*a*	*y*/*b*	*z*/*c*	q_i	B_{equi}, Å^2
Ti(1)	0.3726(2)	0.4496(4)	0.000	0.982(9)	0.24(1)
Nb(1)	0.3726	0.4996	0.000	0.018	0.24
Ti(2)	0.2483(2)	0.2676(4)	0.2514(4)	1.000	0.24(1)
P(1)	0.4497(1)	0.3335(2)	0.2584(4)	1.000	0.21(2)
P(2)	0.1803(1)	0.5018(3)	0.5120(4)	1.000	0.27(2)
Rb(1)	0.10535(6)	0.6921(2)	0.0724(3)	1.000	1.16(2)
Rb(2)	0.38507(7)	0.7839(1)	0.3235(3)	0.968(9)	1.23(2)
P(1)	0.4859(4)	0.480(1)	0.173(6)	1.000	0.62(8)
O(2)	0.5135(4)	0.463(1)	0.3812(6)	1.000	0.54(8)
O(3)	0.4016(4)	0.2012(8)	0.2796(6)	1.000	0.42(7)
O(4)	0.5947(3)	0.1943(9)	0.2384(6)	1.000	0.50(8)
O(5)	0.1145(4)	0.3111(9)	0.5423(6)	1.000	0.51(8)
O(6)	0.1128(4)	0.6905(8)	0.4842(6)	1.000	0.53(8)
O(7)	0.2504(5)	0.543(1)	0.6279(6)	1.000	0.59(8)
O(8)	0.2518(5)	0.4585(9)	0.3987(6)	1.000	0.58(8)
P(1)	0.2229(4)	0.437(9)	0.3900(6)	1.000	0.46(8)
O(10)	0.2219(4)	–0.0387(9)	0.6438(6)	1.000	0.46(8)

Table 4. Interatomic distances in $Rb_{0.98}Ti_{0.99}Nb_{0.01}OPO_4$ crystals

Coordination polyhedra	Distances, Å	Coordination polyhedra	Distances, Å
Ti, Nb(1)–O(1)	2.142(6)	–O(9)	3.096(6)
–O(2)	1.951(6)	–O(10)	2.797(6)
–O(5)	2.080(6)	Rb(2)–O(1)	3.013(7)
–O(6)	2.025(6)	–O(2)	2.736(6)
–O(9)	1.720(6)	–O(3)	2.760(5)
–O(10)	1.966(6)	–O(5)	2.973(7)
Ti(2)–O(3)	2.053(6)	–O(7)	3.191(7)
–O(4)	2.010(5)	–O(8)	2.843(6)
–O(7)	1.955(7)	–O(9)	2.786(6)
–O(8)	1.989(7)	–O(10)	3.148(6)
–O(9)	2.089(7)	P(1)–O(1)	1.519(7)
–O(10)	1.738(7)	–O(2)	1.557(7)
Rb(1)–O(1)	2.752(6)	–O(3)	1.550(5)
–O(2)	3.090(7)	–O(4)	1.543(5)
–O(3)	3.092(7)	P(2)–O(5)	1.538(6)
–O(4)	3.065(6)	–O(6)	1.535(6)
–O(5)	2.866(6)	–O(7)	1.547(7)
–O(7)	3.008(6)	–O(8)	1.539(7)
–O(8)	3.128(6)		

only one of two titanium positions, Ti(1), as was also observed for KTP:Nb crystals [11, 12]. According to these data, the niobium content was 0.01, which is rather close to the value $x = 0.013$ determined by chemical analysis. As to Rb atoms, their deficit is observed only in the Rb(2) positions. The formation of vacancies in the sublattice of rubidium cations accounts for the occurrence of the pronounced relaxation phenomena in such crystals. Analysis of the interatomic distances shows that the degree of distortion of titanium–oxygen octahedra decreases and their symmetry increases, which may cause the decrease in the ferroelectric phase-transition temperature and the reduction in the intensity of the second-harmonic generation under laser irradiation.

REFERENCES

1. R. Masse and J.-C. Grenier, Bull. Soc. Fr. Mineral. Cristallogr. **94**, 437 (1971).
2. G. D. Stucky, M. L. F. Phillips, and T. E. Gier, Chem. Mater. **1**, 492 (1989).
3. V. K. Yanovskii and V. I. Voronkova, Phys. Status Solidi A **93**, 665 (1986).
4. Yu. S. Oseledchik, S. P. Belokrys, V. V. Osadchuk, *et al.*, J. Cryst. Growth **125** (3/4), 639 (1992).
5. C. V. Kannan, S. G. Moorthy, V. Kannan, *et al.*, J. Cryst. Growth **245** (3/4), 289 (2002).
6. Y. Guillien, B. Menaert, J. P. Feve, *et al.*, Opt. Mater. **22** (2), 155 (2003).
7. J. J. Carvajal, R. Sole, J. Gavalda, *et al.*, J. Alloys Compd. **323–324**, 231 (2001).
8. J. J. Carvajal, V. Nikolov, R. Sole, *et al.*, Chem. Mater. **12**, 3171 (2000).
9. V. I. Voronkova, V. K. Yanovskii, T. Yu. Losevskaya, and S. Yu. Stefanovich, J. Appl. Phys. **94** (3), 1954 (2003).
10. C. V. Kannan, Ganesamoorthy, C. Subramanian, and P. Ramasamy, Phys. Status Solidi A **196** (2), 465 (2003).
11. P. A. Thomas and B. E. Watts, Solid State Commun. **73** (2), 97 (1990).
12. O. A. Alekseeva, N. I. Sorokina, I. A. Verin, *et al.*, Kristallografiya **48** (2), 219 (2003) [Crystallogr. Rep. **48**, 205 (2003)].

Translated by T. Dmitrieva

Crystallography Reports, Vol. 50, No. 1, 2005, pp. 142–146. Translated from Kristallografiya, Vol. 50, No. 1, 2005, pp. 150–154.

CRYSTAL GROWTH

Growth from Gas Cavities in a Molten Salt and Properties of Superconducting $Bi_2Sr_2CaCu_2O_{8+\delta}$ Single Crystals

Yu. I. Gorina, G. A. Kalyuzhnaya, N. N. Sentyurina, V. A. Stepanov, and S. G. Chernook

Lebedev Physical Institute, Russian Academy of Sciences, Moscow, 119991 Russia

e-mail: stepanov@sci.lebedev.ru

Received March 3, 2003

Abstract—Perfect single crystals of the high-temperature superconductor $Bi_2Sr_2CaCu_2O_{8+\delta}$ with the superconducting transition temperature T_C = 72–85 K (depending on the crystallization conditions) are obtained by the method of free growth in gas cavities formed in a KCl solution–melt. The specific features of the growth process are in the formation of an enclosed growth gas cavity in a (previously synthesized) blend of a specified phase composition dissolved in KCl and the free crystal growth in this cavity. The combination of growth and high-temperature annealing in the same process made it possible to obtain uniform (ΔT_C = 1.5 K) single crystals with stable superconducting properties. Annealing of the grown single crystals in oxygen or in air in the temperature range 400–850°C confirmed that the crystals with maximum values of T_C are optimally doped.

INTRODUCTION

Among high-temperature superconductors (HTSCs) of the bismuth family with the general formula $Bi_2Sr_2Ca_{n-1}Cu_nO_y$ (n = 1, 2, 3), the $Bi_2Sr_2CaCu_2O_{8+\delta}$ (Bi2212) compound with n = 2 and the superconducting transition temperature $T_{C\,max}$ = 85–95 K has been most widely investigated during the last ten years. Until recently, it was believed that pure (nominally undoped with foreign impurities) Bi2212 single crystals exist in a stable phase that can be easily obtained by several methods. However, the growth of homogeneous Bi2212 single crystals of high structural quality with different controlled doping levels remains a complex technological problem. The most developed techniques are the floating-zone method with a moving solvent [1, 2], which made it possible to grow crystals with a record-high value of $T_{C\,max}$ (95 K), and different modifications of the self-flux method using Bi_2O_3 or CuO [3, 4]. The main purpose of the above studies was to grow optimally doped single crystals and then, using annealing at either increased or reduced partial oxygen pressure, transfer the material to the overdoped or underdoped state, respectively. In this way, the experimental areas of the T_C–p phase diagram (p is the hole density per one CuO_2 layer) were expanded. However, it turned out that the annealing of crystals under different oxygen pressures often leads to chemical segregation in both overdoped and underdoped Bi2212 single crystals [5, 6]. It was noted in [5] that Bi2212 crystals are generally obtained overdoped; therefore, the problem of growing high-quality underdoped Bi-HTSC crystals remains urgent.

We believed it reasonable to apply the method developed by us for growing Bi2201 [7] and Bi2223 [8] high-quality single crystals in gas cavities in molten KCl salt to obtain Bi2212 single crystals having different values of T_C and stable superconducting properties directly after growth. The details of the growth process and its constructive layout were described in detail in [7, 8]. The specific features of the growth process are in the formation of an enclosed growth gas cavity in a solution of a previously synthesized blend of specified phase composition in molten KCl and the free growth of crystals in this cavity.

Apparently, the growth of Bi2212 crystals in a cavity was first reported in [9], where the cavity walls in the blend volume were composed of sintered pellets of the composition $Bi_2O_3 : CaCO_3 : SrCO_3 : CuO$ = 1 : 1 : 1 : 2 and the cavity top was made of the more refractory compound $SrCaCu_4O_6$ to retain highly volatile components during the growth. Superconducting $Bi_{2.2}Sr_{1.8}Ca_{0.75}Cu_{1.89}O_x$ crystals with T_C = 77 K were obtained. However, the growth conditions were not optimized since there occurred simultaneously competing processes of growth of crystals of other phases, for example, $Sr_1Ca_{1.78}Cu_3O_x$, which depleted the growth medium in Ca and Sr and led to the deposition of these phases on the surfaces of Bi2212 crystals.

In 1992, we managed to grow superconducting Bi2212 single crystals with linear sizes up to 1 mm and Bi2223 crystals with sizes up to 100 μm^2 in the form of separately crystallized faceted square plates in small gas cavities in KCl [10]. Introduction of KCl flux into the weight composition (blend : KCl = 1 : 4) allowed us to decrease the growth temperature, expand the regions of existence, and separate the crystallization conditions for these two phases.

1063-7745/05/5001-0142$26.00

Table 1. Composition of the blend and the synthesis conditions

Example	Initial components		Synthesis conditions		Phase composition of the blend			Cavity presence: yes + no –
	chemical composition	cation ratio Bi : Sr : Ca : Cu	temperature, °C	time, h	Bi2212	Bi2223	amplitude of signal $\chi(T)$, arb. units	
1	Bi_2O_3, $SrCO_3$, $CaCO_3$, CuO	2 : 2 : 2 : 4	800	28	MP*		0.9	+
2	Bi_2O_3, $SrCO_3$, $CaCO_3$, CuO	2 : 2 : 2 : 4	840	11	MP		0.8	+
3	Bi_2O_3, $SrCO_3$, $CaCO_3$, CuO	2 : 2 : 2 : 4	830	12	MP		0.7	+
4	Bi_2O_3, SrO, CaO, CuO	2 : 2 : 2 : 4	840	11	MP		0.7	–
5	Bi_2O_3, $SrCO_3$, $CaCO_3$, CuO,	2 : 2 : 1 : 2	850	10	MP		1	–
6	Bi_2O_3, $SrCO_3$, $CaCO_3$, CuO, PbO	2 : 2 : 4 : 6	800	28	MP		0.8	+
7	Bi_2O_3, $SrCO_3$, $CaCO_3$, CuO	2 : 2 : 2 : 4	860	100	<50%	50%	0.8	+
8	Bi_2O_3, $SrCO_3$, $CaCO_3$, CuO	2 : 2 : 4 : 6 + 0.25 Pb	860	130		100%	1	–

* Main phase.

The purpose of this study is to obtain homogeneous Bi2212 single crystals that could be used for physical investigations of the mechanism of high-temperature superconductivity and analysis of the dependences of the superconducting characteristics of crystals on the growth conditions.

RESULTS AND DISCUSSION

In this study, in order to obtain superconducting Bi2212 single crystals, we synthesized blends of different compositions. These compositions and typical techniques of blend preparation are listed in Table 1. The superconducting properties of the blend were monitored by the values of T_C, the transition width ΔT_C, and the signal from a blend sample with a standard volume. These parameters were measured from the temperature dependence of the magnetic susceptibility $\chi(T)$ and by powder X-ray analysis. Table 1 contains also the data on the presence of a growth cavity for the crystals grown from a blend of corresponding composition. It follows from these data that, to form a growth gas cavity, the initial blend should contain an excess amount of copper and calcium (in the form of CuO and $CaCO_3$, respectively) (examples 1, 2, 3) in comparison with the nominal composition 2212. The conditions for the blend annealing were varied in a wide range: t_{ann} was varied from 800 to 840°C and the annealing time was varied from 28 to 11 h. When we used a blend with a large content of the superconducting phase Bi2212 synthesized from oxides CaO and SrO rather than from carbonates (example 4), a growth cavity was not formed. The use of an initial blend of stoichiometric cation composition 2 : 2 : 1 : 2 (example 5), containing the superconducting phase Bi2212 in the amount of about 100%, also did not lead to the formation of a cavity. An increase in the excess of Ca and Cu in the initial blend to the ratio Ca : Cu = 2 : 3 and adding some amount of lead oxide PbO (example 6) is favorable for preparation of Bi2212 single crystals, as will be shown below. For successful growth of superconducting Bi2223 single crystals in a cavity, a blend of complex composition was synthesized (example 7), which contained up to 50% of Bi2223 and excess amounts of CuO, $CaCO_3$, and $SrCO_3$ [11]. When a blend with a 100% content of the Bi2223 phase was used, a cavity was not formed even in the presence of PbO (example 8). Apparently, the following reactions are responsible for the extraction of gaseous components in the melt and the formation of a cavity:

$$2CuO \xrightarrow{t > 800^\circ C} Cu_2O + O_2\uparrow$$

(P_{O_2} ~ 9 Torr, at 850°C [12]),

$$CaCO_3 \xrightarrow{t > 700^\circ C} CaO + CO_2\uparrow$$

(P_{CO_2} ~ 300 Torr, at 850°C [13]).

Also, we cannot exclude the role of $SrCO_3$ in the cavity formation, for which the decomposition reaction

$$SrCO_3 \longrightarrow SrO + CO_2\uparrow$$

proceeds much slower and at higher temperatures.

Crystallization was performed as follows. A blend weight (180 g) was loaded into an Al_2O_3 crucible, heated to 860°C in the hottest zone at the crucible bottom, and kept for 20–24 h with a vertical gradient up to 20 K/cm along the melt column 4–4.5 cm in height. Under these conditions, the blend dissolution occurred simultaneously with the extraction of gaseous components in the lower (hottest) part of the solution–melt and the crystallization of Bi2212 on the surface and in the upper part of the melt. Thus, at the end of the heating cycle, a quasi-closed cavity with a volume of several cubic centimeters was formed in the solution–melt. In this cavity, the growth of crystals occurred simulta-

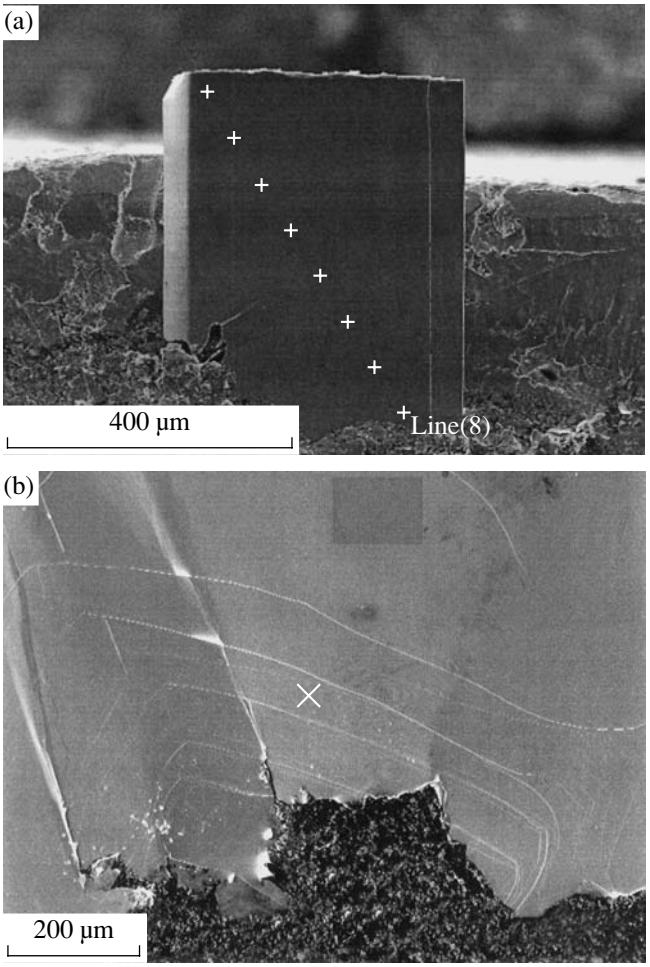

Fig. 1. (a) Part of the $Bi_{2.22}Sr_{1.55}Ca_{1.17}Cu_{2.01}O_{8.04}$ single crystal and (b) the surface of the $Bi_{1.99}Pb_{0.22}Sr_{1.65}Ca_{1.28}Cu_{1.85}O_x$ single crystal with decorated growth steps.

neously with their annealing in the atmosphere of volatile crystal-forming components. For a typical process time of ~100 h, several tens of faceted superconducting mirror-smooth Bi2212 single crystals grew in the cavities. The crystals grown were of two morphological types: rectangular plates 1–2.5 mm^2 × 1–10 μm in size and ribbons 4–5 mm × 0.2–0.5 mm × 1–10 μm in size. Crystals of both types were formed on the cavity top and grew freely downward, into the gaseous medium. The high quality of the grown crystals was ascertained by X-ray diffraction analysis [8] and scanning electron microscopy using a JSM-5910-LV microscope and a Philips CM-30 microscope equipped with an energy-dispersive X-ray spectrometer AN 95S.

Figures 1a and 1b show typical lamellar Bi2212 single crystals. The morphology of the crystal surfaces is characteristic of the layer-by-layer growth of the (100) face. Undoped Bi2212 crystals have no traces of the liquid phase on the surface, which confirms that the feed from the gas phase during the growth occurs through

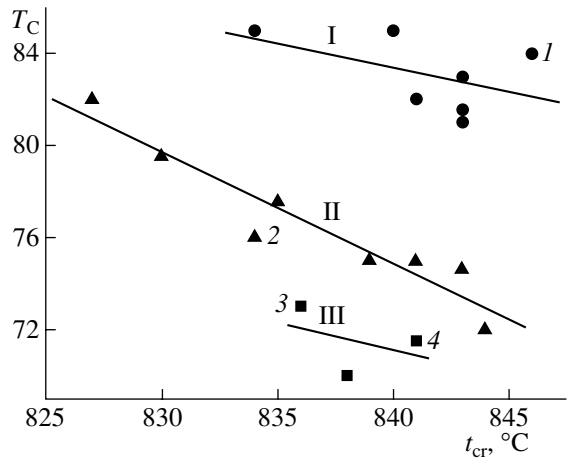

Fig. 2. Dependence of T_C on t_{cr} for three groups of samples with different cation compositions: the ratios Ca/Sr = 0.75–0.77 and Cu/Bi = 0.88–0.9 (group I) and, respectively, 0.59 and 0.8 (group II). Points *1* and *2* correspond to the compositions $Bi_{2.22}Sr_{1.56}Ca_{1.17}Cu_{2.01}O_{8.04}$ and $Bi_{2.22}Sr_{1.80}Ca_{1.20}Cu_{1.78}O_x$, respectively. Points *3* and *4* of group III correspond to the compositions $Bi_{1.90}Pb_{0.27}Sr_{1.92}Ca_{1.18}Cu_{1.74}O_x$ and $Bi_{1.99}Pb_{0.22}Sr_{1.65}Ca_{1.28}Cu_{1.85}O_x$, respectively.

the vapor–solid mechanism [14] with the formation of two-dimensional nuclei on the (100) face (Fig. 1a). The growth rate of lead-doped (Bi,Pb) 2212 single crystals, in comparison with undoped ones, was much higher. Under the same growth conditions, the crystals obtained were 2–4 mm^2 × 5–10 μm in size and the growth occurred through the gas–liquid–solid mechanism; i.e., involving the liquid phase. Decorated lamellar-growth steps (possibly, traces of the Pb-based liquid phase) can be seen in Fig. 1b. The compositions of the crystal measured in different surface regions, each 1 × 1 × 1 μm^3 in size, and on an area of 150 × 150 μm^2 were almost the same. Measurements of the temperature dependence of the magnetic susceptibility $\chi(T)$ showed that the characteristics of the superconducting transition for crystals grown in the same cavity are rather similar. With an increase in the crystallization temperature t_{cr} in the growth cavity, the value of T_C of the crystals grown decreased (Fig. 2). Figure 2 shows the data for the three groups of samples with different cation compositions: samples with compositions in the vicinity of line I have larger values of T_C; they were grown from a blend with higher contents of Ca and Cu in comparison with the samples of group II. The comparative analysis of the cation compositions of the samples of groups I and II shows that, in going from group I to group II, the ratios Ca/Sr and Cu/Bi decrease from 0.75–0.77 and 0.88–0.9 to 0.59 and 0.8, respectively. With a decrease in t_{cr} of the samples corresponding to line I, T_c increased to 85 K. This value (T_C = 85 K with ΔT_C = 1.5–2 K) is maximum for the Bi2212 crystals grown from the gas phase. For crystal 1 with T_C = 84 K,

Table 2. Dependence of the superconducting properties of Bi2212 single crystals on the annealing conditions

	Annealing conditions			Crystals after growth		Crystals after annealing	
	t, °C	time, h	medium	T_C, K	ΔT_C, K	T_C, K	ΔT_C, K
Crystal on the surface of the KCl melt	560	6	in O_2	74–79	5	80–82	2
Crystal in the lower part of the KCl melt	850	100	in blend in air	82.5–75	7	82.1–79.6	2.5
Crystal in a cavity in the KCl melt	400	0.3	in air	76.5–75	1.5	81.5–80	1.5

the total composition was determined. The oxygen content in this sample, which was grown at the highest temperature t_{cr} = 845°C, is $O_{8+0.04}$. It is known that, in overdoped $Bi_2Sr_2CaCu_2O_{8+\delta}$ samples, the value δ of oxygen excess with respect to the stoichiometric composition is 0.1–0.15 atomic fractions. We can conclude that the composition of this crystal is in the range of optimal doping. Line III is shown for three samples (Bi,Pb)2212 with the smallest values of T_C. A comparison of the cation compositions of crystals 2 and 3 (grown at close values of t_{cr} and, therefore, under the same partial oxygen pressure), which correspond to lines II and III, respectively, shows that introduction of Pb leads to a decrease in T_C; the difference in the contents of main cations is small. With an increase in t_{cr} from 836 to 842°C, the total content of Bi and Pb in single crystals 3 and 4 increased from 2.17 to 2.21, due to which T_C decreased from 73 to 71.5 K. This circumstance means that doping with Pb under our conditions leads to a decrease in the carrier concentration in comparison with the optimal value, i.e., shifts the composition of the crystals grown from the gas phase to the undoped region.

To estimate the doping level of the single crystals obtained, we annealed them in oxygen and in air at different temperatures. Table 2 contains the results of annealing of the Bi2212 samples crystallized in different parts of the solution–melt, specifically, on the surface and in the lower part of the melt, as well as in a cavity in the melt. The annealing of the crystals grown in the solution significantly improved their homogeneity: ΔT_C decreased from 5–7 to 2–2.5 K [15]. Note that, for the crystal grown on the surface, T_C increased from 79 to 82 K. Another picture was observed for the crystals grown in the cavity: due to the annealing, the width of the superconducting transition remained narrow (ΔT_C = 1.5 K) and the value of T_C increased. In our opinion, the results obtained indicate that the single crystals grown from the gas phase, immediately after the growth in the cavity, were slightly underdoped, and annealing in air changed their composition with respect to oxygen to the region of optimal doping. Exposure in air for one year did not change the superconducting properties of such crystals. Thus, it was shown that the carrier density and, therefore, the value of T_C of the superconducting Bi2212 solid solution are determined by both the oxygen concentration and the cation composition.

Attempts to construct the phase diagram T_C–x, where x is the charge-carrier density, for the Bi2212 and (Bi,Pb)2212 compounds with different cation compositions have been made previously. Schematic phase diagrams for different cation compositions of Bi2212 were reported in [16]. In [17], the experimental curve T_C–x for six (Bi,Pb)2212 samples is shifted by 0.05x to the undoped region with respect to the generally accepted empirical dependence, in which the carrier density is estimated only from the oxygen concentration.

CONCLUSIONS

Using growth from the gas phase, we obtained Bi2212 and (Bi,Pb)2212 single crystals with T_C = 72–85 K, in which the doping level is determined by the cation composition and partial oxygen pressure in the enclosed growth cavity. Combination of the growth and high-temperature annealing in one process allowed us to obtain homogeneous crystals (ΔT_C = 1.5 K) with stable superconducting properties.

ACKNOWLEDGMENTS

We are grateful to S.I. Vedeneev for the statement of the problem and helpful participation in the discussions and V.V. Rodin for the X-ray phase analysis of the samples.

This study was supported by the Ministry of Industry, Science, and Technology of the Russian Federation (the program “Superconductor,” contract no. 40.012.1.1.1357), the Presidium of the Russian Academy of Sciences (RAS) (the project “Quantum Macrophysics” of the integrated program of the RAS Presidium for 2004), and the Russian Foundation for Basic Research (project nos. 02-02-16247 and 02-02-17133).

REFERENCES

1. Y. DeWilde, N. Miyakawa, P. Guptasarma, *et al.*, Phys. Rev. Lett. **80** (1), 153 (1998).
2. N. Miyakawa, P. Guptasarma, J. F. Zasadzinski, *et al.*, Phys. Rev. Lett. **80** (1), 157 (1998).
3. D. B. Mitzi, L. W. Lombardo, and A. Kapitulnik, Phys. Rev. B **41** (10), 6564 (1990).

4. C. Kendziora, R. J. Kelley, E. Skelton, *et al.*, Physica A (Amsterdam) **257**, 74 (1996).
5. X. S. Wu, L. Lu, and D. L. Zhang, Phys. Rev. B **66**, 134506 (2002).
6. B. Liang, C. T. Lin, A. Maljuk, *et al.*, Physica C (Amsterdam) **366**, 254 (2002).
7. J. I. Gorina, G. A. Kaljuzhnaia, N. N. Sentjurina, *et al.*, Solid State Commun. **126**, 557 (2003).
8. J. I. Gorina, G. A. Kaljuzhnaia, V. P. Martovitsky, *et al.*, Solid State Commun. **110**, 287 (1999).
9. S. J. Guo, K. E. Easterling, S. X. Dou, *et al.*, J. Cryst. Growth **100**, 303 (1990).
10. O. V. Aleksandrov, Yu. I. Gorina, G. A. Kalyuzhnaya, *et al.*, Sverkhprovodimost: Fiz. Khim. Tekhnol. **5** (12), 2333 (1992).
11. Yu. I. Gorina, G. A. Kalyuzhnaya, and N. N. Sentyurina, RF Patent No. 2182194; Byull. Izobret., No. 13 (II), 288 (2002).
12. E. K. Kazenas and D. M. Chizhikov, *Pressure and Composition of Vapor over Oxides of Chemical Elements* (Nauka, Moscow, 1976) [in Russian].
13. V. V. Rodyakin, *Calcium, Its Compounds and Alloys* (Metallurgiya, Moscow, 1967), p. 21 [in Russian].
14. E. I. Givargizov, *Growth of Whiskers and Lamellar Crystals from Vapors* (Nauka, Moscow, 1977), p. 42 [in Russian].
15. J. I. Gorina, G. A. Kaljuzhnaia, V. I. Ktitorov, *et al.*, Solid State Commun. **85** (8), 695 (1993).
16. P. Majewski and H.-L. Su, J. Mater. Sci. **32**, 5137 (1997).
17. A. Kordyuk, S. V. Borisenko, M. S. Golden, *et al.*, Phys. Rev. B **66**, 014502 (2002).

Translated by Yu. Sin'kov

Crystallography Reports, Vol. 50, No. 1, 2005, pp. 147–149. Translated from Kristallografiya, Vol. 50, No. 1, 2005, pp. 155–157.

CRYSTAL GROWTH

Growth of Single Crystals of the High-Pressure Phase of α-PbO_2

T. I. Dyuzheva, L. M. Lityagina, and N. A. Bendeliani

Institute of High Pressure Physics, Russian Academy of Sciences, Troitsk, Moscow oblast, 142092 Russia

e-mail: tid@ns.hppi.troitsk.ru

Received July 11, 2003

Abstract—The technique and results of hydrothermal growth of single crystals of the high-pressure phase of α-PbO_2 are described. Dark brown crystals of predominantly prismatic habit with characteristic sizes of 550 × 100 × 150 μm^3 were obtained at p = 4 GPa by cooling an aqueous solution in the temperature range t = 600–300°C. © *2005 Pleiades Publishing, Inc.*

INTRODUCTION

The β modification of lead dioxide with tetragonal rutile structure (TiO_2, $P4_2/mnm$, Z = 2), which exists in nature in the form of the mineral plattnerite, is stable under normal conditions. A denser (by 2.6%) orthorhombic phase was obtained by applying shear loads (grinding in a mortar) [1]. The structural model proposed for this phase on the basis of the powder X-ray data [2] has been known for more than 50 years as the α-PbO_2 structure type ($Pbcn$, Z = 4). Mainly due to the similarity of the X-ray diffraction patterns, a large number of dense modifications of dioxides and difluorides of different elements were assigned to this type. As rule, these modifications were obtained by applying high pressure to phases with rutile-like structures. Among the compounds characterized by this structural transition, there is, in particular, silica, SiO_2—the most important component of the rocks that form, according to the modern concepts, the inner shells of the Earth. There is no data in the literature on the growth of single crystals and investigations of their structure, although dense modifications of some compounds can exist in the metastable state under normal conditions. In this paper, we report the results on the growth of α-PbO_2 single crystals, which are necessary for further correct description of the α-PbO_2 structure type using complete structural analysis.

EXPERIMENTAL

We used a high-pressure chamber of the Konak type equipped with a cell for hydrothermal growth (see [3]); the working volume of the hermetic platinum ampule was 35 mm^3. Tetragonal lead dioxide of analytical grade and bidistilled water served as reagents. The amount of loaded water was estimated from the ratio of the volumes of lead dioxide and the ampule. A DRON-3M diffractometer and single-crystal Laue and Burger cameras were used for X-ray analysis of the reaction products.

RESULTS AND DISCUSSION

The α-PbO_2 modification, despite the exotic nature of its discovery, seems to be the only phase with a structure of this type, for which the p–t stability field is determined by direct X-ray methods. This circumstance made much easier the search for conditions and the choice of a single-crystal growth technique. In the p–t diagram (Fig. 1), the region of the α phase at 600°C is limited by the lines of equilibrium with plattnerite at 1.6 GPa and the phase with fluorite structure (CaF_2) at 5.8 GPa. When the temperature decreases to room temperature, the equilibrium pressure range is slightly extended [4].

In this case, the growth from a hydrothermal solution appeared to be most appropriate. However, we had to determine the upper temperature limit of the stability of the necessary phase in the presence of an aqueous fluid due to the well-known tendency of lead dioxide to reduction at an insufficiently high partial oxygen pressure. It was found that, at p = 4 GPa and t = 600°C, a yellow deposit with orthorhombic modification of PbO (massicote) is formed on the cell covers. Since this modification was absent in the main mass of the sample, we took the above parameters as the initial working ones. The temperature of the eutectics ice VII[1] + α-PbO_2 + liquid, which formally limits the growth range from below, in view of the insignificant solubility

[1] Ice VI and ice VII are the solid high-pressure phases of H_2O.

1063-7745/05/5001-0147$26.00 © 2005 Pleiades Publishing, Inc.

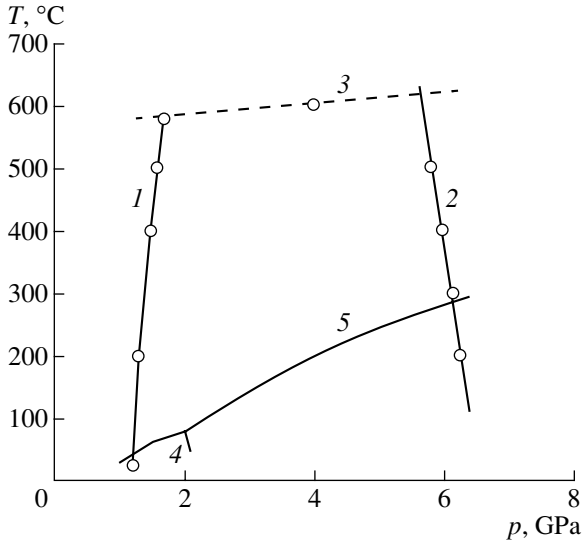

Fig. 1. Region of hydrothermal growth of α-PbO_2. (*1*, *2*) The lines of equilibrium of the α-PbO_2 phase with the rutile-like and fluorite-like phases of PbO_2, respectively [4]; (*3*) the line of decomposition $2PbO_2 \longrightarrow 2PbO$ (massicote) + O_2 (our data); and (*4*, *5*) the melting lines of ice VI and ice VII, respectively [5].

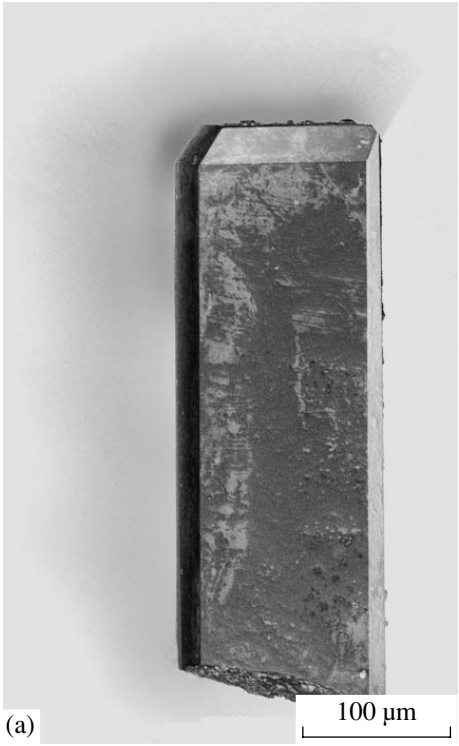

Fig. 2. Morphology of α-PbO_2 crystals: (a) a real crystal and (b) symbols for faces.

of lead dioxide, should not differ strongly from the melting temperature of ice VII (200°C, 4 GPa [5]).

The sample with the composition $xPbO_2 + (1 - x)H_2O$ ($0.05 \le x \le 0.07$) was cooled at $p = 4$ GPa from 600 to 300°C at an average rate of 1.25 K/min. The product extracted from the cell was a well-crystallized dark brown mass with a grain size of 10–30 μm, which contained four or five crystals of the same color and columnar shape with transverse sizes from 40 to 150 μm and a length from 250 to 750 μm (Fig. 2).

The diffraction pattern of an unground powder contained the reflections of only the α-PbO_2 phase with the unit-cell parameters $a = 4.982 \pm 0.005$ Å, $b = 5.962 \pm 0.006$ Å, and $c = 5.458 \pm 0.005$ Å. The Raman spectra of the single crystals contained no bands characteristic of water. The measurements of the crystals in the Laue and Burger cameras revealed that their surface is formed by the faces of orthorhombic prism (110); dipyramid (111); and pinacoids (100), (010) and (001) (Fig. 2). Crystals with a complete set of these faces were not found.

In summary, we should note the poor reproducibility of the growth results (the number and the sizes of the crystals) obtained for the same sets of parameters *p*, *t*, and *x*. As can be seen from the size of grains in the main mass, the cooling could either occur for too long a time in the liquid phase or begin in the two-phase region; in both cases, crystals with sizes larger than 100–150 μm were absent. It is most likely that we deal with a situation related to the weak thermal dependence of the oxide solubility in water (the liquidus line is close to vertical in the *t*–*x* diagram), which is typical of low upper temperature limits. Due to the small sample volume, a substantial error in the required component proportion cannot be avoided when loading water to the ampule. This error is comparable with the change in the solution concentration in the cooling range.

ACKNOWLEDGMENTS

We are grateful to Yu.A. Timofeev for the measurement of the Raman spectra and A. Lyapin for preparation of the photograph.

This study was supported by the Russian Foundation for Basic Research, project no. 03-05-64494.

REFERENCES

1. A. I. Zaslavskiĭ, Yu. D. Kondrashev, and S. S. Tolkachev, Dokl. Akad. Nauk SSSR **75**, 559 (1950).
2. A. I. Zaslavskiĭ and S. S. Tolkachev, Zh. Fiz. Khim. **26**, 743 (1952).
3. T. I. Dyuzheva, L. M. Lityagina, N. A. Bendeliani, *et al.*, Kristallografiya **43** (3), 554 (1998) [Crystallogr. Rep. **43**, 511 (1998)].
4. T. Yagi and S. Akimoto, J. Geophys. Res. **85** (B12), 6991 (1980).
5. C. W. F. T. Pistorius, E. Rapoport, and J. B. Clark, J. Chem. Phys. **48** (12), 5509 (1968).

Translated by Yu. Sin'kov

Crystallography Reports, Vol. 50, No. 1, 2005, pp. 150–153. Translated from Kristallografiya, Vol. 50, No. 1, 2005, pp. 158–161.

CRYSTAL GROWTH

Nucleation in Multidimensional Euclidean Spaces

P. P. Fedorov, G. A. Denisenko, and R. M. Zakalyukin

Shubnikov Institute of Crystallography, Russian Academy of Sciences, Leninskiĭ pr. 59, Moscow, 119333 Russia

e-mail: ppf@newmail.ru

Received August 1, 2003

Abstract—The problem of nucleation of a new phase in the bulk of the old one is considered for *n*-dimensional Euclidean spaces. Under the condition of a constant contact angle with the third phase, an increase in the space dimension results in a sharp decrease in the potential barrier of heterogeneous nucleation and, thus, in a decrease in the probability of homogeneous nucleation. © *2005 Pleiades Publishing, Inc.*

The use of spaces with the dimension $n > 3$ is a useful approach to the description of the structure and properties of some complicated structures such as those of quasicrystals and incommensurate phases [1]. However, some concepts of modern physics admit the existence of multidimensional spaces [2].

It is well known that the basic laws of thermodynamics are equally applicable to three- and two-dimensional systems [3]. Consider the hypothetical extension of the well-known problem [4, 5] of nucleation of a new phase in the bulk of the already existing phase to plane *n*-dimensional space.

We also assume that the phases and their interfaces also exist in the spaces of higher dimensions and that the most important thermodynamic quantities such as temperature, pressure, volume, and surface energy preserve their sense and their interrelations also in the multidimensional spaces.

First, consider homogeneous nucleation [6]. For simplicity, we restrict our consideration to nucleation of the β phase of spherical shape with radius r in *n*-dimensional space, e.g., to crystallization of melt α. The difference in the phase densities is ignored. Let $\Delta\mu_n$ be the difference between the free Gibbs energies (isobaric–isothermal potentials) per unit volume and σ_n be surface energy. Then the change in the free energy during the formation of a new phase is

$$\Delta G_n = -V_n\Delta\mu_n + S_n\sigma_n, \quad (1)$$

where $V_n = \alpha_n r^n$ and $S_n = \beta_n r^{n-1}$ are the volume and the surface in the *n*-dimensional space, respectively. The quantities α_n and β_n are the Jacobi coefficients such that $\beta_n = n\alpha_n$ [7]. Then,

$$\Delta G_n = \alpha_n r^{n-1}(-r\Delta\mu_n + n\sigma_n), \quad (2)$$

where $r \geq 0$. Differentiating Eq. (2) with respect to r and equating the derivative obtained to zero, we arrive at two possible solutions: $r = 0$, $\Delta G_n = 0$ (at $n \geq 3$) and $r_n = (n-1)\sigma_n/\Delta\mu_n$, $\Delta G_n = \alpha_n(n-1)^{n-1}(2n-1)\sigma_n^n/\Delta\mu_n^{n-1}$ (at $n \geq 2$). Thus, at $n \geq 2$, there would exist the critical radius r_n corresponding to the maximum value of the thermodynamic potential, in other words, the phenomenon of a crystal nucleus. The particles of the β phase become stable only after attainment of the critical size. The value of ΔG_n at this point is a potential barrier which should be overcome for the formation of a new phase. For one-dimensional systems, no nuclei can exist: once being formed at $\Delta\mu_n > 0$, these formations should continue growing without any potential barriers. The dependences $\Delta G_n(r)$ at different n are shown in graphical form in Fig. 1.

It should be noted that, with an increase in n, the radius of a hypernucleus (a nucleus with a radius exceeding the critical one) monotonically increases. The potential barrier is related to supercooling ΔT, whereas the dependence of σ_n on temperature is usually ignored. Assuming that $\Delta\mu_n = \Delta T \cdot \Delta H/T_0$, where ΔH and T_0 are the enthalpy and the melting point, respectively, we obtain

$$r_n = (n-1)\sigma_n T_0/\Delta T \cdot \Delta H$$

and

$$\Delta G_n = \alpha_n(n-1)^{n-1}(2n-1)\sigma_n^n T_0^{n-1}/\Delta H^{n-1}\Delta T^{n-1}.$$

Thus, the temperature dependence of the hypernucleus radius is the same irrespective of n. However, the value of the potential barrier varies quite noticeably: it sharply increases with an increase in the space dimension under constant supercooling. High values of the potential barrier hinder crystallization and may give rise to the formation of glass during melt cooling.

With an increase in n, the $\Delta G_n(r)$ curves at small radii, $r \leq r_n$, approach the abscissa. Thus, the probability of fluctuations of the dimensions of nuclei with radii less than the critical one increases.

The conditions for homogeneous nucleation are met rather seldom. Moreover, as a rule, such processes are

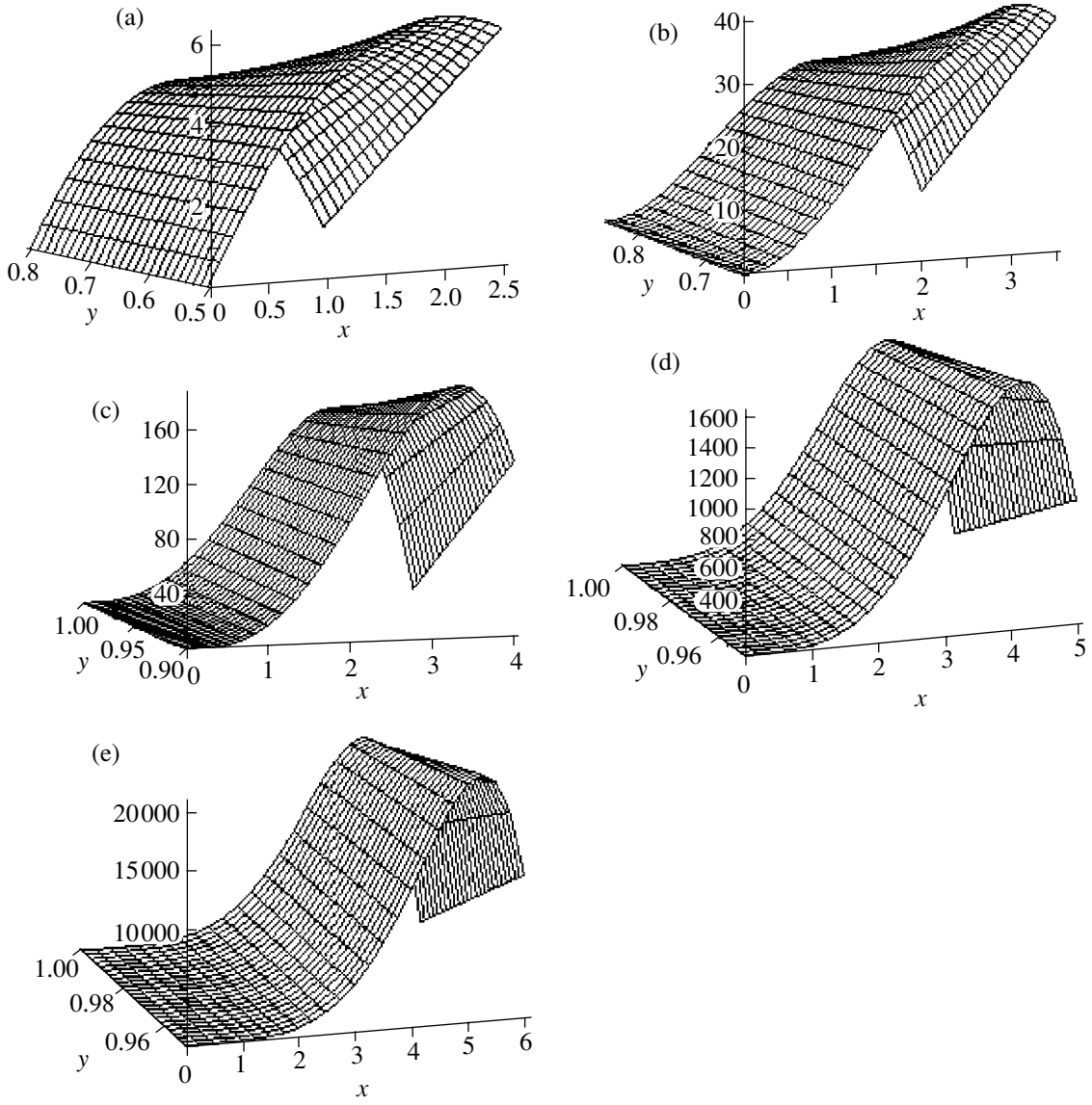

Fig. 1. Free Gibbs energy of formation of a spherical nucleus as a function of its radius and degree of supercooling; x is the radius, and y is $\Delta\mu_n$ in arbitrary units. n = (a) 2, (b) 3, (c) 4, (d) 5, (e) 6.

very difficult to implement in practice. The particles of a new phase are usually formed by the mechanism of heterogeneous nucleation (Fig. 2). If the volume of the initial phase α is in contact with some another phase γ, then the formation of a new phase β from the volume of the old phase is facilitated at the interface because of the surface tension. The value of the wetting angle θ depends on the ratio of the surface energy at the α/β, β/γ, and α/γ interfaces. In this case, $(\pi - \theta)$ is the angle formed by the radius vector of an arbitrary point on a sphere in n-dimensional Euclidean space and the plane of the first $n - 1$ coordinate axes. Assuming that the form of the precipitated phase β only slightly differs from the spherical segment, we may assume that the segment whose curvature radius coincides with the radius of the critical hypernucleus in homogeneous nucleation is also a hypernucleus. This is always accompanied by a considerable gain in the volumetric energy and, therefore, a considerable decrease in the potential barrier, in comparison with their values in homogeneous nucleation.

The ratio of the volume of the spherical segment V_n^S of the height h to the volume of the sphere V_n of the same radius r, $D_n^S = V_n^S/V_n$, in n-dimensional space has the form

$$D_n^S = A_n B_n(q),$$

where $q = h/r$, $A_n = n!!/\pi(n-3)!!$, and $n!!/(n-3)!!$ for even and odd n, respectively, and $B_n(q)$ is given by the

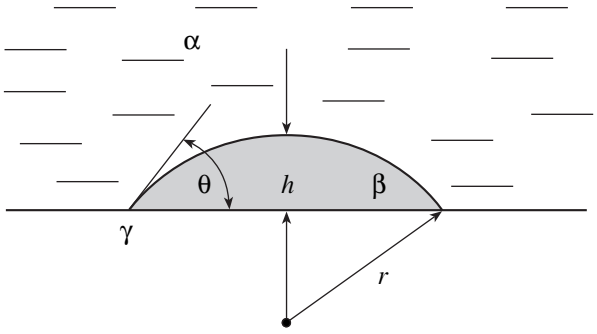

Fig. 2. Scheme of heterogeneous nucleation; α, β, and γ are phases, and θ is the wetting angle.

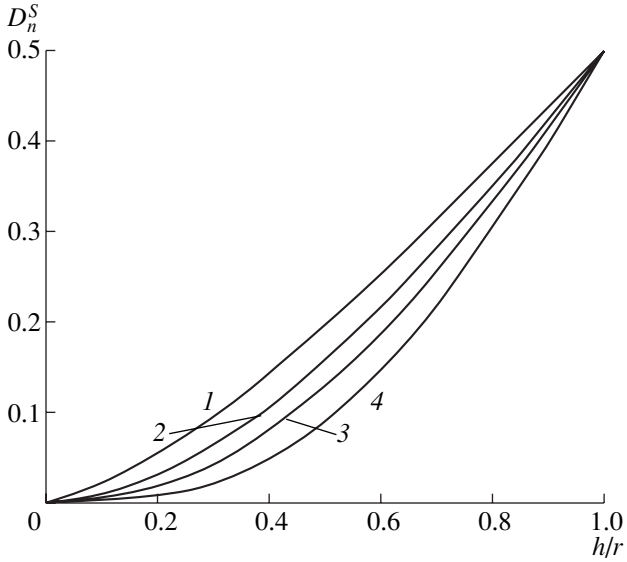

Fig. 3. Dependence of the ratio D_n^S of the volume of a spherical segment of height h to the volume of the sphere of the same radius r on the ratio h/r at several dimensions n of Euclidean space, n = 2, 3, 4, and 6 (curves *1*, *2*, *3*, and *4*, respectively).

expression

$$B_n(q) = \int_0^{\sqrt{q(2-q)}} x^{n-2}[(1-x^2)x^{1/2} - (1-q)]dx.$$

Note also that $[q(2-q)]^{1/2} = \sin\theta$.

Figure 3 illustrates the dependence of the D_n^S ratio for spaces of different dimensions. As is seen from Fig. 3, at small θ, the fraction of the volume (i.e., the value of the potential barrier at fixed θ) sharply decreases with an increase in n. Thus, the probability of homogeneous nucleation decreases with an increase in the space dimension.

Consider the results obtained in the context of the general problem of multidimensional spaces. The physical problem of space dimension may be considered using two different approaches. The first approach goes back to Kant [8], who assumed that the space dimension follows from the concrete form of the law according to which all the bodies act onto one another. In particular, three-dimensional space is explained by the fact that the acting force is inversely proportional to the squared interparticle distance, because any other dependence would have resulted in spaces of other dimensions. In the concrete form, this idea was formulated by Ehrenfest [9, 10] on various examples from mechanics, optics, and quantum mechanics. Thus, the generalization of the potential for a central field to n-dimensional space yields the dependence on distance in the form $r^{(2-n)}$, where $n \geq 3$. It was shown in these works and later studies that the consideration of the analogues of the basic physical phenomena and the generalization of the physical theories to spaces whose dimensions exceed three (four for space–time) gives rise to considerable contradictions (absence of stable orbits in the central field, problem of atomic spectra, etc. [11–14]).

The second approach is well developed [14] and reduces to the introduction of additional dimensions to be able to combine various types of interactions (gravitational, electromagnetic, etc.). This approach resulted in the construction of a model in which a conventional substance is considered in three-dimensional space embedded into a generalized multidimensional space [2].

We used above the first approach.

Constructing the thermodynamics based on statistical physics, we used the laws of mechanics. Therefore, in principle, when constructing its generalizations for spaces with the dimension exceeding three, we expected the manifestation of the above contradictions and, probably, also of some new ones.

As was seen, under the above assumptions, the pure thermodynamic consideration of the concrete problem of nucleation in multidimensional Euclidean spaces gave rise to no contradictions. This may be explained by the fact that, in this case, an important role was played by pure geometrical concepts such as volume and area, whose quantitative expressions depend in the regular way on the space dimension.

On the whole, the question about the manifestation of the specific characteristics of the dynamic behavior of systems in n-dimensional space in various thermodynamic quantities and under conditions of possible phase transitions is still open. It would be interesting to directly simulate growth of crystals in multidimensional spaces using the corresponding modifications of the molecular dynamics and setting the particle interactions in the explicit form by various potentials.

ACKNOWLEDGMENTS

We are grateful to V.A. Chizhikov for discussing the results and valuable remarks. R.M. Zakalyukin is grate-

ful to the Foundation for Promoting Russian Science for support.

The study was supported by the Grant of the President of the Russian Federation, no. NSh 1954.03.02.

REFERENCES

1. S. van Smaalen, L. Palatinus, and M. Schneider, Acta Crystallogr., Sect. A: Found. Crystallogr. **59**, 459 (2003).
2. V. A. Rubakov, Usp. Fiz. Nauk **171**, 913 (2001) [Phys. Usp. **44**, 871 (2001)].
3. A. I. Rusanov, *Phase Equilibriums and Surface Phenomena* (Khimiya, Leningrad, 1967) [in Russian].
4. B. Chalmers, *Principles of Solidification* (Wiley, New York, 1964; Metallurgiya, Moscow, 1968).
5. M. Vollmer, *Kinetik der Phasenbildung* (Steinkopff, Dresden, 1939; Nauka, Moscow, 1986).
6. P. P. Fedorov, in *Abstracts of X National Conference on Crystal Growth* (Moscow, 2002), p. 36.
7. B. A. Rozenfel'd, *Multidimensional Spaces* (Nauka, Moscow, 1966) [in Russian].
8. I. Kant, "Gedanken von der wahren Schätzung der lebendigen Kräfte (1746)," in *Collected Works* (Mysl', Moscow, 1963), Vol. 1, pp. 69–72.
9. P. Ehrenfest, Proc. R. Acad. Sci. Amsterdam **20**, 200 (1917).
10. P. Ehrenfest, Ann. Phys. (Leipzig) **61**, 440 (1920).
11. F. R. Tangherlini, Nuovo Cimento **27**, 636 (1963).
12. L. M. Sokolowski, F. Occhionero, M. Litterio, and L. Amendola, Ann. Phys. (N.Y.) **225**, 1 (1993).
13. C. Lammerzahl and A. Macias, J. Math. Phys. **34**, 4540 (1993).
14. Yu. S. Vladimirov, *Dimension of Physical Space–Time and Combination of Interactions* (Mosk. Gos. Univ., Moscow, 1987) [in Russian].

Translated by L. Man

Crystallography Reports, Vol. 50, No. 1, 2005, pp. 154–159. Translated from Kristallografiya, Vol. 50, No. 1, 2005, pp. 162–168.

CRYSTAL GROWTH

Growth of Cr^{4+} : $LiGaSiO_4$ Single Crystals by Floating-Zone Melting Technique

K. A. Subbotin* and E. V. Zharikov**

** Laser Materials and Technology Research Center, General Physics Institute, Russian Academy of Sciences, ul. Vavilova 38, Moscow, 119991 Russia*

e-mail: soubbot@lsk.gpi.ru

*** Mendeleev University of Chemical Technology, Miusskaya pl. 9, Moscow, 125047 Russia*

Received September 3, 2003

Abstract—The problems of growth of new promising laser crystals Cr^{4+} : $LiGaSiO_4$ by the crucible-free floating-zone method with optical heating are considered. The use of high axial temperature gradients with intense stirring of the melt makes it possible to obtain crystals of satisfactory optical quality from stoichiometric melt, despite the incongruent character of the compound melting. *© 2005 Pleiades Publishing, Inc.*

INTRODUCTION

Single crystals of complex oxides doped with Cr^{4+} ions in tetrahedral coordination are of much interest as active media for solid-state lasers tunable in the range 1.1–1.7 μm, which is important for practical application [1, 2]. For a number of reasons, only two such crystals, Cr^{4+} : $Y_3Al_5O_{12}$ and Cr^{4+} : Mg_2SiO_4, are used presently. However, the relatively poor luminescence kinetics of Cr^{4+} ions in these crystalline hosts cannot ensure the efficient operation of such lasers [3].

It was reported in [4] about the development of a new crystal doped with tetravalent chromium, Cr^{4+} : $LiGaSiO_4$, which, according to the preliminary results of our investigations, can compete with the two above-mentioned materials. This crystal shows intense broadband luminescence in the range 1100–1600 nm, peaked at a wavelength of 1280 nm. The lifetime of the excited state of Cr^{4+} in $LiGaSiO_4$ is 15 μs and the luminescence quantum yield is ~28% (preliminary estimate), which significantly exceeds the corresponding parameters for Cr^{4+} : $Y_3Al_5O_{12}$ and Cr^{4+} : Mg_2SiO_4. Another important advantage of this crystal as a potential laser material is the extremely low coefficients of temperature expansion [5–7], which increases its durability to the effect of high-power thermal and light fields during laser operation.

CRYSTAL STRUCTURE

Lithium gallosilicate $LiGaSiO_4$ belongs to the so-called eucryptite family, the most known representative of which is the natural mineral eucryptite $LiAlSiO_4$ ($LiGaSiO_4$ is isostructural to the high-temperature modification of eucryptite). The crystals of the eucryptite family have phenakite (Be_2SiO_4)-related structure, which is considered as a derivative of the β-Si_3N_4-related structure [8].

The unit-cell parameters of $LiGaSiO_4$ are a = 13.6427(11) Å, c = 9.0965(7) Å, and D_x = 3.44 g/cm^3 [9]. In the crystal structure (Fig. 1), all ions are in tetrahedrally coordinated positions. The cation–oxygen tetrahedra, linked with each other by shared vertices, form columns parallel to the C axis (which is perpendicular to the plane of Fig. 1). Channels of two types exist in this framework: large channels formed by six cation–oxygen tetrahedra (closed in a ring) parallel to the C axis and shallower channels formed by four tetrahedra.

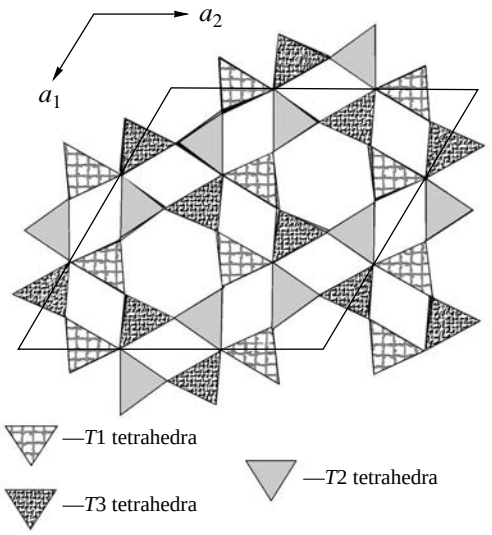

Fig. 1. $LiGaSiO_4$ structure in the view plane perpendicular to the optical axis C (cation–oxygen tetrahedra are shown entirely).

1063-7745/05/5001-0154$26.00 © 2005 Pleiades Publishing, Inc.

These channels provide the ionic conductivity of crystals of this class [10].

According to [11], all tetrahedral cation positions in the $LiGaSiO_4$ structure are divided into three nonequivalent types: $T1$, $T2$, and $T3$. Each of these types is divided into two more nonequivalent subtypes. The $T1$ positions are occupied by Ga ions, whereas Li and Si ions are distributed over the $T2$ and $T3$ positions. This distribution has a strictly regular, layer-by-layer, character (the layers are perpendicular to the C axis): Li and Si ions are located in the $T2$ and $T3$ positions, respectively, in the first layer and vice versa in the second layer. That is why the tetrahedral positions $T2$ and $T3$ in $LiGaSiO_4$ crystals are divided into subtypes $T2_1$ and $T2_2$, and $T3_1$ and $T3_2$, respectively. Each subtype has its own set of interatomic distances and bond angles [11]. Accordingly, gallium–oxygen tetrahedra $T1$, having in different layers different sets of linked tetrahedra occupied by Li and Si ions, are also divided into two subtypes: $T1_1$ and $T1_2$.

The plane in which the centers of the cation positions of the first subtypes ($T1_1$, $T2_1$, $T3_1$) are located is shifted along the C axis by 1/6 of the corresponding parameter with respect to the plane that passes through the centers of the cation positions of the second subtypes ($T1_2$, $T2_2$, $T3_2$). The ordered distribution of cations in the $LiGaSiO_4$ structure leads to the disappearance of the inversion center, which is present in $LiAlSiO_4$ and most other disordered crystals of the eucryptite family, and decreases its sp. gr. from $R\bar{3}$ to $R3$ [9, 11].

Obviously, Cr^{4+} ions in $LiGaSiO_4$ crystals should be primarily incorporated into the sublattice of tetravalent ions of the host (Si^{4+}), i.e., occupy the $T2_2$ and $T3_1$ positions. In addition, it is possible that some (apparently, small) amount of Cr^{4+} ions are located in the sublattice of trivalent ions (Ga^{3+}), i.e., in both subtypes of the $T1$ position.

When crystals are grown from a chromium-doped melt, it is also possible that the activator is partially incorporated into the crystal in the form of Cr^{3+} ions. However, the question of location of these ions in $LiGaSiO_4$ crystals is not trivial, taking into account the absence of octahedral cation positions in this structure (Cr^{3+} ions, in view of their specific electron configuration, have a strong tendency to be located in such positions).

PHASE DIAGRAM

According to [8], the $LiGaSiO_4$ crystal does not undergo polymorphic transformations in the entire temperature range up to the melting point, at least at atmospheric pressure.

We failed to find a complete ternary phase diagram of the Li_2O–Ga_2O_3–SiO_2 system in the available literature. At the same time, there are two quasi-binary cross sections of this three-component system along the $Li_xGa_xSi_{2-x}O_4$ [5] and $Li_{4-3x}Ga_xSiO_4$ [6] lines in the range $0 \le x \le 1$. In both cases, the end member of the cross sections (at $x = 1$) is $LiGaSiO_4$. These quasi-binary cross sections, taken from [5, 6], are shown with small modifications in Figs. 2 and 3, respectively.

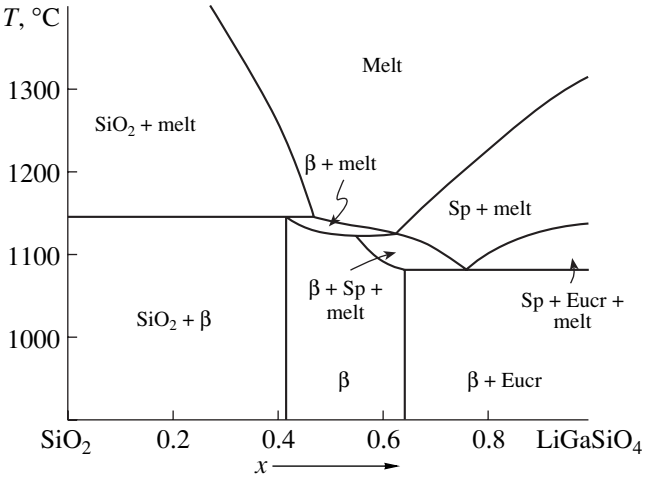

Fig. 2. Quasi-binary cross section of the phase diagram of the three-component system Li_2O–Ga_2O_3–SiO_2 along the $Li_xGa_xSi_{2-x}O_4$ line in the range $0 \le x \le 1$ [5]: Eucr is the eucryptite phase of $LiGaSiO_4$, Sp is the phase of $LiGa_5O_8$ with spinel-like structure, and β is the $Li_{1-y}Ga_{1-y}Si_{2+y}O_6$ solid solution with β-spodumene structure.

It can be seen from both diagrams that melting of $LiGaSiO_4$ is incongruent: the stoichiometric point of this compound is in the primary crystallization field of the highly refractory (about 2000°C) spinel-like compound $LiGa_5O_8$. Note that, as far as can be seen from these two cross sections, the primary crystallization field $LiGa_5O_8$ is very extended and covers almost the entire concentration range in which one would expect $LiGaSiO_4$ to be crystallized. There is only a small region corresponding to the mole ratio $Li_2O : Ga_2O_3 : SiO_2 \sim 1.6 : 0.8 : 2.0$ (Fig. 3) where the existence of the primary crystallization field of the eucryptite phase of $LiGaSiO_4$ can be expected.

The incongruent melting of this compound is the main difficulty in growing high-quality $LiGaSiO_4$ single crystals from melt. In this paper, we describe the methods and procedures that allowed us to overcome this and some other problems and grow for the first time macroscopic $Cr : LiGaSiO_4$ single crystals with high optical quality.

GROWTH OF CRYSTALS

The crystals were grown by the crucible-free floating-zone melting with optical heating in a URN-2-ZP

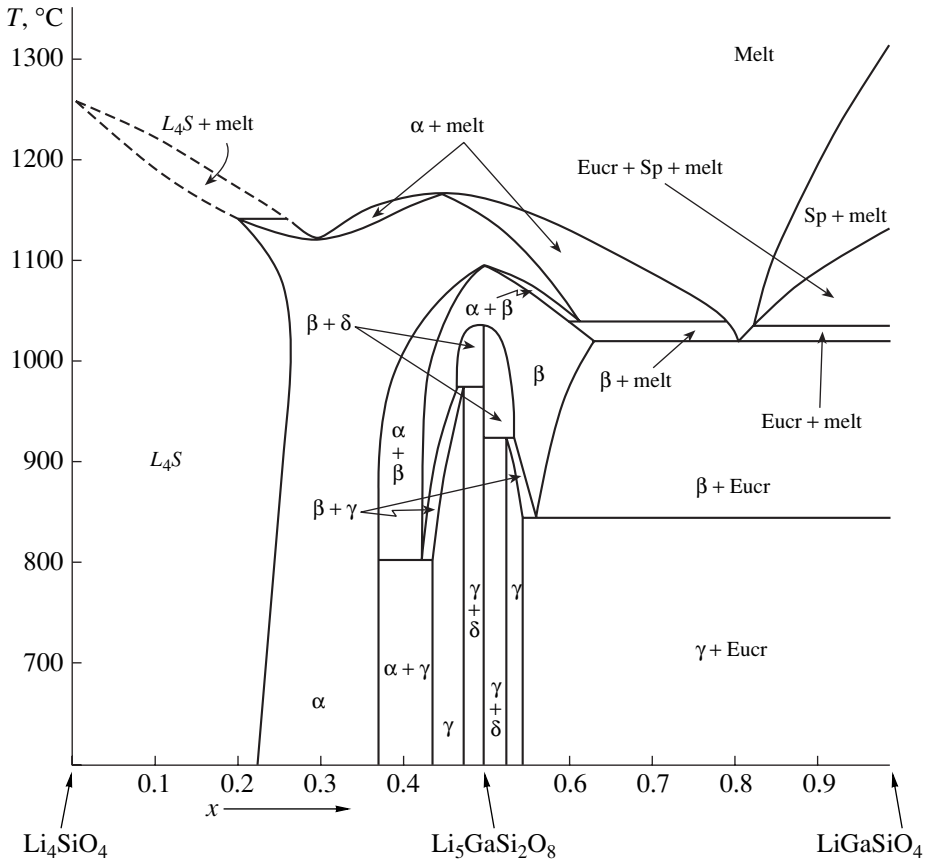

Fig. 3. Quasi-binary cross section of the phase diagram of the three-component system Li_2O–Ga_2O_3–SiO_2 along the $Li_{4-3x}Ga_xSiO_4$ line in the range $0 \le x \le 1$ [6]: Eucr is the eucryptite phase of $LiGaSiO_4$; Sp is the phase of $LiGa_5O_8$ with spinel-like structure; L_4S is a high-temperature phase of Li_4SiO_4; α is the $Li_{4-3x}Ga_xSiO_4$ solid solution (~$0.25 \le x \le$ ~0.6) with tetragonal γ-$LiGaO_2$-like structure; and β, γ, and δ are different phases of $Li_5GaSi_2O_8$.

setup, the optical scheme and the heating unit of which are shown in Figs. 4 and 5, respectively.

To prepare feed rods, the initial agents Li_2CO_3, Ga_2O_3, and SiO_2 of high-purity grade, previously calcinated at 400°C, were weighed on a Sartorius balance. The weighing accuracy was ±0.001 g. Chromium was added in the form of Cr_2O_3 in the amount of 0.1–0.5 wt %. The weights were carefully mixed and then the mixture was pressed into rods 120 mm long and 7 mm in diameter. The rods were fired in a silite furnace at 1000°C for 24 h. The mass of each feed rod after the firing was about 10 g. The mechanical strength of the fired rods was sufficient to mount them on the supplying (upper) shaft of the setup and center them in the normal direction.

Visual observation of the melting of the feed rod in the heating zone of the growth setup suggests that the solid-phase synthesis of $LiGaSiO_4$ during the preliminary firing of the rods in the silite furnace is obviously incomplete. Indeed, when such a rod finds itself in the heating zone (where the rays from a xenon lamp are focused), the solid substance transforms first into a viscous white nontransparent inhomogeneous mass of sour-cream-like consistency, which gradually transforms into a transparent mass with a large number of small light curdlike inclusions. Then these inclusions are slowly (for several minutes) completely dissolved and the melt acquires its final form: a transparent homogeneous mass.

In the absence of single-crystal seeds, the seeding was performed on a polycrystalline base. However, after the actual growth rate became stable, i.e., the velocity of the motion of the crystallization front with respect to the seed (in some cases, it may fluctuate relative to the pulling rate; the factors causing this fluctuation are described below), the geometric selection occurred very rapidly, taking no more than 2 mm over the boule length. After a very short time (1–2 h), the growth process passed into the single-crystal mode. Note that the spontaneous crystal orientation always turned out to be almost parallel to the threefold *C* axis, which was verified by X-ray diffraction measurement of the crystal orientation.

During the growth, a serious destabilizing factor leading to the instability of the growth conditions for Cr : $LiGaSiO_4$ crystals is the strong temperature depen-

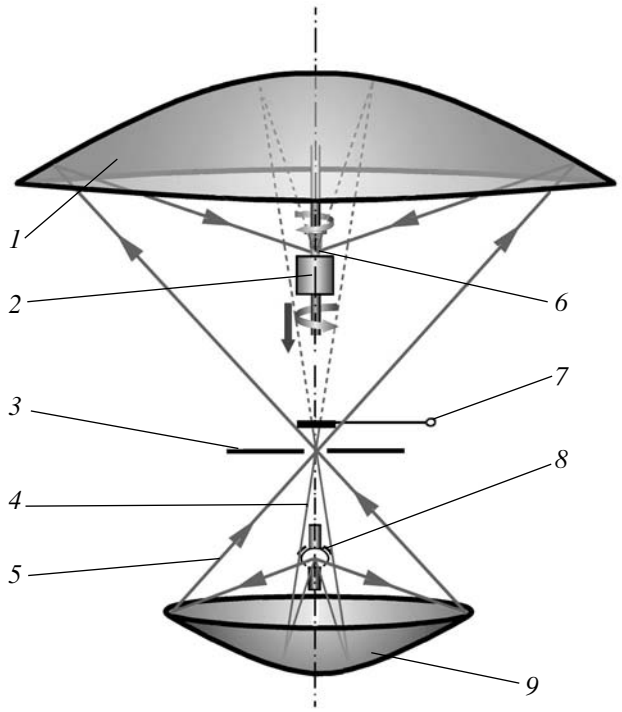

Fig. 4. Optical scheme of a URN-2-ZP crystal growth setup: (*1*) upper elliptical mirror, (*2*) postgrowth annealing furnace, (*3*) diaphragm, (*4*) propagation of "central" rays of the xenon lamp passing through the light shutter only when it is highly open (the dotted line shows the fraction of these rays cut off by the lowered shutter), (*5*) propagation of peripheral rays of the xenon lamp passing through the shutter even when its opening is small, (*6*) melting zone, (*7*) light shutter, (*8*) xenon lamp, and (*9*) lower elliptical mirror.

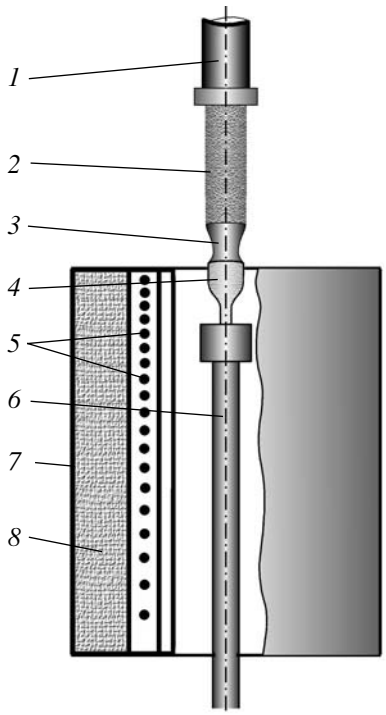

Fig. 5. Heating unit of the URN-2-ZP setup: (*1*) upper shaft, (*2*) feed rod, (*3*) molten zone, (*4*) seed with a growing crystal, (*5*) heating coil of the postgrowth annealing furnace, (*6*) lower shaft, (*7*) housing of the postgrowth annealing furnace, and (*8*) heat-insulating filler in the postgrowth annealing furnace.

dence of the optical absorption of a melt. For example, even at a small (tens of kelvin) superheating of the melt with respect to the liquidus temperature, the optical absorption coefficient of the melt and, therefore, the susceptibility of the system to optical heating increase, which leads to even higher melt superheating. Vice versa, at a small (about 1%) random decrease in the light power, the light absorption of the melt and, therefore, its susceptibility to light heating sharply decrease, which results in even stronger melt cooling.

The decrease in the pulling rate to 1 mm/h and introduction of a larger (up to 0.5 wt %) amount of Cr into the charge allowed us to suppress to some extent these fluctuations and make the growth conditions more or less stable. In this case, the melt becomes more intensively colored and the fraction of residual (temperature-independent) light absorption increases, due to which the relative difference in the susceptibility of the melt to optical heating at different deviations of its temperature from the nominal value becomes much smaller.

Another factor impeding the preparation of high-quality $Cr : LiGaSiO_4$ single crystals is a rather high tendency of melt to glass formation. The transition to the glass formation regime most often occurs during the seeding or in the initial period of the crystal growth, when steady-state thermal fields have not been formed yet. We managed to suppress the glass formation of the melt to a certain extent using large (300–400 K/cm) axial temperature gradients, decreasing the growth rate to 1 mm/h, and optimizing the seeding regimes.

As was noted above, a serious problem in growing $Cr : LiGaSiO_4$ crystals is the incongruent melting of this compound. The narrowness of the primary crystallization field of $LiGaSiO_4$ and the large spacing between this field and the stoichiometric point make it almost impossible to grow lithium gallosilicate crystals from a melt whose initial composition is in this field.

At the same time, taking into account a rather large spacing between the stoichiometric points of $LiGaSiO_4$ and $LiGa_5O_8$, one might expect that, when a stoichiometric blend of $LiGaSiO_4$ composition is heated above the melting temperature of the eucryptite phase (about 1100°C), a very small amount (maybe, only traces) of $LiGa_5O_8$ will be in thermodynamic equilibrium with the melt. The investigations in [5, 6] confirm this suggestion.

This suggestion is also confirmed by our first experiments with the growth of $LiGaSiO_4$ crystals from stoichiometric melt. Indeed, during steady-state growth,

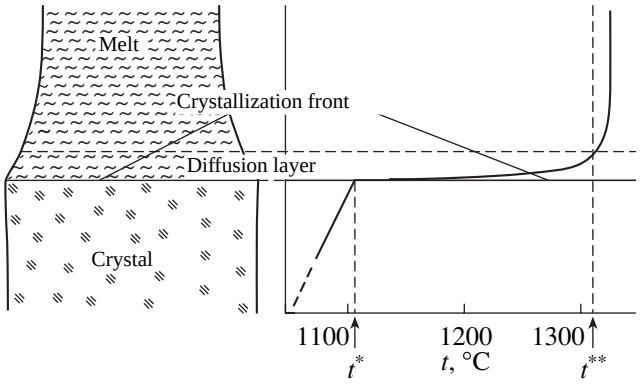

Fig. 6. Schematic axial diagram of the temperature distribution in the melt at large axial gradients and intense melt stirring. t^* is the temperature of crystallization of $LiGaSiO_4$ from stoichiometric melt and t^{**} is the temperature at which crystallization of the $LiGa_5O_8$ phase from a melt of composition $LiGaSiO_4$ begins.

rather sparse (no more than 5 vol %) and small inclusions of solid phase were observed in the melt. According to the microprobe analysis of the quenched melts (lithium and oxygen were not determined), Ga is dominant in these inclusions, along with small (up to 2 wt %) amounts of Si and Cr. The data of Figs. 2 and 3 show unambiguously that these inclusions correspond to the $LiGa_5O_8$ phase, and Si and Cr are dissolved in them.

Sparse inclusions of this phase from 5 to 30 μm in size were also observed in the first grown crystals. In addition, second phases with the ratio Ga : Si varying from 1 : 3 to 1 : 8 were found in these crystals. The morphology of the inclusions of these phases varies from shapeless (obviously, glasslike) formations with a high Si content to angular, often elongated, inclusions with the Ga : Si ratio no higher than 1 : 5. Obviously, in the latter case, we are speaking of numerous stable and metastable phases and solid solutions with structures of β-spodumene, γ-$LiAlO_2$, and others, described in [5, 6]. The occurrence of second phases enriched with Si^{4+} ions in the crystals is likely to be due to the enrichment of the melt with SiO_2, which, in turn, results from the segregation of $LiGa_5O_8$.

The presence of only small amounts of second phases formed during the growth of Cr : $LiGaSiO_4$ from stoichiometric melt using conventional growth conditions gave promises that single-phase crystals can be grown using large (several hundred K/cm) axial temperature gradients and intense melt stirring. Strong stirring is obtained by increasing the rotation rates of the supplying and receiving shafts (Fig. 5) up to 100 rpm.

These external factors should lead to the thermodynamical and hydrodynamical conditions in the melt that result in the formation of a melt nucleus, superheated with respect to the liquidus temperature of the stoichiometric composition $LiGaSiO_4$, and a thin diffusion layer, directly adjacent to the crystallization front (Fig. 6). The temperature in the diffusion layer sharply decreases from the liquidus temperature to the crystallization temperature of Cr : $LiGaSiO_4$. In this case, a small number of $LiGa_5O_8$ particles formed in the diffusion layer should be captured with high probability by the convective flux and transferred to the melt nucleus, superheated with respect to the liquidus temperature, and dissolved in it. The probability of capture of $LiGa_5O_8$ particles by the growing crystal in this scheme should be very low.

Large axial temperature gradients and intense stirring of the melt make it also possible to avoid undesirable effects related to the constitutional supercooling. According to [12], the criterion for the occurrence of the constitutional supercooling can be written as the inequality

$$G/f \le mC(1-k_0)/(k_0D), \quad (1)$$

where G is the axial temperature gradient; f is the actual growth rate; m is the slope of the liquidus curve at the point corresponding to the current melt composition, $\Delta T/\Delta C$; C is the concentration in the melt nucleus of the component accumulation of which in the diffusion layer leads to the constitutional supercooling; k_0 is the equilibrium coefficient of distribution of this component between the crystal and melt; and D is the steady-state diffusivity of this component in the melt.

Constitutional supercooling arises when the value of the right-hand side of inequality (1) is equal to or exceeds the value of the left-hand side. This model was developed for the case of complete absence of convection in a melt. To take into account the convection, a correction coefficient ξ was introduced in [13]:

$$\xi = 1 + (1-k_0)/k_0 \exp(-f\delta/D), \quad (2)$$

where δ is the thickness of the diffusion layer. If convection is present in the melt, the constitutional supercooling occurs when the value of the right-hand side of inequality (1) increases by a factor of ξ as compared to the case when the convection is absent.

Analysis of inequality (1) and Eq. (2) shows that the problem of constitutional supercooling is rather urgent for the growth of Cr : $LiGaSiO_4$ crystals from melt, taking into account the incongruent melting of this compound, multicomponent composition of the system (including the Cr dopant), and high viscosity of the melt (and, therefore, the low diffusivity of the components in it).

Indeed, the crystals grown in conventional thermal and hydrodynamical regimes (in the first stages of the investigation) had a pronounced tendency to the transition to cellular growth, which is known to be a typical consequence of constitutional supercooling. The use of large axial temperature gradients leads to the increase in the value of the left-hand side of inequality (1), whereas intensification of the melt stirring makes the diffusion layer thinner and, therefore, increases the correction coefficient ξ, which is determined from Eq. (2).

Thus, the conditions for constitutional supercooling and transition to cellular growth become unlikely.

The growth experiments performed by us in the second stage, showed the efficiency of the chosen way: when the crystals were grown at high axial temperature gradients and intense stirring, the melt in the stage of steady-state growth was characterized by high transparency and homogeneity; the crystallization front had high stability; and the grown crystals showed satisfactory optical quality, the absence of traces of cellular growth, and an extremely small number of inclusions of second phases.

Generally, the use of overly large temperature gradients leads to the formation of high thermomechanical stresses in crystals and significant cracking of the samples obtained. However, as was noted, crystals of the eucryptite family are characterized by an extremely low coefficients of thermal expansion [5–7], which eliminates this problem to a large extent. Indeed, the crystals grown under these conditions contained almost no cracks. No cracks arose in the crystals when they were mechanically treated, which indicates the absence of high thermomechanical stresses.

Thus, we managed to obtain for the first time $Cr : LiGaSiO_4$ single crystals 6 mm in diameter and 8 mm long, whose optical quality made it possible to perform complex spectroscopic investigations with them, in particular, to record their absorption spectra (see [14]).

ACKNOWLEDGMENTS

We are grateful to V.G. Senin for carrying out microprobe analysis of the samples.

This study was supported by the Russian Foundation for Basic Research, project nos. 02-02-16360 and 03-02-06616.

REFERENCES

1. E. V. Zharikov and V. A. Smirnov, *Wide Gap Luminescent Materials: Theory and Applications* (Kluwer Academic, Nowell, 1997), p. 13.
2. S. Kück, Appl. Phys. B **72**, 515 (2001).
3. C. R. Pollock, D. B. Barber, J. L. Mass, and S. Markgraf, IEEE J. Sel. Top. Quantum Electron. **1** (1), 62 (1995).
4. K. A. Subbotin, V. A. Smirnov, E. V. Zharikov, and I. A. Shcherbakov, in *Technical Digest of XVII Topical Meeting on Advanced Solid-State Lasers* (Québec City, Canada, 2002), Paper TuB19.
5. E. Chavira, P. Quintana, and A. West, Br. Ceram. Trans. J. **86**, 161 (1987).
6. P. Quintana and A. West, J. Solid State Chem. **81** (2), 257 (1989).
7. P. W. McMillan, *Glass Ceramics* (Academic, New York, 1979).
8. M. Behruzi and Th. Hahn, Z. Kristallogr. **133**, 405 (1971).
9. P. Hartman, Z. Kristallogr. **187**, 139 (1989).
10. T. P. Balakireva, O. P. Barinova, and M. V. Provotorov, Tr. Mosk. Khim. Tekhnol. Inst. im. D.I. Mendeleeva, No. 154, 10 (1988).
11. M. E. Fleet, Z. Kristallogr. **180**, 63 (1987).
12. W. A. Tiller, in *The Art and Science of Growing Crystals*, Ed. by J. J. Gilman (Wiley, New York, 1963; Metallurgizdat, Moscow, 1968).
13. D. T. Hurtle, Solid-State Electron. **3**, 37 (1961).
14. T. F. Veremeĭchik, E. V. Zharikov, and K. A. Subbotin, Kristallografiya **48** (6), 1025 (2003) [Crystallogr. Rep. **48**, 974 (2003)].

Translated by Yu. Sin'kov

Crystallography Reports, Vol. 50, No. 1, 2005, pp. 160–166. Translated from Kristallografiya, Vol. 50, No. 1, 2005, pp. 169–176.

CRYSTAL GROWTH

Change of Symmetry and Rotation of Thermal Field as a New Method of Control of Heat and Mass Transfer in Crystal Growth (by Example of β-BaB_2O_4)

A. E. Kokh, N. G. Kononova, T. B. Bekker, V. A. Vlezko, P. V. Mokrushnikov, and V. N. Popov

Institute of Mineralogy and Petrography, Siberian Division, Russian Academy of Sciences, Novosibirsk, Russia

e-mail: kokh@mail.ru

Received November 5, 2003

Abstract—It is suggested to change the symmetry and rotation of thermal field as a method of contact-free control of the heat and mass transfer in crystal growth. By the example of growth of the low-temperature barium borate (β-BaB_2O_4) phase, a technically important crystal with nonlinear-optical properties, it is shown that the use of the suggested method allows one to grow larger crystals of a higher quality. *© 2005 Pleiades Publishing, Inc.*

INTRODUCTION

The search for new methods of control of convective heat and mass transfer in crystal growth is important because it is these processes that often determine the possibility of synthesis of necessary crystals. All the methods of such control may be divided into two groups—contact and contact-free ones. The former are based on the action of a certain physical body contacting the melt, solution, or crystallization medium. These methods are usually based on the mechanical rotation of a crystal and crucible and the use of various partitions, stirrers, shape formers, etc. The latter, contact-free methods, are based on the action of various physical fields on heat and mass transfer. The study of the effect of a gravitational field on crystal growth is usually associated with space materials science. A number of studies showed the relation of inhomogeneities in crystals grown in space with irregular variation of accelerations and, thus, as is assumed, with an irregular mode of convective heat and mass transfer in an ampoule [1, 2].

In recent years, numerous experimental studies and simulation of the effect of electromagnetic fields on convective processes in crystal growth were performed. However, electromagnetic fields affect only electrically conductive and magnetically sensitive media.

Practically all the methods of crystal growth are based on creation of thermal fields of specific configurations. The traditional approach used in crystal growth by many axisymmetric methods (Czochralski, Kyropoulos methods, etc.) is the creation of a stable and stationary external thermal field with a desired axial and radial temperature gradients. The main characteristic of a thermal field is the existence of the symmetry axis of an infinite order, L_∞ [3], coinciding with the furnace axis and the axis of the whole growth setup.

A crystal in a stationary thermal field with the symmetry axis L_∞ grows mainly under the action of an axial temperature gradient. As a rule, the influence of a radial asymmetry of the thermal field is eliminated by the rotation of a growing crystal. However, many recent studies indicate that the axial symmetry of the convective thermal fields in the melts is also changed at some values of growth parameters and thermal properties of the melts. Thus, convection instability in growth of GaAs crystals is indicated in [4]: at certain values of the parameters, thermal convection with the symmetry axis L_∞ was observed on the melt surface. Possible formation of trigonal and pentagonal structure of flows in growth of InSb crystals is indicated in [5]. More complicated structures of flows without axial symmetry were studied in the Si melt in [6–8] The deviation from the cylindrical symmetry of the convective flows in the oxide melts was simulated for Czochralski growth in [9]. Thus, even under conditions of cylindrical symmetry of thermal fields in melts, thermal convection with a symmetry different from L_∞ is possible. This seems to be a property inherent in the system itself. Therefore, setting a certain symmetry of the external thermal field in accordance with the Curie principle, one may expect the attainment of possible symmetrization of the convective flows in the system.

1063-7745/05/5001-0160$26.00

Despite considerable progress in the development of the methods of laboratory and numerical simulation, we still do not reliably know all the details of the structure of volume flows in a melt and, moreover, in a flux. Such knowledge is especially important for crystallization from flux, where an important role is played by various concentration effects. Thus, the model of the concentration-gravitational differentiation of the melt was considered for growth of $LiNbO_3$ crystal [10]. In a Li_2O-depleted (4–5)-mm-thick subsurface layer, the thermocapillary convection prevails with the flow on the surface being directed from the crucible walls to crucible center in the field of a radial temperature gradient. In the main bulk of the melt, the thermogravitational convection caused by the axial temperature gradient is more important. The exchange between these two zones of liquid circulation proceeds via diffusion. The division of the flow structure along the vertical into two convective cells was observed in the three-dimensional simulation of flows in the melt in Czochralski growth of oxides in [11]. An interesting experimental result was also obtained in [12], where the authors visualized in X rays the tracks of solid particles in the Si melt and showed that an increase in the melt height in the crucible reduces the stability of regular axisymmetric convective flows.

It was long believed that all the temperature variations, including those associated with convection, produce a negative effect on the quality of a growing crystal which acquires layer inhomogeneity. In [13–15], the formation of a layered structure was associated with a rhythmic character of crystallization due to a positive temperature gradient, convection of the liquid phase, and a rather narrow temperature interval of crystallization. An important role in this process is played by supercooling dynamics, a driving force of crystal growth. At the same time, recent publications also indicate a positive effect of the stimulated vibrational thermal fields on crystal growth [16, 17]. It was reported [18] that it is possible to grow a highly homogeneous crystal by using the effect of a special low-energy "thermal wave"—a periodic change of the heater temperature with a frequency of 10^{-1} Hz and an amplitude of 1°C. It may be assumed that stimulated temperature oscillations of certain frequency and amplitude hinder the spontaneous oscillatory processes at the crystallization front and, thus, play a positive role in the formation of a crystal of higher structural quality.

Thus, we may draw the following conclusions and formulate the aim of the present study:

—Convective processes in the melt in a cylindrical vessel in a stationary thermal field with the symmetry axis L_∞ may be symmetrized or dissymmetrized and, in the general case, also may be influenced by the vertical concentrational and gravitational differentiation under the action of the geometrical and dynamical parameters of the growth process. This justifies the necessary control of the convective processes by changing the symmetry and rotating the thermal field.

—There are rather contradictory opinions on the effect of temperature oscillations on the crystallization processes. Therefore, it is important to study the effects of temperature oscillations induced by the rotation of a thermal field on the elementary growth process, which, to a large extent, determine the quality of the growing crystal.

METHOD OF SYMMETRY VARIATION AND THERMAL-FIELD ROTATION

The method of change of the symmetry and thermal-field rotation (TFR) was suggested at the Laboratory of Crystal Growth (Institute of Mineralogy and Petrography, Siberian Division, Russian Academy of Sciences) in 1998 [19]. The method reduces to the creation of inhomogeneous stationary and cyclically varying external thermal fields under the action of which the control of the convective heat and mass transfer is performed and a vibrational temperature mode in the growth zone is created. We designed a special furnace with vertically located heating elements and the corresponding control system (commutation of heating elements) and thermal regulation, which allowed us to create stationary and rotating thermal fields with different amplitude and frequency characteristics [20, 21].

Using numerical simulation based on the solution of the Navier–Stokes equation in the Boussinesq approximation, we studied the flows in liquids over the large range of thermal and physical properties at various heating modes of the side walls of a cylindrical vessel by vertical heaters, i.e., under homogeneous nonstationary thermal boundary conditions. It was shown that the change of the symmetry of a stationary thermal field and its rotation at different geometrical parameters of the system, thermal and physical properties of the liquid and its dynamical parameters results in the formation of the convective flows of various intensities with an azimuthal component of the velocity vector. It is also shown that there exist the modes of synchronization of the rotation velocities of the thermal field and the internal liquid flows that provide the formation of close toroidal flows in the melt bulk with the azimuthal component of the velocity vector [22]. Thus, the numerical simulation confirmed the fact that the thermal-field rotation provides the possibility of the contact-free control of the processes of heat and mass transfer in the crystallization medium.

GROWTH OF β-BaB_2O_4 CRYSTALS

Up to now, the TFR method proved to be very successful in the development of the growth technology of a barium metaborate β-BaB_2O_4 (BBO) crystal widely used in nonlinear optics. The existence of the polymorphous $\alpha \Leftrightarrow \beta$ phase transition at 925°C makes it neces-

sary to grow the β phase at temperatures below 925°C ($t_{m\,BBO}$ = 1095°C). With this aim we used crystallization from flux. Its technical implementation is rather similar to that of the Czochralski method. More than ten years of the practice of growth of this crystal showed that the most promising method of BBO growth from flux is the use of Na_2O [23, 24]. The NaF charge also has some advantages [25]; however, because of slow pyrohydrolysis of NaF in air in the course of crystallization, the BaB_2O_4–NaF system is gradually transformed into the BaB_2O_4–Na_2O system [26], which makes growth of reproducible BBO crystals impossible.

Growth of large BBO crystals is limited by high viscosity of the flux, which hinders the stirring, and is also complicated by concentration supercooling resulting in cellular growth of a low-quality material. The most important is the crystal dimension along the optic *Z* axis. The ten years of growth practice resulted in growth of a 25- to 30-mm-long boule and about 20-mm-long optical element at a 5×5 mm^2 aperture. In [25], the use of the BaB_2O_4–NaF system allowed the authors to grow a lens-like crystal with the diameter 100 mm and the height 40 mm; the element prepared from this crystals had the dimensions $21 \times 14 \times 8$ mm^3.

Figure 1 shows the schematic of growth of BBO crystals on a single-crystal seed from flux melted in a crucible. The crucible was placed into a furnace with vertical heating elements. After the determination of the equilibrium temperature by touching the melt with a [0001]-oriented seed, the seed started grow in the center of the flux surface at a low rate of temperature lowering and crystal rotation and pulling: 0.1–2.0°/day, 1–10 rpm, and 0.5–0.2 mm/day, respectively.

In crystal growth at low (1–2 rpm) rotation velocities in thermal fields with the symmetry L_∞ and all the heating elements being switched on and spaced by a distance which ensures uniform thermal flow along the circumference, the natural thermal–gravitational convection prevails (Fig. 2a). In this case, the flow moves upward along the crucible walls (uniformly heated along the circumference), which is accompanied by random separation of the flow into a set of convective streams and formation of a downward flow in the central region. Then one may observe the characteristic starlike convective patters consisting of a large number of rays converging to the center—the cold point. The intensity of the natural thermal convection depends on the axial and radial temperature gradients. The creation of the maximum gradients is usually limited by the furnace design. At the same time, high temperature gradients give rise to stresses and growth of block crystals. Thus, the method of increasing thermal gradients cannot be recognized as preferable.

All attempts to intensify the convective mode by increasing the rotation velocity of a growing crystal gave no desirable result either. With an increase in the rotation velocity of a crystal, convective cells are formed under the crystal in which the flow is directed from their centers to the periphery. Thus, the convective structure in the crucible is divided along the vertical (Fig. 2b). An increase in the rotation velocity of a crystal to create the forced convection along the flux height (Fig. 2c) is accompanied by the formation of a concave crystallization front, an increase in the height of the column of the liquid under the crystal, and the morphological instability with partial or complete decanting of the mother liquor. In the two later cases, one observes, instead of the axisymmetric pattern of convective flows through a growing crystal, either a cellular or an island structure of the flows in the form of dark spots of different shapes described as thermal waves in [27].

Our approach based on the change of the symmetry of a stationary thermal field (Fig. 2d) turned out to be rather effective. An appropriate commutation of the heating elements around the crucible (three heating elements separated by 120° are switched off, Fig. 1b) gives rise to a thermal field with the threefold symmetry axis L_3 [28]. As a result, three well-heated zones are created around the crucible along which the formation of floating-up streams is observed. On the flux surface, one observes a characteristic starlike convective pattern consisting of three intense rays converging at the center. This is the implementation of the Curie symmetry principle—the symmetry elements of the cause are reflected in the symmetry elements of its effect [29]. Three intense ascending flows structurize the media and give rise to convection along the flux height. This results in a considerable intensification of stirring both in the flux bulk and in the vicinity of the crystallization front because of the existence of three intense subsurface flows. Thus, the thickness of the diffuse layer at the crystallization front decreases and, as a result, the manifestation of the effect of the concentration supercooling is delayed so that it becomes possible to grow large crystals.

Now, introduce the notion of the coefficient of the crystal yield—a mass of the crystal related to the lowering of the temperature by 1°C and an initial loading of 1 kg (g/kg °C). Theoretically, this coefficient is proportional to the angle of the slope of the tangent line to the liquidus line on a phase diagram. On the other hand, the yield coefficient characterizes the stirring conditions of the flux, because the moment of the appearance of the concentration supercooling directly depends on these conditions [30]. The table lists the experimental results obtained in growth of BBO crystals from a crucible with the diameter 80 mm in stationary thermal fields with the symmetry L_∞ or L_3. It is seen how the yield coefficient increases with the transition from a stationary thermal field with the symmetry L_∞ to the field with the symmetry L_3. In accordance with the slope of the liquidus curve in the section of the BaB_2O_4–Na_2O phase diagram, BaO–B_2O_3–Na_2O, the theoretical value of the yield coefficient is about 2.5 g/(kg °C) [31]. Thus, if fact, since the yield coefficient depends on the stirring conditions, its deviation

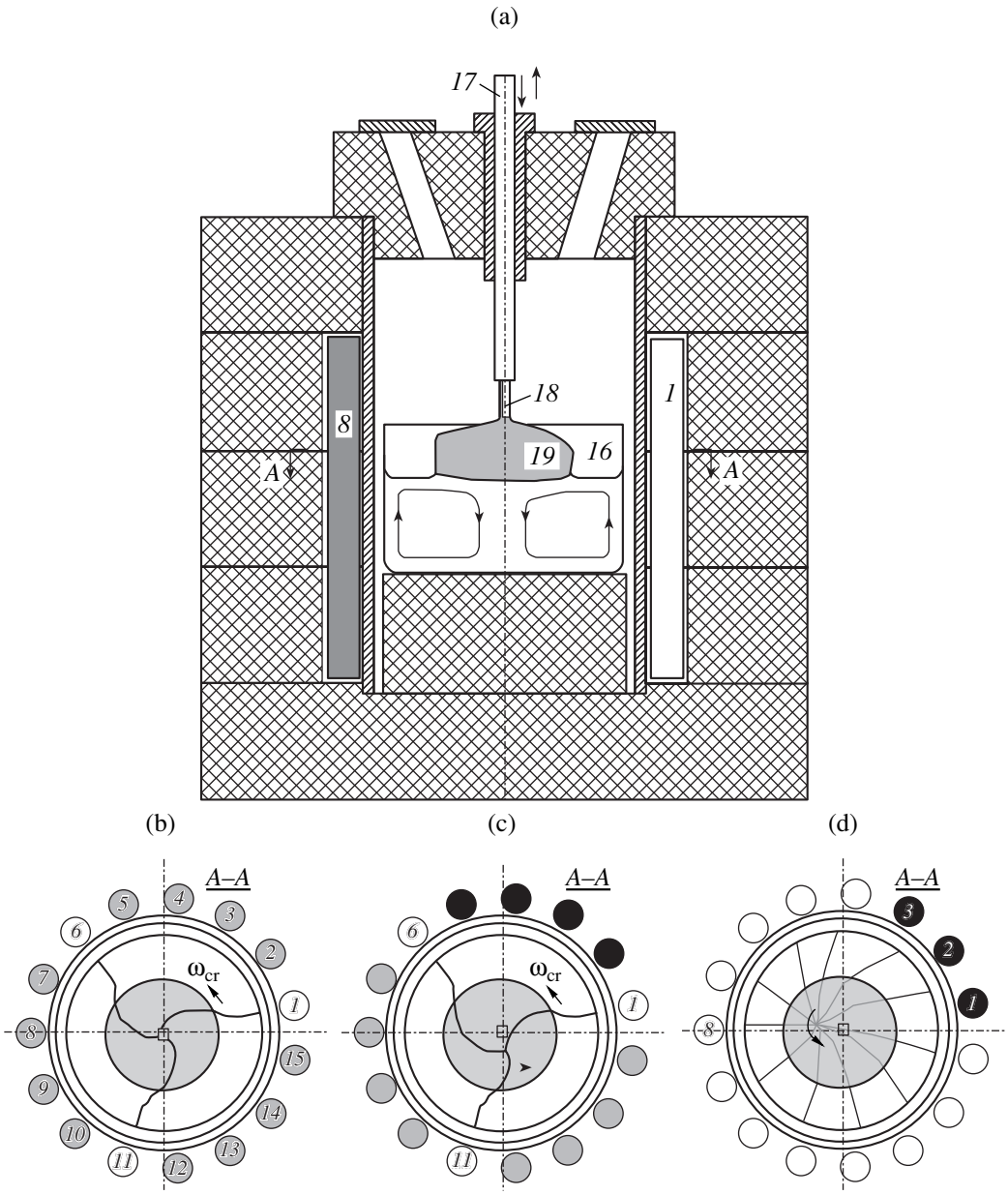

Fig. 1. (a) Schematic of the setup for growing BBO crystals with the change of the symmetry and rotation of the thermal field: (*1–15*) heating elements (black color indicates switched-on elements, and white color indicates switched- off elements), *16* crucible with flux, *17* crystal holder, *18* seed, *19* growing crystal; (b) and (c) creation of thermal fields with the symmetry L_3 and threefold quasi-symmetry qL_3; (d) rotating thermal field curlL_1.

from the theoretical value characterizes the degree of flux homogeneity attained during crystallization under certain thermal conditions. It should be indicated that an increase in the height of the initial flux in growth in the thermal field with the symmetry L_3 does not ensure the concentrational–gravitational differentiation (as is the case in the thermal flux with the symmetry L_∞). Moreover, it increases the velocity of the ascending flow and, thus, intensifies stirring and increases the size of a growing crystal.

Figure 3a shows the photograph of convective flows observed on the free surface of a melt and through a growing crystal in a thermal field with the symmetry L_3. It is a stationary convective pattern consisting of three rays which are curved because of the crystal rotation. The rays converge at the cold point in the crucible center. This does not allow one to completely remove from a crystal the so-called middle column with a large number of gas and solid-phase inclusions, because, in fact, the flow velocity in the center under the crystal has zero value, which results in a more probable capture of

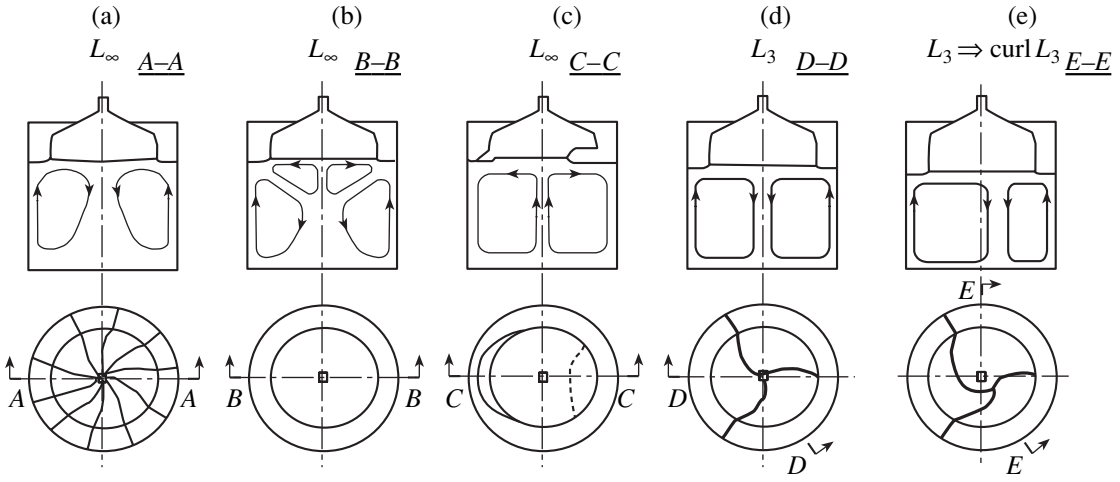

Fig. 2. Schemes of the convective structure in the flux bulk in thermal fields with different symmetries: (a) natural thermogravitational convection, (b) appearance of weak forced convection, (c) prevailing forced convection, (d) azimuth–structured natural thermogravitational convection in a thermal field with the threefold symmetry axis, (e) displacement of the cold point from the center during crystal growth and lowering of the thermal-field symmetry. Rotation velocity of a crystal, ω_{cr}, is (a, d, e) 1–2 rpm, (b) 3–5 rpm, and (c) exceeds 8 rpm.

inclusions by the central region of a growing crystal. These defects may be eliminated. After seeding and initiation of crystal growth, during which the symmetry axis L_3 of the thermal field coincides with the axis of the seed rotation, the heating intensity in the radial zone consisting of heating elements 2–5 is slowly diminished in comparison with the heating intensity in zones consisting of heating elements 7–10 and 12–15 (Figs. 1c and 2e). Thus, the site of the coincidence of the descending convective flows is displaced from the crystal center toward the 11th heating element. The cold point shifts along the radial direction. Thus, no zone with zero convective-flow velocity with respect to the crystal may be formed under the crystal. The symmetry of the thermal field in this case may be described as qL_3—a quasi-symmetry of the third order. It is seen from the table that, in this case, the yield coefficient also increases, i.e., the convective mode is further intensified.

Figure 4 shows the photograph of a BBO crystal grown in the thermal field whose symmetry was changed from L_3 to qL_3. The dimensions of the grown boule allowed us to prepare electro-optical elements with dimensions up to (6–5) × (6–5) × (22–23) mm^3 (cut out along the optic axis) and up to 15 × 15 × 15 mm^3 (cut out along all the other directions). Some crystals weakly scattered a laser beam. One of the possible explanations of this phenomenon is given elsewhere [32]. It should be indicated that crystals grown in thermal fields with the symmetries L_3 or qL_3 had high optical homogeneity and scattered much better than the crystals grown in a thermal field with the symmetry L_∞. This indicates that the temperature variations in the crystal and at the crystallization front, which arise if a rotating crystal intersects the inhomogeneous thermal field, are usually favorable for growth of quality crystals.

Experimental data on growth of BBO crystals from a crucible with the diameter 80 mm in stationary and rotating thermal fields with different symmetries

Thermal-field symmetry	Decrease in temperature during growth, °C	Crystal pulling, mm	Velocity of crystal rotation, rpm	Initial loading, g	Mass of crystal grown, g	Coefficient of crystal yield, g/(kg °C)
L_∞	117	11.6	4	850	121.2	1.2
L_3	110	18.1	4	790	157.7	1.8
qL_3	104	18.6	2	960	190.0	1.9
curlL_1	116	15.2		880	177.0	1.7

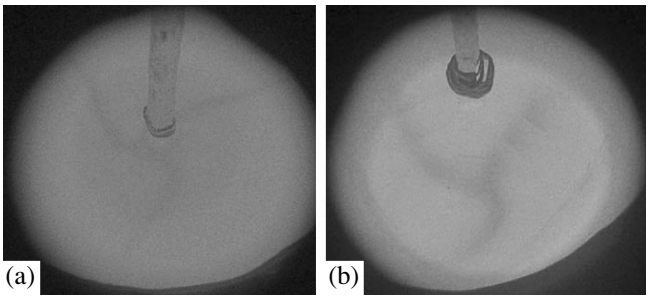

Fig. 3. Convective patterns observed on the free surface and through a growing BBO crystal in a thermal field with the symmetry (a) L_3 (crystal diameter ~40 mm) and (b) qL_3 (crystal diameter ~60 mm).

We also performed experiments on growth of BBO crystals in rotating thermal fields with the symmetry curlL_1 created by successive switching on of the heating elements, e.g., in the sequence 1–2–3 ⟶ 4–5–6 ⟶ 7–8–9 ⟶ …, i.e., by successive one-sided heating of the crucible. In this case, seeding was implemented by touching the flux surface with a seed at the cold point located in the crucible center at a small period of rotation of a thermal field (up to several dozen seconds). In this case, the symmetry of the thermal field remained close to L_∞. Growth was performed without mechanical rotation of a growing crystal. With an increase in the crystal size, the rotation period of the thermal field also increased. The thermal field gradually lost the axial symmetry, L_∞ ⟶ curlL_1, so that it was possible to observe through the growing crystal the displacement of the cold point from the center along the helical trajectory (Fig. 1d). Up to now, the best results have been obtained in growth of BBO crystals in a thermal field with the symmetry curlL_1 and the rotation period 60–75 min. One of the crystals thus grown is shown in Fig. 5; its characteristics are indicated in the table. The top view of the crystal having the shape of a circular disk indicates that the efficiency of the action of a rotating thermal field onto the crystal formation is comparable with the efficiency of the mechanical rotation of the crystal. The axial section shows the formation of a rather large capture cone in the middle region of the crystal, which indicates the appearance and development of the concentration supercooling at the crystallization front. Despite this, the peripheral regions of the crystal are characterized by rather high optical quality.

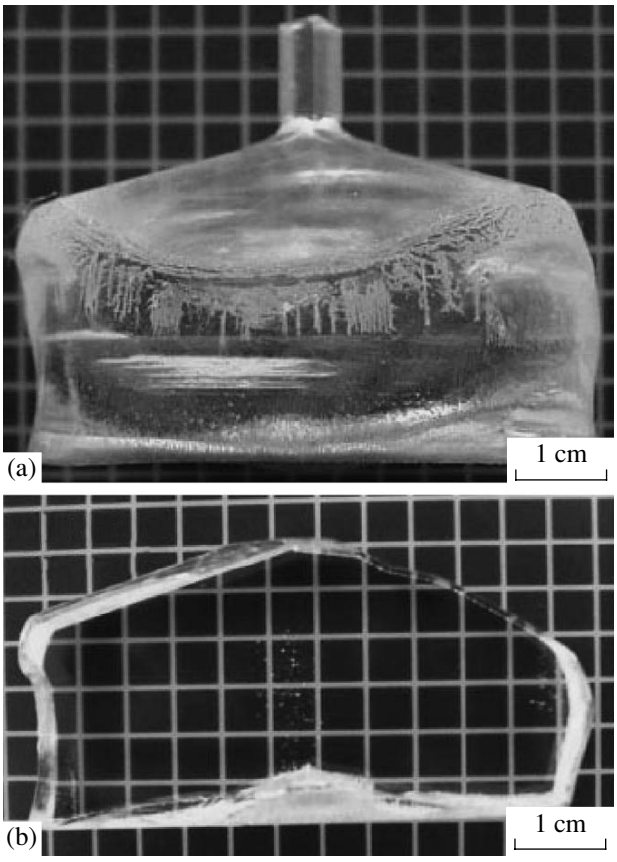

Fig. 4. (a) Side view and (b) axial section of a 16-mm-thick plate cut out from a BBO crystal grown in a thermal field with the symmetry qL_3.

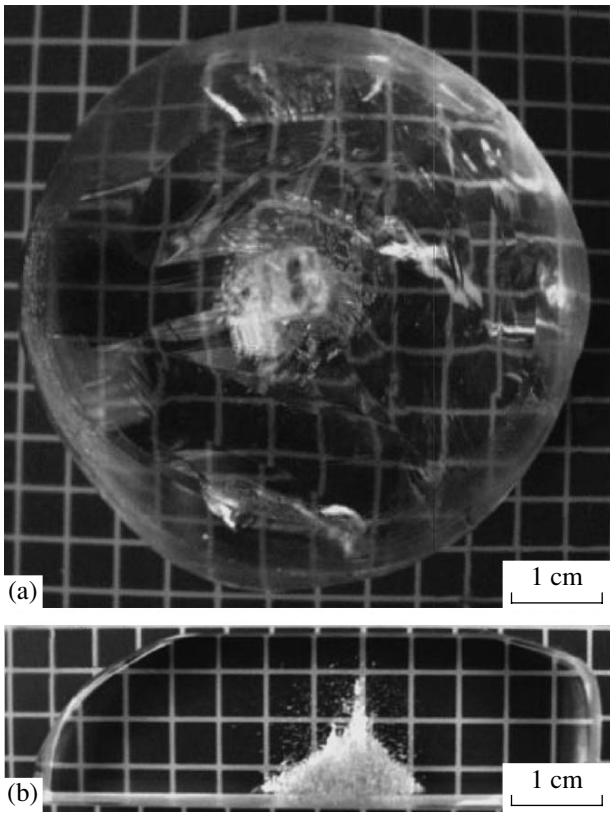

Fig. 5. (a) Top view and (b) axial section of a 20-mm-thick BBO crystal grown in a rotating thermal field with the symmetry curlL_1 without mechanical rotation of the crystal.

These crystals do not scatter a laser beam. This indicates that the stimulated temperature oscillations with the amplitude ~10–15°C at the crystal periphery and the crystallization front arising in a thermal field rotating with the period 60–75 min ensure growth of a single crystal of high structural quality.

CONCLUSIONS

Thus, it is shown that the use of the original approach to the heating concept, i.e., the change of the applied thermal-field symmetry and its rotation, allowed us to improve the growth technology of technically important barium borate crystals widely used in nonlinear optics. Obviously, the symmetry variants of stationary and rotating thermal fields considered do not exhaust all possible variants of the fields and, therefore, also do not exhaust all the possibilities provided by the new method.

REFERENCES

1. V. S. Zemskov and M. R. Raukhman, *Hydromechanics and Heat and Mass Exchange under Production of Materials* (Nauka, Moscow, 1990), p. 131 [in Russian].
2. T. Nakamura, T. Nishinaga, P. Ge, and C. Huo, J. Cryst. Growth **211**, 441 (2000).
3. Yu. I. Sirotin and M. P. Shaskol'skaya, *Fundamentals of Crystal Physics*, 2nd ed. (Nauka, Moscow, 1979; Mir, Moscow, 1982).
4. V. I. Polezhaev, O. A. Bessonov, N. V. Nikitin, and S. A. Nikitin, J. Cryst. Growth **230**, 40 (2001).
5. M. Iwamoto, M. Akamatsu, T. Nakao, and H. Ozoe, in *Abstracts of 1st Asian Conference on Crystal Growth and Crystal Technology* (Sendai, Japan, 2000), p. 370.
6. K.-W. Yi, V. B. Booker, M. Eguchi, *et al.*, J. Cryst. Growth **156**, 383 (1995).
7. D. Vizman, J. Friedrich, and G. Muller, in *Proceedings of Sixth International Conference on Advanced Computational Methods in Heat Transfer* (WIT Press, Southampton, 2000), p. 137.
8. I. Yu. Evstratov, V. V. Kalaev, A. I. Zhmakin, *et al.*, J. Cryst. Growth **230**, 22 (2001).
9. B. Basu, S. Enger, M. Breuer, and F. Durst, J. Cryst. Growth **230**, 148 (2001).
10. I. Baumann, J. Cryst. Growth **144**, 193 (1994).
11. Q. Xiao and J. J. Derby, J. Cryst. Growth **152**, 169 (1995).
12. M. Watanabe, M. Eguchi, K. Kakimoto, *et al.*, J. Cryst. Growth **151**, 285 (1995).
13. L. S. Milevskiĭ, Kristallografiya **6** (2), 249 (1961) [Sov. Phys. Crystallogr. **6**, 193 (1961)].
14. K. Morisane, A. Vitt, and H. Gates, *Distribution of Impurities in Single Crystals* (Mir, Moscow, 1968).
15. A. I. Landau, Fiz. Met. Metalloved. **6** (1), 148 (1985).
16. T. Jung and G. Muller, J. Cryst. Growth **171**, 373 (1997).
17. V. G. Kosushkin, in *Proceedings of Fourth International Conference on Single Crystal Growth and Heat and Mass Transfer* (Inst. of Physics and Power Engineering, Obninsk, 2001), Vol. 2, p. 395.
18. V. G. Kosushkin, B. G. Zakharov, Yu. A. Serebryakov, and S. A. Nikitin, in *Proceedings of II All-Russian Symposium on Processes of Heat and Mass Transfer and Growth of Single Crystals and Thin-Film Structures* (GNTs FÉEI, Obninsk, 1997), p. 232.
19. A. E. Kokh, Doctoral Dissertation in Engineering (Inst. of General Physics, Russian Academy of Sciences, Moscow, 2003).
20. A. E. Kokh, V. E. Kokh, and N. G. Kononova, Prib. Tekh. Éksp., No. 1, 157 (2000) [Instrum. Exp. Tech. **43**, 145 (2000)].
21. A. E. Kokh, A. S. Vakulenko, and V. E. Kokh, Prib. Tekh. Éksp., No. 6, 136 (2000) [Instrum. Exp. Tech. **43**, 852 (2000)].
22. A. E. Kokh, V. N. Popov, and P. W. Mokrushnikov, J. Cryst. Growth **230**, 155 (2001).
23. R. S. Feigelson, R. J. Raymakers, and R. K. Route, J. Cryst. Growth **97**, 352 (1989).
24. D. Y. Tang, W. R. Zeng, and Q. L. Zhao, J. Cryst. Growth **123**, 445 (1992).
25. W. Chen, A. Jiang, and G. Wang, J. Cryst. Growth **256**, 383 (2003).
26. P. P. Fedorov, A. E. Kokh, and N. G. Kononova, Usp. Khim. **71** (8), 741 (2002).
27. S. Nakamura, M. Eguchi, T. Azami, and T. Hibiya, J. Cryst. Growth **207**, 55 (1999).
28. A. E. Kokh, N. G. Kononova, and P. W. Mokruchnikov, J. Cryst. Growth **216**, 359 (2000).
29. M. P. Shaskol'skaya, *Crystallography* (Vysshaya Shkola, Moscow, 1976) [in Russian].
30. R. Laudise and R. Parker, *The Growth of Single Crystals; Crystal Growth Mechanisms: Energetics, Kinematics and Transport* (Prentice Hall, New York, 1970; Mir, Moscow, 1974).
31. P. P. Fedorov, N. G. Kononova, A. E. Kokh, *et al.*, Zh. Neorg. Khim. **47** (7), 1150 (2002).
32. A. E. Kokh, N. G. Kononova, P. P. Fedorov, *et al.*, Kristallografiya **47** (4), 616 (2002) [Crystallogr. Rep. **47**, 559 (2002)].

Translated by L. Man

Crystallography Reports, Vol. 50, No. 1, 2005, pp. 20–26. From Kristallografiya, Vol. 50, No. 1, 2005, pp. 27–33.

DIFFRACTION AND SCATTERING OF IONIZING RADIATION

Indications of the Magnetic State in the Charge Distributions of MnO, CoO, and NiO. III: Antiferromagnetism of NiO[1]

J. -P. Vidal*, G. Vidal-Valat*, and K. Kurki-Suonio**

** Laboratoire d'Analyse Multipolaire des Répartitions de Charges Expérimentales, Université Montpellier 2, 34095 Montpellier Cedex 05, France*

e-mail: jpgvidal@univ-montp2.fr

*** Department of Physics, University of Helsinki, P.O. Box 64, FIN-00014, Finland*

Received July 2, 2002

Abstract—X-ray diffraction intensities were measured from antiferromagnetic NiO. The data were submitted to a nonparametric multipole analysis aimed at formulation of experimentally valid statements on the nature of charge distribution. Strong "bonding maxima" appear between the Ni⟨100⟩O nearest neighbors in the region of the oxygen atoms involving NiO coupling. An electronic cage structure is also observed. This is parallel to the observations on MnO and CoO but different in nature, being formed by separate cubic cages for the cations instead of the oxygen, and without a clear indication of an extended network buildup. *© 2005 Pleiades Publishing, Inc.*

INTRODUCTION

This is the third part of an investigation aiming at finding characteristics of the different magnetic states of the first-row transition metal monoxides MnO, CoO, and NiO with help of a multipolar interpretation of their charge densities on the basis of accurate X-ray diffraction data. This paper reports the study of NiO at 298 K, where it is antiferromagnetic and weakly covalent.

The background of the investigation has been discussed in detail in the preceding papers concerning MnO and CoO [1, 2]. In addition, only in paper [3] was there any mention of the periodic Hartree–Fock method

[1] This article was submitted by the authors in English.

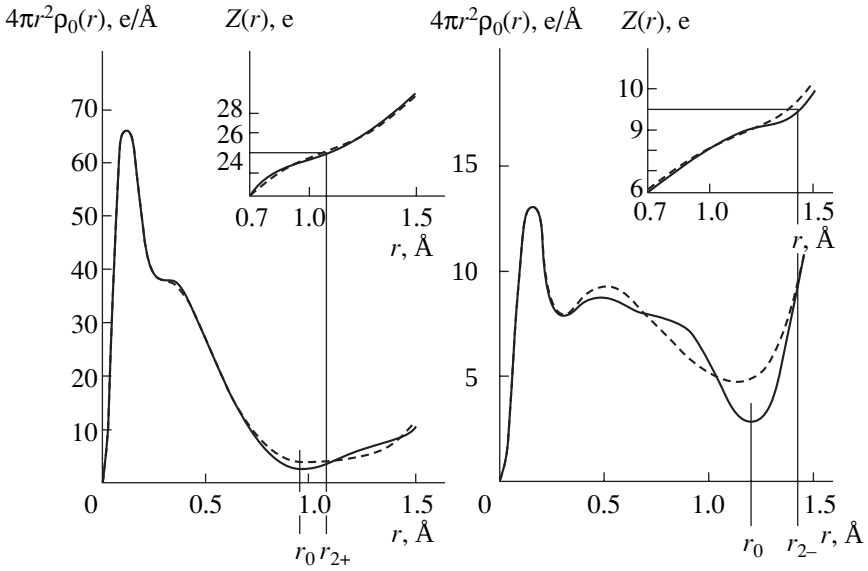

Fig. 1. Radial accumulation-of-charge densities $s_0(r)$ and electron counts $Z_0(r)$ around the ionic sites in the antiferromagnetic state of NiO at 298 K: experimental (solid lines), and reference model (dashed lines). The radii r_0 of "best separation," or minimum s_0, and the radii r_{2+} and r_{2-}, where the electron counts that correspond to double ionization of the ions are indicated for the experimental curves.

1063-7745/05/5001-0020$26.00 © 2005 Pleiades Publishing, Inc.

for calculation of electronic and magnetic properties of NiO. Description in terms of Mulliken charges yields, for example, values for net charges and bond populations. These parameters, tied by definition to the theoretical basis sets, are, however, not directly comparable with our results representing the integral properties of the experimental charge density or their deviations from the most simple charge-density model.

Preparation of the NiO sample and experimental procedures, as well as treatment of data, were identical with those applied in the investigation of CoO [2]. Therefore, only the details which are specific to NiO are presented.

EXPERIMENTAL PROCEDURES

A single crystal of NiO of full stoichiometry was kindly provided by the Laboratoire de Chimie des Solides, Université d'Orsay, France. It was synthesized by float-zone refining techniques from high-purity powder 5N. The crystal was cleaved several times parallel to the (001) crystal faces. It was hard and, when sufficiently thin, optically fully transparent with a glittering emerald green color. The surface of cleavage was seen to be perfectly smooth. The sample chosen for the X-ray diffraction measurements was a parallelepiped of size $0.140 \times 0.166 \times 0.191$ mm^3.

An accurate X-ray diffraction study was carried out for the antiferromagnetic phase at 298 K, which is well below the Néel temperature.

No antiferromagnetic distortion from the NaCl-type structure could be detected. So, the NiO crystal attained a face-centered cubic structure of the symmetry group $Fm\bar{3}m$. Least-squares refinement based on the X-ray diffraction pattern yielded a lattice constant of 4.169(2) Å.

Background, Lorentz, and polarization corrections were made for the intensities, as described by [4], as well as the absorption corrections of Busing and Levy [5] using a linear absorption factor of 25.266 mm^{-1}.

The TDS contaminations were evaluated with the program described in [6] using the elastic constants from [7]. These effects were small, less than 3% in intensity, owing to the hardness of the compound.

TREATMENT OF DATA

The data were submitted to the "direct multipole analysis" as described in the papers I and II on MnO and CoO, respectively. All that is said about the analysis in the context of the reference model and of the representation of results holds, even in detail, except for data referring specifically to the Ni atom and to the numerical values used or obtained, and will not be repeated here.

Table 1. Structure factors for NiO at 298 K

hkl	$2\sin\theta/\lambda$, Å^{-1}	F_0	F_c	δF_0	*y*
000	0.0000		144.000		
111	0.4155	64.5542	64.0979	0.3000	0.814
200	0.4797	101.3563	101.7546	0.3600	0.671
220	0.6784	81.6294	81.0661	0.2800	0.846
311	0.7955	49.0912	48.8074	0.2000	0.947
222	0.8309	67.8186	67.9548	0.2200	0.894
400	0.9595	57.9203	58.7623	0.2800	0.948
331	1.0455	38.8308	37.8826	0.1600	0.975
420	1.0727	51.7354	51.9476	0.1800	0.963
422	1.1751	47.0126	46.7107	0.0800	0.967
333	1.2474	31.2755	30.8269	0.1200	0.985
511	1.2464	30.0476	30.8269	0.1000	0.988
440	1.3569	38.7198	39.2371	0.1500	0.985
531	1.4191	25.5984	26.1219	0.1000	0.992
442	1.4391	35.7992	36.4847	0.1600	0.984
600	1.4391	37.2116	36.4847	0.1500	0.981
620	1.5170	34.1881	34.1735	0.1200	0.986
533	1.5729	22.4179	22.8432	0.0800	0.994
622	1.5911	31.6273	32.1993	0.1300	0.988
444	1.6618	31.0151	30.4865	0.1600	0.987
551	1.7130	20.1959	20.4434	0.0800	0.996
711	1.7130	20.8307	20.4434	0.0800	0.995
640	1.7297	29.1224	28.9795	0.1000	0.992
642	1.7950	27.5818	27.6368	0.1100	0.993
553	1.8424	18.9250	18.5985	0.0800	0.996
731	1.8424	18.8033	18.5985	0.0800	0.996
800	1.9189	25.4622	25.3260	0.1100	0.994

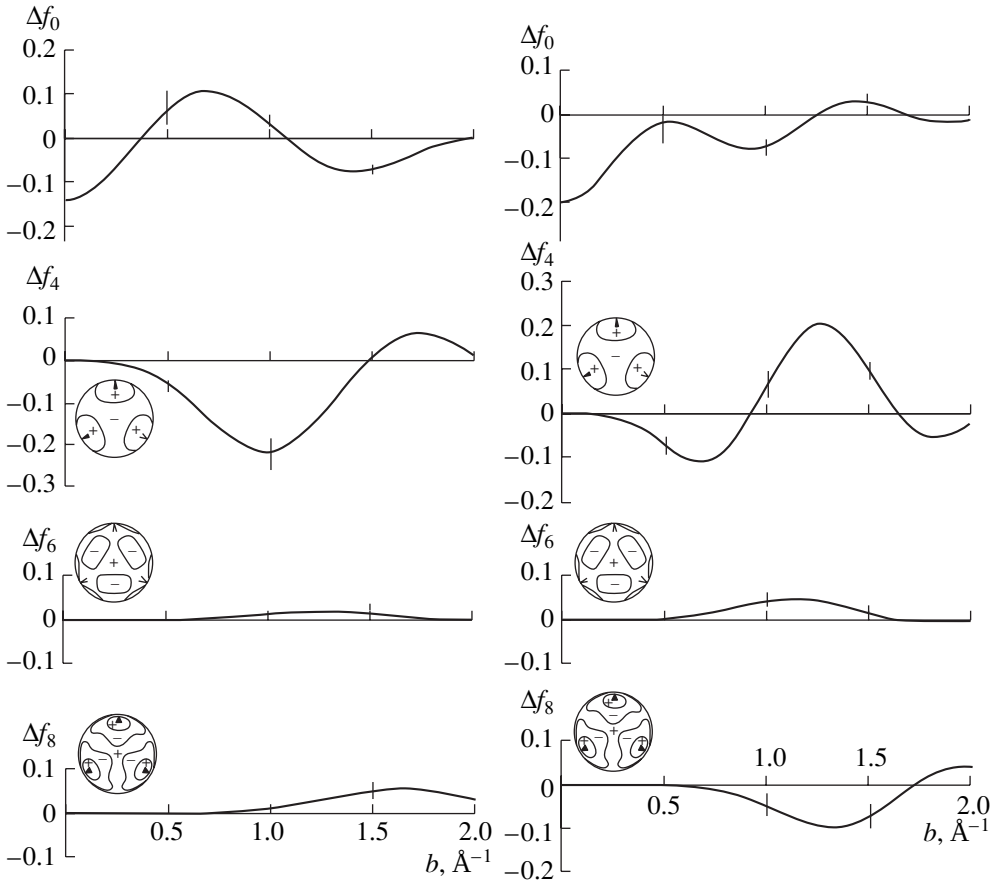

Fig. 2. Radial multipolar scattering factors of the ions in the antiferromagnetic state of NiO at 298 K for Ni^{2+} and O^{2-} within the partitioning radii R_{Ni} = 1.05 Å and R_O = 1.30 Å. The results refer to cubic harmonics normalized to the maximum value $K_n(\theta, \varphi)$ = 1, and the curves represent deviations Δf_n from the reference model.

For the Ni^{2+} ion of the reference model, the relativistic Hartree–Fock values of the International Tables for Crystallography [8] were used with the anomalous scattering factors f' = 0.285 and f'' = 1.113 from [9] for MoK_α.

Table 2. Spherical characteristics of the ionic electron distributions: radius r_0 of best separation at which the radial accumulation-of-charge density $s_0(r)$ reaches its minimum; the minimum radial density $s_{0\,min} = s_0(r_0)$; the electron count $Z_0 = Z_0(r_0)$ within the radius of best separation; and the radii r_{2+} and r_{2-}, where the electron counts reach the values 26 e and 10 e corresponding to the doubly ionized states

Ni^{2+}	r_0, Å	s_{0min}, e/Å	Z_0, e	r_{2+}, Å
Experimental 298 K	0.95	3.317	25.64	1.07
Reference model 298 K	1.05	4.031	26.09	1.03
O^{2-}	r_0, Å	s_{0min}, e/Å	Z_0, e	r_{2-}, Å
Experimental 298 K	1.20	2.775	8.97	1.43
Reference model 298 K	1.15	4.766	8.74	1.37

For NiO, the isotropic mosaic-spread extinction gave a lower R factor, 0.006, than the particle-size extinction, 0.007, and yielded the value $g = 0.040(2) \times 10^4$ rad^{-1} for the mosaic spread parameter and values B_{Ni} = 0.316 (0.016) Å^2 and B_O = 0.426 (0.047) Å^2 for the isotropic Debye–Waller factors. No additional significant improvement was obtained by any of the more sophisticated models.

In the successive iterative local Fourier-refinement of the scale and Debye–Waller factors, the scale factors remained unchanged, while B_{Ni} = 0.313 Å^2 and B_O = 0.420 Å^2 were obtained as the final refined values of the Debye–Waller factors of the reference model.

The results are represented by figures and tables in correspondence with the studies on MnO and CoO.

Colored versions of Fig. 5 are available at the Internet address http://bus.cines.fr/vidaljp/mag3D.

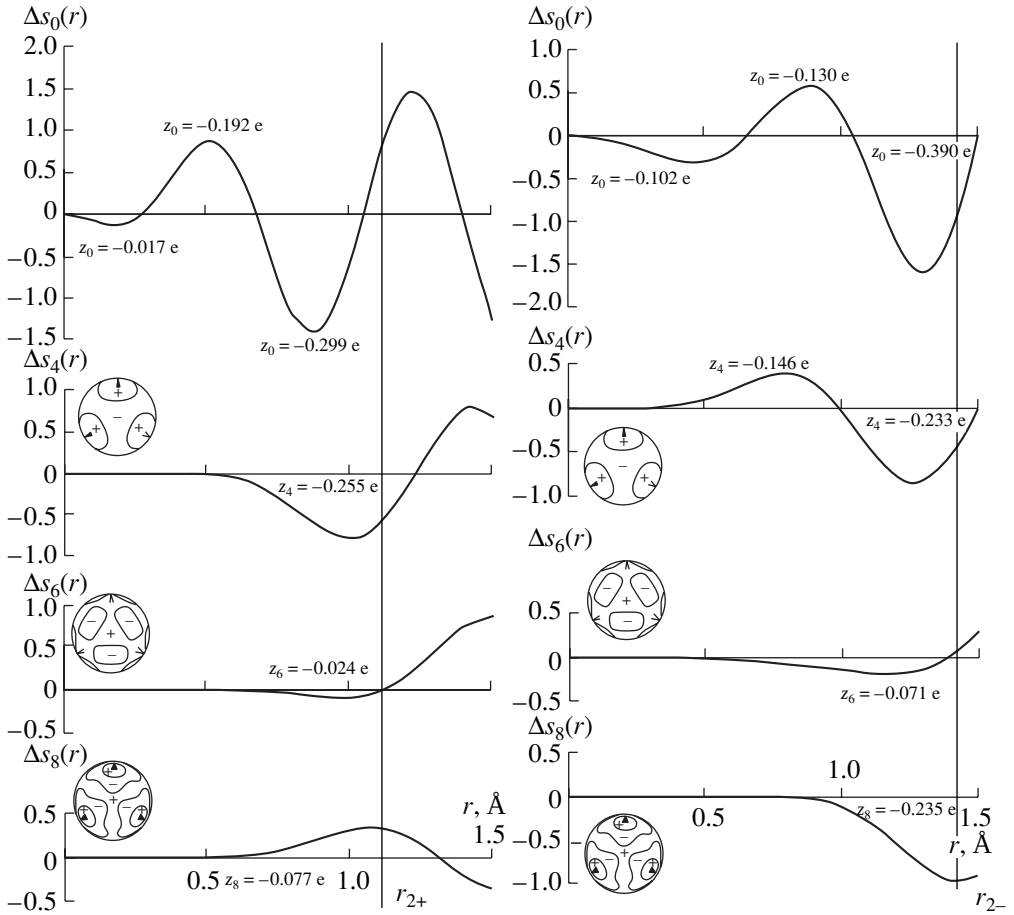

Fig. 3. Multipolar accumulation-of-charge densities $s_n(r)$ around the ionic sites in the antiferromagnetic state of NiO at 298 K for Ni^{2+} and O^{2-}. The curves represent deviations Δs_n from the reference model.

DISCUSSION

The radial density $s_0(r)$ of the oxygen in Fig. 1 has a clear resemblance to the oxygen in CoO. There is a "bump" similar to the intermediate maximum observed in CoO with a corresponding reduction of density at lower *r*. In NiO, this feature, however, clearly belongs to the main peak of oxygen and does not cause any ambiguity of the radius of best separation. According to the minimum value of $s_0(r)$, the separation of the oxygen from its surroundings is as good as in the paramagnetic MnO. The electron count of the oxygen peak is now the "normal" 9 e as in MnO, in accordance with the earlier observations on oxide peaks [10, 11].

The separating minimum of the cation is deeper and sharper than in the reference model, as in CoO and in the antiferromagnetic MnO. The shape of the minimum is even sharper and leads to a well-defined radius of best separation, although the minimum density $s_0(r_0)$ in NiO is essentially larger than in the antiferromagnetic CoO and about the same as in the antiferromagnetic MnO. The electron count of the peak is close to 26 e and corresponds to the doubly ionized state Ni^{2+}. The value $s_0(r_0)$ is, however, remarkably higher than one would expect for an ion [4, 10].

The density maps in Fig. 4 form the final tool of the analysis. In the map representations, the only significant features are those which are significant in the angular-integral representation in Fig. 3. Thus, no notice needs to be paid to the different densities at the ionic centers in any of the maps. Similarly, any local features of the Fourier maps that do not appear in the multipolar maps in Fig. 4 do not arise from the integral systematics of the low-order multipoles and must be regarded insignificant. Comparison with the multipolar maps makes it possible to determine how features in the Fourier maps originate from the different atoms [12].

Features denoted by *A*, *B*, and *C* in the maps and in Fig. 5 deserve to be discussed. These notations indicate correspondences with features of the CoO density maps, which are labeled similarly.

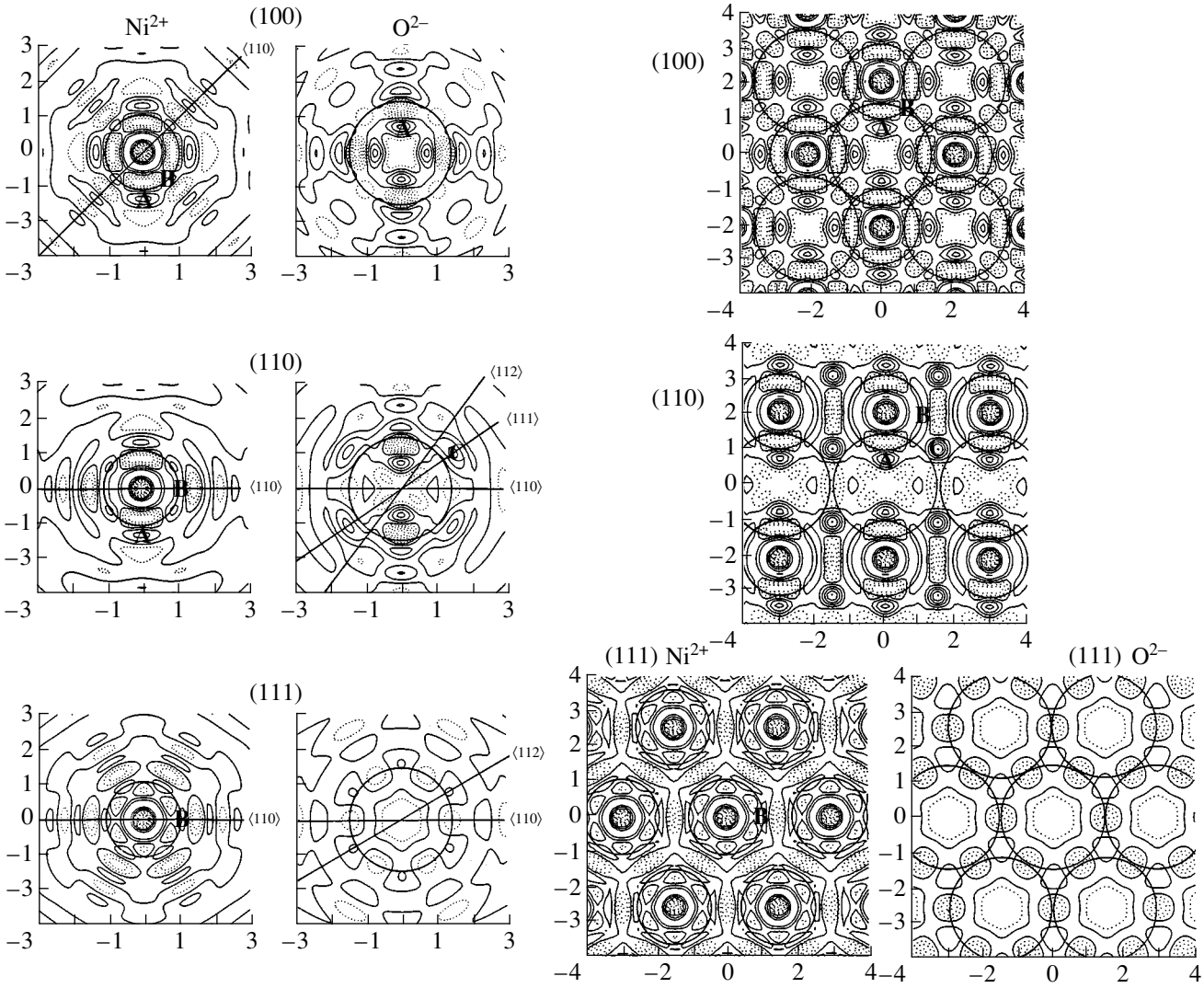

Fig. 4. Difference density maps of the multipole expansions up to $n = 8$, together with the corresponding Fourier difference-density maps on the lattice planes (100), (110), and (111), that pass through the ionic sites in the antiferromagnetic state of NiO at 298 K. The circles indicate the radii of doubly ionized ions. Solid lines indicate positive values; dashed lines, negative values; and dotted lines, zero values.

Feature A, with density maxima between the nearest neighbors O⟨100⟩Ni, looks much like covalent metal–oxygen bonding as in CoO. It is well within the oxygen area, unlike in CoO, where it is in the cation region. Still, we note from the multipolar maps that, as in the antiferromagnetic CoO, these maxima belong to the three-dimensional integral behavior of both ions. It should, thus, be interpreted as a result of an O⟨100⟩Ni coupling; this may be an indication of a superexchange effect.

The "bump" in the radial density $s_0(r)$ of oxygen in Fig. 1 has, thus, a different origin than the similar-looking intermediate maxima in CoO. This is caused by "bonding feature" A, whereas in CoO the maxima were related to the electronic-cage formation around the oxygen by the "B feature" that also caused the localization of the outer electrons of the O^{2-} ions.

Additionally, an electronic-cage structure appears here that is formed by the B-feature. While each oxygen atom had an octahedral cage of its own in the paramagnetic CoO, there is a cubic cage surrounding each Ni atom of the antiferromagnetic NiO, as shown in Fig. 5. According to the multipolar maps, this is strictly a feature of Ni without any significant coupling to the other features.

Feature C is visible in the (110) Fourier map as strong local maxima between the O⟨111⟩Ni neighbors. In the multipolar maps, it is present in the (110) oxygen map, but only as a much weaker effect. Therefore, it is strictly a feature of oxygen with somewhat questionable significance, like the corresponding features in

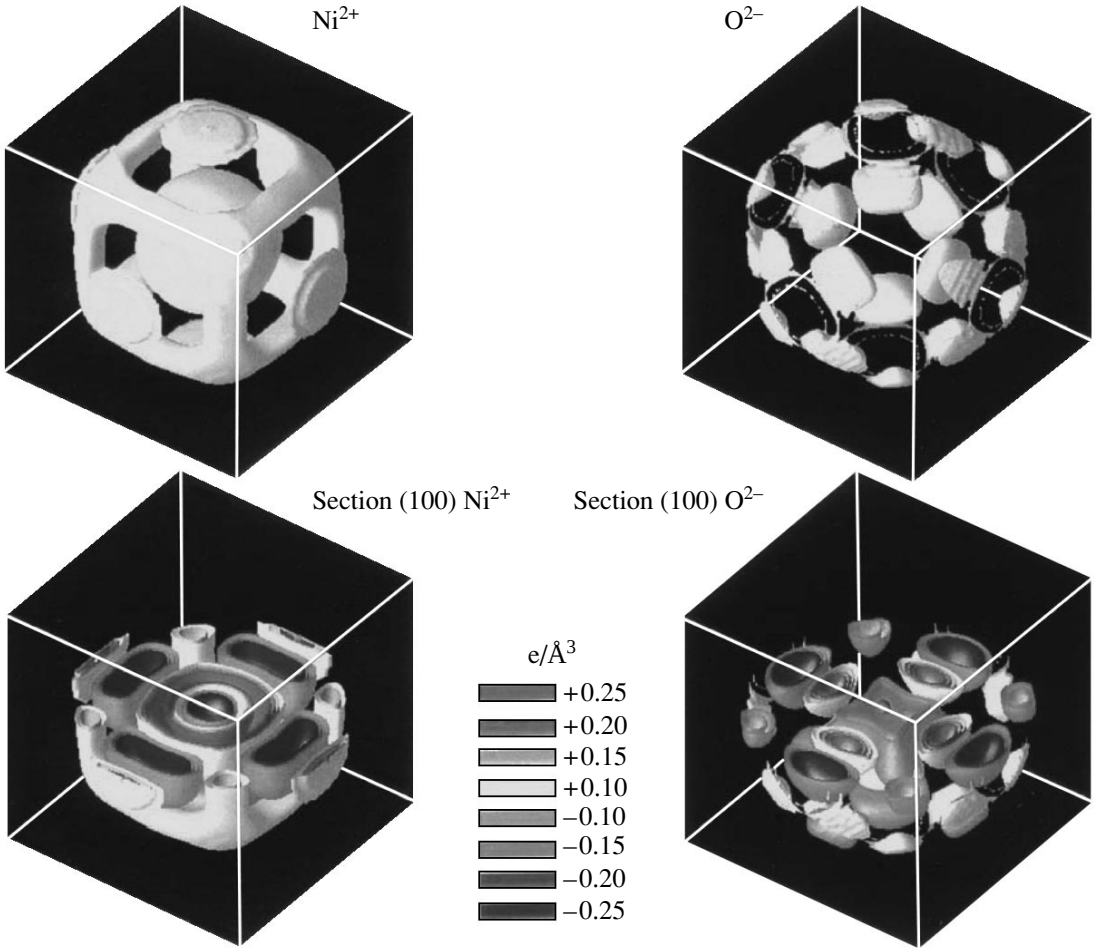

Fig. 5. Three-dimensional view on the equivalue surfaces of the ionic multipole expansions in the antiferromagnetic state of NiO at 298 K. For the color version of this figure, see http://bus.cines.fr/vidaljp/mag3D.

MnO, while in CoO it was interpreted to be an indication of electronic O⟨111⟩Co coupling. The C-maxima are also well separated from the other features both in the Fourier maps and in the multipolar maps. There is, thus, no clear indication of an extended network buildup, which is contrary to CoO, where the net buildup was quite strong, particularly in the antiferromagnetic state.

The problem of estimating the significance of such features in real space as revealed by the present method of analysis, in comparison with the accuracies obtained for the model parameters in the traditional fitting methods, has been discussed by [12]. While the significance or insignificance is merely due to the accuracy of measured data, it is expressed only by the errors bars in $\Delta f_n(b)$, reflecting the large-scale integral nature of the information, and cannot be transformed into local accuracy statements. Local features can be regarded significant to the relative extent expressed by the error bars as far as they are parts of the integral multipolar behavior.

ACKNOWLEDGMENTS

We thank the CINES, Centre Informatique National de l'Enseignement Supérieur (Montpellier, France), for financial support and technical assistance.

REFERENCES

1. J.-P. Vidal, G. Vidal-Valat, K. Kurki-Suonio, and R. Kurki-Suonio, Kristallografiya **47** (3), 391 (2002) [Crystallogr. Rep. **47**, 347 (2002)].
2. J.-P. Vidal, G. Vidal-Valat, K. Kurki-Suonio, and R. Kurki-Suonio, Kristallografiya **49** (3), 422 (2004) [Crystallogr. Rep. **49**, 357 (2004)].
3. R. Dovesi, R. Orlando, C. Roetti, *et al.*, Phys. Status Solidi B **217**, 63 (2000).

4. J.-P. Vidal, G. Vidal-Valat, M. Galtier, and K. Kurki-Suonio, Acta Crystallogr., Sect. A: Cryst. Phys., Diffr., Theor. Gen. Crystallogr. **37**, 826 (1981).
5. W. R. Busing and H. A. Levy, Acta Crystallogr. **10**, 180 (1957).
6. M. Merisalo and J. Kurittu, J. Appl. Crystallogr. **1**, 179 (1978).
7. K. G. Subhadra and D. B. Sirdeshmukh, Indian J. Pure Appl. Phys. **16**, 693 (1978).
8. *International Tables for X-ray Crystallography* (Kluwer Academic, Dordrecht, 1999), Vol. C.
9. D. T. Cromer and D. Liberman, J. Chem. Phys. **53**, 1891 (1970).
10. G. Vidal-Valat, J.-P. Vidal, and K. Kurki-Suonio, Acta Crystallogr., Sect. A: Cryst. Phys., Diffr., Theor. Gen. Crystallogr. **34**, 594 (1978).
11. G. Vadal-Valat, J.-P. Vidal, K. Kurki-Suonio, and R. Kurki-Suonio, Acta Crystallogr., Sect. A: Cryst. Phys., Diffr., Theor. Gen. Crystallogr. **43**, 540 (1987).
12. K. Kurki-Suonio, in *Proceedings of Symposium Franco–Finlandais: Structure de la Matiere, Repartitions Electroniques dans les Cristaux, Paris, 1993*, Ed. by J.-P. Vidal (Montpellier, 1994), p. F1; in *Structural Studies of Crystals: Honour of the 75th Anniversary of Academician Boris Vaĭnshteĭn*, Ed. by V. Simonov (Nauka, Moscow, 1996), pp. 46–64 [in Russian].

Crystallography Reports, Vol. 50, No. 1, 2005, pp. 27–30. Translated from Kristallografiya, Vol. 50, No. 1, 2005, pp. 34–37.

DIFFRACTION AND SCATTERING OF IONIZING RADIATION

Electron Density Distribution in Crystals with Potassium Perchlorate Structure

Yu. N. Zhuravlev and A. S. Poplavnoĭ

Kemerovo State University, ul. Krasnaya 6, Kemerovo, 650043 Russia

e-mail: zhur@kemsu.ru

Received June 19, 2003

Abstract—Within the theory of local electron density functional, the difference densities in crystals of perchlorates, perbromates, and sulfates of metals with potassium perchlorate structure are calculated by the sublattice method. It is shown that the difference-density distribution qualitatively coincides with the experimental deformation-density distribution. Oxygen atoms in nonequivalent crystallographic positions exhibit a different character of electron charge redistribution, which results in their different charge states and different forces of chemical bonding in molecular anions. The mechanisms of charge redistribution in sulfates differ qualitatively from those for perchlorates. © *2005 Pleiades Publishing, Inc.*

INTRODUCTION

In our previous studies [1, 2], we developed a sublattice method for investigating the chemical bonds in predominantly ionic and ionic-molecular crystals. Calculations of the difference densities for sodium nitrate [2], sodium and silver nitrites [3], magnesium and calcium carbonates [4], and dolomite [5] showed qualitative agreement with experimentally determined deformation-density maps. The main features of these density distributions are the presence of charge maxima on the bond lines *A*–O (*A* = C, N) (the bonding maximum) and behind the oxygen atoms, located symmetrically with respect to the bond lines (pair maxima, determining the charge state and chemical activity). At the atomic positions, the density is negative (in elementary charge units e). The distributions are anisotropic and different for crystals with calcite and sodium nitrite structures. In the case of calcite structure, the density maxima are isolated, whereas for crystals with sodium nitrite structure a bonding maximum is linked to one of the pair maxima by common lines of rather high density. In dolomite crystals, the pair maxima are asymmetric, which is due to the different polarizing action of magnesium and calcium cations.

In the crystals investigated in [2–5], oxygen atoms occupy equivalent crystallographic positions. Accordingly, the *A*–O bond forces in the molecular anion AO_n^{m-} are equal. It is of interest to investigate the features of the formation of electron density and chemical bonds in compounds with nonequivalent oxygen sublattices. Convenient objects of investigation are compounds with potassium perchlorate structure, because (i) a series of such compounds exists and (ii) the deformation-density maps of $KClO_4$ were determined experimentally [6] and, thus, can be used for comparison with the results of theoretical calculations.

$KClO_4$ has an orthorhombic lattice with the sp. gr. D_{2h}^{16} and four formula units in the unit cell [7]. Oxygen and chlorine atoms form a tetrahedron, in which the bond lengths are nonequivalent: $Cl–O_1$ = 1.423 Å, $Cl–O_2$ = 1.431 Å, and $Cl–O_{3,4}$ = 1.444 Å. In $MClO_4$ (*M* = Rb, Cs), the bond lengths change weakly with an increase in the atomic number of the cation, whereas the *M*–O bond length increases significantly [8]. $TlBrO_4$ [9] and M_2SO_4 (*M* = K, Rb, Cs) [10] have a similar structure.

METHOD OF STUDY

In the sublattice method, the difference density is calculated, which is defined as the difference between the crystal valence density and the sublattice density. The sublattices are formed of atoms bonded with each other by the symmetry elements of the space group of the crystal; they are electrically neutral. The structural parameters in all cases are set according to the real geometric structure. It follows from the condition of normalization of electron density to the number of electrons that the integral of the difference density over the unit cell is equal to zero and, therefore, the maps $\Delta\rho(\mathbf{r})$ contain regions with both positive and negative densities, which visualizes the charge redistribution between the sublattices. Thus, the difference density contains the most important information about the mechanism of the formation of chemical bonds in crystals, determining the role of each sublattice in this process.

The electron density is calculated within the theory of the local electron density functional using nonlocal BSH pseudopotentials and a basis of numerical sp^3d^5

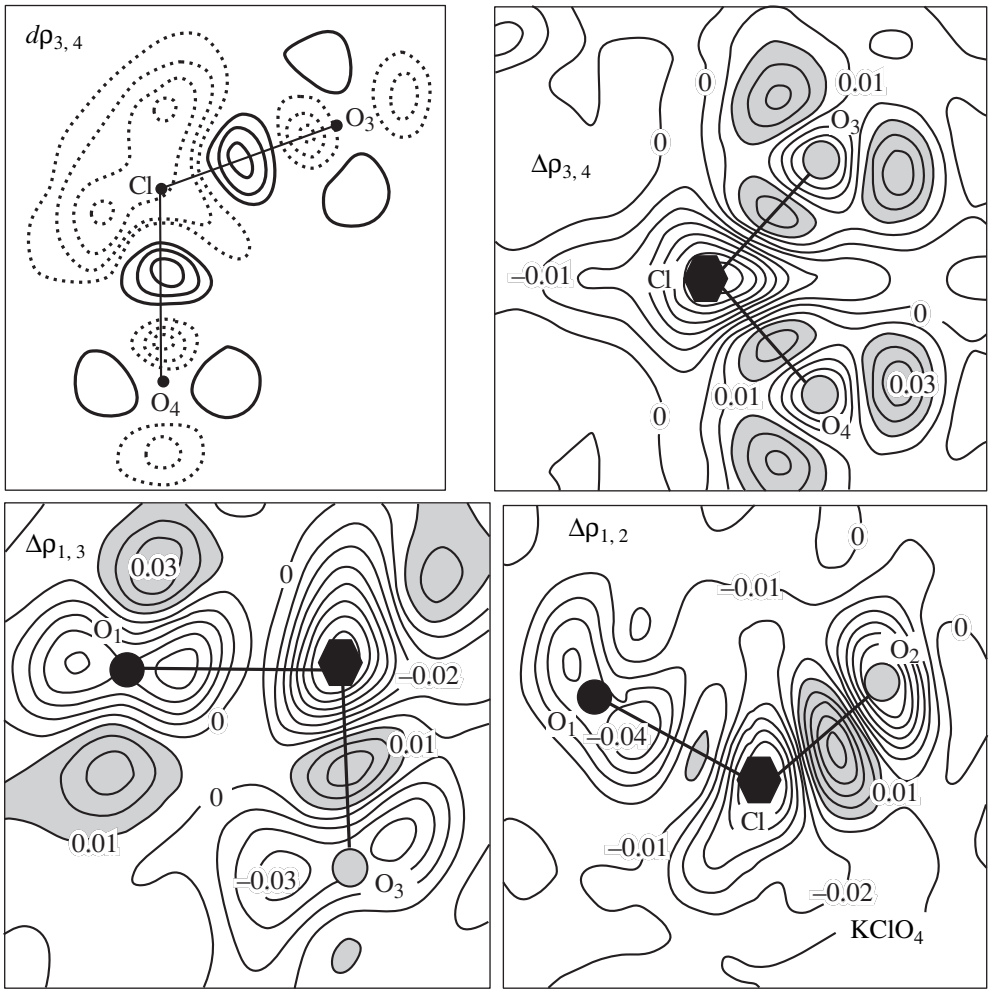

Fig. 1. Distributions of the experimental deformation $d\rho$ [6] and difference $\Delta\rho$ densities in $KClO_4$. Oxygen atoms are enumerated in accordance with their positions in the anion.

pseudoorbitals. These were obtained by solving the Schrödinger equation with the same pseudopotentials. The occupation numbers were varied so as to obtain a diagram of atomic energy levels similar to the experimentally observed one. The details of the numerical implementation of the method were reported in [11].

RESULTS AND DISCUSSION

Figure 1 shows the difference-density distributions in the plane with equivalent ($\Delta\rho_{3,4}$) and nonequivalent ($\Delta\rho_{1,3}$, $\Delta\rho_{1,2}$) oxygen atoms and the deformation-density distribution $d\rho_{3,4}$ (to compare theory with experiment) [6] for $KClO_4$. The values of densities are given in units of e Å^{-3}. The regions of positive values of $\Delta\rho$ are shaded gray. Negative values of the deformation density are indicated by dotted lines.

The experimental deformation-density maps in the O_3–Cl–O_4 plane exhibit bonding maxima on the bond lines (0.3 e Å^{-3}) and pair maxima behind oxygen atoms (0.1 e Å^{-3}). The deformation density is negative in a fairly large area near the position of the chlorine atom and areas corresponding to the p_σ orbitals of the oxygen atoms. The deformation density is distributed similarly in magnesium and calcium carbonates [12]. In view of the nonequivalence of the crystallographic positions of oxygen atoms in $KClO_4$, the deformation-density distributions are different in other planes containing chlorine and oxygen atoms. For example, in the O_2–Cl–O_3 plane, the deformation-density distribution is similar to that in Fig. 1, but the pair maxima differ both in shape and magnitude; in the O_1–Cl–O_2 plane, the deformation-density distribution is similar to that for $NaNO_2$ [13].

Let us now consider the difference density. As can be seen from Fig. 1, the most characteristic features of the difference and deformation densities are the same. The difference density is negative near the atomic positions and beyond the anion. $\Delta\rho_{3,4}$ has maximum values at the midpoints of the bond lines Cl–$O_{3,4}$ and behind

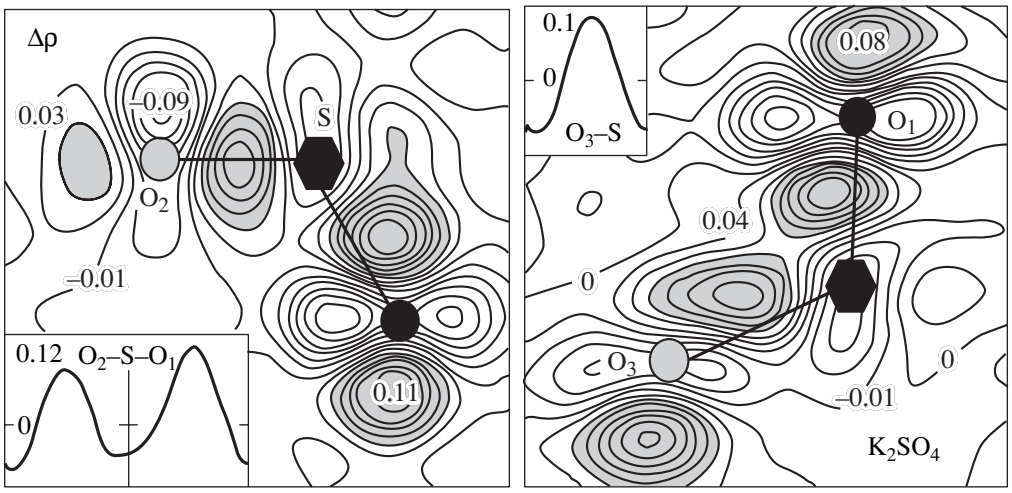

Fig. 2. Difference-density distributions in the O_2–S–O_1 and O_1–S–O_3 planes in K_2SO_4.

the oxygen atoms; the maxima are symmetric with respect to these lines. In view of the equivalence of the oxygen atoms $O_{3,4}$, the maximum values are equal to each other. The difference-density distribution in $MgCO_3$ is similar [4].

In the planes with nonequivalent oxygen atoms, the density distributions $\Delta\rho_{1,3}$ and $\Delta\rho_{1,2}$ are qualitatively different. This is especially true for the redistribution of electron charge near the $O_{1,2}$ atoms. It can be seen that in the vicinity of the O_1 atom the electron charge is transferred from the p_σ area to the p_π area. As a result of this redistribution, a covalent bond with a characteristic charge maximum at the midpoint is formed between the O_1 and Cl atoms. However, the maximum charge turns out to be not as large as for O_3 atoms, for which the charge transfer from the p_π area to the p_σ area occurs. A similar situation is realized in the O_1–Cl–O_2 plane, where the maximum at the Cl–O_2 bond takes the largest value and the pair maxima behind the oxygen atoms are the smallest. Thus, due to the hybridization of anion sublattices, the charge is nonuniformly redistributed to the bonding areas between the oxygen and chlorine atoms and pair areas behind the atoms. The result of this is the difference in the charge states of oxygen atoms and the forces of their chemical bonds with chlorine.

The difference-density distribution in other perchlorates is qualitatively similar to that in $KClO_4$. With an increase in the atomic number of the cation, the Cl–$O_{3,4}$ bond tends to weaken. In $TlBrO_4$, the shortest Br–O distance corresponds to the Br–$O_{3,4}$ bond. As a result, the difference-density maxima on the Br–O_1 and Br–O_2 bond lines are small and shifted closer to the Br atom. At the same time, the Br–$O_{3,4}$ bond is the strongest.

In K_2SO_4, in contrast to $KClO_4$, K atoms form two sublattices and O atoms form three sublattices: S–O_1 = 1.4727 Å, S–O_2 = 1.4675 Å, and S–$O_{3,4}$ = 1.4703 Å. The distance between oxygen atoms is shortest for the O_1–$O_{3,4}$ bond (2.3926 Å).

The difference-density distributions in the O_1–S–O_2 and O_1–S–O_3 planes are shown in Fig. 2. Here, the hybridization of the oxygen and sulfur sublattices leads to the charge transfer from the p_π area to the p_σ area for all oxygen atoms. As a result, difference-density maxima arise on the S–O bond lines (see inset in Fig. 2), which indicate that the chemical bond between these atoms is covalent. In this case, the maximum on the S–O_1 line is the largest. However, as for $O_{3,4}$ atoms, it is shifted from the line midpoint. Instead of pair maxima, charge transfer to the antibonding area behind oxygen atoms is observed in sulfates. It is possible that such a charge redistribution is responsible for different physicochemical properties of perchlorates and sulfates of alkali metals. The values of antibonding maxima are also different for nonequivalent oxygen atoms. Thus, the difference-density distributions show that the oxygen atoms in an anion are in different charge states and interact differently with the sulfur atom and with each other.

Comparison with potassium perchlorate shows that, due to the different character of electron redistribution, the maxima of $\Delta\rho$ on the anion bond lines are larger and the difference between nonequivalent oxygen atoms is much smaller in potassium sulphate. Different polarizing actions of nonequivalent cation sublattices facilitate the decrease in the degree of nonequivalence of the oxygen sublattices.

REFERENCES

1. Yu. N. Zhuravlev and A. S. Poplavnoĭ, Zh. Strukt. Khim. **42**, 860 (2001).

2. Yu. N. Zhuravlev and A. S. Poplavnoĭ, Zh. Strukt. Khim. **42**, 1056 (2001).
3. Yu. N. Zhuravlev and A. S. Poplavnoĭ, Kristallografiya **47**, 810 (2001) [Crystallogr. Rep. **47**, 744 (2001)].
4. Yu. N. Zhuravlev and A. S. Poplavnoĭ, Fiz. Tverd. Tela (St. Petersburg) **43**, 1984 (2001) [Phys. Solid State **43**, 2067 (2001)].
5. Yu. N. Zhuravlev and A. S. Poplavnoĭ, Zh. Strukt. Khim. **44**, 541 (2003).
6. J. W. Bats and H. H. Fuess, Acta Crystallogr., Sect. B: Struct. Crystallogr. Cryst. Chem. **38**, 2116 (1982).
7. Y. Sawada, Mater. Res. Bull. **28**, 867 (1993).
8. J. Granzin, Z. Kristallogr. **184**, 157 (1988).
9. J. C. Gallucci, R. E. Gerkin, and W. J. Reppart, Acta Crystallogr., Sect. C: Cryst. Struct. Commun. **45**, 701 (1989).
10. D. Liu, H. H. Lu, J. R. Hard, and F. G. Uliman, Phys. Rev. B **44**, 7387 (1991).
11. Yu. N. Zhuravlev, A. S. Poplavnoĭ, and Yu. M. Basalaev, Izv. Vyssh. Uchebn. Zaved., Fiz., No. 3, 96 (2000).
12. E. N. Maslen, V. A. Streltsov, and N. R. Streltsova, Acta Crystallogr., Sect. B: Struct. Sci. **51**, 929 (1995).
13. T. Gohda, M. Ichikawa, T. Guastafsson, and I. Olovsson, Acta Crystallogr., Sect. B: Struct. Sci. **56**, 11 (2000).

Translated by Yu. Sin'kov

Crystallography Reports, Vol. 50, No. 1, 2005, pp. 31–35. Translated from Kristallografiya, Vol. 50, No. 1, 2005, pp. 38–42.

DIFFRACTION AND SCATTERING OF IONIZING RADIATION

Numerical Separation of Background in X-ray Diffraction Studies

S. A. Suevalov and I. G. Kaplan

Ural State University, Yekaterinburg, Russia

e-mail: sergey.suevalov@usu.ru

Received December 25, 2002

Abstract—A method for the separation of X-ray background is suggested. The method is based on the integral digital filtration of experimental diffraction patterns and their "smoothening" and the subsequent combination of the smoothened and initial diffraction patterns. The combined diffraction pattern thus obtained is smoothened again, and the whole procedure is repeated anew. The criterion for concluding the iteration procedure (background criterion) is suggested to be the attainment of the situation where a certain percent of the points of the initial diffraction pattern would be below the background line determined. It is shown that, in some instances, the method yields more appropriate results than the traditional methods. The application of the new method is not limited by X-ray diffraction alone. © *2005 Pleiades Publishing, Inc.*

INTRODUCTION

The importance of the background separation on X-ray diffraction patterns is tightly associated with the problems of determining phase composition and widespread use of the methods of determination of various crystal structures based on the graphical representation of experimental intensities of X-ray diffraction reflections. No matter how paradoxical this may seem, the problem of separation of background from X-ray diffraction reflections is complicated by the existence of many methods of its solution. It is well known that an experimental diffraction pattern consists of the informative part (signal) proper and the noninformative part (noise). Noise may be caused by various factors, e.g., inelastic scattering, electron noise, etc. The separation of the maxima of the coherent Bragg scattering from the remaining part of scattering may be considered, to a large extent, as the art of the experimenter. The traditional method of solution of the problem is the Fourier analysis of diffraction patterns. For example, the method of separation of X-ray background is implemented in the packages of programs of full-profile analysis GSAS [1] and FULLPROF [2]. The method of Fourier analysis seems to be quite reasonable and, because it is practically the only existing method for the solution of the problem, it has been never criticized. Moreover, Fourier analysis also allowed attainment of very good results in processing of other signals. One may make several remarks on Fourier analysis of X-ray diffraction patterns. The determination of the Fourier transform (Fourier integral) for a discrete limited set of points is insufficiently correct by definition. Once the Fourier transform is determined, we have to use a certain criterion in order to separate the low- and the high-frequency signals. The problem of the selection (formulation) of such a criterion should be considered as a certain type of art.

THEORY OF THE METHOD

Consider the iteration process of separation of X-ray background on the whole and use an arbitrary filter of the iteration type possessing the property

$$I_i^{k+1} = P(I_i^k), \quad i \in [1, \ldots, N]. \tag{1}$$

Here, I_i^{k+1} is the current $(k + 1)$th iteration, I_i^k is the result attained at the previous iteration, N is the number of the experimental points, and P is a certain filter possessing certain properties which will be considered via the convenient and traditional representation in terms of the transformation into a Fourier integral. We believe that the conclusions made below do not depend on the type of the transformation used.

When expanding iterations into the Fourier integral, we may present the mechanism of the filter P's action in the following way. There exists a certain limiting frequency ω_b^k (subscript b indicates the background) at which the low-frequency component (background) (l) is cut off from the high-frequency component (peaks) (h) possessing the following properties (ω_b^k = const):

$$I_{(F)}^{k+1(h)}/I_{(F)}^{k+1(l)} = (1-\alpha)(I_{(F)}^{k(h)}/I_{(F)}^{k(l)}), \tag{2}$$

where α is an infinitesimal parameter of the filter action ($0 < \alpha < 1$). The lower index (F) indicates that we deal with the Fourier transform of the X-ray diffraction pat-

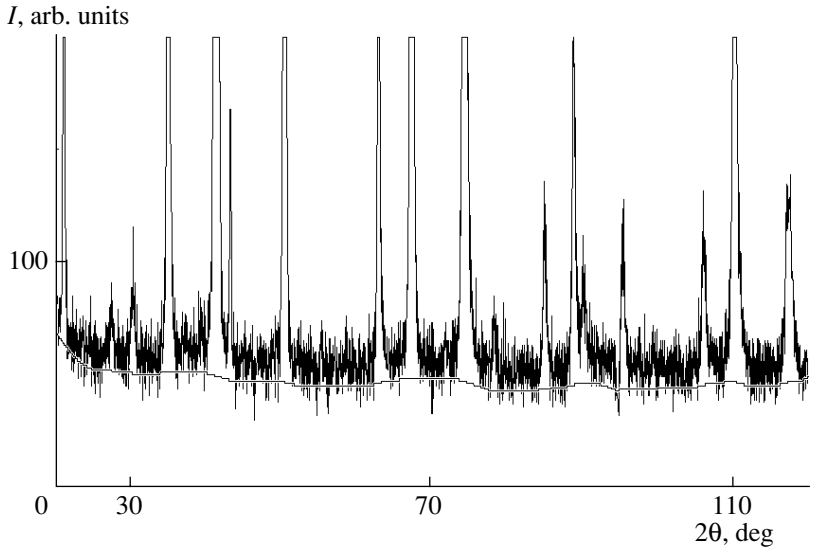

Fig. 1. Part of the diffraction patterns from magnetite $FeFe_2O_4$ and the separated background. The intensity of the highest peak is about 3500 pulses.

tern. In other words, the fraction of the high-frequency component of the signal should decrease with each new iteration *k*. If $k \longrightarrow \infty$, we have

$$\lim_{k \to \infty} (I_{(F)}^{k(h)} / I_{(F)}^{k(l)}) = 0. \quad (3)$$

In other words, the high-frequency component goes to zero. Determining the frequency ω_b^k by some empirical method, and applying the inverse Fourier transformation of the low-frequency component at sufficiently large *k*, we obtain a certain function which may be considered as the function of the X-ray background line. However, it is impossible to evaluate *a priori* neither ω_b^k nor *k* or α for an arbitrary filter and an arbitrary diffraction pattern.

Now, we have to impose the following conditions

$$\omega_b^{k+1} = (1 - \beta)\omega_b^k, \quad (4)$$

where $\beta \geq 0$. The case $\beta = 0$ was considered above (see Eq. (3)), whereas at $\beta > 0$ and $k \longrightarrow \infty$, we have

$$\lim_{k \to \infty} \omega_b^k = 0. \quad (5)$$

In other words, the inverse Fourier transformation yields

$$I_{b,i} = C, \quad i \in [1, \ldots, N]. \quad (6)$$

It follows from the normalization conditions that $C = \min(I_i)$. This result corresponds to a straight line passing through the point with the minimum intensity and which is parallel to the abscissa. Obviously, in practice, this trivial background function is not very useful. Of course, we may also assume that

$$\beta_k = f(I_i^k), \quad i \in [1, \ldots, N], \quad (7)$$

i.e., to describe β_k as a certain function of the signal shape (e.g., by using a certain polynomial). In this case, at certain *k* values, β_k may be either greater or less than zero. At the appropriately selected function *f*, it is possible to hope that $\omega_b^k > 0$ and

$$\lim_{k \to \infty} \omega_b^k = \omega_b > 0. \quad (8)$$

Now, the background function has a sufficiently appropriate form. The type of filtration used is not exceptional for processing diffraction patterns if criterion (2) is fulfilled. The mechanism of the filter action with respect to the parameters α, β, *k*, and *f* is empirical.

Thus, the problem of background separation is reduced to the selection of a simple and unique background criterion. This may be a certain conditional fraction of the points on a diffraction pattern with the intensities lower that the desirable background line. The evaluation of the fraction of the background points may be rather crude, because this does not affect the final result.

We suggest separating the X-ray diffraction background by the methods of digital integral filtration without opposing it to the method of the Fourier filtration. The method is rather simple and, in the majority of cases, efficient. Its algorithm is also rather simple: the initial diffraction pattern is smoothened by averaging the intensity of a certain central point with the intensities of some neighboring points. The next operation consists in the following: the intensities of the initial

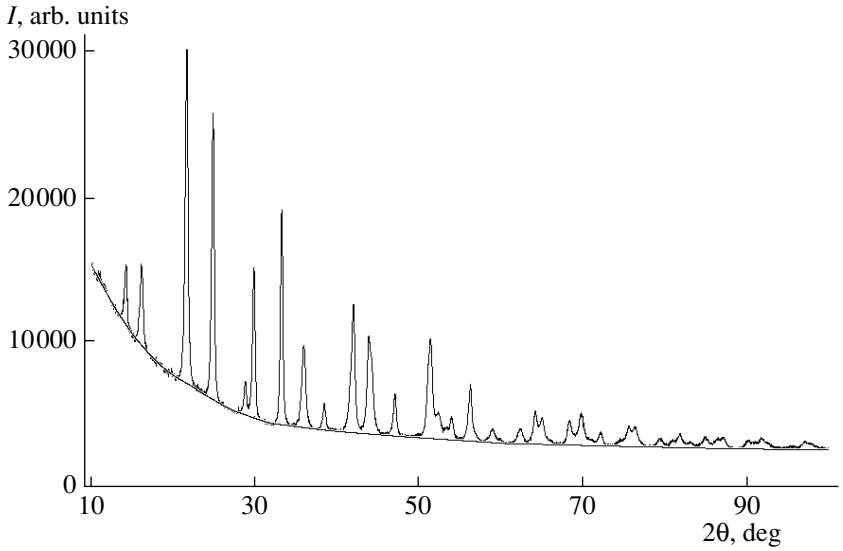

Fig. 2. Diffraction pattern from $Pb_2Fe(CN)_6$ and the separated background.

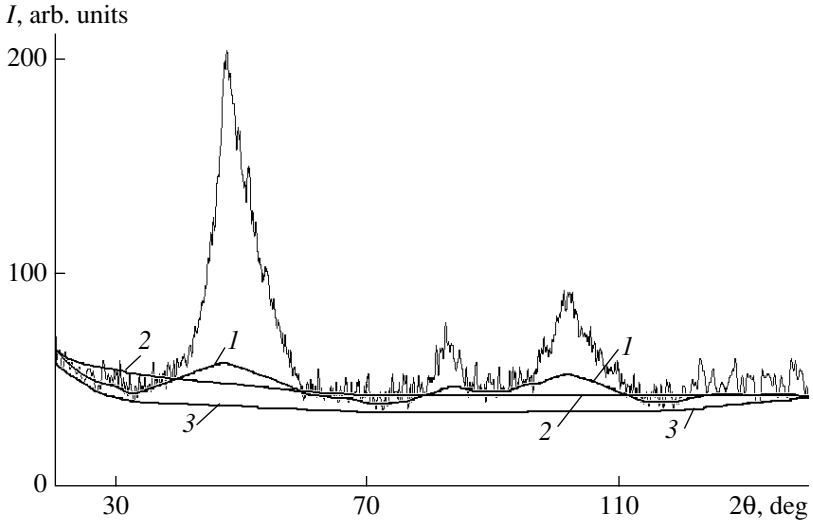

Fig. 3. Strongly amorphized sample. Background lines: (*1*) at integration points attaining 1 and (*2*) 10%; (*3*) formal method (see text below).

diffraction pattern higher than the intensities of the smoothened diffraction pattern are substituted by the intensities of the points of the smoothened diffraction pattern. Thus, the upper parts of the diffraction pattern (X-ray diffraction peaks) are truncated. Then, the diffraction pattern thus modified is subjected to new smoothening, the intensities of the initial diffraction pattern are changed again, etc. In other words, the method consists of several iterations. In principle, smoothening may be made not only as was described above but by any other method. After a certain sufficiently large number of iterations, the diffraction pattern thus obtained represents the X-ray background. As the simplest mechanism of the integral filtration, one may use, e.g., the following expression:

$$\bar{I}_i = (1/N) \sum_{i-(N-1)/2}^{i+(N-1)/2} I_j, \qquad (9)$$

where $\bar{I}_i$ is the integrated (smoothened) intensity value at the point i, I_j is the initial intensity value, and N is the number of averaged points.

For conventional high-quality diffraction patterns, N may be equal to one or several percent of the total number of the points. This factor is empirical and indicates that the width of the interval of averaging should be

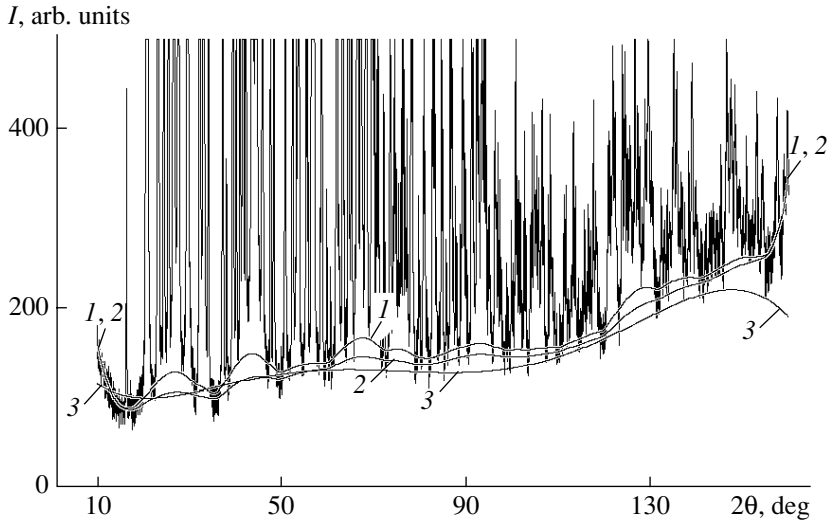

Fig. 4. Part of the $PbSO_4$ diffraction pattern and background line separated with the use of the criterion of (*1*) 15 and (*2*) 10% of the total number of the points lying below the background line (the number of the integration points 1%). Curve (*3*) is the background line obtained using the FULLPROF program [2], test example.

comparable with the width of X-ray diffraction peaks on the initial diffraction pattern. To decrease the effect of peak displacement in the direction of the filter action, a double passage of the integral filter is used: in the forward and backward directions. The problem of the filter action at the ends of the diffraction patterns is solved by decreasing the number N of the averaged points with an approach to the diffraction-pattern boundaries. Thus, the first point closest to the edge is not taken in averaging, point 2 is averaged with points 1 and 3, point 3 is averaged with points 1, 2, 4, and 5, etc., up to the attainment of the number of averaged points equal to the given N.

With due regard for the above iteration procedure, the action of filter (9) satisfies conditions (2) and (4) at $\beta > 0$, i.e., in principle, acts in the same way as the Fourier and other filters. However, the rigorous mathematical proof of this statement seems to be rather complicated.

RESULTS AND DISCUSSION

The criterion used to cease the iteration procedure is a certain percent of points with intensities lower than the separated background line of their total number in the initial diffraction pattern (say, 5%). This is an empirical factor selected experimentally. As an illustration, we consider here a part of the diffraction pattern of natural magnetite $FeFe_2O_4$ (JCPDC, 19-629) (DRON 4.13, CoK_∞, 40 kV, 30 mA, C-monochromator of the diffracted beam, 0.03° step, time of pulse collection 15 s) after the separation of background (program for editing the primary data XRL Edit [3] based on the method mentioned above) (Fig. 1) and the diffraction patterns of lead ferrocyanide (transmission experiment) (Fig. 2).

The method of background separation may be used not only in processing X-ray diffraction patterns, but also in some other instances. Thus, it may be used for processing derivatograms (especially in the determination of thermal effects). However, one has to remember that the method is "directional" with respect to the ordinate axis and yields the approximation in the downward direction: from large to small values. This signifies that only positive (exceeding the background) signal values will be determined. In the opposite direction of the substitution of the initial-signal parameters (in iterations), the negative values may be determined as well. Combining these two methods, one may single out the background for a signal having both a positive and a negative value with respect to the background.

One of the method limitations is its sensitivity to the ratio of the width of the signal (peak) line to the width of the integration band (number of averaged points). This is demonstrated by the example of background determination for diffuse peaks from a substantially amorphized sample with a line half-width of about 8° (5% of points below the background line)

The above formal method of separation of X-ray diffraction background is purely phenomenological. It is based on the construction of a number of straight lines (it is possible to use polynomials) passing trough the lowest points of the diffraction pattern in the following way. All the points of this region of the diffraction pattern (except for two lowest ones used in the construction of the local line) should lie lower than this line.

The efficiency of the method suggested here is illustrated by the popular example of the diffraction pattern of lead sulfate (package of programs GSAS [1]

(PbSO4dat) and FULLPROF [2] (Pbsox.dat), processing by XRL Edit [3]) (Fig. 4).

In conclusion, we should like to emphasize that this method may be used not only in the one-dimensional case of conventional diffraction patterns. After a slight modification, it may also be used for processing the data obtained on multi-circle diffractometers, textured patterns, and various images.

REFERENCES

1. A. C. Larson and R. B. Von Dreele, *GSAS LANSCE, MS-H805* (Los Alamos National Laboratory, Los Alamos, 1986), NM 87545, http://www.ccp14.ac.uk/ccp/ccp14/ftp-mirror.
2. J. Rodriguez-Carvajal, *FullProf* (Laboratoire Leon Brillouin, CEA-CNRS), http://www.ccp14.ac.uk/.
3. S. A. Suevalov, *XRL_Edit* (LRSA KFKS Ural. Gos. Univ., Yekaterinburg, 2002), http://xray.physics.usu.ru; *Paper Presented at III Ural Regional School–Seminar of Young Scientists and Students on Physics of Condensed State* (Ural. Gos. Univ., Yekaterinburg, 1999); http://www2.usu.ru/physics/conden_state/.

Translated by L. Man

Crystallography Reports, Vol. 50, No. 1, 2005, pp. 36–41. Translated from Kristallografiya, Vol. 50, No. 1, 2005, pp. 43–48.

STRUCTURE OF INORGANIC COMPOUNDS

Structural Study of $K_{0.93}Ti_{0.93}Nb_{0.07}OPO_4$ Single Crystals at 30 K

A. P. Dudka*, I. A. Verin*, V. N. Molchanov*, M. K. Blomberg, O. A. Alekseeva*, N. I. Sorokina*, N. E. Novikova*, and V. I. Simonov***

** Shubnikov Institute of Crystallography, Russian Academy of Sciences, Leninskiĭ pr. 59, Moscow, 119333 Russia*

e-mail: dudka@ns.crys.ras.ru

*** Physics Faculty, Helsinki State University, Helsinki, Finland*

Received April 5, 2004

Abstract—The structure of a $K_{0.93}Ti_{0.93}Nb_{0.07}OPO_4$ single crystal is studied at the temperature 30 K. The measurements are performed on a four-circle HUBER-5042 diffractometer with a DISPLEX DE-202 cryostat. Processing of the diffraction data and the preliminary refinement of the model are performed using the ASTRA program package. The final refinement of the structure model is made using the JANA2000 program complex. The refinement shows that the structure of a $K_{0.93}Ti_{0.93}Nb_{0.07}OPO_4$ crystal at $T = 30$ K is similar to its structure at room temperature. No phase transitions are revealed. Slight temperature-induced displacements of the potassium positions in the large cavities of the mixed framework are established. © *2005 Pleiades Publishing, Inc.*

INTRODUCTION

Crystals of potassium titanyl phosphate of the composition $KTiOPO_4$ (KTP) and the solid solutions based on them belong to the class of ferroelectrics–superionics. The characteristic feature of these compounds is the combination of the phenomena of electric ordering, nonlinear optical characteristics, and high ionic conductivity. All these properties may be controlled within certain limits using isomorphous replacement. For directional change of these properties in the crystals of this family, it is necessary to establish the relations between their chemical composition, atomic structure, and physical properties.

The present study continues the structural studies of niobium-doped potassium titanyl phosphate crystals [1–3]. Earlier, we studied KTP : Nb crystals with 4 at % Nb [1, 2] and also with 7 and 11 at % Nb [3]. The crystal structure of these solid solutions consists of a three-dimensional framework of $(Ti,Nb)O_6$ octahedra and PO_4 tetrahedra which share their vertices. The framework has broad twisted channels along the *c* axis which are filled with potassium cations. It has been established [3] that with an increase of the content of pentavalent niobium substituting tetravalent titanium, the valence difference is compensated by the vacancies in the potassium positions. The remaining potassium atoms are statistically distributed over a large number of positions. The reliable localization of potassium positions with low occupancy requires the conduction of low-temperature studies.

There are experimental low-temperature data on the structure of KTP single crystals described by the general formula $ATiOXO_4$, where A = Na, Rb, or Tl and X = P, or As [4–6]. Sodium-doped KTP crystals were studied by the X-ray diffraction method at 10.5 K [4]. With a decrease of the temperature, the crystal showed no phase transition, and the rigid framework of Ti octahedra and P tetrahedra changed only slightly. However, both crystallographically independent potassium cations were displaced from their positions along the *c* axis by 0.033 Å. In the $RbTiOAsO_4$ structure [5], lowering of the temperature from 295 to 9.6 K resulted in analogous displacements of both rubidium cations along the *c* axis by ~0.04 Å. In this case as well, no phase transitions were recorded. Finally, the study of $TlTiOPO_4$ single crystals at 11 K [6] showed disorder of thallium ions over eight positions with the preferable filling of two of these positions along the *c* axis. The rigid framework of this structure also showed no considerable changes with lowering of the temperature.

The present study was undertaken to study $K_{0.93}Ti_{0.93}Nb_{0.07}OPO_4$ single crystals by the X-ray diffraction method at the temperature 30 K.

EXPERIMENTAL

The $K_{0.93}Ti_{0.93}Nb_{0.07}OPO_4$ single crystals for the study were obtained by spontaneous crystallization from melt in the K_2O–Nb_2O_5–TiO_2–P_2O_5 system by the method described elsewhere [7] at the Physics Faculty of Moscow State University [3]. The spherical sample for the X-ray study had a diameter of 0.21 mm and was prepared from a homogeneous single crystal.

The measurements were performed on a four-circle HUBER-5042 diffractometer with a DISPLEX DE-202 cryostat (APD Cryogenics Inc.). The angular positions of the goniometer were set with an accuracy of 0.001°. The cryostat with a double closed cycle in the temperature range 20–250 K ensured temperature stability within ±0.05 K. The computer-controlled system worked in the LINUX operation system (SPEC package of programs) with a flexible scheme of operations appropriate for logical solutions of a wide spectrum of diffraction problems. We wrote special programs for precision determination of the unit-cell parameters within the SPEC package programs which provided the measurement of the integrated reflection intensities and their preliminary processing for subsequent use in crystallographic computations.

The sample was glued to a glass fiber by bee wax to exclude possible stresses in the sample at low temperatures. The unit-cell parameters of the orthorhombic crystal were determined by the least squares method using 56 diffraction reflections in the angular range $39° < \theta < 45°$. At 30 K, these parameters were a = 12.794(2) Å, b = 6.398(2) Å, and c = 10.596(3) Å. The set of integrated intensities at 30 K was obtained by stepwise (discrete) $\omega/2\theta$ scanning in two octants of the reciprocal space, $(\bar{h}, k, l)$ and $(h, \bar{k}, \bar{l})$, $\sin\theta/\lambda < 1.00$ Å^{-1}. Altogether, 4955 reflection profiles were recorded. The analysis of diffraction reflections shown gave results consistent with the centrosymmetric sp. gr. $Pna2_1$ determined at room temperature. The reflections from the $(\bar{h}kl)$ and $(h\bar{k}\bar{l})$ octants were not averaged because they formed Friedel pairs. In the refinement, we took into account the correction for anomalous scattering.

The analysis of the diffraction-peak profiles (each profile was measured at 96 points) revealed the displacement of the peaks from the middle of the measurement interval. The repeated refinement of the orientation matrix of the crystal did not eliminate the peak displacements. In some instances, the displacements were so pronounced that the peak profile seemed to be truncated on one side. It should be indicated that the cryostat was supplied with helium via rather a hard hose, which deteriorated the sample alignment and, as a result, gave rise to reflection displacement from the scanning interval. The reflections in different regions were distorted indifferently. The intensity of the $(\bar{h}kl)$ reflections were underestimated in comparison with the intensity of $(h\bar{k}\bar{l})$ reflections from the opposite octant. The displacements were especially pronounced for reflections with large $\bar{h}$ indices. No regular dependence of intensities on the scattering angle was observed. To reduce the effect of the experimental errors on the refined structural parameters, we used a special procedure of experimental-data processing. The processing of the diffraction data and the preliminary refinement of the model was performed by the ASTRA (now called MMM [8, 9]) system of programs. To compensate the truncation of the reflection profiles due to their displacement to the ends of the scanning interval, the boundaries of the peaks from different parts of the data set were determined in different ways. With this aim, we modified the program described in [8]. For strongly distorted $(\bar{h}kl)$ reflections, the far angular boundary of the peak was taken to be that corresponding to the last point of 96 measured ones. For the $(h\bar{k}\bar{l})$ reflections, we determined the peak boundaries using the statistical Lehmann–Larsen [10] method for strong reflections and the Grant–Gabe [11] method for weak reflections. Then the boundary values were used to calculate the anisotropic law of boundary changes according to Blessing [12]. The calculation of the integrated intensities and their standard deviations was performed by the background–peak–background method. It is well known that, when measuring the reflection profiles in the limited range of the scattering angles (the Hanson method for fast data collection [13]) one encounters a change of the scale factor if the aperture used has insufficient dimensions and if the peaks are truncated. In other words, the different truncation of peaks observed in our case may be compensated, to some extent, by the introduction of anisotropic scale factors for the data sets $(\bar{h}kl)$ and $(h\bar{k}\bar{l})$ in [14].

Table 1. Displacements of cations (Å) with lowering of the temperature from 293 to 30 K

Atom	Δx	Δy	Δz
K(1)	0.002(1)	0.006(1)	0.024(1)
K(2)	0.018(1)	0.006(1)	0.040(1)
K(3)	−0.011(1)	0.015(1)	−0.086(1)
K(4)	0.000(1)	−0.116(1)	−0.868(1)
Ti(1)	−0.004(1)	0.001(1)	0.000(1)
Ti(2)	0.003(1)	−0.003(1)	−0.002(1)
P(1)	0.002(1)	−0.001(1)	0.001(1)
P(2)	−0.004(1)	0.000(1)	0.001(1)

The absorption and *Lp* corrections for a spherical sample with $\mu R = 0.31$ were introduced by the conventional method used in the ASTRA package. The conventional model refinement over the complete initial data set with the use of the isotropic scaling factor yielded high reliability factors: $R_w(F^2)/R(F)$ = 8.93/4.30% over 4955 reflections and 170 refined parameters. Refinement with the anisotropic scale factor (the number of refined parameters increased to 175) reduced the reliability factors to $R_w(F^2)/R(F)$ = 8.07/4.03%. Then, the refinement was performed sepa-

rately over the $(\bar{h}kl)$ and $(h\bar{k}\bar{l})$ data sets. The refinement over 2505 independent $(\bar{h}kl)$ reflections yielded much worse reliability factors $R_w(F^2)/R(F)$ = 6.01/3.14% in comparison with the refinement over 2450 $(h\bar{k}\bar{l})$ reflections which yielded the reliability factors $R_w(F^2)/R(F)$ = 4.51/2.48%. Both these results are better than the result obtained over the whole data set. In both cases, we refined 175 parameters with anisotropic scaling factors. Of course, the scaling factors in the refinement over half of the data set reflections turned out to be different. To bring both data sets to the same scale, all the intensities of the first and second set were divided into their scale factors. After this procedure, both data sets were combined into one set. The refinement over the combined data set gave $R_w(F^2)/R(F)$ = 5.95/2.81% (4955 reflections, 170 parameters). The structure model thus refined is quite satisfactory in terms of crystal chemistry. The procedure of combination of the data sets in the ASTRA package is performed automatically as a part of the algorithm of the interexperimental minimization [9]. The rejection of only 21 reflections with the maximum experimental distortions and the refinement over 4934 reflections reduced the reliability factors to $R_w(F^2)/R(F)$ = 5.20/2.76%.

The results of the structure-model refinement over the data set obtained by bringing the two parts of the data set to the same scale have an obvious advantage. Naturally, this procedure levels the experimental errors only partly. In parallel with the refinement using the ASTRA package, we also refined the model using the JANA2000 program [15] over the data set obtained after data processing described above. The concluding reliability factors $R_w(F^2)/R(F)$ = 3.09/2.79% were obtained in the refinement of 170 parameters over 4832 reflections.

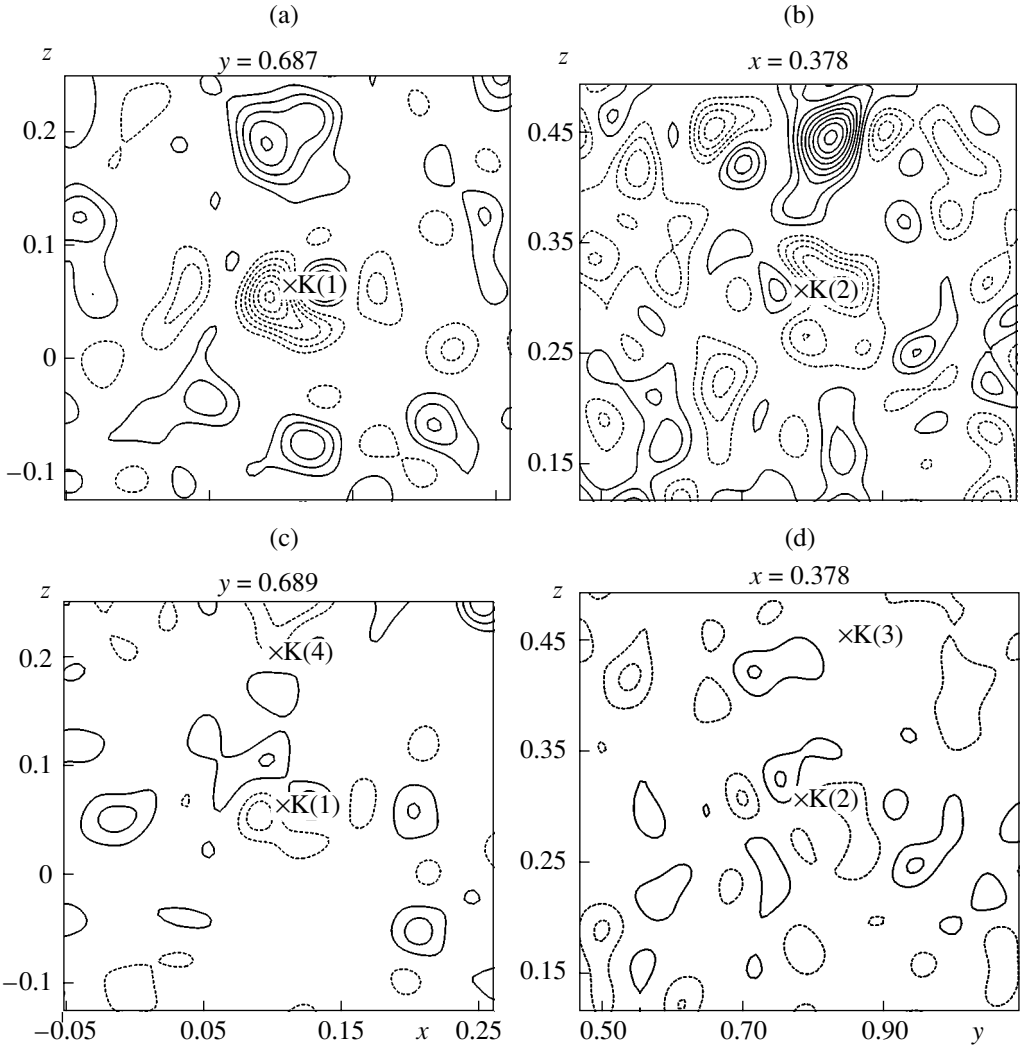

Fig. 1. Sections of difference electron-density syntheses of the $K_{0.93}Ti_{0.93}Nb_{0.07}OPO_4$ structure made parallel to the (*x*0*z*) plane at the temperature 30 K. Isolines are spaced by 0.163 e/Å^3. (a) Section through the K(1) atoms, (b) section through the K(2) atoms, (c) section through the K(1) and K(4) atoms, (d) section through the K(2) and K(3) atoms.

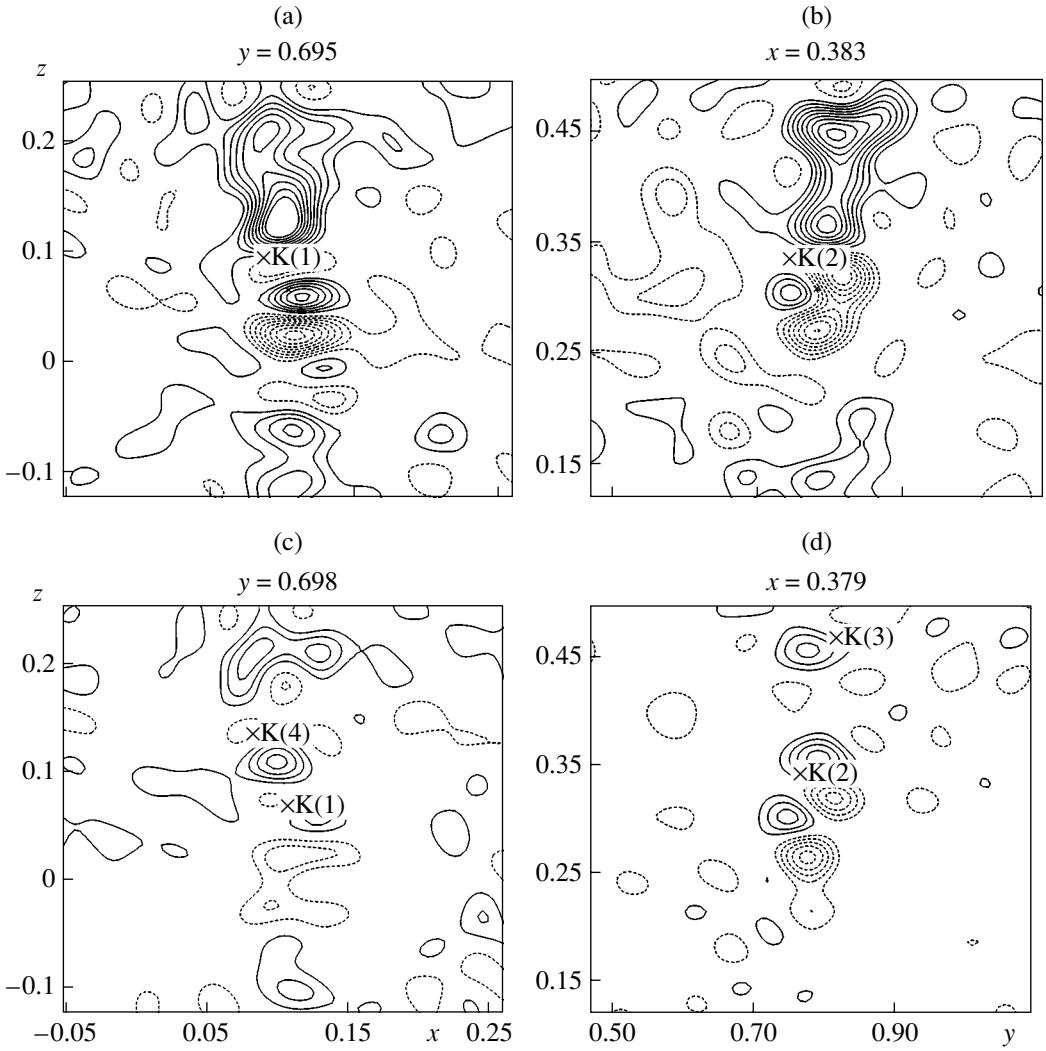

Fig. 2. Sections of difference electron-density syntheses of the $K_{0.93}Ti_{0.93}Nb_{0.07}OPO_4$ structure parallel to the (x0z) plane at the temperature 293 K. Isolines are spaced by 0.163 e/Å^3. (a) Section through the K(1) atoms, (b) section through the K(2) atoms, (c) section through the K(1) and K(4) atoms, (d) section through the K(2) and K(3) atoms.

RESULTS AND DISCUSSION

The refinement showed that the crystal structure at T = 30 K is similar to the structure at room temperature. The crystal underwent no phase transitions. The coordinates and occupancies of Ti and P atoms remained the same as they were at T = 293 K. The difference electron density syntheses calculated on the basis of the model with two main potassium positions, K(1) and K(2) (Figs. 1a and 1b), showed the peaks of the residual electron density: a peak with a height of 1.33 e/Å^3 at a distance of 1.39 Å from the K(1) atom and a peak with a height of 3.73 e/Å^3 at a distance of 1.63 Å from the K(2) atom. We refined the structural parameters of the model with due regard for the split positions of potassium atoms. Figures 1c and 1d show the difference electron density syntheses with subtracted K(1), K(2), K(3), and K(4) atoms with the corresponding occupancies. For comparison, the similar electron density syntheses at T = 293 K [3] are shown in Fig. 2. The occupancies of the potassium positions change with lowering of the temperature and are equal to 0.792 for K(1), 0.780 for K(2), 0.164 for K(3), and 0.059 for K(4). At room temperature, these occupancies were 0.702, 0.773, 0.148, and 0.168, respectively. The total occupancy of the potassium positions at T = 30 K is 1.795, and at room temperature this occupancy is 1.791; i.e., the total occupancies are the same within the accuracy of our measurements. It is established that at low temperatures, all four potassium cations are displaced mainly along the c axis (Table 1).

These displacements are equal to 0.024(1) for K(1) and 0.040(1) Å for K(2), which well agrees with the data obtained in [4, 5]. At temperatures lower than room temperature, small changes in coordinates were observed for K(3) and K(4) atoms. The maximum displacements along the c axis for these atoms are

Table 2. Atomic coordinates, position occupancies q, and equivalent parameters of atomic thermal vibrations B_{eq} (Å^2) in the $K_{0.93}Ti_{0.93}Nb_{0.07}OPO_4$ structure at T = 30 K

Atom	x/a	y/b	z/c	q	B_{eq}
Ti(1)	0.37261(2)	0.4996(1)	0	0.857(2)	0.27(1)
Nb(1)	0.37261(2)	0.4996(1)	0	0.143	0.27(1)
Ti(2)	0.24734(5)	0.2658(1)	0.2501(1)	1	0.35(1)
P(1)	0.4984(1)	0.3377(1)	0.2570(1)	1	0.27(1)
P(2)	0.1821(1)	0.5013(1)	0.5091(1)	1	0.27(1)
K(1)	0.1048(1)	0.6970(1)	0.0627(1)	0.792(2)	0.60(2)
K(2)	0.3778(1)	0.7806(1)	0.3048(1)	0.780(2)	0.55(2)
K(3)	0.4035(4)	0.8418(7)	0.4516(6)	0.164(3)	1.23(11)
K(4)	0.099(1)	0.698(3)	0.202(2)	0.059(3)	2.51(51)
O(1)	0.4858(2)	0.4842(4)	0.1457(2)	1	0.41(4)
O(2)	0.5101(1)	0.4692(4)	0.3790(2)	1	0.39(4)
O(3)	0.4000(1)	0.1986(3)	0.2758(2)	1	0.39(4)
O(4)	0.5947(1)	0.1950(3)	0.2393(2)	1	0.35(4)
O(5)	0.1127(1)	0.3101(3)	0.5368(2)	1	0.29(4)
O(6)	0.1123(1)	0.6916(3)	0.4846(2)	1	0.43(4)
O(7)	0.2529(2)	0.5395(3)	0.6246(2)	1	0.41(4)
O(8)	0.2540(2)	0.4610(3)	0.3951(2)	1	0.40(4)
O(9)	0.2237(1)	0.0413(4)	0.3851(2)	1	0.37(4)
O(10)	0.2241(1)	–0.0359(3)	0.6383(2)	1	0.41(5)

0.086(1) and 0.868(1) Å, respectively. The distance between the positions of the K(1) and K(4) atoms is 1.48 Å (0.83 Å at T = 293 K), and between the K(2) and K(3) atoms this distance is 1.64 Å (1.71 Å at T = 293 K).

The coordinates of the basis atoms of the structure, the occupancies q by atoms of their crystallographic positions, and the equivalent isotropic parameters of their thermal vibrations, B_{eq}, are listed in Table 2.

The results of the X-ray diffraction study of a $K_{0.93}Ti_{0.93}Nb_{0.07}OPO_4$ single crystal at 30 K confirmed the structural model determined earlier at room temperature [3]. Since the atomic thermal vibrations considerably decrease with lowering of the temperature, a decrease in the temperature to 30 K allowed us to localize the potassium atoms in the additional positions more accurately. The established displacement of potassium positions associated with lowering of the temperature revealed in our study agrees well with the results of the structural studies of $KTiOPO_4$ [4, 16] and $TlSbOGeO_4$ [17] crystals over a large temperature range. It was established [4, 16, 17] that with an increase of the temperature, potassium and thallium positions are not only gradually displaced along the c axis but are also split. It is this displacement and splitting of cation positions in large cavities of the mixed framework that are mainly responsible for the ferroelectric phase transition observed in crystals of the potassium titanyl phosphate family.

ACKNOWLEDGMENTS

This study was supported by the Presidential Program for Leading Scientific Schools, project NSh-1642.2003.2.

REFERENCES

1. T. Yu. Losevskaya, O. A. Alekseeva, V. K. Yanovskiĭ, *et al.*, Kristallografiya **45** (5), 809 (2000) [Crystallogr. Rep. **45**, 739 (2000)].
2. O. A. Alekseeva, M. K. Blomberg, V. N. Molchanov, *et al.*, Kristallografiya **46** (4), 710 (2001) [Crystallogr. Rep. **46**, 642 (2001)].
3. O. A. Alekseeva, N. I. Sorokina, I. A. Verin, *et al.*, Kristallografiya **48** (2), 238 (2003) [Crystallogr. Rep. **48**, 205 (2003)].

4. S. T. Norberg, A. N. Sobolev, and V. A. Streltsov, Acta Crystallogr., Sect. B: Struct. Sci. **59**, 353 (2003).
5. J. Almgren, V. A. Streltsov, A. N. Sobolev, *et al.*, Acta Crystallogr., Sect. B: Struct. Sci. **5**, 712 (1999).
6. M. K. Blomberg, M. J. Merisalo, N. I. Sorokina, *et al.*, Kristallografiya **43** (5), 801 (1998) [Crystallogr. Rep. **43**, 748 (1998)].
7. V. I. Voronkova and V. K. Yanovskiĭ, Izv. Akad. Nauk SSSR, Neorg. Mater. **24**, 273 (1988).
8. A. P. Dudka, A. A. Loshmanov, and B. A. Maksimov, Poverkhnost, No. 2, 28 (2001).
9. A. P. Dudka, Kristallografiya **47** (1), 163 (2002) [Crystallogr. Rep. **47**, 152 (2002)].
10. M. S. Lehmann and F. K. Larsen, Acta Crystallogr., Sect. A: Cryst. Phys., Diffr., Theor. Gen. Crystallogr. **30**, 580 (1974).
11. D. F. Grant and E. J. Gabe, J. Appl. Crystallogr. **11**, 114 (1978).
12. R. H. Blessing, Crystallogr. Rev. **1**, 3 (1987).
13. J. C. Hanson, K. D. Watenpaugh, L. Sieker, and L. H. Jensen, Acta Crystallogr., Sect. A: Cryst. Phys., Diffr., Theor. Gen. Crystallogr. **35**, 616 (1979).
14. Z. Shakked, Acta Crystallogr., Sect. A: Found. Crystallogr. **39**, 278 (1983).
15. V. Petricek and M. Dusek, *JANA2000. Crystallographic Computing System* (Inst. of Physics, Praha, 2000).
16. P. Delarue, C. Lecomte, M. Jannin, *et al.*, J. Phys.: Condens. Matter. **11**, 4123 (1999).
17. E. L. Belokoneva, Usp. Khim. **67** (3), 559 (1994).

Translated by L. Man

Crystallography Reports, Vol. 50, No. 1, 2005, pp. 42–47. Translated from Kristallografiya, Vol. 50, No. 1, 2005, pp. 49–54.

STRUCTURE OF INORGANIC COMPOUNDS

Crystal Structure of Holtite I

S. S. Kazantsev*, D. Yu. Pushcharovsky, M. Pasero***, S. Merlino***, N. V. Zubkova**, Yu. K. Kabalov**, and A. V. Voloshin******

** Shubnikov Institute of Crystallography, Russian Academy of Sciences, Leninskiĭ pr. 59, Moscow, 119333 Russia*

*** Faculty of Geology, Moscow State University, Vorob'evy gory, Moscow, 119899 Russia*

**** Department of Sciences of Earth, University of Pisa, Pisa, 56126 Italy*

***** Institute of Geology, Kol'skiĭ Division, Russian Academy of Sciences, Apatity, Russia*

Received April 18, 2003

Abstract—The crystal structure of As-containing holtite **I** is refined (Ital Structures diffractometer, 939 crystallographically independent reflections, anisotropic approximation, $R = 0.047$). The parameters of the orthorhombic unit cell are $a = 4.695(1)$ Å, $b = 11.906(3)$ Å, $c = 20.38(3)$ Å, sp. gr. *Pnma*, $Z = 4$. On the whole, the structural formula obtained, $(Si_{2.43}Sb_{0.36}As_{0.21})BO_3[(Al_{0.62}Ta_{0.26}\square)Al_2(Al_{0.98}\square)_2(Al_{0.94}\square)_2O_{12}](O,OH,\square)_{2.65}$, corresponds to the electron-probe analysis data. The statistical replacement of $(Si,As)O_4$ tetrahedra by pyramidal $[SbO_3]$ groups is confirmed. The X-ray diffraction spectra of holtite **I** are compared with those of holtite **II**. © *2005 Pleiades Publishing, Inc.*

INTRODUCTION

Holtite $(Ta,Al)Al_6(BO_3)(Si,Sb)_3O_{12}(O,OH)_3$ [1], first discovered in Western Australia in 1971, is also found in pegmatites of two other deposits. The study of the holtite composition from the Voroni Tundry deposit (Kola Peninsula) revealed two As-containing varieties differing by their antimony contents [2]: holtite **I** discovered earlier is characterized by a low Sb content, whereas holtite **II** has high Sb content. Two types of holtite also differ by Si content. Additionally, according to [3], two different holtite samples from the Greenbushes deposit in Australia and different holtite crystals from the Szklary deposit in Poland also had the same composition characteristics. One of the samples of the Australian holtite is the holotype of this mineral.

Holtite **I** occurring in the zones of tantalum mineralization of granitic pegmatites of the Kola Peninsula forms well-faceted short prismatic crystals and is the earliest formation of all the other tantalum-containing minerals. Holtite **II** discovered more recently is characterized by a fine fiber state and substitutes the earlier tantalum-containing minerals [2]. The presence of both holtite forms in all the deposits and the absence of any intermediate compositions allow one to consider these forms as independent holtite varieties whose difference is determined by the Si : (Sb + As) ratio equal to 7 : 3 in holtite **II** and 8.5 : 1.5 in holtite **I**. Thus, holtite **I** occupies the intermediate position between holtite **II** and dumortierite containing no antimony at all. It was noticed [4] that the diffuse layers on X-ray diffraction patterns of holtite **I** indicate possible differences in the arrangement of tetrahedral cations occupying the neighboring tunnels in the polyhedral framework of the structure. The present study was aimed at establishing structural relationships between antimony-depleted holtite **I** from the granitic pegmatites of the Kola Peninsula and holtite **I** from the Greenbushes deposit in Western Australia [4]. Moreover, we also have the intention to reveal the structural features of the still unstudied holtite **II**.

EXPERIMENTAL

Electron-probe analysis of the samples of holtite **I** and holtite **II** allowed us to establish the following main components (wt %): Al_2O_3 47.34, Sb_2O_5 6.65, Ta_2O_5 13.79, Nb_2O_5 0.17, SiO_2 22.31, and As_2O_5 3.42 for holtite **I** and Al_2O_3 46.45, Sb_2O_5 21.29, Ta_2O_5 11.03, Nb_2O_5 0.18, SiO_2 17.31, and As_2O_5 2.45 for holtite **II**. We calculated the structural formula proceeding from the elemental complex $Si_3B[Al_7O_{17}(OH)_2]$ [2, 4]. The stoichiometric coefficients in the formulas of both holtite varieties were obtained from the calculations for the sum of cations (excluding boron) equal to 10. The chemical formulas thus obtained have the form $(Al_{6.47}Ta_{0.43})(BO_3)(Si_{2.59}Sb_{0.29}As_{0.21})O_{12}(O,OH)_3$ for holtite **I** and $(Al_{6.40}Ta_{0.36})(BO_3)(Si_{2.11}Sb_{0.97}As_{0.15}) \cdot O_{12}(O,OH)_3$ for holtite **II**.

Diffraction data were recorded on a $0.16 \times 0.05 \times 0.04$ mm holtite **I** single crystal on an automatic Ital Structures diffractometer. The crystallographic characteristics and the main parameters of the experiment are listed in Table 1.

The unit-cell parameters are obtained using the angular parameters of 10 reflections with $2\theta \sim 13°$. These unit-cell parameters were refined using all the reflections recorded. The additional data for the reflec-

tions of 11 layer lines (–1 *k l* … 11 *k l*) collected on an automated Nonius CAD4 diffractometer (MoK_α radiation, graphite monochromator) did not confirm the initially assumed doubling of the *a* parameter characteristic of structurally close dumortierite.

The absorption correction was introduced by ψ-scanning. The structure was refined based on the atomic coordinates from [4] within the sp. gr. *Pnma*, first, in the isotropic approximation to $R = 0.05$ over 884 reflections with $|F| > 4\sigma(F)$ using the SHELX-97 complex [5]. At the following stages, the refinement of the electron content of the cationic positions and the introduction of the anisotropic thermal corrections reduced the reliability factor $R(F)$ to 0.047. A variant of the cation distribution was established on the basis of refinement of the electron content of the cationic positions, preservation of the positive thermal corrections and electroneutrality of the chemical formula, and the balance of valence strengths. On the whole, the structural formula $(Si_{2.43}Sb_{0.36}As_{0.21})BO_3[(Al_{0.62}Ta_{0.26})Al_2(Al_{0.98})_2(Al_{0.94})_2 \cdot O_{12}](O,OH)_{2.65}$ corresponds to the electron-probe analysis data. At the same time, the variant indicated above should be considered as the optimum compromise between the experimental results of chemical and structural analysis of the crystal under question.

The final coordinates of the basic atoms, thermal parameters, and the results of the calculation of the balance of valence strengths performed in accordance with [6] are given in Tables 2 and 3, respectively. The O(10) position undersaturated with the valence strengths admits the simultaneous presence of O^{2-} anions and $(OH)^-$. The projection of the structure drawn using the DIAMOND 2 program is shown in Fig. 1.

All the attempts to select an appropriate single crystal of holtite **II** failed. Therefore, in order to establish the differences between holtite **II** and holtite **I** crystals, we obtained X-ray diffraction spectra of powder samples of holtite **I** and holtite **II** in the angular range $8° < 2\theta < 115.68°$ on an automated ADP-2 diffractometer (Co$K_{\alpha 1}$-radiation, Fe filter) with an exposure of 15 s at each point at a scanning rate of 0.02°. The diffraction data obtained were processed using the Wyriet 3.3 complex [7].

The unit-cell parameters refined from the powder diffraction data are $a = 4.6880(1)$ Å, $b = 11.884$ Å, $c = 20.35(3)$ Å for holtite **I** and $a = 4.6875(1)$ Å, $b = 11.881$ Å, $c = 20.418(9)$ Å for holtite **II**. The basic model used for the Rietveld refinement of both structures was the model obtained earlier from the X-ray diffraction data on a single crystal of holtite **I**. The refinement of the crystal structure of the powder sample of holtite **I** yielded satisfactory *R* factors, $R_{wp} = 0.027$, $R_F = 0.029$, $S = 1.23$, and confirmed the model based on the single-crystal data. The comparison of the calculated and observed spectra for this sample is presented in Fig. 2.

Table 1. Crystallographic and experimental data

Formula	$(Si_{2.43}Sb_{0.36}As_{0.21})BO_3 \cdot [(Al_{0.62}Ta_{0.26})Al_2(Al_{0.98})_2 \cdot (Al_{0.94})_2O_{12}](O,OH,)_{2.65}$
Unit-cell parameters, Å	$a = 4.695(1)$, $b = 11.906(3)$, $c = 20.38(3)$
Sp. gr., *Z*	*Pnma*, 4
V, Å^3	1139.2
ρ_{calc}, g/cm^3	3.738
μ, mm^{-1}	4.89
Molecular weight	2564.17
F_{000}	1231.4
Diffractometer	Ital Structures
Wave length, Å	0.71069
$2\theta_{max}$, deg	60
Number of measured reflections	1008
Number of crystallographically independent reflections	939
Number of reflections with $\|F\| > 4\sigma(F)$	884
R_{av}, %	0.9
Number of parameters to be refined	110
R_F(iso), %	5.02
R_F(aniso), %	4.69
$wR(F)$	2.67
GOF	1.017
$\Delta\rho_{max}$, e/Å^3	1.06
$\Delta\rho_{min}$, e/Å^3	–1.18

At the same time, the refinement of the structure of holtite **II** within the framework of the same model was unstable and, thus, could not give an answer to the question about its structural differences from holtite **I** We may only state the presence of some additional reflections in its X-ray diffraction spectrum (Fig. 3) which cannot be indexed based on the parameters indicated above. It is not excluded that this is associated with an impurity of another mineral.

DESCRIPTION OF THE STRUCTURE AND DISCUSSION

In many respects, the crystal structure of holtite **I** is close to dumortierite's structure; both structures are

Table 2. Coordinates, thermal parameters, and position occupancies (q) of basic atoms

Atom	*x/b*	*y/b*	*z/c*	*q*	U^*_{eq}, Å^2
Al(1)	0.4014(3)	0.75	0.24989(7)	0.616(1) – Al 0.258(1) – Ta	0.012(2)
Al(2)	0.5576(2)	0.61046(8)	0.47309(4)	1	0.008(3)
Al(3)	0.0593(2)	0.4905(1)	0.43184(5)	0.982(5)	0.009(2)
Al(4)	0.0599(2)	0.3597(9)	0.29009(5)	0.937(6)	0.011(3)
Si(1)	0.0889(3)	0.75	0.40642(6)	0.81 – Si 0.09 – As	0.015(1)
Sb(1')	0.1140(6)	0.75	0.3853(1)	0.1	0.005(2)
Si(2)	0.5888(2)	0.52312(8)	0.32877(5)	0.81 – Si 0.06 – As	0.0136(7)
Sb(2')	0.6092(3)	0.5636(1)	0.31676(8)	0.13	0.010(1)
O(1)	0.3784(7)	0.75	0.4564(1)		0.009(1)
O(2)	0.1569(9)	0.75	0.3304(2)	0.9	0.026(2)
O(3)	0.8928(4)	0.6389(1)	0.4551(1)		0.009(1)
O(4)	0.4029(4)	0.4341(1)	0.2822(1)		0.009(1)
O(5)	0.3957(4)	0.5509(1)	0.3944(1)		0.008(1)
O(6)	0.8831(4)	0.4509(1)	0.3512(1)		0.010(1)
O(7)	0.6593(6)	0.6331(2)	0.2886(1)	0.87	0.018(1)
O(8)	0.1715(7)	0.25	0.3493(1)		0.011(2)
O(9)	0.2536(4)	0.3506(1)	0.4476(1)		0.007(1)
O(10)**	0.7567(7)	0.25	0.2739(1)		0.013(2)
O(11)	0.7511(4)	0.4669(1)	0.4887(1)		0.07(1)
B	0.231(1)	0.25	0.4665(2)		0.012(3)

* The U_{eq} values are calculated based on the anisotropic thermal atomic displacements.
** O(10)=OH, O.

discussed in [4, 8]. The structure of holtite **I** has an octahedral framework formed by two types of nonequivalent columns of Al octahedra. In the first column, the pairs of equivalent Al octahedra share faces, whereas in the second column, the Al(2) and Al(3) octahedra share their edges. The broad hexagonal channels in this framework (the transverse dimension of the channel, i.e., the average distance between the oxygen atoms lying at the opposite "walls," is 5.24 Å) are occupied by the [(Al,Ta)O_3] columns formed by the Al and Ta octahedra (Al(1) octahedra) sharing their faces (Fig. 1). These columns are linked to the octahedral framework via SiO_4 tetrahedra in which some silicon atoms are replaced by arsenic atoms. The distances in the Al octahedra (average (Al,Ta)–O = 1.994, average Al–O = 1.905, 1.908, 1.907 Å) and (Si, As) tetrahedra (average (Si,As)–O = 1.648 and 1.647 Å) are close to their standard values. The BO_3 triangles are located in another narrower type of channels formed by Al octahedra. The average B–O distance is 1.372 Å.

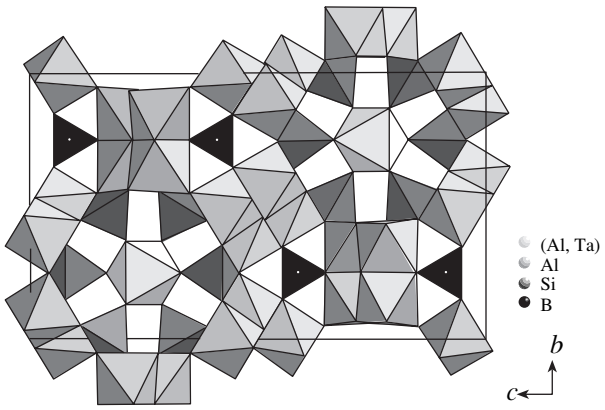

Fig. 1. Holtite structure projected along the [100] direction.

One of the main differences between the dumortierite and holtite structures consists in different filling of such hexagonal tunnels. For holtite, the partial alternation of aluminum and tantalum atoms in the cationic position Al(1) is characteristic, whereas for dumortier-

Table 3. Calculation of the balance of valences at anions

Cation/Anion	O(1)	O(2)	O(3)	O(4)	O(5)	O(6)	O(7)	O(8)	O(9)	O(10)	O(11)
Al(1)		0.238					0.236				
		0.222					0.267				
		0.207					0.204				
Ta(2)		0.192					0.231				
Al(2)	2×0.515		0.529		0.49				0.505		0.427
											0.525
Al(3)			0.452		0.508	0.504			0.467		0.536
											0.479
Al(4)				0.555		0.546		2×0.542		2×0.407	
				0.517						2×0.322	
Si(1)	0.663	0.908	0.743								
As(1)	0.115	0.157	0.129								
Sb(1)	0.111	–	0.127								
Si(2)				0.717	0.754	0.677	0.914				
As(2)				0.083	0.175	0.078	0.108				
Sb(2)				0.138	0.167	0.125					
B								0.929	1.032		
Σ	1.919	1.924	1.98	2.01	2.094	1.93	1.906	2.013	2.004	1.458	1.967

ite, this position is fully occupied by Al atoms. Similar to the crystal structure of holtite from Australia [4], some $(Si,As)O_4$ tetrahedra are replaced by SbO_3 groups (Fig. 4). In the process of such replacement, oxygen vacancies are formed in the O(2) and O(7) positions, which agrees with the partial occupancy of the Al(1) position and is accompanied by a noticeable increase in the thermal corrections for the indicated oxygen atoms.

Inside the $[SbO_3]$ complexes, three elongated Sb–O distances (average 1.920(2) Å) are formed. At the same

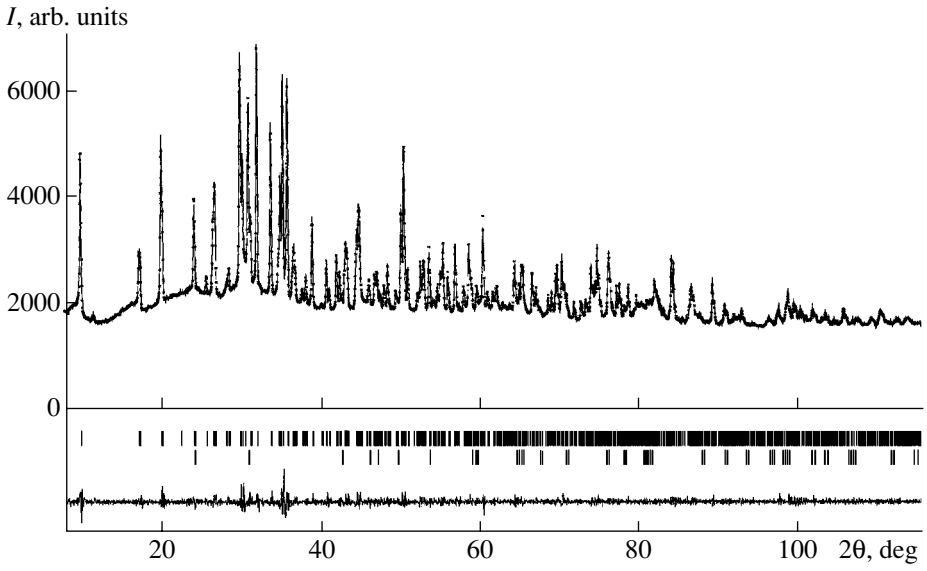

Fig. 2. Calculated (crosses) and observed (solid line) X-ray spectra of the powder of holtite **I**. Vertical bars indicate all possible Bragg reflections. The line in the lower part shows the difference between the observed and calculated spectra.

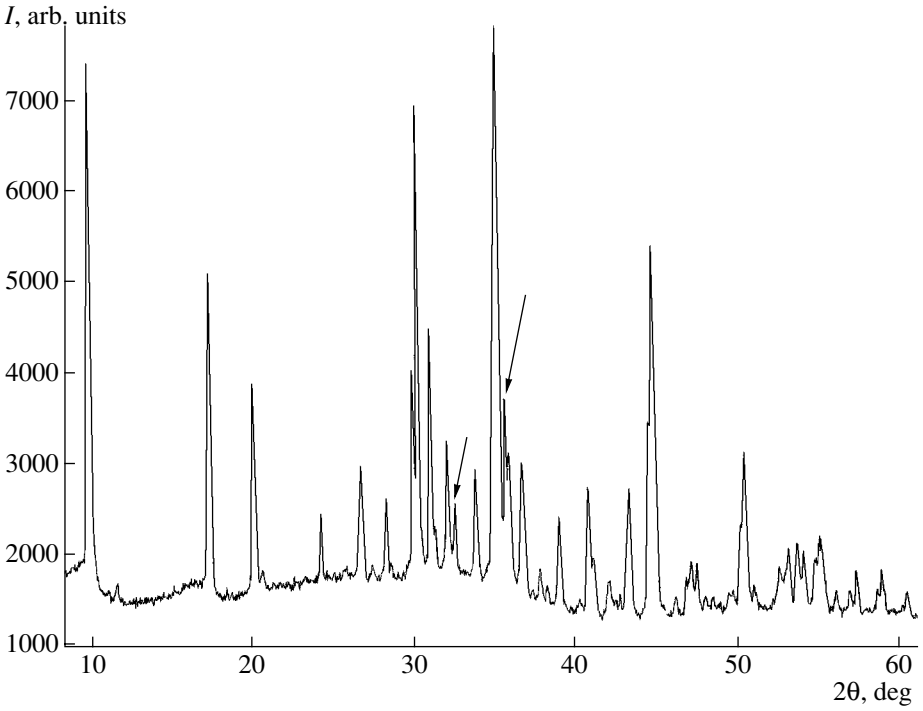

Fig. 3. X-ray diffraction spectrum of the powder of holtite **II**. The arrows indicate the two most intense reflections that cannot be indexed based on the nit-cell parameters indicated.

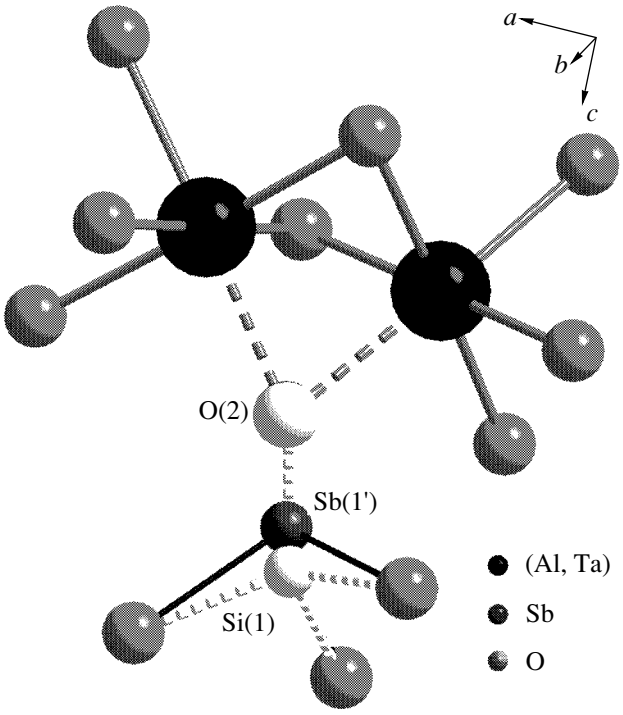

Fig. 4. The SbO_3 group in the structure of holtite **I**. Light spheres indicate the statistically occupied Si(1) and O(2) positions.

time, the distances between Sb and statistically occupied silicon and O(2) and O(7) positions are shortened considerably: {Sb(1')–[Si(1),As(1)] = 0.480(2) Å, Sb(2')–[Si(2),As(2)] = 0.549(1) Å}, and {Sb(1')–O(2) = 1.102(1) Å, Sb(2')–O(7) = 1.034(2) Å}. This corresponds to their mutually excluding location in the crystal structure. Moreover, such a configuration of the closest oxygen environment of the antimony atoms allows one to describe its stereochemistry as SbO_3E with lone electron pairs in the positions occupied by O(2) and O(7) in the $Si(1)O_4$ and $Si(2)O_4$ tetrahedra, respectively [9]. In this case, antimony is assumed to be present only in the valence state Sb^{3+}.

In [4], possible ordered replacement of silicon–oxygen tetrahedra by SbO_3 groups in the channels is admitted. It is not excluded that this may also happen in holtite **II** with an increase in the Sb content.

ACKNOWLEDGMENTS

This study was supported by the Russian Foundation for Basic Research, project no. 03-05-64054, and the program Russian Universities. N.V. Zubkova was supported by a grant of the president of the Russian Federation, no. MK 1046.2004.5. D.Yu. Pushcharovsky was supported by the program of the Russian–Italian Scientific Cooperation, project 1, appendix 3. The authors are also grateful to R.K. Rastsvetaeva for a number of valuable remarks.

REFERENCES

1. M. W. Pryce, Miner. Mag. **38**, 21 (1971).
2. A. V. Voloshin, Ya. A. Pakhomovskiĭ, and O. A. Zalkind, *Mineral Associates and Minerals of the Magmatic Complexes of the Kola Peninsula* (Kol. Fil. Akad. Nauk SSSR, 1987), p. 14 [in Russian].
3. L. A. Groat, E. S. Grew, T. S. Ercit, and A. Pieczka, in *Abstracts of the 18th General Meeting of the International Mineralogical Association* (Edinburgh, 2002), p. 209.
4. B. F. Hoskins, W. G. Mumme, and M. W. Pryce, Miner. Mag. **53**, 457 (1989).
5. G. M. Sheldrick, *SHELX97. Program for the Solution and Refinement of Crystal Structures* (Siemens Energy and Automation, Madison, WI, 1997).
6. N. E. Brese and M. O'Keeffe, Acta Crystallogr., Sect. B: Struct. Sci. **47**, 192 (1991).
7. J. Schneider, *Profile Refinement on IBM PC's. Workshop on the Rietveld Method* (Petten, 1989).
8. P. M. Moore and T. Araki, Neues Jahrb. Mineral., Abh. **132**, 231 (1978).
9. A. Wells, *Structural Inorganic Chemistry* (Clarendon Press, Oxford, 1984; Mir, Moscow, 1987), Vol. 2.

Translated by L. Man

Crystallography Reports, Vol. 50, No. 1, 2005, pp. 48–51. Translated from Kristallografiya, Vol. 50, No. 1, 2005, pp. 55–58.

STRUCTURE OF INORGANIC COMPOUNDS

Synthesis and Structure of New Thorium Phosphate $CaGdTh(PO_4)_3$

M. P. Orlova*, A. I. Orlova*, E. R. Gobechiya, Yu. K. Kabalov**, and G. I. Dorokhova****

** Department of Chemistry, Nizhni Novgorod State University, pr. Gagarina 23, Nizhni Novgorod, 603950 Russia*

e-mail: ormp@uic.nnov.ru

*** Faculty of Geology, Moscow State University, Vorob'evy gory, Moscow, 119992 Russia*

Received May 20, 2003

Abstract—Phosphate $CaGdTh(PO_4)_3$ was prepared by thermal treatment of a mixture of oxides. The final temperature was 1400°C. The phosphate was characterized by powder X-ray diffraction analysis and IR spectroscopy. The crystal structure was studied by the Rietveld method. The compound crystallizes in the monazite structure type (sp. gr. $P2_1/n$). A comparative analysis of the structures of this phosphate and cerium orthophosphate $CePO_4$ was carried out. © *2005 Pleiades Publishing, Inc.*

INTRODUCTION

The development of crystalline materials for immobilization of hazardous constituents of wastes from nuclear reactor fuel processing is an urgent problem, which has stimulated interest in natural minerals, including orthophosphates. Among the compounds used for these purposes, the monazite-like structure has attracted attention. Due to chemical, thermal, and radiation stability, this structure provides a high safety barrier for immobilized wastes during their storage for a long time and in the case of their disposal in geological formations [1].

Monazite is a relatively rare mineral, which occurs as an accessory mineral in granites, gneisses, aplites, and pegmatites and as rounded grains in weathering products of these rocks [2]. This mineral is stable over a wide range of conditions in various geological processes and is characterized by the ability to include lanthanides, actinides, and many other elements, which isomorphously replace cerium. Monazite species contain lanthanides (La > Nd > Pr > Sm > Gd) as constant isomorphous components up to a ratio of 1 : 1. Substantial amounts of the following elements were also found in monazite: Th (up to 32%), Si (up to 6.1%), Y (up to 5.1%), U (up to 6.6%), Ca (up to 6%), and S (up to 3%). Thorium and uranium replace cerium according to the schemes Th(U)Ca ⟶ 2Ce and Th(U)Si ⟶ CeP to form the mineral cerphosphorhuttonite $ThCeSiPO_8$. This is intermediate between monazite and huttonite (a monoclinic polymorph of thorite), which is isostructural with monazite. The second (tetragonal) modification of thorite is isostructural with zircon [3]. Cerium(III) orthophosphate $CePO_4$ (sp. gr. $P2_1/n$) [4] is a synthetic analogue of monazite.

It was demonstrated [5, 6] that lanthanides in oxidation state 3+ (cerium, samarium, europium, gadolinium), actinides in oxidation state 4+ (thorium, uranium, neptunium, plutonium), and cerium (4+) can be simultaneously involved in monazite-like phosphate compounds. It should also be noted that plutonium-containing phosphate ceramics with monazite-like structures were prepared in [7].

In this study, we examined new phosphate $CaGdTh(PO_4)_3$, which is a representative of a large group of compounds described by the general formula $B^{II}R^{III}M^{IV}(PO_4)_3$ with a cation-to-anion ratio of 1 : 1. The known orthophosphates of this group include alkaline-earth metals, cadmium, lanthanides (neodymium, samarium, europium, gadolinium), cerium(IV), thorium, and uranium(IV) [6].

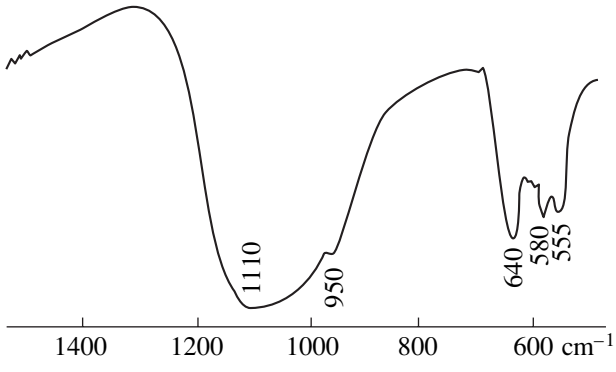

Fig. 1. IR spectrum of phosphate $CaGdTh(PO_4)_3$.

1063-7745/05/5001-0048$26.00 © 2005 Pleiades Publishing, Inc.

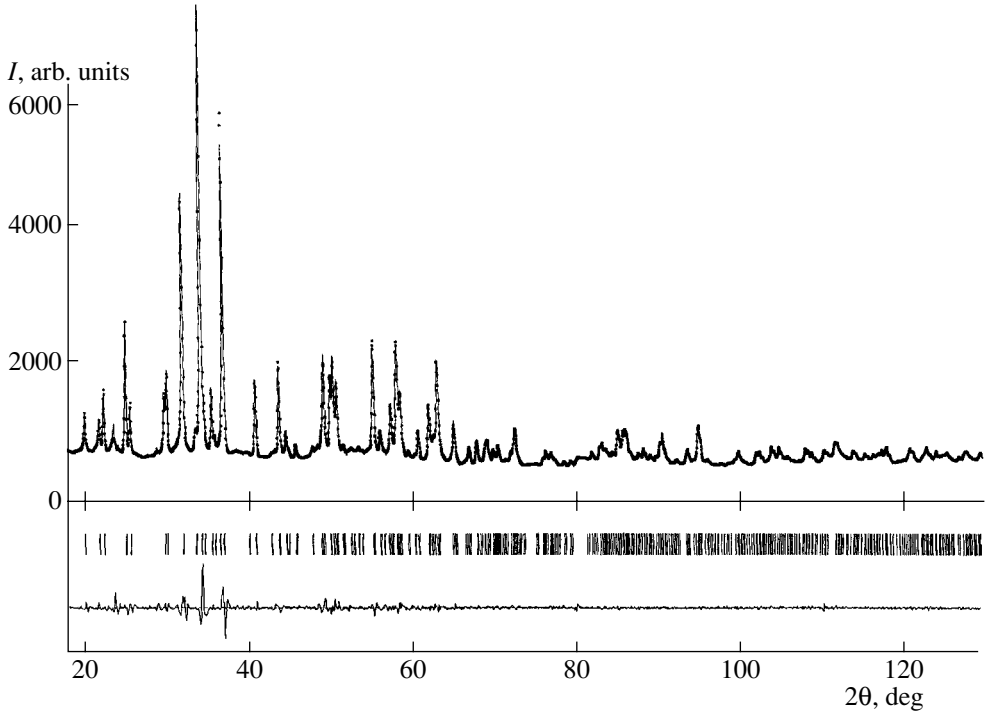

Fig. 2. X-ray diffraction spectra of phosphate $CaGdTh(PO_4)_3$. The theoretical and experimental spectra are shown by asterisks and a solid line, respectively.

EXPERIMENTAL

The procedure for the synthesis of the phosphate was described in [8]. Thorium oxide ThO_2 (reagent grade), gadolinium oxide Gd_2O_3 (reagent grade), calcium nitrate $Ca(NO_3)_2 \cdot 4H_2O$ (reagent grade), and H_3PO_4 (reagent grade) were used as the starting components. Stoichiometric amounts of metal oxides (thorium and gadolinium) were mixed, a 1 M solution of the calcium salt was added, and then a 1 M solution of phosphoric acid was added slowly with stirring. The resulting suspension was dried at 80°C for 24 h, heated, and kept successively at 600, 800, 1000, and 1200°C for 24 h at each temperature. Thermal treatment was alternated with grinding. As a result, a white polycrystalline compound was obtained.

The sample thus prepared was studied by IR spectroscopy, powder X-ray diffraction analysis, and X-ray structural analysis. The IR absorption spectrum was recorded on a Specord-75 IR spectrophotometer in the frequency range 1800–400 cm^{-1}. A sample was prepared as a neat film on a KBr substrate. The IR spectral pattern is analogous to that of cerium orthophosphates, which indicates that the compound under study belongs to orthophosphates. In the region of asymmetric stretching vibrations, the IR spectrum (Fig. 1) shows one broad band with a maximum at 1110 cm^{-1} instead of four narrow bands characteristic of cerium orthophosphate. This fact is indicative of strong disorder of the cations in the equivalent positions of the crystal structure of thorium phosphate.

The X-ray diffraction spectrum for thorium phosphate $CaGdTh(PO_4)_3$ was measured on an ADP-2 diffractometer and processed using the WYRIET program (version 3.3) [9]. The crystal structure of

Table 1. Unit-cell parameters and results of refinement of the crystal structure of $CaGdTh(PO_4)_3$

Parameters of refinement	
a, Å	6.6801(1)
b, Å	6.8849(1)
c, Å	6.3802(1)
β, deg	103.777(2)
V, Å^3	284.99
Space group	$P2_1/n$
2θ-scan range, deg	18.00–130.00
Number of reflections	682
Number of parameters in refinement	32
R_{exp}	3.54
R_{wp}	3.47
R_p	2.40
R_B	2.78
R_F	2.29
DWD*	0.14
S**	0.98

* The Durbin–Watson statistics.
** Goodness of fit [3].

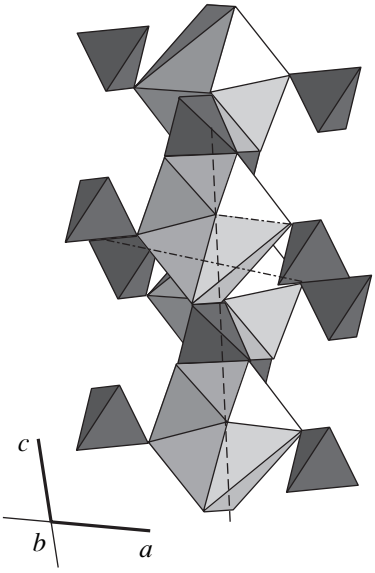

Fig. 3. Fragment of the $CaGdTh(PO_4)_3$ structure.

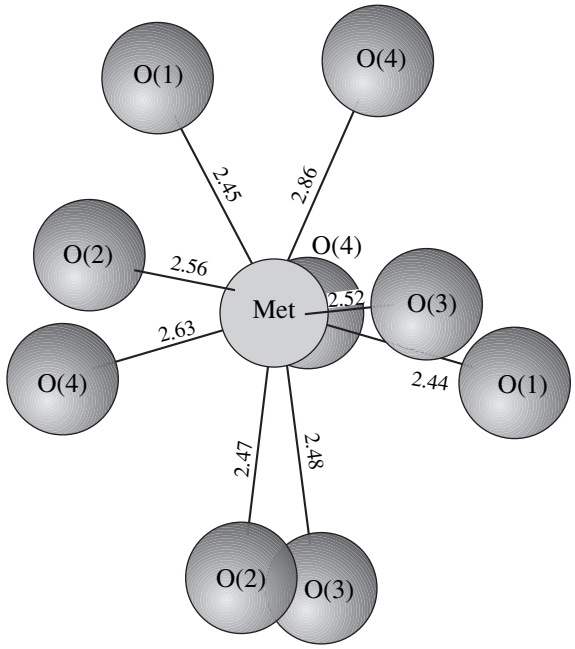

Fig. 4. Fragment of the structure of the $CaGdTh(PO_4)_3$ compound; the Met–O bond lengths in the Met polyhedron.

$CaGdTh(PO_4)_3$ was refined within the sp. gr. $P2_1/n$ using the structure of phosphate $Ca_{0.5}Ce_2(PO_4)_3$ [10] as the starting model. The peak profiles were approximated by the Pearson VII function. The crystal structure was refined isotropically by successively adding the parameters to be refined during graphical modeling of the background throughout the refinement until the *R* factors ceased to change. The structural parameters for six independent positions ([Ca, Gd, Ce], P, and four oxygen positions) were refined. Selected details of the X-ray data collection and the results of refinement of the $CaGdTh(PO_4)_3$ structure are given in Table 1. The calculated and experimental X-ray diffraction spectra of thorium phosphate are shown in Fig. 2 (dotted and solid lines, respectively).

The atomic coordinates, isotropic displacement parameters, and occupancies of the cation positions are listed in Table 2.

The crystal-chemical formula of the phosphate under study is $Ca_{1/3}Gd_{1/3}Th_{1/3}PO_4$.

RESULTS AND DISCUSSION

A metal atom in the structure of the new thorium phosphate, like in the monazite structure, is surrounded by nine oxygen atoms. $MetO_9$ polyhedra can be considered as strongly distorted monocapped square antiprisms. $[PO_4]$ orthotetrahedra share edges and vertices with cerium polyhedra to form a dense framework (Fig. 3).

A comparison of the interatomic distances in nine-vertex polyhedra of thorium phosphate and monazite [4] demonstrates that $MetO_9$ polyhedra are only slightly distorted. All interatomic distances have similar values, except for the Met–O(4) distance (2.86(1) Å for thorium phosphate and 2.779(6) Å for $CePO_4$) (Fig. 4). PO_4 tetrahedra are more strongly distorted, as

Table 2. Atomic coordinates, occupancies, and displacement parameters for the $CaGdTh(PO_4)_3$ structure

Position	Occupancy	*x*	*y*	*z*	B_{iso}
[Ca/Gd/Th]	1	0.2189(6)	0.1612(6)	0.3968(6)	0.84(2)
P	1	0.197(6)	0.161(2)	0.884(2)	1.40(9)
O(1)	1	0.244(5)	0.513(4)	0.438(5)	1.1(3)
O(2)	1	0.020(5)	0.104(4)	0.692(4)	1.9(3)
O(3)	1	0.368(4)	0.215(4)	0.781(4)	1.9(3)
O(4)	1	0.111(4)	0.328(5)	−0.001(5)	0.9(2)

evidenced by the O–P–O bond angles ($\Delta_{max-min}$ = 9.3° and 14.4° for $CePO_4$ and $CaGdTh(PO_4)_3$, respectively). The unit-cell parameters of $CaGdTh(PO_4)_3$ are smaller than those of monazite. The structure is uniformly contracted along the *a* and *b* axes to the same extent (by 1.5%), whereas the contraction along the *c* axis is somewhat smaller (by approximately 1%). The contraction along all axes resulted in a decrease in the unit-cell volume (4%). These anisotropic changes in the unit-cell parameters are associated with the distortion of phosphate tetrahedra.

The contraction of the structure can be explained by the replacement of cerium with calcium, gadolinium, or thorium: nine-vertex polyhedra are occupied predominantly by cations with smaller ionic radii ($r_{Ce(III)}$ = 1.20 Å, $r_{Ca(II)}$ = 1.18 Å, $r_{Gd(III)}$ = 1.1 Å, and $r_{Th(IV)}$ = 1.09 Å, according to Shannon and Prewitt [11]).

We plan to perform detailed analysis of monazite-like structures of various compounds separately.

ACKNOWLEDGMENTS

We are grateful to V.S. Kurazhkovskaya for her help in recording and interpreting the IR spectrum.

This study was supported by the Russian Foundation for Basic Research (project nos. 01-03-33013 and 03-05-64054) and the program Universities of Russia.

REFERENCES

1. *Radioactive Waste Forms for the Future*, Ed. by W. Lutze and R. S. Ewing (North-Holland, Amsterdam, 1988), p. 495.
2. S. A. Povarennykh, *Crystal Chemical Studies of Minerals* (Naukova Dumka, Kiev, 1966), p. 416 [in Russian].
3. *Minerals*, Ed. by N. V. Chukhrov (Naukova Dumka, Kiev, 1976), Vol. 3.1, p. 273 [in Russian].
4. G. W. Beall, L. A. Boatner, D. F. Millica, and W. O. Milligan, J. Inorg. Nucl. Chem. **43** (1), 101 (1981).
5. Yu. F. Volkov, Radiokhimiya **41** (2), 161 (1999).
6. A. I. Orlova, D. B. Kitaev, and D. B. Kemenov, Radiokhimiya **45** (2), 97 (2003).
7. Yu. F. Volkov, S. V. Tomilin, A. I. Lukinykh, *et al.*, Radiokhimiya **44** (4), 293 (2002).
8. A. I. Orlova, D. B. Kitaev, G. N. Kazantsev, *et al.*, Radiokhimiya **44** (4), 299 (2002).
9. J. Schneider, in *Profile Refinement on IBM-PC: Proceedings of International Workshop on the Rietveld Method* (Petten, Holland, 1989), p. 71.
10. N. V. Zubkova, Yu. K. Kabalov, A. I. Orlova, *et al.*, Kristallografiya **48** (3), 445 (2003) [Crystallogr. Rep. **48**, 401 (2003)].
11. R. D. Shannon, Acta Crystallogr., Sect. A: Cryst. Phys., Diffr., Theor. Gen. Crystallogr. **32**, 751 (1976).

Translated by T. Safonova

Crystallography Reports, Vol. 50, No. 1, 2005, pp. 52–57. Translated from Kristallografiya, Vol. 50, No. 1, 2005, pp. 59–64.

STRUCTURE OF INORGANIC COMPOUNDS

Synthesis and Structure of New Phases of the $A_{m-1}Bi_2B_mO_{3m+3}$ (m = 2) Type

G. A. Geguzina, A. T. Shuvaev, E. T. Shuvaeva, L. A. Shilkina, and V. G. Vlasenko

Research Institute of Physics, Rostov State University, pr. Stachki 194, Rostov-on-Don, 344090 Russia

e-mail: denis@ip.rsu.ru

Received May 29, 2003

Abstract—Three polycrystalline bismuth-containing layered perovskite-like oxides are synthesized by high-temperature solid-state reactions. One of these compounds was described previously, namely, $Bi_3Ti_{1.5}W_{0.5}O_9$, for which the unit cell parameters a = 5.372(5) Å, b = 5.404(4) Å, and c = 24.95(2) Å are determined in this study. The other two compounds, namely, $Na_{0.75}Bi_{2.25}Nb_{1.5}W_{0.5}O_9$ with the unit cell parameters a = 5.463(1) Å, b = 5.490(7) Å, and c = 24.78(0) Å and $Ca_{0.5}Bi_{2.5}Ti_{0.5}Nb_{1.5}O_9$ with the unit cell parameters $a = b$ = 3.843(2) Å and c = 24.97(6) Å, are synthesized for the first time. The compositions of these compounds are based on the composition of the well-known compound Bi_3TiNbO_9 with a high Curie temperature (T_C = 1223 K), in which bismuth, niobium, and titanium atoms are partially or completely replaced by other atoms. The experimental and calculated interplanar distances determined from the X-ray diffraction patterns of the studied compounds are presented. © *2005 Pleiades Publishing, Inc.*

INTRODUCTION

Bismuth-containing layered perovskite-like oxides of the general formula

$$A_{m-1}Bi_2B_mO_{3m+3}, \quad (1)$$

where m takes on values from 1 to 10 (1, 1.5, 2, 2.5, 3, 3.5, 4, 5, 6, 7, 8, 9, 10), have been studied for a long time [1–14]. The structure of these compounds is formed by alternating stacks composed of perovskite-like layers of the composition $[A_{m-1}B_mO_{3m+1}]^{2-}$ and bismuth–oxygen layers of the composition $[Bi_2O_2]^{2+}$, which are aligned parallel to each other and are perpendicular to the c axis [6, 10]. Each stack contains m perovskite-like layers.

The bismuth-containing layered perovskite-like oxides known to date belong to a relatively small structural family [15, 16]. Virtually all representatives of this family are ferroelectrics with high Curie temperatures [10–14]. This has given impetus to the search for new bismuth-containing layered perovskite-like oxides and their synthesis [17, 18]. The present work is aimed at solving these problems. The synthesis and structural investigation of new bismuth-containing layered perovskite-like oxides will make it possible not only to extend the family of these compounds but also to elucidate how different atoms in their composition affect the possibility of forming a layered structure, the structural parameters, the phase transition temperatures, and the physical properties.

Although the number of known bismuth-containing layered perovskite-like oxides with m = 2 is rather large, the systematics [15] and analysis of the conditions for the formation of these compounds [11] indicate that the possibility exists of preparing their new representatives. The smallest lattice parameters a and b and the highest Curie temperature (T_C = 1223 K) are observed for the Bi_3TiNbO_9 compound [10]. In this respect, it is of interest to investigate how variations in its composition affect the unit cell parameters and the Curie temperature. For this purpose, we chose eight compositions with m = 2, in which the Bi^{III}, Ti^{IV}, and (or) Nb^{V} atoms in the Bi_3TiNbO_9 compound were partially or completely replaced by other atoms. The bismuth atoms were replaced by Na^{I}, K^{I}, or Ca^{II} atoms, whereas the titanium and (or) niobium atoms were replaced by Fe^{III}, Ta^{V}, and (or) W^{VI} atoms [17]. As a result, we synthesized three single-phase polycrystalline oxides of the following compositions: $Bi_3Ti_{1.5}W_{0.5}O_9$, $Na_{0.75}Bi_{2.25}Nb_{1.5}W_{0.5}O_9$, and $Ca_{0.5}Bi_{2.5}Ti_{0.5}Nb_{1.5}O_9$. Bismuth-containing layered perovskite-like oxides with the second and third compositions were prepared for the first time. The $Bi_3Ti_{1.5}W_{0.5}O_9$ compound was described earlier by Kikuchi [19]. However, the unit cell parameters of this compound were determined with a low accuracy and the properties and phase transitions were not investigated in [19]. The X-ray diffraction patterns of the other five new compounds contain the lines assigned to the main phase with a layered structure and additional lines attributed to impurities.

1063-7745/05/5001-0052$26.00 © 2005 Pleiades Publishing, Inc.

Table 1. Chemical composition, X-ray density, synthesis conditions, and unit cell parameters of the orthorhombic and tetragonal phases of bismuth-containing layered perovskite-like oxides

Composition no.	Chemical composition, (ρ, g/cm^3)	Heat treatment conditions	Parameters (Å) and volume (Å^3) of the unit cell						
		temperature (°C) – time (h)	$a_{orthorh}$ or a_{tetr}	$b_{orthorh}$ or b_{tetr}	c	$a^{-exp}_{pseudotetr}$	$a^{-calcd}_{pseudotetr}$	$V_{un.cell}$	$V_{pseudotetr.cell}$
Orthorhombic unit cells, space group $Fmmm = D^{23}_{2h}$ (69)									
1	$Bi_3Ti_{1.5}W_{0.5}O_9$ (8.62)	$t_1 = 740 – 3$, $t_2 = 850 – 4$, $t_3 = 1100 – 1$	5.372(3)	5.404(4)	24.95(2)	3.810	3.817	724.3	362.2
	$Bi_3Ti_{1.5}W_{0.5}O_9$ (8.62) [19]	$t = 1100$ in air	5.38	5.40	24.96	3.81	3.82	722.4	362.3
2	$Na_{0.75}Bi_{2.25}Nb_{1.5}W_{0.5}O_9$ (7.75)	$t_1 = 800 – 2$, $t_2 = 900 – 2$	5.463(5)	5.490(7)	24.79(1)	3.873	3.852	743.1	371.9
Tetragonal unit cell, space group $I4/mmm = D^{17}_{4h}$ (139)									
3	$Ca_{0.5}Bi_{2.5}Ti_{0.5}Nb_{1.5}O_9$ (8.62)	$t_1 = 800 – 2$, $t_2 = 900 – 2$	3.848(4)	3.848(4)	24.98(4)	3.843	3.874	368.9	369.8

CHEMICAL COMPOSITIONS OF THE COMPOUNDS SYNTHESIZED

When formulating the compositions of the three synthesized compounds, the Bi^{III} atoms in the *A* positions and the Ti^{IV} or Nb^{V} atoms in the *B* positions in the Bi_3TiNbO_9 structure were partially or completely replaced by other atoms whose valences did not lead to disturbance of the valence balance of the chemical formulas. The chemical formula of bismuth-containing layered perovskite-like oxides of the complex composition can be written in the form

$$(A^1_{\alpha_1},\ldots,A^i_{\alpha_i},\ldots,A^p_{\alpha_p})Bi_2(B^1_{\beta_1},\ldots,B^j_{\beta_j},\ldots,B^q_{\beta_q})O_{3m+3}, \quad (2)$$

where $\sum_{i=1}^{p}\alpha_1 = m-1$ and $\sum_{j=1}^{q}\beta_j = m$. According to formulas (1) and (2), the composition of each of the bismuth-containing layered perovskite-like oxides synthesized can be represented in two variants

$$\begin{aligned} Bi_3Ti_{1.5}W_{0.5}O_9 &= (\underline{Bi})Bi_2(\mathbf{Ti}_{1.5}\mathbf{W}_{0.5})O_9;\\ Na_{0.75}Bi_{2.25}Nb_{1.5}W_{0.5}Q_9 &= (\mathbf{Na}_{0.75}Bi_{0.25})Bi_2(\mathbf{Nb}_{1.5}\mathbf{W}_{0.5})O_9;\\ Ca_{0.5}Bi_{2.5}Ti_{0.5}Nb_{1.5}O_9 &= (\mathbf{Ca}_{0.5}Bi_{0.5})Bi_2(\mathbf{Ti}_{0.5}Nb_{1.5})O_9. \end{aligned} \quad (3)$$

In the second variant of the above formulas, two bismuth atoms located in $(Bi_2O_2)^{2-}$ layers are taken out of the parentheses that include atoms occupying the A^i or B^j positions in perovskite-like layers. In the Bi_3TiNbO_9 lattice, the atoms marked with bold type partially or completely replace either bismuth atoms in the *A* positions, or titanium (niobium) atoms in the *B* positions, or these atoms in all positions simultaneously. In composition **1**, the unsubstituted atoms Bi^{III} are underlined.

In composition **1**, one niobium atom is replaced by one-half the titanium atom and one-half the tungsten atom. In this case, the content of Ti^{IV} atoms increases, whereas the content of bismuth atoms remains unchanged. In composition **2**, one titanium atom was replaced by one-half the niobium atom and one-half the tungsten atom, whereas the Bi^{III} atoms are partially replaced by sodium atoms. In composition **3**, the content of titanium atoms is halved, the content of niobium atoms in the B^j positions is twice increased, and one-half the Bi^{III} atom in the A^i positions is replaced by one-half the Ca^{II} atom. As a result, the perovskite-like layers do not contain Nb^{V} atoms in composition **1** and titanium atoms in composition **2**. According to the X-ray diffraction data, compounds **1** and **2** crystallize in the orthorhombic crystal system (space group $Fmmm = D^{23}_{2h}$) and compound **3** crystallizes in the tetragonal system (space group $I4/mmm = D^{12}_{4h}$) (Table 1).

SAMPLE PREPARATION AND EXPERIMENTAL TECHNIQUE

Polycrystalline (ceramic) samples of new bismuth-containing layered perovskite-like oxides and $Bi_4Ti_3O_{12}$ were prepared by high-temperature solid-state reactions in two or three stages with thorough stirring of the stoichiometric mixture of the initial components and intermediate reaction products. The synthesis of bismuth-containing layered perovskite-like oxides, especially with a complex composition, involves a number of problems. In particular, it is necessary to

choose the initial components and an optimum combination of temperatures and durations of the intermediate and final sinterings in such a way that the corresponding reaction proceeds to completion (see Table 1).

The compounds Bi_2O_3, $CaCO_3$, $NaHCO_3$, Nb_2O_5, TiO_2, and WO_3 (predominantly high-purity grade) were used as initial components of the batch. The samples for sintering were prepared from powders of a mixture of initial components in the form of disks 10 mm in diameter and 3–4 mm thick. The synthesis was performed in a laboratory muffle furnace in air. The first sinterings were carried out at relatively low temperatures (from 1013 to 1073 K). The temperatures of subsequent sinterings were increased by 100–200 K. The duration of each sintering was relatively short (no longer than 4 h).

It should be noted that, after the first stage of the synthesis, the main phase in samples of the compounds under investigation was a layered phase of the specified composition with an orthorhombic or tetragonal structure. The subsequent sinterings were performed in order to complete the reaction. The optimum synthesis conditions were chosen and the unit cell parameters of the perovskite-like oxides were determined (with a relative error of no more than ±0.05%) using X-ray powder diffraction analysis at room temperature.

The structures of compounds **1**–**3** were investigated on a DRON-2 diffractometer (Fe$K\alpha_{1,2}$ radiation, Mn filter). The diffraction patterns in the 2θ range from 4° to 110° were obtained using an automatic recorder (scan speed, 0.5 and 1 deg/min; writing speed, 600 mm/h). The intensities of the diffraction lines were determined from their height at the maximum with respect to the background. The X-ray diffraction patterns were indexed by the analytical technique. According to the indexing, the space group *Fmmm* was assigned to compounds **1** and **2**, whereas the space group *I*4/*mmm* was attributed to compound **3**. The unit cell parameters were refined by the least-squares procedure with the use of all the reflections measured in the experiment.

In order to confirm the reliability of the unit cell parameters thus determined, we calculated the de Wolff factors M_{20} [20] for all the studied compounds. This factor characterizes the magnitude of the mean deviation of the reciprocals of the interplanar distances for the first 20 lines in the observed diffraction pattern from the corresponding quantities d_{hkl}, which were calculated within the used model for the lines possible in the same angle range. The de Wolff factor depends on the number N_{pos} of possible (calculated) lines and the magnitude of the mean deviation $|\overline{\Delta Q}|$. In this work, the factor M_{20} was calculated from the formula

$$M_{20} = \frac{1}{2d_{20}^2|\overline{\Delta Q}|}\frac{}{N_{pos}}(|\overline{\Delta Q}|N_{pos}), \qquad (4)$$

where $Q_i = \frac{1}{d_{(i)exp}^2} - \frac{1}{d_{(i)calcd}^2}$ and i is the number of observed reflection.

The X-ray diffraction patterns of all the three compounds synthesized did not contain lines that could be attributed to both the unreacted components of the initial batch or the other phases formed upon sintering. This confirms the assumption that these compounds have a single-phase composition.

STRUCTURES OF THE PHASES SYNTHESIZED

Tables 2 and 3 present the interplanar distances (both determined in the experiment and calculated in accordance with the chosen lattice parameters); the indices *h*, *k*, and *l*; and the relative intensities of the reflections for the orthorhombic and tetragonal bismuth-containing layered perovskite-like oxides, respectively. The calculated reliability factors M_{20} for all the compounds and, especially, sufficiently small mean deviations of the calculated 2θ angles from the experimentally observed 2θ angles (see Tables 2, 3) demonstrate that the X-ray diffraction patterns are reliably indexed within the assigned space groups.

The unit cell parameters of the new orthorhombic and tetragonal bismuth-containing layered perovskite-like oxides of compositions **2** and **3**, the previously known orthorhombic bismuth-containing oxide of composition **1**, and the initial Bi_3TiNbO_9 compound (according to the data available in the literature) are listed in Table 1. The mean parameters of the pseudotetragonal unit cells, which were determined experimentally ($\bar{a}^{exp}_{pseudotetr}$) and calculated directly from the specified chemical composition ($\bar{a}^{calcd}_{pseudotetr}$) according to the method proposed in [11], and the unit cell volumes $V_{un.cell}$ and $V_{pseudotetr.cell}$, which were obtained from the experimental data, are also given in Table 1. The parameters $\bar{a}^{exp}_{pseudotetr}$ were calculated from the experimental parameters $a_{orthorh}$ and $b_{orthorh}$ of the orthorhombic unit cell with the use of the formula [9]

$$\bar{a}^{exp}_{pseudotetr} = (a_{orthorh} + b_{orthorh})/2\sqrt{2}. \qquad (5)$$

Moreover, Table 1 presents the unit cell parameters of the tetragonal phases of bismuth-containing layered perovskite-like oxides $a_{tetr} = b_{tetr}$ and c, their unit cell volumes $V_{un.cell}$, and the parameters calculated for the tetragonal unit cell according to the above method [11].

The reliability of the unit cell parameters and unit cell volumes determined for the bismuth-containing layered perovskite-like oxides under investigation and the identity of their compositions to the specified compositions (i.e., their single-phase composition) can also be judged from the following indirect evidence. First,

Table 2. Experimental (d_{exp}) and calculated (d_{calcd}) interplanar distances (Å); relative intensities (I/I_0); indices h, k, and l; and reliability factors for indexing of lines in the X-ray diffraction patterns of the orthorhombic phases of bismuth-containing layered perovskite-like oxides

Phase	$Bi_3Ti_{1.5}W_{0.5}O_9$			$Na_{0.75}Bi_{2.25}Nb_{1.5}W_{0.5}O_9$		
$h\ k\ l$ and factors	I/I_0	d_{exp}	d_{calcd}	I/I_0	d_{exp}	d_{calcd}
0 0 2				23	12.39	12.39
0 0 4	14	6.25	6.24	10	6.20	6.20
1 1 1	10	3.768	3.767	5	3.826	3.826
1 1 3	4	3.466	3.464	10	3.505	3.506
0 0 8	4	3.119	3.119	44	3.099	3.097
1 1 5	100	3.028	3.029	100	3.050	3.051
0 2 0	21	2.702	2.702	25	2.745	2.745
2 0 0	20	2.686	2.686	25	2.731	2.731
1 1 7				3	2.611	2.613
0 0 10	13	2.495	2.495	30	2.478	2.478
0 2 4	3	2.480	2.479			
0 2 6	6	2.264	2.266	2	2.288	2.286
2 0 6	7	2.257	2.256	4	2.279	2.278
1 1 9	6	2.241	2.242	5	2.345	2.244
0 2 8				3	2.055	2.054
1 1 11	2	1.948	1.949			
2 0 8				5	2.049	2.049
2 2 0	16	1.9047	1.9049	17	1.9359	1.9362
2 2 2				4	1.9137	1.9130
2 2 4				7	1.8477	1.8480
0 2 10	9	1.8328	1.8330	12	1.8389	1.8393
2 0 10	15	1.8282	1.8280	16	1.8350	1.8353
0 0 14				3	1.7704	1.7700
2 2 6	2	1.7309	1.7318			
1 1 13	4	1.7143	1.7140	10	1.7106	1.7102
0 2 12				4	1.6506	1.6502
1 3 1	3	1.7034	1.7038			
2 2 8				5	1.6420	1.6418
1 3 5	11	1.6148	1.6158	18	1.6380	1.6376
3 1 5	13	1.6094	1.6091	19	1.6322	1.6320
0 0 16				3	1.5484	1.5488
1 1 15	7	1.5241	1.5243	10	1.5201	1.5201
2 2 10	7	1.5138	1.5141	7	1.5259	1.5261
0 2 14	2	1.4876	1.4871	4	1.4873	1.4875
2 0 14	2	1.4851	1.4850	4	1.4852	1.4854
1 3 9	3	1.4536	1.4540			
3 1 9	2	1.4489	1.4491			
0 0 18				3	1.3766	1.3767
0 4 0	8	1.3511	1.3510	5	1.3726	1.3724
4 0 0	8	1.3436	1.3431	5	1.3657	1.3657
2 2 14	4	1.3012	1.3014			
1 1 17				4	1.3640	1.3642
0 0 20	4	1.2475	1.2474			
1 1 19	6	1.2413	1.2414			
3 3 5	13	1.2308	1.2307			
2 4 0	9	1.2066	1.2069			
4 2 0	9	1.2025	1.2027			
1 3 15	15	1.1915	1.1915			
3 1 15	15	1.1888	1.1888			
Factor	M_{20} = 45.72 (0.0001, 38)			M_{20} = 55.27 (0.0001, 27)		

Table 3. Experimental (d_{exp}) and calculated (d_{calcd}) interplanar distances (Å); relative intensities (I/I_0); indices *h*, *k*, and *l*; and reliability factors for indexing of lines in the X-ray diffraction patterns of the tetragonal phase $Ca_{0.5}Bi_{2.5}Ti_{0.5}Nb_{1.5}O_9$

h, *k*, *l* and factor	I/I_0	d_{exp}	d_{calcd}
0 02	7	12.52	12.49
0 0 4	8	6.25	6.24
1 0 1	4	3.799	3.798
1 0 3	10	3.489	3.489
0 0 8	7	3.126	3.122
1 0 5	100	3.049	3.046
1 1 0	21	2.719	2.718
1 0 7	3	2.614	2.615
0 0 10	16	2.497	2.497
1 1 6	6	2.277	2.276
1 0 9	8	2.253	2.250
1 1 8	5	2.049	2.050
1 0 11	2	1.957	1.955
2 0 0	14	1.922	1.922
1 1 10	18	1.839	1.839
0 0 14	2	1.785	1.784
1 0 13	6	1.718	1.718
2 1 3	3	1.683	1.683
2 1 5	15	1.6251	1.6252
0 0 16	2	1.5612	1.5610
1 0 15	9	1.5272	1.5278
1 1 14	2	1.4917	1.4913
2 1 9	2	1.4613	1.4612
0 0 18	2	1.3876	1.3875
2 2 0	2	1.3588	1.3588
Factor	M_{20} = 55.58 (0.00012, 30)		

the difference between the parameters $\bar{a}^{calcd}_{pseudotetr}$ calculated from the lengths of the unstrained interatomic bonds A^i–O and B^j–O and the experimental parameters $\bar{a}^{exp}_{pseudotetr}$ is considerably less than 1% (the accuracy of the method proposed in [11]). This primarily indicates that the compositions of the synthesized compounds correspond to the specified compositions.

Second, the similarity of the compositions of the prepared compounds to the nominal compositions is confirmed by the fact that the volumes of the pseudotetragonal (for the orthorhombic bismuth-containing perovskite-like oxides) and tetragonal unit cells for all the bismuth-containing perovskite-like oxides synthesized regularly vary as compared to the unit cell volume of the initial compound. These volumes are determined primarily by the sizes of the oxygen-octahedral structural framework, which is formed by the B^j atoms. Therefore, these volumes depend on the valence of the B^j atoms replacing the Ti^{IV} and Nb^{V} atoms in the lattice of the initial compound, their content, and the lengths of the unstrained interatomic bonds B^j–O [16].

An increase in the valence of the B^j atoms replacing the niobium atoms in perovskite-like layers of the initial lattice and a simultaneous decrease in the length of the unstrained W^{VI}–O interatomic bond lead to a regular decrease in the parameters $V_{pseudotetr.cell}$ and $\bar{a}^{exp}_{pseudotetr}$ for compound **1**. By contrast, an increase both in the valence of the B^j atoms replacing the Ti^{IV} atoms and in the length of the unstrained Nb^{V}–O interatomic bond result in an increase in the parameters $V_{pseudotetr.cell}$ and $\bar{a}^{exp}_{pseudotetr}$ for compound **2**, even though the W^{VI} atoms involved in a shorter interatomic bond partially occupy the B^j positions. It is worth noting that, in this case, the A^i atoms replacing the Bi^{III} atoms play a secondary role.

The replacement of the bismuth atoms by the Na^{I} or Ca^{II} atoms, which have a lower valence and form unstrained A^i–O bonds that are shorter than the Bi–O bonds in compounds **2** and **3**, only slightly affects the unit cell volume $V_{pseudotetr.cell}$ but leads to a decrease in the parameter *c*. The lattice parameter $\bar{a}^{exp}_{pseudotetr}$ substantially decreases for structure **2** and remains virtually unchanged for structure **3**.

CONCLUSIONS

Thus, two new bismuth-containing layered perovskite-like oxides of complex compositions with $m = 2$ and one oxide described previously were synthesized. The compositions of the oxides synthesized were identified on the basis of close agreement between the experimental and calculated parameters of their structures. It was demonstrated that the unit cell parameters of these compounds regularly change with a variation in the chemical composition.

ACKNOWLEDGMENTS

This work was supported by the Ministry of Education of the Russian Federation (project no. E00-3.4-560) and the Russian Foundation for Basic Research (project no. 02-03-33225).

REFERENCES

1. B. Aurivillius, Ark. Kemi **1**, 463 (1949).
2. B. Aurivillius, Ark. Kemi **1**, 499 (1949).
3. B. Aurivillius, Ark. Kemi **2**, 512 (1950).
4. B. Aurivillius and P. H. Fang, Phys. Rev. **126**, 893 (1962).
5. E. C. Subbarao, J. Phys. Chem. Solids **23**, 665 (1962).

6. G. I. Ismailzade, V. I. Nesterenko, F. A. Mirishli, and P. G. Rustamov, Kristallografiya **12**, 468 (1967) [Sov. Phys. Crystallogr. **12**, 400 (1967)].
7. G. A. Smolenskiĭ, V. A. Isupov, and A. I. Agranovskaya, Fiz. Tverd. Tela (Leningrad) **3**, 895 (1971) [Sov. Phys. Solid State **3**, 651 (1971)].
8. T. Kikuchi, A. Watanabe, and K. Uchida, Mater. Res. Bull. **12**, 299 (1977).
9. T. Kikuchi, Mater. Res. Bull. **14**, 1561 (1979).
10. G. A. Smolenskiĭ, V. A. Bokov, V. A. Isupov, N. N. Kraĭnik, R. E. Pasynkov, A. I. Sokolov, and N. K. Yushin, *Physics of Ferroelectric Phenomena* (Nauka, Leningrad, 1985) [in Russian].
11. G. A. Geguzina, E. G. Fesenko, and E. T. Shuvaeva, Ferroelectrics **167**, 311 (1995).
12. V. A. Isupov, Ferroelectrics **189**, 211 (1996).
13. L. A. Reznichenko, O. N. Razumovskaya, L. A. Shilkina, and N. V. Dergunova, Neorg. Mater. **32**, 474 (1996).
14. V. A. Isupov, Neorg. Mater. **33**, 1106 (1997).
15. G. A. Geguzina, Kristallografiya **47**, 983 (2002) [Crystallogr. Rep. **47**, 913 (2002)].
16. G. A. Geguzina, *Advances in Structure Analysis* (Chech and Slovak Crystallographic Association, Praha, 2000), p. 223.
17. G. A. Geguzina, A. T. Shuvayev, S. G. Gakh, and E. T. Shuvayeva, Kristallografiya **48**, 395 (2003) [Crystallogr. Rep. **48**, 359 (2003)].
18. G. A. Geguzina, A. T. Shuvayev, E. T. Shuvayeva, *et al.*, Kristallografiya **48**, 450 (2003) [Crystallogr. Rep. **48**, 406 (2003)].
19. T. Kikuchi, J. Less-Common Met. **48**, 319 (1976).
20. P. M. de Wolff, J. Appl. Crystallogr. **1**, 108 (1968).

Translated by O. Borovik-Romanova

Crystallography Reports, Vol. 50, No. 1, 2005, pp. 58–60. Translated from Kristallografiya, Vol. 50, No. 1, 2005, pp. 65–67.

STRUCTURE OF ORGANIC COMPOUNDS

Crystal Structure of *L*-Serine Phosphate

Yu. I. Smolin*, A. E. Lapshin*, and G. A. Pankova**

** Grebenshchikov Institute of Silicate Chemistry, Russian Academy of Sciences, ul. Odoevskogo 24/2, St. Petersburg, 199155 Russia*

e-mail: smolin@isc.nw.ru

*** Institute of Macromolecular Compounds, Russian Academy of Sciences, Bol'shoĭ pr. 31, St. Petersburg, 119004 Russia*

Received March 4, 2003

Abstract—The crystal structure of *L*-serine phosphate ($C_3O_3NH_7 \cdot H_3PO_4$) is determined by single-crystal X-ray diffraction. The unit cell parameters are as follows: $a = 9.134(5)$ Å, $b = 9.489(5)$ Å, $c = 4.615(5)$ Å, $\gamma = 99.54(5)°$, space group $P2_1$, and $Z = 2$. The amino group of serine is protonated by a hydrogen atom of the phosphoric acid. The $H_2PO_4^{1-}$ ions are linked by hydrogen bonds into infinite ribbons aligned along the twofold screw axes. The ribbons form layers alternating with layers of serine molecules, which are directly linked by hydrogen bonds. © *2005 Pleiades Publishing, Inc.*

INTRODUCTION

Owing to their specific structural features, inorganic derivatives of protein amino acids are of great interest for both the search for new pyroelectric and piezoelectric materials and the understanding of the role played by the electrical characteristics of protein amino acids in the processes occurring in living organisms. The structures of β-alanine, *DL*-alanine, sarcosine, and *L*-alanine phosphates were studied earlier in [1, 2]. The aim of this work is to determine the crystal structure of *L*-serine phosphate, which, according to the data available in the structural database [3], has not been investigated yet. *L*-serine phosphate exhibits piezoelectric properties [4].

EXPERIMENTAL

The crystals studied were prepared through slow evaporation of a saturated aqueous solution containing serine and H_3PO_4 at pH < 2 in an LKB-Bromma thermostat operating in the temperature range from –10 to +40°C with an error of 0.5°. The temperature of the solution decreased from 25 to 8°C at a rate of 1°C daily. The unit cell parameters of the crystal are as follows: $a = 9.134(5)$ Å, $b = 9.489(5)$ Å, $c = 4.615(5)$ Å, $\gamma = 99.54(5)°$, space group $P2_1$, and $Z = 2$.

The intensities of X-ray reflections were measured in layers on an automated single-crystal diffractometer operating according to the perpendicular beam scheme using MoK_α radiation monochromated with pyrolytic graphite. A total of 1572 unique nonzero reflections with $I \geq 3\sigma(I)$ were measured in the index range $h(0.15)$ $k(–15.15)$, and $l(0.4)$ up to $2\theta_{max} = 72°$. The integrated intensities and the correction for the background were determined using an algorithm of the profile analysis [5]. The stability of the crystal was checked by periodic measurements of the intensities of the control reflection. The coordinates of the non-hydrogen atoms were determined by direct methods with the AREN program package [6]. All the hydrogen atoms were located from a series of difference syntheses that alternated with the least-squares refinement of the positional and thermal atomic parameters on $F^2(hkl)$ with the SHELXL97 program [7]. The thermal parameters of the non-hydrogen and hydrogen atoms were refined in the anisotropic and isotropic approximations, respectively. The final R_1 and wR_2 factors calculated for all the reflections measured are 0.038 and 0.10, respectively. The total number of the parameters refined was 149; $S = 1.03$. The results of the refinement are given in Table 1. The projection of the structure of *L*-serine phosphate along the *c* axis is shown in the figure, which was drawn using the ORTEP III program [8].

The crystal data have been deposited with the Cambridge Structural Database (no. CCDC 201070).

RESULTS AND DISCUSSION

As is seen from the figure, the amino group of serine is protonated by a hydrogen atom of phosphoric acid. Tetrahedral $H_2PO_4^{1-}$ ions are linked by strong hydrogen bonds to form infinite ribbons along the twofold screw axes. The adjacent ribbons form slightly puckered layers of $H_2PO_4^{1-}$ tetrahedra along the *b* axis. These negatively charged layers alternate with layers formed by protonated serine molecules. The bond lengths and angles in the serine molecule and $H_2PO_4^{1-}$ ion are listed in Table 2. It follows from Table 2 that the $H_2PO_4^{1-}$ ion

Table 1. Atomic coordinates and equivalent thermal parameters

	X(*DX*)	*Y*(*DY*)	*Z*(*DZ*)	U_{eq}/U_{iso}, Å^2
P	0.43388(2)	0.79911(2)	0.70174(7)	0.02227(5)
O(1)	0.35697(8)	0.72732(8)	0.4419(2)	0.0303(2)
O(2)	0.58746(7)	0.88023(8)	0.6463(2)	0.0328(2)
O(3)	0.33155(8)	0.89883(8)	0.8307(3)	0.0328(2)
O(4)	0.44552(9)	0.68102(7)	0.9351(3)	0.02986(19)
O(5)	–0.02974(9)	0.11195(9)	0.8997(3)	0.0405(3)
O(6)	–0.09911(8)	0.30888(8)	0.7168(4)	0.0409(2)
C(1)	–0.01213(9)	0.21464(9)	0.7413(3)	0.0261(2)
C(2)	0.12008(9)	0.24718(9)	0.5409(3)	0.0260(2)
C(3)	0.20541(12)	0.39629(10)	0.5851(4)	0.0348(3)
O(7)	0.25781(12)	0.40275(9)	0.8690(3)	0.0488(3)
N	0.21870(9)	0.14158(9)	0.5975(3)	0.0279(2)
H(1)	0.370(2)	0.9563(19)	0.955(7)	0.055(5)
H(2)	0.413(2)	0.693(2)	1.088(6)	0.062(6)
H(3)	–0.161(2)	0.290(2)	0.794(6)	0.065(7)
H(4)	0.0909(15)	0.2373(16)	0.335(4)	0.034(4)
H(5)	0.1411(19)	0.4743(19)	0.552(5)	0.050(5)
H(6)	0.278(2)	0.403(2)	0.453(7)	0.055(6)
H(7)	0.326(2)	0.486(2)	0.919(10)	0.091(8)
H(8)	0.2634(15)	0.1572(16)	0.761(5)	0.031(4)
H(9)	0.284(2)	0.145(2)	0.463(7)	0.059(6)
H(10)	0.1592(15)	0.0473(16)	0.617(5)	0.034(4)

Table 2. Selected bond lengths (*d*, Å) and angles (ω, deg)

Bond	Angle	Bond	Angle
$H_2PO_4^{1-}$			
P–O(1)	1.496(2)	O(1)–P–O(2)	115.1(1)
P–O(2)	1.506(2)	O(1)–P–O(3)	107.5(1)
P–O(3)	1.555(2)	O(2)–P–O(3)	110.9(1)
P–O(4)	1.570(2)	O(1)–P–O(4)	107.9(1)
		O(2)–P–O(4)	108.3(1)
		O(3)–P–O(4)	106.9(1)
L-Serine			
O(5)–C(1)	1.207(2)	O(5)–C(1)–O(6)	126.5(2)
O(6)–C(1)	1.296(2)	O(5)–C(1)–C(2)	122.0(1)
C(1)–C(2)	1.512(2)	O(6)–C(1)–C(2)	111.5(2)
C(2)–N	1.478(2)	N–C(2)–C(1)	108.0(1)
C(2)–C(3)	1.512(2)	N–C(2)–C(3)	109.5(2)
C(3)–O(7)	1.393(3)	C(1)–C(2)–C(3)	112.3(2)
		O(7)–C(3)–C(2)	106.8(2)

Table 3. Hydrogen bonds and C–H bonds

A–H···*D*	*A*–H, Å	H···*D*, Å	*A*···*D*, Å	*AHD*, deg
O(3)–H(1)···O(2)$^{i)}$	0.83(3)	1.77(2)	2.559(2)	158(2)
O(4)–H(2)···O(1)$^{ii)}$	0.78(3)	1.76(3)	2.537(3)	175(2)
O(6)–H(3)···O(1)$^{iii)}$	0.67(2)	1.90(2)	2.545(2)	164(3)
O(7)–H(7)···O(4)	0.95(2)	1.98(2)	2.916(2)	165(4)
N–H(8)···O(2)$^{iv)}$	0.86(2)	2.30(2)	3.117(3)	158(2)
N–H(9)···O(2)$^{v)}$	0.86(3)	1.91(3)	2.763(3)	170(2)
N–H(10)···O(5)$^{vi)}$	0.97(2)	2.02(2)	2.868(2)	144(2)
C(2)–H(4)	0.99(2)			
C(3)–H(5)	1.03(2)			
C3–H(6)	0.90(3)			

Symmetry codes: (i) $1 - x, 2 - y, z + 1/2$; (ii) $x, y, 1 + z$; (iii) $-x, 1 - y, z + 1/2$; (iv) $1 - x, 1 - y, z + 1/2$; (v) $1 - x, 1 - y, z - 1/2$; (vi) $-x, -y, z - 1/2$.

has a distorted tetrahedral structure, because the P–OH bonds are significantly longer than the P–O bonds. The Flack parameter (0.01) confirms the validity of the configuration described. The bond lengths and angles in the serine molecule agree well with the values reported earlier in [9, 10]. The hydrogen atoms of the NH_3 group form hydrogen bonds with oxygen atoms of both the phosphate groups belonging to the same ribbon and the serine molecules. The adjacent ribbons are linked via serine molecules, which form hydrogen bonds involving hydroxyl groups, on the one hand, and NH_3 groups, on the other hand. Thus, in addition to the electrostatic

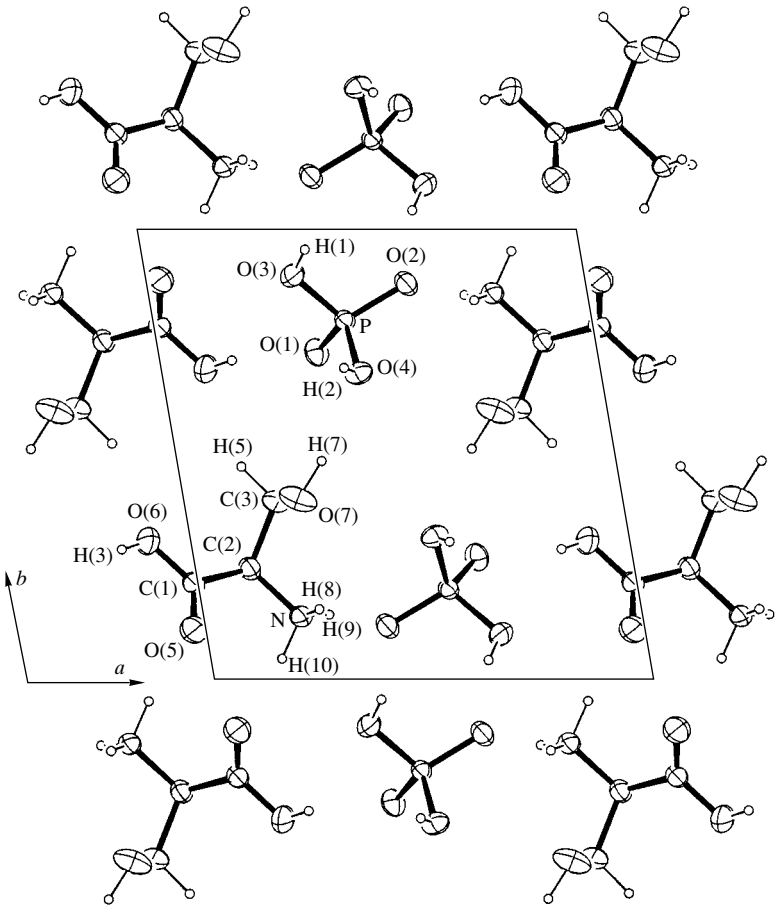

Projection of the structure along the *c* axis. The non-hydrogen atoms are drawn as ellipsoids of thermal vibrations. The H atoms are represented by circles of arbitrary radius.

interaction, an extended hydrogen bond system is formed in the structure. The geometric parameters of hydrogen bonds are given in Table 3.

ACKNOWLEDGMENTS

This work was supported by the Russian Foundation for Basic Research, project no. 01-02-17163.

REFERENCES

1. M. T. Averbuch-Pouchot, A. Durif, and J. C. Guite, Acta Crystallogr., Sect. C: Cryst. Struct. Commun. **44**, 1968 (1988).
2. Yu. I. Smolin, A. E. Lapshin, and G. A. Pankova, Kristallografiya **48**, 318 (2003) [Crystallogr. Rep. **48**, 283 (2003)].
3. F. H. Allen, Acta Crystallogr., Sect. B: Struct. Sci. **58**, 380 (2002).
4. V. V. Lemanov, S. N. Popov, and G. A. Pankova, Fiz. Tverd. Tela (St. Petersburg) **44** (10), 1840 (2002) [Phys. Solid State **44**, 1929 (2002)].
5. S. Oatley and S. French, Acta Crystallogr., Sect. A: Cryst. Phys., Diffr., Theor. Gen. Crystallogr. **38**, 537 (1982).
6. V. N. Andrianov, Kristallografiya **32** (1), 228 (1987) [Sov. Phys. Crystallogr. **32**, 130 (1987)].
7. G. M. Sheldrick, *SHELXL97: Program for the Refinement of Crystal Structures* (Univ. of Göttingen, Germany, 1997).
8. M. N. Burnett and C. K. Johnson, ORTEP III: Report ORNL-6895 (Oak Ridge National Laboratory, Tennessee, 1996).
9. T. J. Kistenmacher, G. A. Rand, and E. Marsh, Acta Crystallogr., Sect. B: Struct. Crystallogr. Cryst. Chem. **30**, 2573 (1974).
10. M. N. Frey, M. S. Lenmann, T. F. Koetzle, and W. C. Hamilton, Acta Crystallogr., Sect. B: Struct. Crystallogr. Cryst. Chem. **29**, 4 (1973).

Translated by I. Polyakova

Crystallography Reports, Vol. 50, No. 1, 2005, pp. 61–71. Translated from Kristallografiya, Vol. 50, No. 1, 2005, pp. 68–78.

STRUCTURE OF ORGANIC COMPOUNDS

X-ray Mapping in Heterocyclic Design: XV. Tricyclic Heterocycles Based on 2-Oxo-2,5,6,7-Tetrahydro-1*H*-Cyclopenta[*b*]pyridine-3-Carbonitrile

O. S. Mazina, V. B. Rybakov, S. I. Troyanov, E. V. Babaev, and L. A. Aslanov

Moscow State University, Vorob'evy gory, Moscow, 119992 Russia

e-mail: rybakov@biocryst.phys.msu.su

Received March 22, 2004

Abstract—The structures of five compounds are studied using single-crystal X-ray diffraction: 2-oxo-2,5,6,7-tetrahydro-1*H*-cyclopenta[*b*]pyridine-3-carbonitrile [a = 15.641(8) Å, b = 9.373(5) Å, c = 7.387(4) Å, β = 92.91(5)°, Z = 4, space group $P2_1/c$]; 1-[2-(4-chlorophenyl)-2-oxoethyl]-2-oxo-2,5,6,7-tetrahydro-1*H*-cyclopenta[*b*]pyridine-3-carbonitrile [a = 4.728(4) Å, b = 28.035(11) Å, c = 11.184(3) Å, Z = 4, space group $P2_12_12_1$]; 2-[2-(4-chlorophenyl)-2-oxoethoxy]-6,7-dihydro-5*H*-cyclopenta[*b*]pyridine-3-carbonitrile [a = 10.1202(13) Å, b = 11.2484(18) Å, c = 13.4323(19) Å, β = 102.05(1)°, Z = 4, space group $P2_1/c$]; 2-(4-chlorophenyl)-3*a*,6,7,8-tetrahydrocyclopenta[*e*][1.3]oxazolo[3.2-*a*]pyridine-4-carboxamide perchlorate [a = 7.702(2) Å, b = 9.599(3) Å, c = 23.798(5) Å, β = 93.44(2)°, Z = 4, space group $P2_1/c$]; and (3-amino-6,7-dihydro-5*H*-cyclopenta[*b*]furo[3.2-*e*]pyridin-2-yl)(4-chlorophenyl)methanone [a = 7.3273(2) Å, b = 13.390(3) Å, c = 28.792(8) Å, Z = 8, space group *Pbca*]. The structures are solved using direct methods and refined by the full-matrix least-squares procedure in the anisotropic approximation to R = 0.0580, 0.0724, 0.0469, 0.0477, and 0.0418, respectively. © *2005 Pleiades Publishing, Inc.*

INTRODUCTION

This work continues our investigations into the chemical and structural features of tricyclic heterocycles based on 3-cyano-2(1*H*)-pyridones. The well-studied cyclization reactions of the products of pyridone phenacylation lead to the formation of furo[2.3-*b*]pyridine and 5-indolizinone derivatives [1, 2]. In our previous work, we demonstrated that the possible heterocyclization reactions are not exhausted by the previously studied processes. Examples of the revealed transformations of cyanopyridone **Ia**, which is fused to a cyclohexane ring [3], are presented by the following scheme (see Scheme 1):

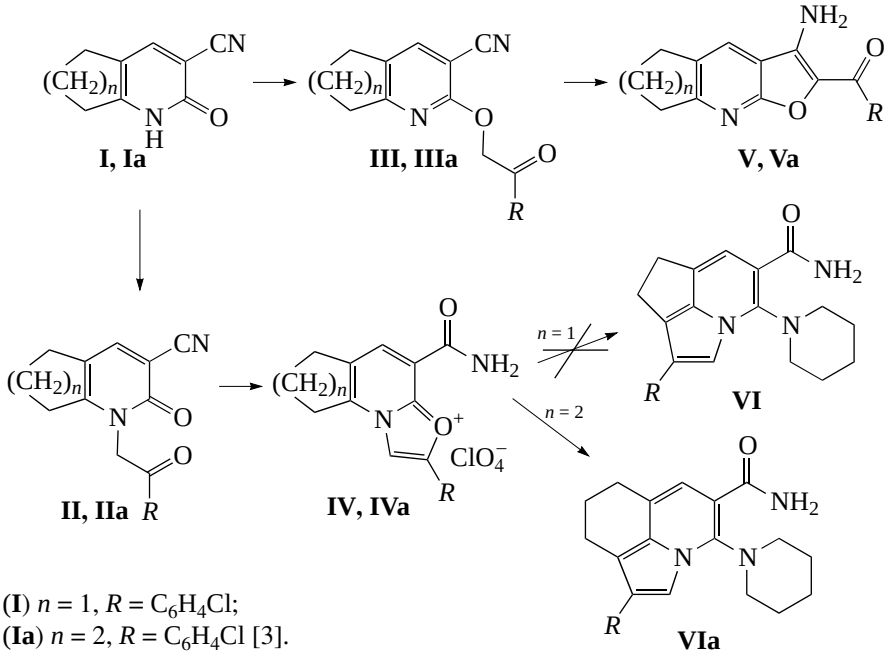

(**I**) n = 1, R = C_6H_4Cl;
(**Ia**) n = 2, R = C_6H_4Cl [3].

Scheme 1.

1063-7745/05/5001-0061$26.00 © 2005 Pleiades Publishing, Inc.

In this work, we investigated similar heterocyclization reactions on the basis of cyanopyridone **I** containing a cyclopentene fragment. It was found that the phenacylation reaction of pyridone **I** proceeds in a similar way with the formation of *N* and *O* isomers. The resultant mixture of isomers was successfully separated using silica gel chromatography. The *O* isomer (compound **III**) under the action of a base easily closes the ring with the formation of tricyclic furopyridine **V**. The *N* isomer (compound **II**) in an acid medium is cyclized into tricyclic cation **IV**. By analogy with the transformation of compounds **IVa**–**VIa**, we expected that the recyclization of salt **IV** would result in the formation of compound **VI**, which is a representative of the previously unknown tricyclic system.

However, it turned out that the reaction of compound **IV** with a secondary amine (performed according to a procedure similar to the reaction of salt **IVa** [3]) is accompanied by a strong resinification of the reaction mixture. Upon treatment of the reaction mixture with water and extraction with chloroform, the organic layer acquired a bright yellow color. At the same time, the mass spectral analysis of the substance obtained from the organic extract showed the presence of a peak corresponding to initial cation **IV**.

In order to account for the observed features, we can assume that cation **IV** most likely undergoes opening of the oxazole ring with the formation of a colored zwitterion intermediate (ilide) (**VII**):

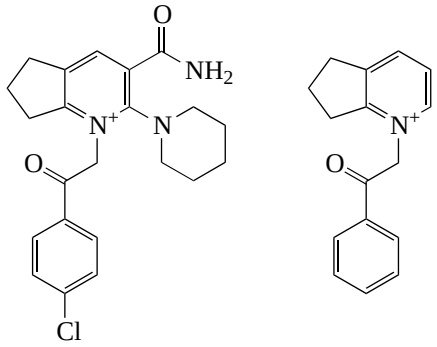

VII **VIII**

Scheme 2.

Further cyclization of this ilide into tricyclic compound **VI** is impossible, most probably, due to steric stresses arising upon closure of the pyrrole ring. It should be noted that early attempts to prepare this tricyclic compound with the use of salt **VIII**, which is structurally similar to ilide **VII**, also failed (see Scheme 2 [4]).

EXPERIMENTAL

Compounds **I**–**V** were synthesized according to Scheme 3. The physicochemical characteristics of the compounds synthesized are presented in Table 1.

2-Oxo-2,5,6,7-tetrahydro-1*H*-cyclopenta[*b*]pyridine-3-carbonitrile (I). This compound was prepared

Table 1. Physicochemical characteristics of the compounds synthesized

Compound	T_m, °C	^{1}H NMR* (*DM*SO-d_6)
I	257	12.71 (s, 1H, 1-NH); 7.99 (s, 1H, 4-CH); 2.80 and 2.64 (t, 7.7 Hz and 7.5 Hz, 2H, 6-CH_2 and 8-CH_2)[a]; 2.03 (q, 7.5 Hz, 2H, 7-CH_2)
II	244	8.13 (s, 1H, 4-CH); 8.09 and 7.69 (d, 8.6 Hz, 2H, 14-CH + 15-CH and 17-CH + 18-CH)[b]; 5.59 (s, 2H, 11-CH_2); 2.89 and 2.78 (t, 7.7 Hz and 7.5 Hz, 2H, 6-CH_2 and 8-CH_2)[a]; 2.06 (q, 7.6 Hz, 2H, 7-CH_2)
III	253	8.03 and 7.64 (d, 8.3 Hz, 2H, 14-CH + 15-CH and 17-CH + 18-CH)[b]; 7.97 (s, 1H, 4-CH); 5.76 (s, 2H, 11-CH_2); 2.93 and 2.76 (t, 7.6 Hz and 7.7 Hz, 2H, 6-CH_2 and 8-CH_2)[a]; 2.11 (q, 7.5 Hz, 2H, 7-CH_2)
IV	218	9.50 (s, 1H, 11-CH); 8.68 (s, 1H, 4-CH), 8.33 and 8.24 (s, 1H, 31-NH_2); 8.10 and 7.8 (d, 8.6 Hz, 2H, 14-CH + 15-CH and 17-CH + 18-CH)[b]; 3.43 and 3.21 (t, 7.7 Hz and 7.6 Hz, 2H, 6-CH_2 and 8-CH_2)[a]; 2.41 (q, 7.6 Hz, 2H, 7-CH_2)
V	312	8.25 (s, 1H, 4-CH); 8.10 and 7.63 (d, 8.7 Hz, 2H, 14-CH + 15-CH and 17-CH + 18-CH)[b]; 7.55 (s, 2H, 31-NH_2); 2.99 (m, 4H, 6-CH_2 + 8-CH_2); 2.14 (q, 7.5 Hz, 2H, 7-CH_2)

* The assignment of the signals is given in accordance with the atomic numbering used in X-ray diffraction analysis (Figs. 1–5).
[a] The opposite assignment of CH_2 groups is possible.
[b] The opposite assignment of CH groups is possible.

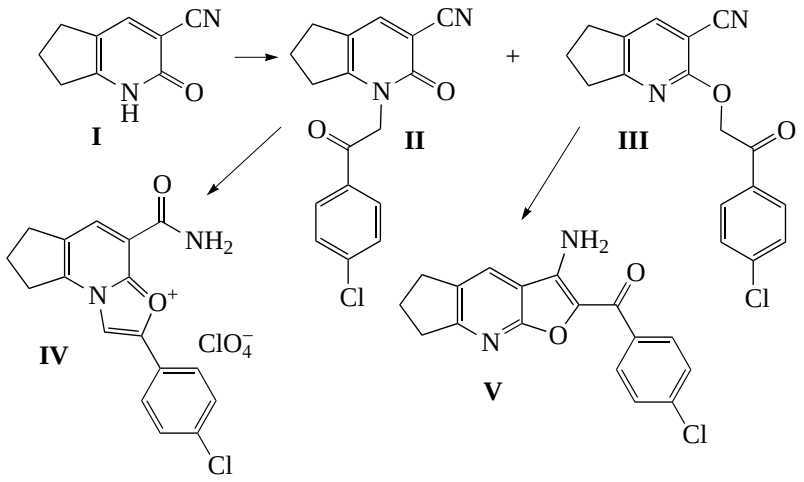

Scheme 3.

according to the procedure described in [5]. The yield was 26%.

1-[2-(4-Chlorophenyl)-2-oxoethyl]-2-oxo-2,5,6,7-tetrahydro-1*H*-cyclopenta[*b*]pyridine-3-carbonitrile (II) and 2-[2-(4-chlorophenyl)-2-oxoethoxy]-6,7-dihydro-5*H*-cyclopenta[*b*]pyridine-3-carbonitrile (III). These compounds were synthesized according to a procedure similar to that proposed in [1]. Potassium hydroxide (6.25 mmol) and ethanol (5 ml) were placed in a round-bottomed flask. Compound **I** (6.25 mmol) was added portionwise with stirring to the prepared solution. The mixture was left to stand in an ultrasonic bath for 40 min, and then the alcohol was evaporated with a rotary evaporator. Dimethylformamide (10 ml) and *n*-chlorophenacyl bromide (6.25 mmol) were added to the dry residue. The mixture was allowed to stand at elevated temperature ($T \sim 50$°C) for 18 h with stirring. After completing the reaction (controlled by thin-layer chromatography indicating the absence of compound **I**), the reaction mixture was cooled, evaporated to a thick paste, and poured into water. The precipitate was filtered off and dried in air. The mixture of *N* and *O* isomers (*O* isomer has a higher mobility) was separated using a column (sorbent, SiO_2; chloroform : hexane = 1 : 1). The yields of compounds **II** and **III** were equal to 45 and 41%, respectively.

2-(4-Chlorophenyl)-3*a*,6,7,8-tetrahydrocyclopenta[*e*][1.3]oxazolo[3.2-*a*]pyridine-4-carboxamide perchlorate (IV). Compound **IV** was prepared from compound **II** according to a procedure similar to that described in [6]. Compound **II** (1 g) was dissolved in 96% H_2SO_4 (2 ml) and left to stand for a night. 70% $HClO_4$ (5 ml) was added to water (50 ml), and the H_2SO_4 mixture was poured into the prepared solution. The precipitate was filtered off, washed on a filter with water, and dried. The yield of compound **IV** was 97%.

(3-Amino-6,7-dihydro-5*H*-cyclopenta[*b*]furo[3.2-*e*]pyridin-2-yl)(4-chlorophenyl)methanone (V). This compound was prepared using a procedure similar to that proposed by Gewald [1]. Compound **III** was boiled in absolute methanol with a threefold excess of sodium methylate for 16 h. The precipitate was filtered off, washed on a filter with methanol, and dried. The yield of compound **V** was 67%.

Compound **I** upon recrystallization from glacial acetic acid formed needle-shaped colorless crystals. The crystals completely cracked in air for 30 s after their removal from the solution. The crystals suitable for X-ray diffraction analysis were chosen in a stream or cooled nitrogen under a binocular microscope in polarized light. The experimental intensities of diffraction reflections were measured on an IPDS automated diffractometer (MoK_α radiation, graphite monochromator, ω scan mode) at $T = 190(2)$ K. The experimental set of diffraction data was processed with the X-RED-1.07 program package [7].

The experimental intensities of diffraction reflections for single crystals of compounds **II**–**V** were measured on a CAD4 automated diffractometer [8] (CuK_α radiation, graphite monochromator, ω scan mode) at room temperature. The unit cell parameters of compounds **II**, **III**, **IV**, and **V** were determined and refined using 25 reflections in the θ ranges 24°–26.5°, 21°–25°, 30°–35°, and 25°–29°, respectively. No correction for absorption was introduced because of the small linear absorption coefficients of the compounds studied and the small sizes of their crystals. The primary processing of the sets of diffraction data was performed with the WinGX program package [9].

All the subsequent calculations were carried out with the SHELX97 program package [10]. The crystal structures, except for structure **II**, were determined by direct methods, and then the positional and thermal parameters for all the non-hydrogen atoms were refined in the anisotropic approximation. For compound **II**, the parameters of the chlorine atom were refined in the anisotropic approximation and the refinement of all the other atoms was performed in the isotropic approxima-

Table 2. Crystal data, data collection, and refinement parameters for structures **I**, **II**, **III**, **IV**, and **V**

Empirical formula	$C_9H_8N_2O \cdot C_2H_4O_2$ **I**	$C_{17}H_{13}ClN_2O_2$ **II**	$C_{17}H_{13}ClN_2O_2$ **III**	$C_{17}H_{15}ClN_2O_2 \cdot ClO_4$ **IV**	$C_{17}H_{13}ClN_2O_2$ **V**
Molecular weight	220.23	312.76	312.76	413.20	312.76
Crystal system	Monoclinic	Orthorhombic	Monoclinic	Monoclinic	Orthorhombic
Space group	$P\,2_1/c$	$P\,2_12_12_1$	$P\,2_1/c$	$P\,2_1/c$	$P\,bca$
a, Å	15.641(8)	4.728(4)	10.1202(13)	7.702(2)	7.3273(18)
b, Å	9.373(5)	28.035(11)	11.2484(18)	9.599(3)	13.390(3)
c, Å	7.387(4)	11.184(3)	13.4323(19)	23.798(5)	28.792(8)
β, deg	92.91(5)	90.0	102.05(1)	93.44(2)	90.0
V, Å^3	1081.6(10)	1482.2(15)	1495.4(4)	1756.3(8)	2824.9(12)
Z	4	4	4	4	8
ρ_{calcd}, g/cm^3	1.352	1.401	1.389	1.563	1.471
$\mu(K_\alpha)$, cm^{-1}	0.100	2.365	2.335	3.687	2.473
θ range, deg	2.61–28.19	3.15–44.90	4.47–74.89	3.72–74.93	3.07–59.97
Crystal size, mm	0.3 × 0.3 × 0.3	0.1 × 0.1 × 0.1	0.3 × 0.3 × 0.3	0.3 × 0.3 × 0.3	0.3 × 0.3 × 0.3
Number of reflections measured	4989	1293	3199	3700	2037
Number of unique reflections/Number of reflections refined	1832/155	1189/98	3065/199	3612/252	2037/207
R_1/wR^2 [$I \geq 2\sigma(I)$]	0.0580/0.1193	0.0724/0.1468	0.0469/0.1181	0.0477/0.1251	0.0418/0.0859
$\Delta\rho_{max}/\Delta\rho_{min}$, e/Å^3	0.216/–0.176	0.226/–0.198	0.149/–0.271	0.357/–0.268	0.159/–0.142

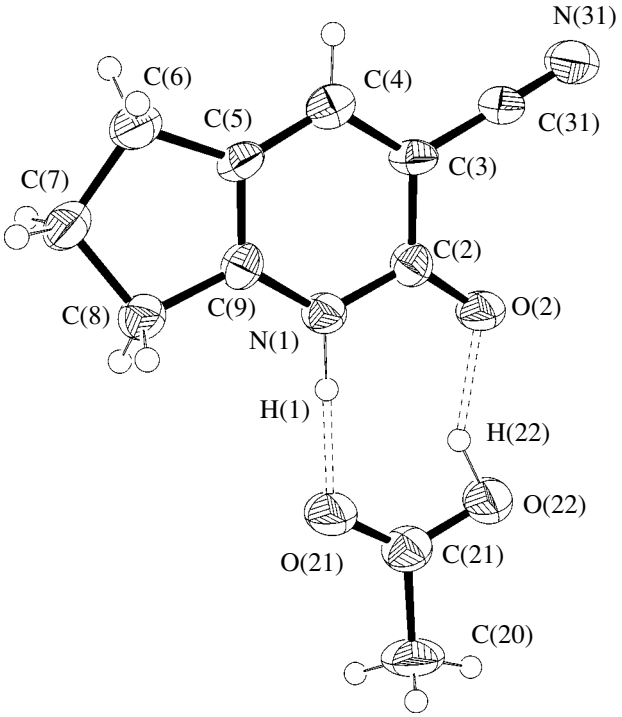

Fig. 1. Molecular structure, atomic numbering, and spatial arrangement of hydrogen bonds in compound **I**.

tion. The hydrogen atoms, except the hydrogen atoms involved in the formation of hydrogen bonds, were located from geometric considerations and refined as riding atoms together with the corresponding carbon atoms. The thermal parameters of these hydrogen atoms were calculated from those of the corresponding carbon atoms [$U_{iso}(H) = 1.2U_{eq}(C)$ for the aromatic hydrogen atoms and $U_{iso}(H) = 1.5U_{eq}(C)$ for the aliphatic hydrogen atoms]. The hydrogen atoms involved in the formation of hydrogen bonds were located from the electron-density difference syntheses and independently refined in the isotropic approximation.

The crystal data for structures **I**–**V** (CIF files) have been deposited with the Cambridge Structural Database (deposit CCDC nos. 0.000000–0.000004).

The main parameters of the X-ray diffraction experiments and crystal data for the compounds are summarized in Table 2.

The spatial arrangement of atoms in molecules and their numbering are depicted in Figs. 1–5 obtained with the ORTEP-3 graphic program package [11, 12].

The interatomic distances and bond angles in the studied structures are presented in Tables 3–12.

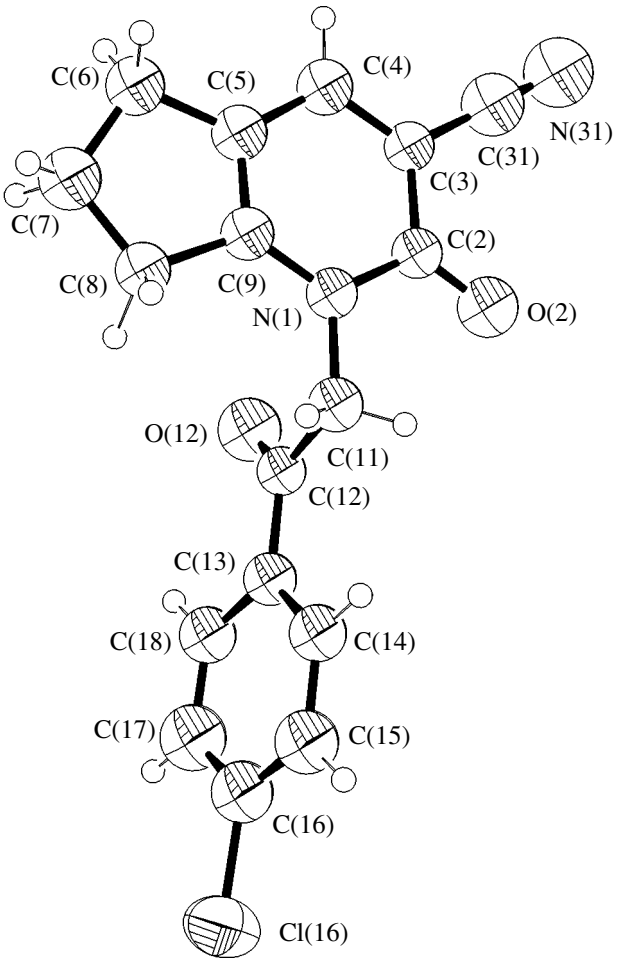

Fig. 2. Molecular structure and atomic numbering for compound **II**.

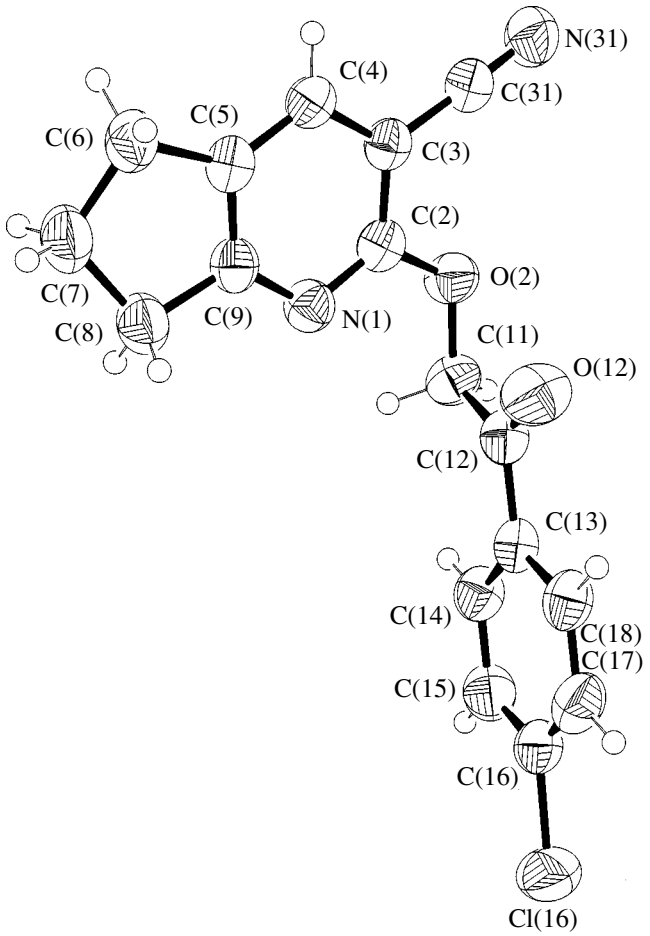

Fig. 3. Molecular structure and atomic numbering for compound **III**.

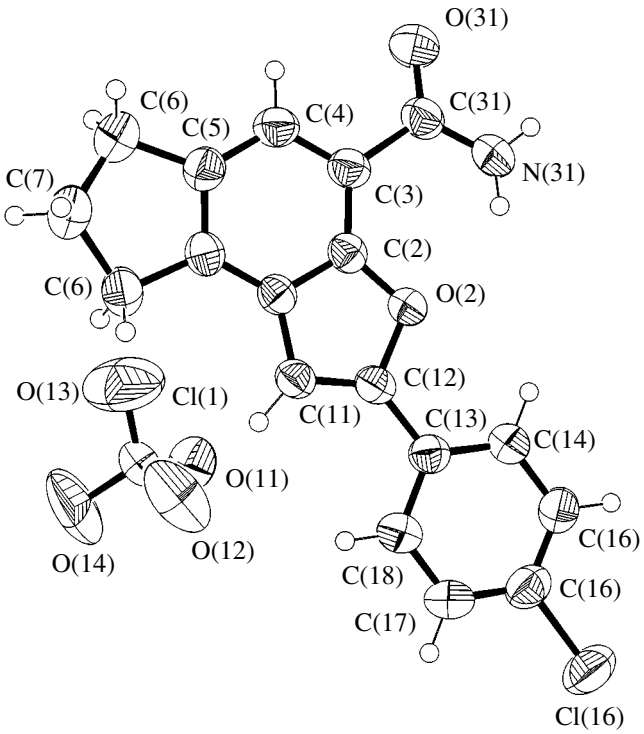

Fig. 4. Molecular structure and atomic numbering for compound **IV**.

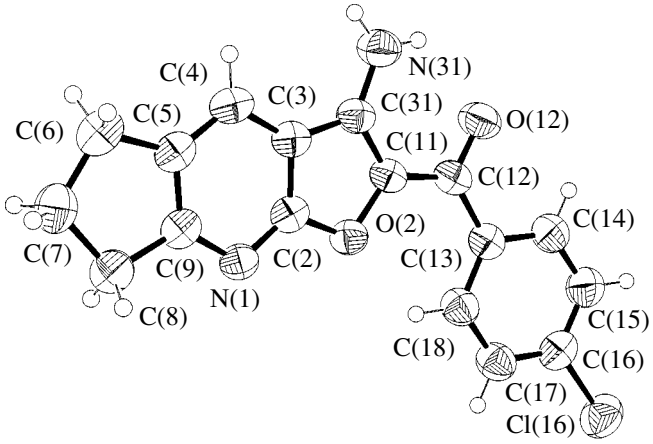

Fig. 5. Molecular structure and atomic numbering for compound **V**.

Table 3. Selected bond lengths *d* (Å) in structure **I**

Bond	*d*	Bond	*d*
N(1)–C(9)	1.365(5)	C(5)–C(6)	1.498(6)
N(1)–C(2)	1.377(5)	C(6)–C(7)	1.553(6)
N(1)–H(1)	1.12(6)	C(7)–C(8)	1.537(6)
C(2)–O(2)	1.258(5)	C(8)–C(9)	1.506(6)
C(2)–C(3)	1.445(5)	C(31)–N(31)	1.164(6)
C(3)–C(4)	1.387(6)	C(20)–C(21)	1.518(6)
C(3)–C(31)	1.428(7)	C(21)–O(21)	1.228(6)
C(4)–C(5)	1.404(6)	C(21)–O(22)	1.308(6)
C(5)–C(9)	1.379(5)	O(22)–H(22)	0.97(7)

Table 4. Selected bond angles ω (deg) in structure **I**

Angle	ω	Angle	ω
C(9)–N(1)–C(2)	123.0(4)	C(4)–C(5)–C(6)	131.8(4)
C(9)–N(1)–H(1)	125(3)	C(5)–C(6)–C(7)	104.0(4)
C(2)–N(1)–H(1)	112(3)	C(8)–C(7)–C(6)	106.6(4)
O(2)–C(2)–N(1)	120.1(4)	C(9)–C(8)–C(7)	102.7(4)
O(2)–C(2)–C(3)	124.8(5)	N(1)–C(9)–C(5)	122.3(4)
N(1)–C(2)–C(3)	115.1(5)	N(1)–C(9)–C(8)	125.3(4)
C(4)–C(3)–C(31)	121.0(4)	C(5)–C(9)–C(8)	112.4(4)
C(4)–C(3)–C(2)	122.0(5)	N(31)–C(31)–C(3)	179.3(6)
C(31)–C(3)–C(2)	117.0(4)	O(21)–C(21)–O(22)	125.1(4)
C(3)–C(4)–C(5)	119.9(4)	O(21)–C(21)–C(20)	121.0(5)
C(9)–C(5)–C(4)	117.7(4)	O(22)–C(21)–C(20)	113.9(5)
C(9)–C(5)–C(6)	110.5(4)	C(21)–O(22)–H(22)	87(4)

RESULTS AND DISCUSSION

In molecules **I** (Fig. 1) and **II** (Fig. 2), the six-membered heterocyclic fragments have a planar structure in which the maximum deviations of atoms from the plane are equal to 0.04 and 0.06 Å, respectively. The C(31)–N(31) nitrile groups and the O(2) exocyclic oxygen atoms in both molecules lie in the plane of the heterocyclic fragment. In the cyclopentene fragments of molecules **I** and **II**, only the C(7) atoms deviate from their planes by 0.31 and 0.25 Å, respectively.

The analysis of the bond lengths in the C(3)–C(4)–C(5)–C(9) fragments in molecules **I** and **II** (Tables 3, 5) indicates a quasi-diene character of the fragments

Table 5. Selected bond lengths *d* (Å) in structure **II**

Bond	*d*	Bond	*d*
Cl(16)–C(16)	1.740(12)	C(6)–C(7)	1.495(15)
N(1)–C(9)	1.362(12)	C(7)–C(8)	1.487(14)
N(1)–C(2)	1.387(12)	C(8)–C(9)	1.514(13)
N(1)–C(11)	1.462(12)	C(11)–C(12)	1.484(13)
C(2)–O(2)	1.211(10)	C(12)–O(12)	1.211(11)
C(2)–C(3)	1.444(12)	C(12)–C(13)	1.431(14)
C(3)–C(4)	1.385(13)	C(13)–C(18)	1.364(13)
C(3)–C(31)	1.426(15)	C(13)–C(14)	1.396(14)
C(31)–N(31)	1.131(14)	C(14)–C(15)	1.393(14)
C(4)–C(5)	1.407(15)	C(15)–C(16)	1.357(13)
C(5)–C(9)	1.341(13)	C(16)–C(17)	1.406(15)
C(5)–C(6)	1.502(14)	C(17)–C(18)	1.363(14)

Table 6. Selected bond angles ω (deg) in structure **II**

Angle	ω	Angle	ω
C(9)–N(1)–C(2)	122.0(9)	C(5)–C(9)–N(1)	123.7(10)
C(9)–N(1)–C(11)	121.6(8)	C(5)–C(9)–C(8)	108.9(10)
C(2)–N(1)–C(11)	116.5(9)	N(1)–C(9)–C(8)	127.0(10)
O(2)–C(2)–N(1)	121.1(10)	N(1)–C(11)–C(12)	115.3(9)
O(2)–C(2)–C(3)	124.0(10)	O(12)–C(12)–C(13)	122.5(10)
N(1)–C(2)–C(3)	114.8(10)	O(12)–C(12)–C(11)	117.1(10)
C(4)–C(3)–C(31)	121.5(10)	C(13)–C(12)–C(11)	120.4(10)
C(4)–C(3)–C(2)	121.8(10)	C(18)–C(13)–C(14)	116.2(11)
C(31)–C(3)–C(2)	116.7(10)	C(18)–C(13)–C(12)	121.3(11)
N(31)–C(31)–C(3)	178.8(15)	C(14)–C(13)–C(12)	122.4(10)
C(3)–C(4)–C(5)	119.6(11)	C(15)–C(14)–C(13)	122.4(11)
C(9)–C(5)–C(4)	117.9(11)	C(16)–C(15)–C(14)	118.3(12)
C(9)–C(5)–C(6)	112.4(11)	C(15)–C(16)–C(17)	121.1(12)
C(4)–C(5)–C(6)	129.7(11)	C(15)–C(16)–Cl(16)	119.1(10)
C(7)–C(6)–C(5)	103.8(9)	C(17)–C(16)–Cl(16)	119.8(9)
C(8)–C(7)–C(6)	107.5(10)	C(18)–C(17)–C(16)	117.9(12)
C(7)–C(8)–C(9)	105.7(10)	C(17)–C(18)–C(13)	123.9(13)

Table 7. Selected bond lengths *d* (Å) in structure **III**

Bond	*d*	Bond	*d*	Bond	*d*	Bond	*d*
N(1)–C(2)	1.315(2)	C(3)–C(31)	1.430(2)	C(7)–C(8)	1.532(3)	C(13)–C(18)	1.388(2)
N(1)–C(9)	1.344(2)	C(31)–N(31)	1.140(2)	C(8)–C(9)	1.496(2)	C(14)–C(15)	1.383(2)
C(2)–O(2)	1.363(2)	C(4)–C(5)	1.380(2)	C(11)–C(12)	1.514(3)	C(15)–C(16)	1.378(3)
C(2)–C(3)	1.408(2)	C(5)–C(9)	1.382(2)	C(12)–O(12)	1.209(2)	C(16)–C(17)	1.376(3)
O(2)–C(11)	1.431(2)	C(5)–C(6)	1.507(3)	C(12)–C(13)	1.489(2)	C(16)–Cl(16)	1.741(2)
C(3)–C(4)	1.394(2)	C(6)–C(7)	1.537(3)	C(13)–C(14)	1.387(2)	C(17)–C(18)	1.376(3)

Table 8. Selected bond angles ω (deg) in structure **III**

Angle	ω	Angle	ω
C(2)–N(1)–C(9)	115.97(14)	N(1)–C(9)–C(8)	123.80(15)
N(1)–C(2)–O(2)	119.69(14)	C(5)–C(9)–C(8)	111.17(16)
N(1)–C(2)–C(3)	124.09(15)	O(2)–C(11)–C(12)	110.59(14)
O(2)–C(2)–C(3)	116.19(15)	O(12)–C(12)–C(13)	121.42(18)
C(2)–O(2)–C(11)	116.80(13)	O(12)–C(12)–C(11)	119.79(16)
C(4)–C(3)–C(2)	118.34(15)	C(13)–C(12)–C(11)	118.79(14)
C(4)–C(3)–C(31)	121.07(15)	C(14)–C(13)–C(18)	118.95(16)
C(2)–C(3)–C(31)	120.58(15)	C(14)–C(13)–C(12)	123.41(16)
N(31)–C(31)–C(3)	178.1(2)	C(18)–C(13)–C(12)	117.63(15)
C(5)–C(4)–C(3)	118.17(15)	C(15)–C(14)–C(13)	120.53(18)
C(4)–C(5)–C(9)	118.32(16)	C(16)–C(15)–C(14)	119.05(18)
C(4)–C(5)–C(6)	130.62(16)	C(17)–C(16)–C(15)	121.50(18)
C(9)–C(5)–C(6)	111.05(16)	C(17)–C(16)–Cl(16)	119.20(17)
C(5)–C(6)–C(7)	103.06(16)	C(15)–C(16)–Cl(16)	119.28(17)
C(8)–C(7)–C(6)	106.77(17)	C(16)–C(17)–C(18)	118.91(19)
C(9)–C(8)–C(7)	103.46(16)	C(17)–C(18)–C(13)	121.04(17)
N(1)–C(9)–C(5)	125.03(16)		

Table 9. Selected bond lengths *d* (Å) in structure **IV**

Bond	*d*	Bond	*d*	Bond	*d*	Bond	*d*
N(1)–C(9)	1.360(2)	C(31)–O(31)	1.207(3)	C(7)–C(8)	1.551(3)	C(16)–C(17)	1.380(4)
N(1)–C(2)	1.365(2)	C(31)–N(31)	1.328(3)	C(8)–C(9)	1.490(3)	C(16)–Cl(16)	1.739(2)
N(1)–C(11)	1.398(2)	N(31)–H(31*A*)	0.80(3)	C(11)–C(12)	1.338(3)	C(17)–C(18)	1.380(3)
C(2)–O(2)	1.337(2)	N(31)–H(31*B*)	0.85(3)	C(12)–C(13)	1.457(3)	Cl(1)–O(14)	1.380(2)
C(2)–C(3)	1.391(3)	C(4)–C(5)	1.391(3)	C(13)–C(14)	1.384(3)	Cl(1)–O(13)	1.405(3)
O(2)–C(12)	1.400(2)	C(5)–C(9)	1.373(3)	C(13)–C(18)	1.390(3)	Cl(1)–O(12)	1.419(2)
C(3)–C(4)	1.377(3)	C(5)–C(6)	1.509(3)	C(14)–C(15)	1.391(3)	Cl(1)–O(11)	1.423(2)
C(3)–C(31)	1.517(3)	C(6)–C(7)	1.513(4)	C(15)–C(16)	1.374(3)		

under consideration and a similar structure of the bicyclic fragments of the studied compounds.

Compound **I** is suitable for single-crystal X-ray diffraction analysis in the form of the adduct with acetic acid. In the crystal structure, the molecule of this compound is bound to the acetic acid molecule by the O(22)–H(22)···O(2) and N(1)–H(1)···O(21) hydrogen bonds (Fig. 1, Table 13).

In molecule **III**, the pyridine ring is planar: the maximum deviation of the atoms from the plane is equal to 0.06 Å. The C(31), N(31), and O(2) atoms also lie in

Table 10. Selected bond angles ω (deg) in structure **IV**

Angle	ω	Angle	ω
C(9)–N(1)–C(2)	121.30(16)	N(1)–C(9)–C(5)	118.69(18)
C(9)–N(1)–C(11)	130.60(17)	N(1)–C(9)–C(8)	126.98(18)
C(2)–N(1)–C(11)	108.07(15)	C(5)–C(9)–C(8)	114.32(18)
O(2)–C(2)–N(1)	108.88(16)	C(12)–C(11)–N(1)	106.59(16)
O(2)–C(2)–C(3)	129.49(18)	C(11)–C(12)–O(2)	109.22(16)
N(1)–C(2)–C(3)	121.63(18)	C(11)–C(12)–C(13)	133.07(18)
C(2)–O(2)–C(12)	107.25(14)	O(2)–C(12)–C(13)	117.72(17)
C(4)–C(3)–C(2)	116.66(19)	C(14)–C(13)–C(18)	119.26(19)
C(4)–C(3)–C(31)	117.89(18)	C(14)–C(13)–C(12)	121.93(18)
C(2)–C(3)–C(31)	125.45(19)	C(18)–C(13)–C(12)	118.80(19)
O(31)–C(31)–N(31)	123.1(2)	C(13)–C(14)–C(15)	120.6(2)
O(31)–C(31)–C(3)	118.5(2)	C(16)–C(15)–C(14)	118.9(2)
N(31)–C(31)–C(3)	118.32(19)	C(15)–C(16)–C(17)	121.5(2)
C(31)–N(31)–H(31*A*)	115.2(19)	C(15)–C(16)–Cl(16)	119.4(2)
C(31)–N(31)–H(31*B*)	123.2(17)	C(17)–C(16)–Cl(16)	119.12(18)
H(31*A*)–N(31)–H(31*B*)	122(3)	C(16)–C(17)–C(18)	119.2(2)
C(3)–C(4)–C(5)	121.49(19)	C(17)–C(18)–C(13)	120.5(2)
C(9)–C(5)–C(4)	120.20(19)	O(14)–Cl(1)–O(13)	113.1(2)
C(9)–C(5)–C(6)	109.0(2)	O(14)–Cl(1)–O(12)	109.09(17)
C(4)–C(5)–C(6)	130.8(2)	O(13)–Cl(1)–O(12)	108.4(2)
C(5)–C(6)–C(7)	104.1(2)	O(14)–Cl(1)–O(11)	110.76(19)
C(6)–C(7)–C(8)	108.0(2)	O(13)–Cl(1)–O(11)	105.72(16)
C(9)–C(8)–C(7)	101.18(18)	O(12)–Cl(1)–O(11)	109.73(15)

Table 11. Selected bond lengths *d* (Å) in structure **V**

Bond	*d*	Bond	*d*	Bond	*d*	Bond	*d*
Cl(16)–C(16)	1.7324(5)	C(3)–C(31)	1.4313(6)	C(5)–C(6)	1.4999(6)	C(13)–C(18)	1.3817(6)
N(1)–C(2)	1.3284(5)	C(31)–N(31)	1.3461(6)	C(6)–C(7)	1.5273(7)	C(13)–C(14)	1.3892(6)
N(1)–C(9)	1.3510(5)	C(31)–C(11)	1.3749(6)	C(7)–C(8)	1.5364(6)	C(14)–C(15)	1.3764(6)
C(2)–O(2)	1.3695(5)	N(31)–H(31*A*)	0.858(3)	C(8)–C(9)	1.4982(6)	C(15)–C(16)	1.3684(7)
C(2)–C(3)	1.3891(6)	N(31)–H(31*B*)	0.863(3)	C(11)–C(12)	1.4335(6)	C(16)–C(17)	1.3725(6)
O(2)–C(11)	1.4121(5)	C(4)–C(5)	1.3722(6)	C(12)–O(12)	1.2461(5)	C(17)–C(18)	1.3856(6)
C(3)–C(4)	1.3999(6)	C(5)–C(9)	1.3993(6)	C(12)–C(13)	1.4881(6)		

this plane. The C(7) atom deviates from the plane of the cyclopentene fragment by 0.35 Å.

The analysis of the interatomic distances in the pyridine fragment of molecule **III** (Table 7) shows that the C–C bond lengths are more equalized as compared to those in molecules **I** and **II**. This is the main difference between structure **III** and the structures considered above.

In structure **IV**, the oxazolopyridine bicycle has a planar structure. The maximum deviation of the atoms from the plane is equal to 0.02 Å. The atoms of the O(31)–C(31)–N(31) amide group almost completely lie in this plane. The C(7) atom of the cyclopentene fragment deviates from the plane by 0.31 Å.

The O(31)–C(31)–N(31)H_2 amide group in molecule **IV** is rotated by 5.82° with respect to the plane of the oxazolopyridine bicycle and forms the intramolecular hydrogen bond with the O(2) oxygen atom of the five-membered fragment of the bicycle. Moreover, the hydrogen atoms of the amide group are involved in the formation of the hydrogen bonds with the perchlorate anions and, thus, link molecules into centrosymmetric dimers in the crystal packing (Fig. 6 [13]; Table 13).

Table 12. Selected bond angles ω (deg) in structure **V**

Angle	ω	Angle	ω
C(2)–N(1)–C(9)	111.90(3)	C(9)–C(8)–C(7)	103.57(4)
N(1)–C(2)–O(2)	120.09(3)	N(1)–C(9)–C(5)	125.35(3)
N(1)–C(2)–C(3)	128.31(3)	N(1)–C(9)–C(8)	122.80(4)
O(2)–C(2)–C(3)	111.60(3)	C(5)–C(9)–C(8)	111.85(3)
C(2)–O(2)–C(11)	105.38(3)	C(31)–C(11)–O(2)	110.18(3)
C(2)–C(3)–C(4)	117.83(3)	C(31)–C(11)–C(12)	126.45(4)
C(2)–C(3)–C(31)	105.81(3)	O(2)–C(11)–C(12)	123.29(3)
C(4)–C(3)–C(31)	136.36(4)	O(12)–C(12)–C(11)	116.09(3)
N(31)–C(31)–C(11)	126.97(4)	O(12)–C(12)–C(13)	119.30(4)
N(31)–C(31)–C(3)	125.99(3)	C(11)–C(12)–C(13)	124.60(4)
C(11)–C(31)–C(3)	107.03(4)	C(18)–C(13)–C(14)	117.90(4)
C(31)–N(31)–H(31*A*)	119.9(2)	C(18)–C(13)–C(12)	125.45(3)
C(31)–N(31)–H(31*B*)	120.1(2)	C(14)–C(13)–C(12)	116.65(4)
H(31*A*)–N(31)–H(31*B*)	120.0(3)	C(15)–C(14)–C(13)	121.20(4)
C(5)–C(4)–C(3)	116.38(4)	C(16)–C(15)–C(14)	119.63(4)
C(4)–C(5)–C(10)	120.21(4)	C(15)–C(16)–C(17)	120.79(4)
C(4)–C(5)–C(6)	129.04(4)	C(15)–C(16)–Cl(16)	119.40(3)
C(9)–C(5)–C(6)	110.75(3)	C(17)–C(16)–Cl(16)	119.81(4)
C(5)–C(6)–C(7)	104.30(3)	C(16)–C(17)–C(18)	119.20(4)
C(6)–C(7)–C(8)	108.61(3)	C(13)–C(18)–C(17)	121.27(4)

Table 13. Parameters of interatomic contacts in the studied structures

D–H	*d*(*D*–H)	*d*(H···*A*)	*wD*H*A*	*d*(*D*···*A*)	*A*
			I		
N(1)–H(1)	1.12	1.64	169	2.75	O(21)
O(22)–H(22)	0.97	1.85	134	2.64	O(2)
			IV		
N(31)–H(31*A*)	0.80	2.18	173	2.97	O(14) [*x* + 1, *y* + 1, *z*]
N(31)–H(31*B*)	0.85	2.27	131	2.90	O(2)
N(31)–H(31*B*)	0.85	2.29	126	2.87	O(11) [–*x* + 1, –*y* + 1, –*z*]
			V		
N(31)–H(31*A*)	0.86	2.16	124	2.73	O(12)
N(31)–H(31*B*)	0.86	2.25	162	3.08	N(1) [–*x* + 1/2, *y* + 1/2, *z*]

The structure of the oxazolopyridinium cation can be described by three resonance structures

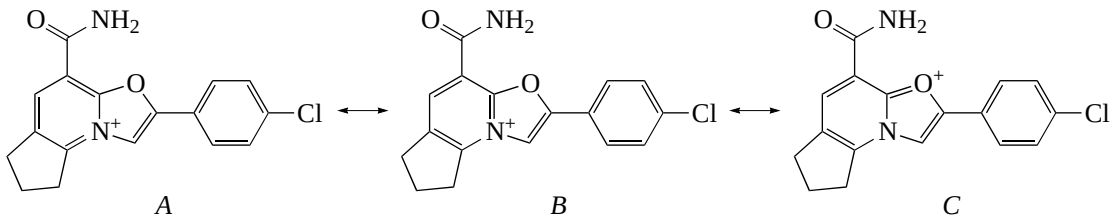

A *B* *C*

Scheme 4.

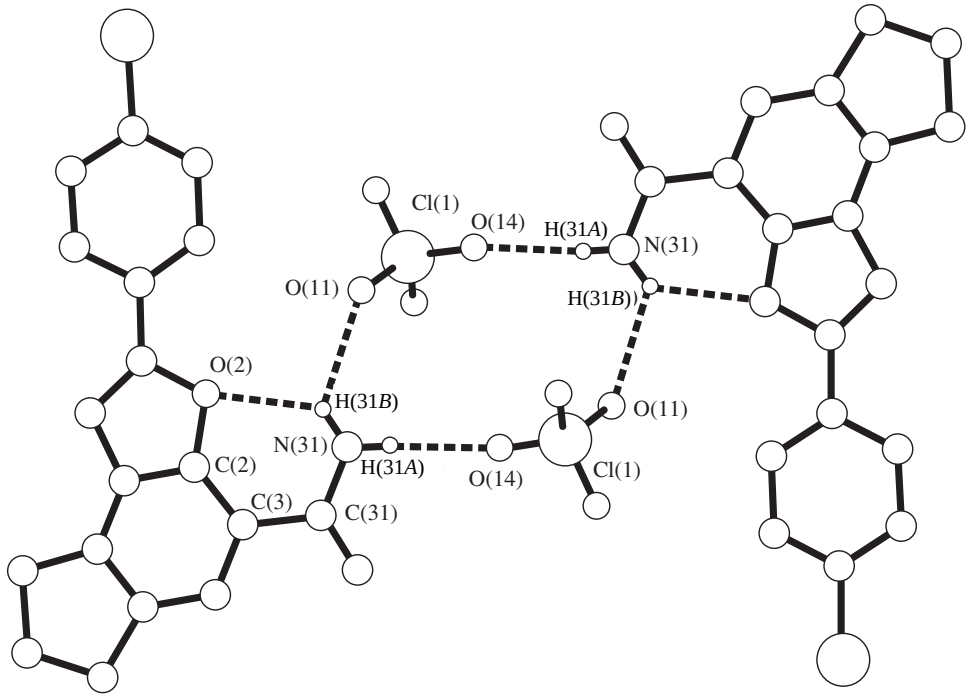

Fig. 6. Spatial arrangement of hydrogen bonds in structure **IV**.

A comparison of the interatomic distances in the C(3)–C(4)–C(5)–C(9) fragment (Table 9) allows us to assume that resonance form *A* should make the least contribution, because the bond lengths in the fragment are characterized by a quasi-diene distribution. A considerable shortening of the N(1)–C(9) bond as compared to the C–N single bond indicates a possible conjugation of the lone electron pair of the bridging nitrogen atom with the diene fragment and then through the chain with the exocyclic amide group of the molecule. Formally, the molecule under investigation contains two amide fragments N(1)–C(2)–O(2) and N(31)–C(31)–O(31). A comparison of the N(1)–C(2) and C(2)–O(2) bond lengths with the corresponding N(31)–C(31) and C(31)–O(31) bond lengths (Table 9) demonstrates that the bonds in the endocyclic amide fragment are longer than those in the exocyclic amide fragment (the lengths of these bonds are shorter than the lengths of the C–O and C–N single bonds). The C(11)–C(12) bond length corresponds to the carbon–carbon double bond length. The analysis of the bond lengths and their ratio does not permit us to make an unambiguous inference regarding the assignment of particular bonds in the amide fragment of the bicycle to single and double bonds. For the molecule under consideration, the bond lengths can be more correctly treated as alternating and the real molecular structure should be most adequately described by a superposition of resonance forms *B* and *C*:

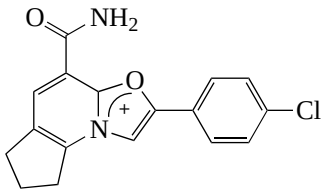

Scheme 5.

In compound **V** (Fig. 5), the heterocyclic bicycle has a planar structure in which the maximum deviation of atoms from the plane is equal to 0.03 Å. In the cyclopentene fragment of the molecule, the C(7) atom deviates from the plane by 0.16 Å.

The bond lengths in the pyridine ring are characterized by an aromatic distribution similar to the distribution of the bond lengths in the pyridine ring of molecule **III**.

The hydrogen atoms of the amino group and the nitrogen atom of the pyridine ring form intermolecular hydrogen bonds that link molecules into chains. Moreover, the amino group participates in the formation of the intramolecular hydrogen bond (Table 13, Fig. 7 [13]).

The *n*-chlorobenzoyl groups in molecules **II**, **III**, and **V** and the *n*-chlorophenyl group in molecule **IV** have planar structures to within 0.03, 0.1, 0.1, and 0.01 Å, respectively. The distribution of the bond lengths in the phenyl ring of all the aforementioned

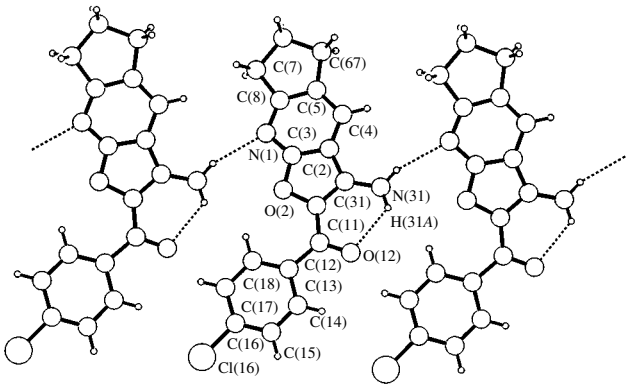

Fig. 7. Spatial arrangement of hydrogen bonds in structure **V**.

molecules corresponds to an aromatic structure. In molecule **II**, the deviations of the O(12) and C(11) atoms from the plane of the *n*-chlorobenzoyl group are equal to 0.12 and 0.26 Å, respectively. The O(12) and C(11) atoms in molecules **III** and **V** lie in the plane of the phenyl ring. The *n*-chlorobenzoyl groups of molecules **II** and **III** are virtually perpendicular to the plane of the heterocyclic fragments: the corresponding dihedral angles between the planes are equal to 74.26° and 87.03°, respectively. The *n*-chlorophenyl ring of molecule **IV** lies in the plane of the heterocyclic fragment, because the dihedral angle between the heterocycle and phenyl planes is only 1.64°. In molecule **V**, the dihedral angle between the planes of the phenyl ring and the heterocyclic tricycle is equal to 9.29°. The small dihedral angle and the planar structure of the $H_2N(31)$–C(31)=C(11)–C(12)=O(12) fragment suggest that the *n*-chlorobenzoyl group and the amino group are conjugated through the double carbon–carbon bond of the furane ring.

ACKNOWLEDGMENTS

We would like to thank Prof. E. Kemnitz (Institute für Chemie, Humboldt Universität, Berlin) for kindly providing an opportunity to perform the low-temperature diffractometric experiment. We also acknowledge the support of the Russian Foundation for Basic Research in the payment of the license for using the Cambridge Structural Database (project no. 02-07-90322).

REFERENCES

1. K. Gewald, J. Prakt. Chem. **318**, 313 (1976).
2. C.-F. Lin, Y.-F. Lin, Y.-C. Lo, *et al.*, Heterocycles **53**, 15 (2000).
3. O. S. Mazina, V. B. Rybakov, V. V. Chernyshev, E. V. Babaev, and L. A. Aslanov, Kristallografiya **49** (2004) (in press).
4. V. Boekelheide and K. Fahrenholtz, J. Am. Chem. Soc. **83**, 458 (1961).
5. J. B. Paine, J. Heterocycl. Chem. **24**, 351 (1987).
6. E. V. Babaev, A. V. Efimov, D. A. Maiboroda, and K. Jug, Eur. J. Org. Chem. 193 (1998).
7. *X-RED-1.07: STOE Data Reduction Program* (STOE and CIE, Darmstadt, Germany, 1996).
8. *Enraf–Nonius CAD4 Software: Version 5.0* (Enraf–Nonius, Delft, Netherlands, 1989).
9. L. J. Farrugia, J. Appl. Crystallogr. **32**, 837 (1999).
10. G. M. Sheldrick, *SHELX97: Program for the Solution and Refinement of Crystal Structures* (Univ. of Göttingen, Germany, 1997).
11. M. N. Burnett and C. K. Johnson, ORTEP. Report ORNL 6895 (Oak Ridge National Laboratory, Tennessee, USA, 1996).
12. L. J. Farrugia, J. Appl. Crystallogr. **30**, 565 (1997).
13. A. L. Spek, *PLUTON97* (Univ. of Utrecht, Netherlands, 1997).

Translated by O. Borovik-Romanova

Crystallography Reports, Vol. 50, No. 1, 2005, pp. 72–77. Translated from Kristallografiya, Vol. 50, No. 1, 2005, pp. 79–83.

STRUCTURE OF ORGANIC COMPOUNDS

Crystal Structure and Spectral Characteristics of 2,4,7-Trinitro-9-Fluorenone

L. Kh. Minacheva*, V. S. Sergienko*, S. B. Strashnova, O. V. Avramenko**, O. V. Koval'chukova**, O. A. Egorova**, and B. E. Zaĭtsev****

** Kurnakov Institute of General and Inorganic Chemistry, Russian Academy of Sciences, Leninskiĭ pr. 31, Moscow, 119991 Russia*

*** Russian University of Peoples' Friendship, ul. Miklukho-Maklaya 6, Moscow, 117198 Russia*

Received April 9, 2003

Abstract—The crystal structure of 2,4,7-trinitro-9-fluorenone $C_{13}H_5N_3O_7$ is determined by X-ray diffraction analysis. The crystals are monoclinic, a = 4.024(1) Å, b = 16.763(3) Å, c = 18.250(4) Å, β = 96.32(3)°, V = 1223.6(5) Å^3, Z = 4, space group $P2_1/c$, and R = 0.0640 for 605 reflections with $I > 2\sigma(I)$. The crystal is built of planar isolated molecules. The compound is characterized using IR and electronic absorption spectroscopy.

INTRODUCTION

9-Fluorenone (**I**) [1] and its derivatives, which exhibit interesting spectroscopic and photochemical properties, have been studied thoroughly. In particular, the Cambridge Structural Database (Version 5.23, April 2001 [2]) includes structural data for 26 substituted 9-fluorenones containing from one to four nitro groups in different positions, namely, 2-mono-, 2,7-di-, 2,5-di-, 4,5-di-, 2,4,7-tri-, and 2,4,5,7-tetranitro-9-fluorenones.

This paper reports on the results of spectroscopic and X-ray diffraction studies of 2,4,7-trinitro-9-fluorenone (*TNF*, **II**).

EXPERIMENTAL

Yellow single crystals of compound **II**, suitable for X-ray diffraction analysis, were isolated by recrystallization from acetone. The melting temperature of compound **II** falls in the range 199–201°C.

The IR spectra of crystals **II** prepared as KBr pellets and Nujol mulls were recorded on a Specord 75IR spectrophotometer in the range 400–4000 cm^{-1}.

The electron absorption spectra of ethanol solutions of *TNF* were measured on a Specord UV–VIS spectrophotometer in the wavelength range 200–700 nm.

Crystals **II** ($C_{13}H_5N_3O_7$, M = 315.20) are monoclinic, a = 4.024(1) Å, b = 16.763(3) Å, c = 18.250(4) Å, β = 96.23(3)°, V = 1223.6(5) Å^3, ρ_{calcd} = 1.711 g/cm^3, $\mu(MoK_\alpha)$ = 0.143 mm^{-1}, $F(000)$ = 640, Z = 4, and space group $P2_1/c$.

The experimental data (2959 reflections, of which 2081 are unique; R_{int} = 0.0693) were collected on an Enraf–Nonius CAD4 automated diffractometer (room temperature, graphite monochromator, ω scan mode, θ_{max} = 25.0°) from a transparent platelike crystal 0.07 × 0.32 × 0.49 mm in size. The reflections were collected in the index ranges $-1 \le h \le 4$, $0 \le k \le 19$, $-21 \le l \le 21$. In the course of data processing, the Lorentz and polarization factors were introduced. The anisotropy of absorption was ignored because of the small absorption coefficient.

The structure was solved by direct methods (SHELXS86 [3]) and refined on F^2 by the full-matrix least-squares procedure (SHELXL93 [4]). All the atoms of the structure (except for the O(4), O(4*X*), and hydrogen atoms) were refined anisotropically. The positions of the H atoms were calculated from geometric considerations (C–H, 0.93 Å) and refined within a riding model. In this refinement, the isotropic thermal parameters U_H of the H atoms were assigned values larger than the thermal parameters U_C of the carbon atoms attached to the parent atoms by a factor of 1.2. The oxygen atom of one of the nitro groups statistically occupies two positions, O(4) and O(4*X*), with occupancy factors refined to 0.64(6) and 0.36(6), respectively.

The final discrepancy factors are as follows: R_1 = 0.0640, wR_2 = 0.1548, and $GOOF$ = 0.989 for 605 reflections with $I > 2\sigma(I)$; and R_1 = 0.2876 and wR_2 = 0.2647 for all reflections. The total number of reflections refined is 207. The values of $\Delta\rho_{max}$ and $\Delta\rho_{min}$ are 0.447 and –0.237 e/Å^{-3}, respectively.

The atomic coordinates and thermal parameters are listed in Table 1. The interatomic distances and bond angles are given in Table 2.

RESULTS AND DISCUSSION

Structure **II** is built of isolated molecules (Fig. 1). Except for the nitro groups, the molecule is virtually planar [the mean atomic deviation from the best plane

Table 1. Atomic coordinates and thermal parameters U_{iso}/U_{eq} (Å^2) in structure **II**

Atom	*x*	*y*	*z*	U_{iso}/U_{eq}
N(1)	0.035(2)	0.4133(5)	−0.0686(5)	0.068(2)
N(2)	−0.026(3)	−0.0703(5)	0.2240(5)	0.091(3)
N(3)	0.428(2)	0.1972(5)	0.2598(5)	0.076(2)
O(1)	−0.174(2)	0.4053(5)	−0.1199(4)	0.108(3)
O(2)	0.211(2)	0.4711(4)	−0.0609(4)	0.108(3)
O(3)	0.127(2)	−0.0854(4)	0.2854(4)	0.126(3)
O(4)	−0.222(3)	−0.1114(8)	0.1963(7)	0.082(4)
O(4*X*)	−0.117(5)	−0.124(1)	0.170(1)	0.073(6)
O(5)	0.340(2)	0.2005(4)	0.3230(4)	0.098(2)
O(6)	0.656(2)	0.2389(5)	0.2381(4)	0.097(2)
O(7)	−0.315(2)	0.1005(3)	−0.0282(3)	0.080(2)
C(1)	0.162(2)	0.2317(5)	0.0927(4)	0.048(2)
C(2)	−0.017(2)	0.2168(4)	0.0236(4)	0.049(2)
C(3)	−0.059(2)	0.2746(5)	−0.0308(4)	0.053(2)
H(3*A*)	−0.174	0.264	−0.076	0.064
C(4)	0.079(2)	0.3480(5)	−0.0129(5)	0.058(2)
C(5)	0.252(2)	0.3650(5)	0.0532(5)	0.057(2)
H(5*A*)	0.339	0.416	0.062	0.069
C(6)	0.300(2)	0.3063(5)	0.1070(4)	0.056(2)
H(6*A*)	0.422	0.317	0.152	0.067
C(7)	0.154(2)	0.1581(4)	0.1375(4)	0.040(2)
C(8)	−0.027(2)	0.0998(5)	0.0947(4)	0.051(2)
C(9)	0.089(2)	−0.0238(5)	0.1213(5)	0.058(2)
H(9*A*)	−0.209	−0.014	0.092	0.070
C(10)	0.034(2)	0.0082(4)	0.1917(4)	0.054(2)
C(11)	0.205(2)	0.0632(5)	0.2363(4)	0.056(2)
H(11*A*)	0.282	0.050	0.285	0.067
C(12)	0.262(2)	0.1377(4)	0.2087(4)	0.046(2)
C(13)	−0.147(2)	0.1324(4)	0.0210(4)	0.051(2)

Table 2. Selected bond lengths (*d*, Å) and angles (ω, deg) in structure **II**

Bond	*d*	Bond	*d*
N(1)–O(1)	1.19(1)	N(1)–O(2)	1.20(1)
N(1)–C(4)	1.49(1)	N(2)–O(3)	1.24(1)
N(2)–O(4)	1.12(2)	N(2)–O(4*X*)	1.35(2)
N(2)–C(10)	1.47(1)	N(3)–O(5)	1.24(1)
N(3)–O(6)	1.25(1)	N(3)–C(12)	1.47(1)
O(7)–C(13)	1.19(1)	C(1)–C(2)	1.40(1)
C(1)–C(6)	1.38(1)	C(1)–C(7)	1.48(1)
C(2)–C(3)	1.38(1)	C(2)–C(13)	1.51(1)
C(3)–C(4)	1.37(1)	C(4)–C(5)	1.36(1)
C(5)–C(6)	1.39(1)	C(7)–C(8)	1.40(1)
C(7)–C(12)	1.37(1)	C(8)–C(9)	1.40(1)
C(8)–C(13)	1.48(1)	C(9)–C(10)	1.35(1)
C(10)–C(11)	1.37(1)	C(11)–C(12)	1.38(1)
Angle	ω	Angle	ω
O(1)N(1)O(2)	122.5(9)	O(1)N(1)C(4)	118.2(8)
O(2)N(1)C(4)	119.3(8)	O(3)N(2)O(4)	122(1)
O(3)N(2)O(4*X*)	126(1)	O(3)N(2)C(10)	117.1(8)
O(4)N(2)C(10)	120(1)	O(4*X*)N(2)C(10)	111(1)
O(5)N(3)O(6)	124.1(9)	O(5)N(3)C(12)	117.5(8)
O(6)N(3)C(12)	118.3(8)	C(2)C(1)C(6)	119.0(7)
C(2)C(1)C(7)	107.9(6)	C(6)C(1)C(7)	133.1(7)
C(1)C(2)C(3)	122.0(7)	C(1)C(2)C(13)	109.6(6)
C(3)C(2)C(13)	128.3(7)	C(2)C(3)C(4)	116.3(7)
N(1)C(4)C(3)	118.8(7)	N(1)C(4)C(5)	117.6(7)
C(3)C(4)C(5)	123.6(8)	C(4)C(5)C(6)	119.9(8)
C(1)C(6)C(5)	119.2(7)	C(1)C(7)C(8)	108.3(6)
C(1)C(7)C(12)	135.1(7)	C(8)C(7)C(12)	116.5(7)
C(7)C(8)C(9)	122.9(7)	C(7)C(8)C(13)	110.2(6)
C(9)C(8)C(13)	126.8(7)	C(8)C(9)C(10)	116.5(7)
N(2)C(10)C(9)	119.7(8)	N(2)C(10)C(11)	117.2(7)
C(9)C(10)C(11)	123.1(8)	C(10)C(11)C(12)	119.2(7)
N(3)C(12)C(7)	120.4(7)	N(3)C(12)C(11)	117.7(7)
C(7)C(12)C(11)	121.8(7)	O(7)C(13)C(2)	127.6(7)
O(7)C(13)C(8)	128.4(7)	C(2)C(13)C(8)	103.9(6)

(plane 1) is 0.026 Å, and the maximum deviation (0.047 Å) is observed for the C(7) atom]. The angles formed by the planes of the benzene rings with the five-membered ring are 1.3° and 2.7°, and the angle between the planes of the benzene rings is 3.6°. The nitro groups are rotated with respect to plane 1 through different angles. The planes of the nitro groups N(1)O(1)O(2) (plane 2) and N(2)O(3)O(4) (plane 3) in the 7- and 2-positions are nearly parallel to plane 1 [the angles 1/2 and 1/3 are 16.2° and 14.1°, respectively; for the second position of the nitro group N(2)O(3)O(4*X*) (plane 3*X*), the angle is 26.3°], whereas the N(3)O(5)O(6) nitro group in the 4-position (plane 4) is rotated with respect to plane 1 through an angle of 46.4°. The planes of the nitro groups form the following angles: 2/3, 4.6° (2/3*X*, 33.9°); 2/4, 51.0°; 3/4, 46.5° (3*X*/4, 68.2°).

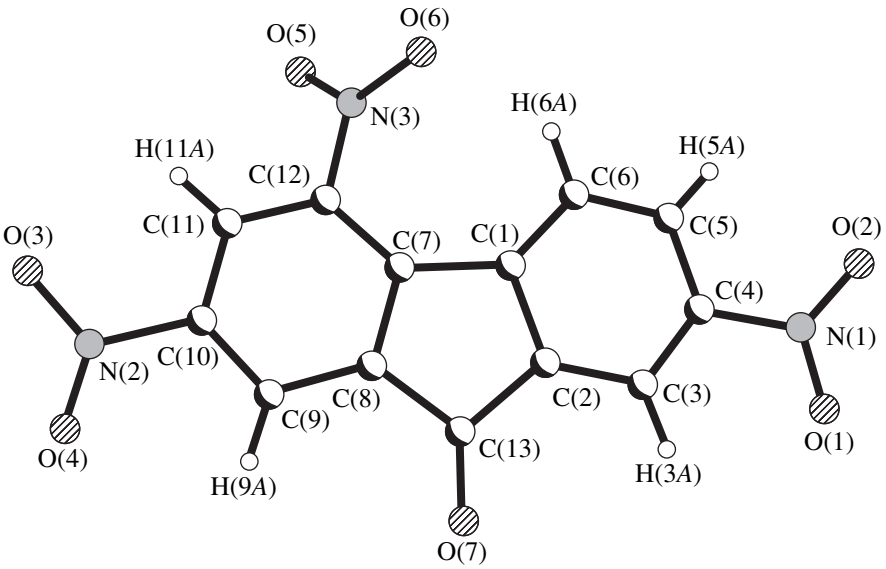

Fig. 1. Structure of molecule **II**.

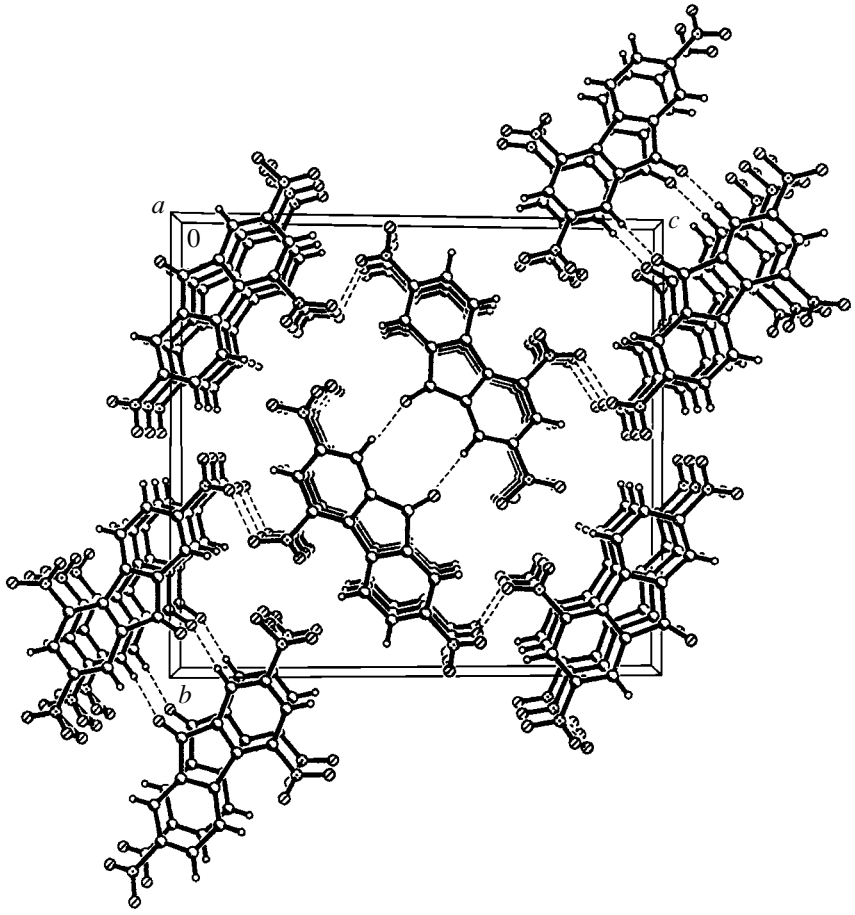

Fig. 2. Molecular packing in structure **II** (projection along the *a* axis).

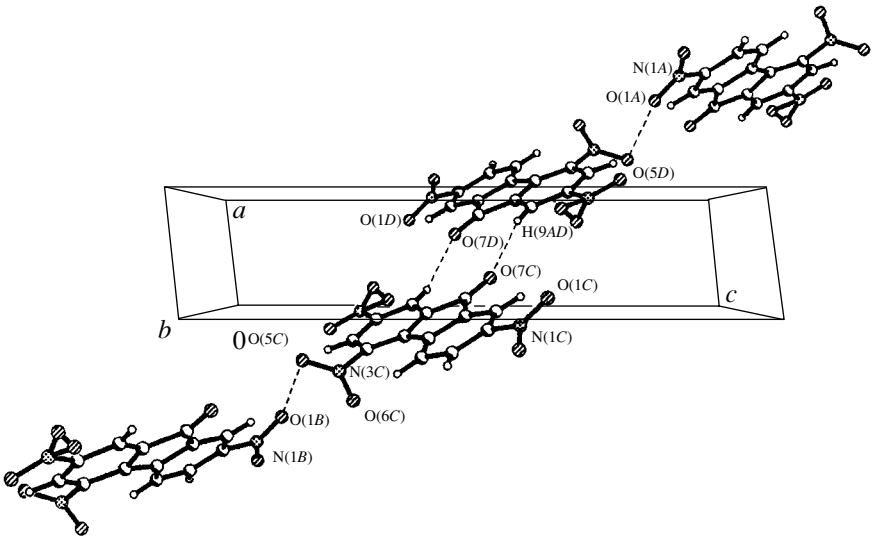

Fig. 3. A fragment of framework structure **II**.

In the crystal, centrosymmetric pseudodimers are distinguished due to the short C–H···O contact (possibly, hydrogen bond) between the O(7) carbonyl oxygen atom and the H(9*A*) atom of the dinitrosubstituted benzene ring of another molecule that is related to the former molecule by the center of symmetry [O(7)···H(9*A*), 2.58 Å; O(7)···C(9), 3.48(1) Å; the O(7)H(9*A*)C(9) angle is 163°]. The pseudodimers are packed into columns aligned along the shortest parameter *a* and arranged according to the base-centered motif (Fig. 2). The oxygen atoms of the two nitro groups form short contacts between the columns [O(5)···O(1) (1 + *x*, 1/2 – *y*, 1/2 + *z*), 2.76(1) Å], due to which the framework structure is formed (Fig. 3).

Earlier [5], the crystal structure of another monoclinic polymorphic modification of *TNF* (**III**) was determined. Polymorphs **II** and **III** are identical in composition, even though structure **III** (*a* = 22.470 Å, *b* = 5.652 Å, *c* = 10.278 Å, β = 105.51°, *V* = 1257.7 Å^3, and ρ_{calcd} = 1.675 g/cm^3) is slightly looser: in **III**, the unit cell volume is larger by 34 Å^3 and the density ρ_{calcd} is lower by 0.036 g/cm^3 than those in **II**. Planar molecules in structures **II** and **III** (pseudodimers in **II** and layers in **III**) are packed into columns aligned along the shortest period (the *a* axis in **II** and the twofold screw axis or the *b* period in **III**). In structure **III**, the shortest intermolecular contacts O(NO_2)···C(H) (3.08 Å) and O(NO_2)···O(NO_2) (3.03 Å) are directed along the short *b* axis of the crystal.

In addition to the crystal structures of polymorphs **II** and **III**, we determined the structures of seven *TNF* complexes of the composition *TNF* · *L* or 2*TNF* · *L* with organic molecules (*L*): for the former composition, *L* is pyrido(1",2" : 1',2')imidazo(4',5' : 4,5)imidazo(1,2-*a*)pyridine (**IV**) [6], 2,6- or 2,7-dimethylnaphthalene [7], the *p*-tricyanovinylphenyl-dicyanomethide in the tetramethylammonium salt) [8], and hexamethylbenzene [9]; and for the latter composition, *L* is tetrakis(phenylethynyl)ethene [10, 11] and 1,6-bis(*N*-carbazolyl)-2,4-hexadiyne [12]. In the case where the *L* molecules are also planar as *TNF*, the molecular packing in the crystals of complexes *nTNF* · *L* (*n* = 1 or 2) is similar to that in crystals **II** and **III**. For example, in crystal **IV** [6], planar molecules of *TNF* and dipyridosubstituted 1,3,4,6-tetraazapentalene *L* are packed according to a stacking motif. Molecules of *TNF* and *L*, which are not exactly parallel, alternate (the *TNF*/*L* dihedral angle is 8.0°, and the mean interplanar spacing is 3.3 Å). The molecules are arranged in such a way that the monosubstituted benzene ring of *TNF* is situated over the center of the bicyclic imidazo[4,5-*d*]imidazole system of *L*.

Table 3 presents the averaged geometric parameters of two *TNF* polymorphs **II** and **III**, the unsubstituted 9-fluorenone molecule **I** [1], and 4-phenylthio-2,7-dinitro-9-fluorenone (**V**) [13]. As it is seen from Table 3, three substituents in the 2-, 4-, and 7-positions of molecules **II**, **III**, and **V** and their nature (the presence of bulky 4-thiophenyl substituent in structure **V**) produce a minor effect on the geometric parameters of the 9-fluorenone skeleton of the molecules. In the benzene rings, the CCC angles at the nitrosubstituted carbon atoms are significantly larger than the CCC(u) angles at the unsubstituted C atoms and exceed to a lesser degree the CCC(j) angles at the junction between the five-membered and six-membered rings. The tricyclic system of thirteen carbon atoms in all the four molecules **I**–**III** and **V** is almost planar.

The bands in the IR spectrum of *TNF* were assigned according to the data obtained for the unsubstituted fluorenone. In particular, the spectrum of crystalline *TNF*

Table 3. Averaged geometric parameters of 9-fluorenone (**I**) and its nitrosubstituted derivatives **II**, **III**, and **V**

Parameter	$C_{13}H_8O$ **I**	$C_{13}H_5N_3O_7$ **II**	$C_{13}H_5N_3O_7$ **III**	$C_{19}H_{10}N_2O_5S$ **V**
Distances, Å				
N–O		1.21(1)	1.212(7)	1.220(3)
C–C (5-m)	1.486(5)	1.49(1)	1.497(7)	1.490(4)
C–C (bzn)	1.383(5)	1.38(1)	1.384(7)	1.387(4)
C=O	1.220(4)	1.19(1)	1.209(7)	1.212(3)
Angles, deg				
ONO		123.3(9)	124.2(5)	124.1(2)
ONC		118.1(8)	118.3(5)	117.9(2)
CCC(NO_2)		122.8(8)	123.5(5)	123.0(3)
CCC(u)	120.4(3)	118.2(7)	117.2(5)	118.3(3)
CCC(j)	121.7(3)	120.1(7)	120.8(5)	121.2(3)
CCC(5-m)	108.4(3)	109.0(6)	108.9(4)	108.7(3)
CC(9)(5-m)	105.8(3)	103.9(6)	104.6(4)	105.2(3)
CCO	127.1(3)	128.0(7)	127.7(5)	127.4(2)
NO_2/fl		14.1*, 46.4	3.7, 32.7	5.0, 15.9
		16.2	15.3	
bzn/5-m	~1	2.0	1.3	1.3
bzn/bzn	~1	3.6	1.5	1.5
Reference	[1]	This work	[5]	[13]

Note: The conventional designations are as follows: 5-m is the five-membered ring; bzn is the benzene ring; CCC(NO_2) and CCC(u) are the angles in the benzene rings at the nitrosubstituted and unsubstituted C atoms, respectively; CCC(j) are the angles in the benzene rings at the C atoms lying at the junction between the benzene and five-membered rings; CC(9)C is the angle at the carbon atom of the carbonyl group; NO_2/fl are the angles of rotation of the nitro groups sequentially in the 2-, 4-, and 7-positions with respect to the fluorenone skeleton; and bzn/5-m and bzn/bzn are the dihedral angles between the planes of the benzene and five-membered rings and benzene rings, respectively.
* Data for the N(2)O(3)O(4) nitro group in the 2-position of structure **II** [the occupancy factor for the position of the O(4) atom is 0.64(6)].

exhibits a narrow band of the ν(CO) stretching vibrations at a frequency of 1730 cm^{-1}. This band is observed at a frequency 10 cm^{-1} lower than that in the spectrum of the unsubstituted fluorenone due to the inductive effect of the nitro groups. In the range of stretching vibrations of nitro groups, doublet bands of symmetric and asymmetric vibrations are observed at frequencies $\nu^{as}(NO_2)$ = 1520 and 1540 cm^{-1} and $\nu^{s}(NO_2)$ = 1350 and 1371 cm^{-1}. The pronounced splitting of these bands can be explained by the nonequivalent contributions from the nitro groups to the conjugation in the molecule. The high-frequency components are attributed to the vibrations of the nitro group in the 2-position, which, according to the X-ray diffraction data, is rotated with respect to the plane by 46°. In the range of stretching vibrations of aromatic bonds, the spectra contain a doublet band of medium intensity ν(CH) = 3076/3088 cm^{-1} and a weak band at 3101 cm^{-1}.

The electronic absorption spectrum contains a weak band at a wavelength of 435 nm due to the $n \longrightarrow \pi^*$ transition and the bands at 387, 302, 260, and 222 nm due the $\pi \longrightarrow \pi^*$ transitions.

REFERENCES

1. H. R. Luss and D. L. Smith, Acta Crystallogr., Sect. B: Struct. Crystallogr. Cryst. Chem. **28** (3), 884 (1972).
2. F. H. Allen and O. Kennard, Chem. Design Automat. News **8** (1), 31 (1993).
3. G. M. Sheldrick, Acta Crystallogr., Sect. A: Found. Crystallogr. **46** (5), 467 (1990).

4. G. M. Sheldrick, *SHELXL93: Program for the Refinement of Crystal Structures* (Univ. of Göttingen, Germany, 1993).
5. D. L. Dorset and A. Hybl, Acta Crystallogr., Sect. B: Struct. Crystallogr. Cryst. Chem. **28** (11), 3122 (1972).
6. M. P. Groziak, S. R. Wilson, G. L. Clauson, and N. J. Leonard, J. Am. Chem. Soc. **108** (25), 8002 (1986).
7. T. Sizuki, H. Fujii, T. Miyashi, and Y. Yamashita, J. Org. Chem. **57**, 6744 (1992).
8. D. J. Sandman, S. J. Gramatica, T. J. Holmes, and A. F. Richter, Mol. Cryst. Liq. Cryst. **59**, 241 (1980).
9. J. N. Brown, L. D. Cheung, L. M. Trefonas, and R. J. Majeste, J. Cryst. Mol. Struct. **4**, 361 (1974).
10. F. Diederich, D. Philip, and P. Seiler, Chem. Commun., No. 2, 205 (1994).
11. H. Taniguchi, K. Hayashi, K. Nishioka, *et al.*, Chem. Lett. 1921 (1994).
12. Z. Yu, N. Zhu, and D. Zhu, Wuji Huaxue Xuebao **3**, 663 (1987).
13. O. V. Chelysheva, L. A. Chetkina, V. K. Bel'skiĭ, and A. M. Andrievskiĭ, Kristallografiya **34** (4), 1020 (1989) [Sov. Phys. Crystallogr. **34**, 617 (1989)].

Translated by I. Polyakova

Crystallography Reports, Vol. 50, No. 1, 2005, pp. 78–84. Translated from Kristallografiya, Vol. 50, No. 1, 2005, pp. 84–90.

STRUCTURE OF ORGANIC COMPOUNDS

Investigation of Structural Transformations in Pyridine Nitrate at Low Temperatures and High Pressures

D. P. Kozlenko*, J. W. Wasicki, V. P. Glazkov***, S. E. Kichanov*, W. Nawrocik**, and B. N. Savenko***

** Joint Institute for Nuclear Research, ul. Zholio-Kyuri 6, Dubna, Moscow oblast, 141980 Russia*
e-mail: ekich@nf.jinr.ru
*** Mickiewicz University, Umultowska 85, Poznan, 61-614 Poland*
**** Russian Research Center Kurchatov Institute, pl. Kurchatova 1, Moscow, 123182 Russia*
Received July 14, 2003

Abstract—The structural transformations in pyridine nitrate *Py*HNO_3 ($C_5D_5NHNO_3$) are investigated by neutron diffraction in the temperature range 16–300 K at normal pressure and in the high-pressure range 0–3.5 GPa at room temperature. A new high-pressure phase with a monoclinic structure (space group $P2_1/c$) is revealed in the *Py*HNO_3 compound at pressures $P > P_{tr} \sim 1$ GPa. The geometry of hydrogen bonds and the coordination of the *Py*H^+ and NO_3^- ions in the structure of the *Py*HNO_3 compound are studied as a function of the temperature and pressure. © *2005 Pleiades Publishing, Inc.*

INTRODUCTION

A large number of pyridine salts belong to the group of molecular–ionic crystals with interionic hydrogen bonds. Depending on the symmetry and sizes of the anions, these compounds can exhibit a great variety of interesting phenomena, such as phase transitions, ferroelectricity, and orientational dynamical disorder of the pyridine cations [1–4].

It is known that the properties of the pyridine nitrate *Py*HNO_3 ($C_5H_5NHNO_3$) differ significantly from those of other pyridine salts. The reorientation frequency of pyridine cations in this compound at room temperature is considerably less than that observed in other pyridine compounds. The *Py*HNO_3 pyridine nitrate neither exhibits ferroelectric properties nor undergoes order–disorder phase transitions, which have been revealed in other pyridine compounds such as *Py*BF_4 [1], *Py*ClO_4 [2], *Py*ReO_4 [3], and *Py*IO_4 [4]. It is believed that these differences in the properties of the *Py*HNO_3 compound are associated with the formation of strong hydrogen bonds between *Py*H^+ ($C_5H_5NH^+$) and NO_3^- ions [5].

Recent structural investigations of a number of pyridine salts at high pressures up to 0.33 GPa have revealed that the compressibility coefficients of these compounds are rather large [5] and can be comparable to the compressibility coefficients characteristic of molecular crystals [6]. Therefore, the high pressures applied to pyridine salts can lead to noticeable changes in the interatomic distances and interatomic interaction potentials and induce phase transitions in these compounds, as is the case in many molecular crystals, for example, in solid benzene C_6H_6 [7].

Under normal conditions, the *Py*HNO_3 compound has a monoclinic structure (space group $P2_1/c$) with the unit cell parameters a = 3.905 Å, b = 12.286 Å, c = 13.437 Å, β = 90.5°, and Z = 4 [8]. Lewicki *et al.* [9] performed an NMR investigation of the dynamics of the *Py*HNO_3 salt at high pressures up to 0.75 GPa and showed that the reorientation of *Py*H^+ cations occurs between potential barriers of different heights [9]. It has been found that the asymmetry parameter, which accounts for the difference between the potential barriers heights, decreases with an increase in the temperature and changes with an increase in the pressure. However, no phase transitions in the pyridine nitrate have been observed at pressures up to 0.75 GPa.

In this work, the crystal structure of the deuterated pyridine nitrate $C_5D_5NHNO_3$ was studied using neutron diffraction in the temperature range 16–300 K at high pressures up to 3.5 GPa. The deuterated compound $C_5D_5NHNO_3$ (which is isostructural to the $C_5H_5NHNO_3$ salt) was chosen as the object of our investigation, because the deuterium atoms are more suitable for neutron diffraction experiments owing to their better characteristics as compared to hydrogen atoms that are characterized by a very large incoherent neutron scattering cross section.

EXPERIMENTAL TECHNIQUE

For our experiments, we used samples of the $C_5D_5NHNO_3$ compound with a deuterium content of approximately 99%.

The neutron diffraction experiments were performed on a DN-12 spectrometer [10] installed on an

IBR-2 pulsed high-flux reactor (Frank Laboratory of Neutron Physics, Joint Institute for Nuclear Research, Dubna) with the use of high-pressure chambers equipped with sapphire anvils [11]. The neutron diffraction measurements were carried out in the temperature range 16–300 K and at high pressures from 0 to 3.5 GPa. The pressure in the chamber was measured from the shift of the luminescence line of ruby to an accuracy of 0.05 GPa. The low-temperature measurements were performed using a special cryostat based on a closed-cycle helium refrigerator. The samples to be studied had a volume $V \sim 2$ mm^3. The neutron diffraction patterns were recorded at a scattering angle $2\theta = 90°$. The resolution of the diffractometer $\Delta d/d$ at a wavelength $\lambda = 2$ Å was equal to 0.015. The characteristic time taken for one spectrum to be measured was 20 h. The neutron diffraction data were processed by the Rietveld method according to the MRIA [12] and Fullprof [13] program packages.

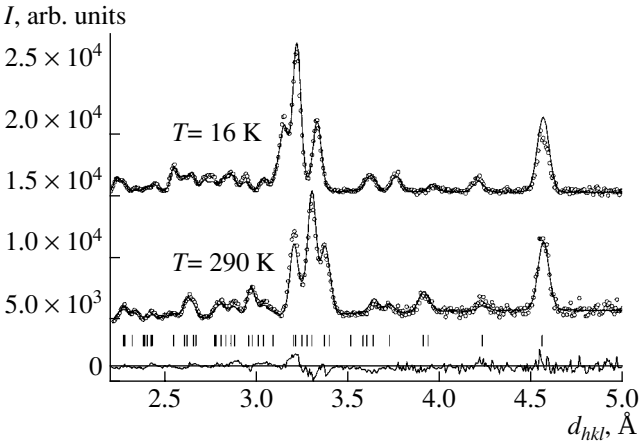

Fig. 1. Fragments of the neutron diffraction patterns of the *Py*HNO_3 compound at a pressure $P = 0$ GPa and temperatures $T = 290$ and 16 K and their processing by the Rietveld method. Points are the experimental data. The calculated profiles, the difference curve (at $T = 290$ K), and the calculated positions of the diffraction peaks are shown.

RESULTS AND DISCUSSION

Figure 1 shows the neutron diffraction patterns of the *Py*HNO_3 compound under normal pressure and at temperatures of 290 and 16 K. A decrease in the temperature is not accompanied by structural phase transformation in the *Py*HNO_3 compound. This is in agreement with the results of previous investigations [5, 9]. The neutron diffraction patterns were analyzed by the Rietveld method, which made it possible to determine the unit cell parameters at different temperatures (Table 1). A decrease in the temperature from 290 to 16 K leads to the following changes in the unit cell parameters: the unit cell parameter *a* decreases from 3.904(5) to 3.759(5) Å, the unit cell parameter *c* decreases from 13.514(7) to 13.400(7) Å, and the β angle decreases from 90.7(2)° to 87.9(2)°, whereas the unit cell parameter *b* increases from 12.361(7) to 12.448(7) Å. The unit cell parameters determined for $T = 290$ K agree well with the data obtained by Serewicz *et al.* [8]. The bulk thermal expansion coefficient $\alpha = 1/V(dV/dT)p$ for the pyridine nitrate at normal pressure was calculated to be $\alpha = 1.43 \times 10^{-4}$ K^{-1}, which is somewhat smaller than the bulk thermal expansion coefficient $\alpha = 2.8 \times 10^{-4}$ K^{-1} obtained by Bobrowicz-Sarga *et al.* [5]. The difference between the bulk thermal expansion coefficients determined in [5] and in this work is most likely associated with the nonlinear temperature dependence of the unit cell volume *V* for the *Py*HNO_3 compound [5]. The bulk thermal expansion coefficient α calculated in this work can be treated as the mean thermal expansion coefficient in the temperature range 16–300 K. It should also be noted that, in [5], the bulk thermal expansion coefficient α was determined in the temperature range close to room temperature in which the dependence $V(T)$ exhibits a nearly linear behavior and the relative change in the unit cell volume is larger in magnitude.

The neutron diffraction patterns of the *Py*HNO_3 compound at pressures of 0.3 and 1.6 GPa are depicted in Fig. 2. The diffraction patterns measured at a pressure $P = 1.1$ GPa and higher are characterized by substantial changes in the integrated intensities and the positions of a number of diffraction peaks. Note that neither the appearance of new diffraction peaks nor the

Table 1. Unit cell parameters of the *Py*HNO_3 compound at different pressures and temperatures

P, GPa	*T*, K	*a*, Å	*b*, Å	*c*, Å	β, deg
0	290	3.904(3)	12.361(6)	13.513(6)	90.7(2)
0	290	3.905	12.286	13.47	90.5
0	16	3.759(3)	12.448(6)	13.400(6)	87.9(2)
0.3	290	3.810(5)	12.321(8)	13.440(8)	90.4(2)
1.1	290	3.618(5)	11.949(8)	12.927(8)	90.7(2)
1.6	290	3.580(5)	11.944(8)	12.891(8)	90.8(2)
2.4	290	3.551(6)	11.910(8)	12.850(8)	90.8(2)
3.5	290	3.507(9)	11.81(1)	12.81(1)	91.6(4)

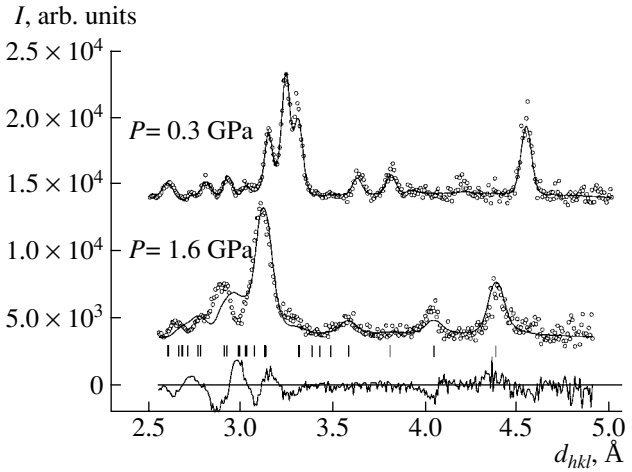

Fig. 2. Fragments of the neutron diffraction patterns of the *Py*HNO_3 compound at pressures P = 0.3 and 1.6 GPa and a temperature T = 290 K and their processing by the Rietveld method. Points are the experimental data. The calculated profiles, the difference curve, and the calculated positions of the diffraction peaks (at P = 1.6 GPa) are shown.

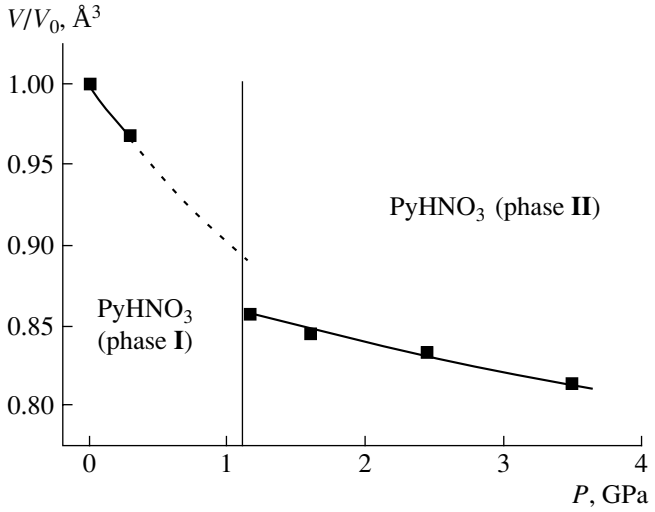

Fig. 3. Pressure dependences of the unit cell volume for the *Py*HNO_3 compound. The errors in determining the experimental points do not exceed the symbol sizes. Solid lines correspond to the interpolation of the experimental data by the Birch equation for phases **I** and **II**. The dotted line indicates the hypothetical pressure dependence of the unit cell volume for the *Py*HNO_3 compound in the pressure range 0.3–1.1 GPa.

disappearance of any one of the already existing peaks in the diffraction patterns measured at lower pressures (P < 1.1 GPa) were observed. The pressure dependences of the unit cell parameters (Table 1) and the unit cell volume (Fig. 3) were obtained by processing the neutron diffraction data. For pressure P = 1.1 GPa, these dependences exhibit a jump that corresponds to the relative change in the unit cell volume $\Delta V/V$ = 11%. These findings indicate that the pyridine nitrate at high pressures undergoes an orientational phase transition without a change in symmetry of the crystal lattice. Since no phase transitions are revealed in the *Py*HNO_3 compound at pressures up to 0.75 GPa, we can argue that the transition pressure is close to $P_{tr} \sim 1$ GPa. Both of the structural modifications of the pyridine nitrate that exist under normal and high pressures at room temperature have a monoclinic structure (space group $P2_1/c$) and can differ only in the mutual orientation of the molecular ions *Py*H^+ and NO_3^-. In what follows, the *Py*HNO_3 modifications existing at normal and high pressures will be referred to as phases **I** and **II**, respectively.

Table 2. Compressibility parameters and unit cell volumes at normal pressure for phases **I** and **II** of the *Py*HNO_3 compound

	PyHNO_3 (phase **I**)	*Py*HNO_3 (phase **II**)
B_0, GPa	8(1)	35(4)
B_1	4	4
V_0, Å^3	652.1(5)	577.1(5)

The properties of phases **I** and **II** of pyridine nitrate (Fig. 3) can be described by the Birch equation of state [14]:

$$P = (3/2)B_0(x^{-7/3} - x^{-5/3}) \times [1 + 3/4(B_1 - 4)(x^{-2/3} - 1)], \quad (1)$$

where $x = (V/V_0)$ is the relative change in the volume; V_0 is the unit cell volume at P = 0; and B_0 and B_1 are the empirical parameters, which have the meaning of the bulk modulus at equilibrium and its first derivative with respect to the pressure, respectively. Since the data on the compressibility of different phases of the *Py*HNO_3 compound were obtained over a rather narrow range of pressures, the parameters B_0 and B_1 could not be determined independently of one another. For this reason, the parameters B_0 and V_0 for phases **I** and **II** of pyridine nitrate (Table 2) were calculated by interpolating the experimental data on the dependence $V(P)$ with the use of relationship (1) at a fixed parameter B_1 = 4. The calculated parameter B_0 = 8 GPa for phase **I** of the *Py*HNO_3 compound corresponds to the isothermal compressibility coefficient $\beta_T = 1/B_0 = 0.125$ GPa^{-1}, which is in good agreement with the results obtained in [5] and is comparable in magnitude to the compressibility coefficients β_T for molecular crystals free from hydrogen bonds, for example, naphthalene and anthracene [6]. The bulk modulus B_0 = 35 GPa for high-pressure phase **II** of the *Py*HNO_3 pyridine nitrate is considerably larger than that for phase **I**. This suggests that the orientational phase transition induced by a high

pressure in the $PyHNO_3$ compound leads to the formation of the structure with a closer packing of atoms.

Previous structural investigations performed by different methods for molecular and molecular–ionic crystals [15–17] have revealed that, as a rule, the effect of high pressures up to 10 GPa (or even more) brings about a decrease in the distances between the centers of molecular ions or molecules in the structure, whereas the lengths of intramolecular bonds remain virtually unchanged. Let us now assume that high pressures lead only to a change in the distances between the centers of the PyH^+ and NO_3^- ions and in their mutual arrangement. Moreover, it is assumed that the PyH^+ and NO_3^- molecular ions are not compressible and have fixed values of the intramolecular bond lengths and bond angles, which are known at normal pressure [8, 9]. The use of this "rigid-molecule" approximation makes it possible to reduce considerably the number of independent structural parameters and to analyze the change in the mutual arrangement of the PyH^+ and NO_3^- ions in different phases of the $PyHNO_3$ compound by varying the temperature and the pressure during the processing of the neutron diffraction data according to the Rietveld method with the Fullprof program package [13].

Now, we introduce the orthogonal molecular system of coordinates (X_m, Y_m, Z_m), which is related to the PyH^+ (or NO_3^-) ion, and the crystallographic system of coordinates (X_c, Y_c, Z_c), which is related to the unit cell in the crystal. In this case, the position of the PyH^+ (or NO_3^-) ion in the unit cell is determined by a set of six parameters, namely, the coordinates (x_0, y_0, z_0) of the origin of the molecular system of coordinates (X_m, Y_m, Z_m) with respect to the crystallographic system of coordinates (X_c, Y_c, Z_c) and the Euler angles (φ, θ, ψ) [18] characterizing the mutual orientation of these coordinate systems.

The interatomic bond lengths and bond angles in the PyH^+ and NO_3^- ions used in our calculations are listed in Table 3. These parameters were calculated from the known coordinates of the C, N, O [8], and D (H) [9] atoms and the unit cell parameters of the $PyHNO_3$ compound under normal conditions. For the PyH^+ ion, the center of the hexagon *K*, which is formed by the carbon and nitrogen atoms, is chosen as the origin of the molecular system of coordinates (X_m, Y_m, Z_m). The directions of the coordinate axes are chosen as follows: the Z_m axis is aligned parallel to the vector **KC2**, the X_m axis is directed along the vector [**KC3** × **KC2**] (perpendicular to the hexagon plane), and the Y_m axis is perpendicular to the X_m and Z_m axes (Fig. 4). For the NO_3^- ion, the position of the nitrogen atom is chosen as the origin of the molecular system of coordinates (X_m, Y_m, Z_m).

Table 3. Intramolecular bond lengths (l_i) and bond angles (γ_i) in the $PyHNO_3$ compound under normal conditions

PyH^+		NO_3^-	
Bond	l_i, Å	Bond	l_i, Å
N1–C1	1.356	N2–O1	1.265
C1–C2	1.351	N2–O2	1.210
C2–C3	1.348	N2–O3	1.226
C3–C4	1.344		
C4–C5	1.360		
C5–N1	1.308		
N1–H1	1.034		
N1–D1	1.091		
N1–D2	1.097		
N1–D3	1.093		
N1–D4	1.091		
N1–D5	1.096		
Angle	γ_i, deg	Angle	γ_i, deg
N1–C1–C2	120.57	O1–N2–O2	118.85
C1–C2–C3	118.60	O1–N2–O3	117.94
C2–C3–C4	120.30	O2–N2–O3	123.21
C3–C4–C5	120.20		
C5–N1–C1	119.77		
H1–N1–C1	119.79		
D1–C1–C2	119.51		
D2–C2–C3	120.65		
D3–C3–C4	120.09		
D4–C4–C5	119.58		

The directions of the coordinate axes are chosen as follows: the Z_m axis is aligned parallel to the vector **NO3**, the X_m axis is directed along the vector [**NO2** × **NO3**] (perpendicular to the plane of the triangle formed by the nitrogen and oxygen atoms), and the Y_m axis is perpendicular to the X_m and Z_m axes (Fig. 4). The X_c and Y_c axes of the orthogonal crystallographic system of coordinates are aligned parallel to the *a* and *b* axes of the monoclinic unit cell of the $PyHNO_3$ compound, respectively. The Z_c axis is perpendicular to the X_cY_c plane (Fig. 4) and is close in direction to the *c* axis of the unit cell of the $PyHNO_3$ compound, because the monoclinicity angle $\beta = 90.7°$ only slightly differs from 90°.

Table 4 presents the coordinates (x_0, y_0, z_0) and the Euler angles (φ, ψ, θ), which specify the positions and the mutual orientation of the PyH^+ and NO_3^- ions in the structure of the $PyHNO_3$ compound at different temperatures and pressures. These coordinates and angles were determined from analyzing the neutron diffraction data by the Rietveld method.

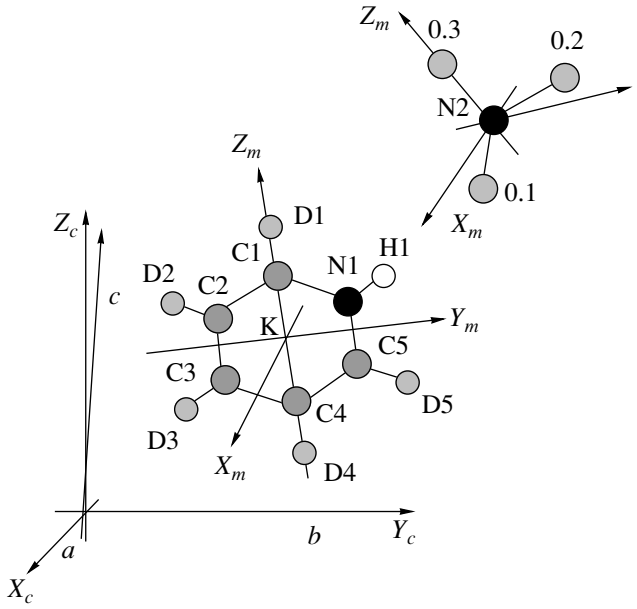

Fig. 4. Relation of the molecular coordinate systems (X_m, Y_m, Z_m) of the *Py*H$^+$ and NO_3^- ions to the crystallographic coordinate system (X_c, Y_c, Z_c).

In phase **I** of the *Py*HNO$_3$ compound (Fig. 5) under normal pressure, the coordinates (x_0, y_0, z_0) and the Euler angles (φ, θ, ψ) of the *Py*H$^+$ and NO_3^- ions remain nearly constant with a decrease in the temperature (Table 4). As the pressure increases to 0.3 GPa, the coordinates (x_0, y_0, z_0) of the *Py*H$^+$ and NO_3^- ions, the Euler angles (φ, θ, ψ) of the *Py*H$^+$ ion, and the angle θ of the NO_3^- ion change insignificantly. The relative change in these parameters does not exceed 1%. However, for the NO_3^- ion, the Euler angle φ decreases from 60° to 48.1° and the angle ψ decreases from 49.7° to 40.9° (Table 4).

It is worth noting that the diffraction peaks in the neutron diffraction patterns of high-pressure phase **II** of the *Py*HNO$_3$ compound (Fig. 2) overlap to a considerably greater extent than those in the neutron diffraction patterns of normal-pressure phase **I**. As a consequence, there is a correlation between the structural parameters obtained by the processing of the former diffraction patterns. Hence, the coordinates (x_0, y_0, z_0) and the Euler angles (φ, θ, ψ) calculated for phase **II** of the *Py*HNO$_3$ compound are approximate and the *R* factors, which characterize the degree of agreement between the calculated and experimental diffraction patterns, are somewhat worse than those for phase **I**. The coordinates (x_0, y_0, z_0) and the Euler angles (φ, θ, ψ) calculated for the *Py*H$^+$ and NO_3^- ions in phase **II** of the *Py*HNO$_3$ pyridine nitrate at a pressure P = 1.6 GPa and at room temperature are given in Table 4. These parameters are consistent with the possible structural model for phase **II** of the *Py*HNO$_3$ compound; however, other structural variants of this phase must not be ruled out.

The pressure-induced orientational phase transition to modification **II** of the *Py*HNO$_3$ pyridine nitrate (Fig. 5) leads to a change in the mutual orientation of the *Py*H$^+$ and NO_3^- ions. Note that the positions of their

Table 4. Coordinates of the centers (x_0, y_0, z_0) and the Euler angles (φ, θ, ψ) of the *Py*H$^+$ and NO_3^- ions in the structure of the *Py*HNO$_3$ compound at different pressures and temperatures

P, GPa		0			0.3	1.6
T, K		290	290 [8]	16	290	290
*Py*H$^+$	x_0	0.049(3)	0.050(3)	0.051(3)	0.038(3)	−0.035(6)
	y_0	0.233(4)	0.230(1)	0.228(4)	0.230(4)	0.226(8)
	z_0	0.008(2)	0.003(1)	−0.005(2)	0.012(2)	0.008(5)
	φ, deg	274.2(2)	275.1(2)	273.2(2)	274.0(2)	272.5(2)
	θ, deg	42.9(2)	39.5(2)	44.2(2)	41.6(2)	72.8(2)
	ψ, deg	93.8(2)	93.0(2)	94.4(2)	92.9(2)	9.3(9)
NO_3^-	x_0	−0.501(5)	−0.490(3)	−0.466(5)	−0.490(5)	−0.522(8)
	y_0	0.477(5)	0.483(1)	0.488(5)	0.482(2)	0.468(8)
	z_0	0.216(4)	0.209(1)	0.213(4)	0.223(4)	0.210(7)
	φ, deg	59.0(2)	57.0(2)	62.3(2)	48.1(2)	63.8(7)
	θ, deg	74.9(2)	74.5(2)	75.8(2)	74.0(2)	76.5(7)
	ψ, deg	49.7(2)	47.8(2)	52.3	40.9(2)	76.8(7)
R_p, %		4.46		6.57	7.82	13.8
R_{wp}, %		3.27		6.04	7.46	15.3

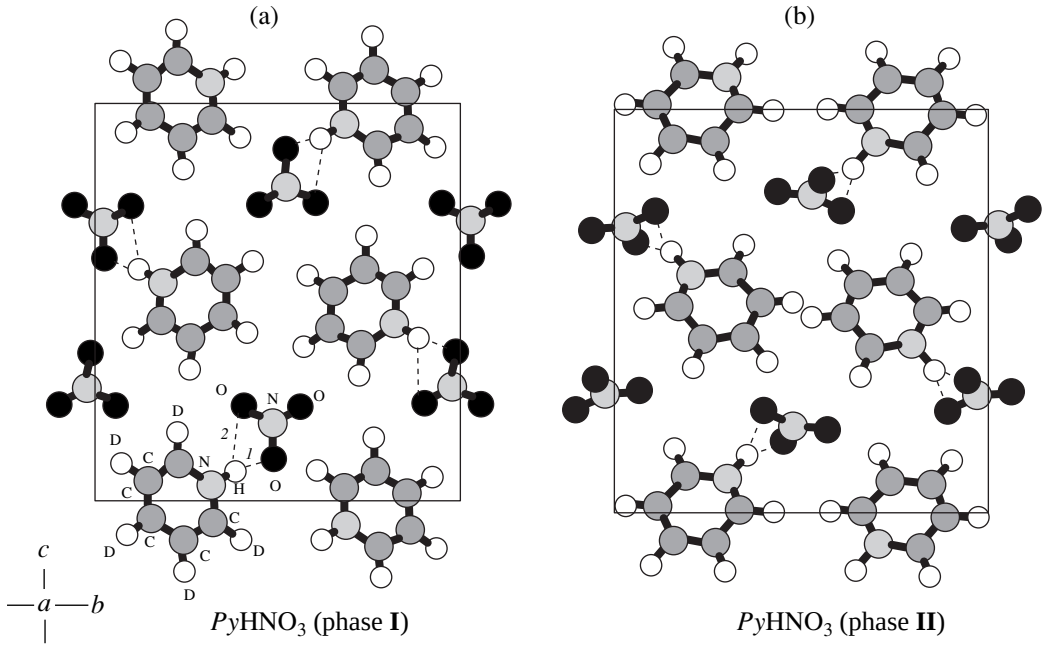

Fig. 5. Projections of the monoclinic crystal structure (space group $P2_1/c$) of (a) normal-pressure phase **I** and (b) high-pressure phase **II** of the deuterated pyridine nitrate $C_5D_5NHNO_3$ onto the crystallographic plane (*bc*).

centers, which are specified by the coordinates (x_0, y_0, z_0), remain approximately identical to those in phase **I** observed at normal pressure (Table 4). The phase transition results in a considerable change in the Euler angles of the PyH^+ and NO_3^- ions. As the pressure increases from 0.3 to 1.6 GPa, the angle θ increases from 42.9° to 72.8° and the angle ψ decreases from 93.8° to 9.3° for the PyH^+ ion, whereas the angle ψ for the NO_3^- ion increases from 49.7° to 76.8°.

In monoclinic phase **I** of the $PyHNO_3$ pyridine nitrate, the PyH^+ and NO_3^- ions are linked together by two hydrogen bonds of different lengths: N–H···O_1 and N–H···O_2 (Fig. 5). The calculated lengths of these bonds under normal conditions, namely, l_1 = 2.73(4) Å and l_2 = 3.14(5) Å, are in good agreement with the data obtained in [8]. A decrease in the temperature from 290 to 16 K results in an insignificant increase in the length of the stronger hydrogen bond to l_1 = 2.77(4) Å and a moderate increase in the length of the second hydrogen bond to l_2 = 3.23(5) Å. In this case, the N–H–O_1 and N–H–O_2 angles formed by the hydrogen bonds increase from 169.0° to 175.5° and from 126.5° to 127.4°, respectively (Table 5). In the structure of phase **I**, the nearest environment of each NO_3^- ion involves eight PyH^+ ions (Fig. 5). The distances between the centers of the NO_3^- ion (the N2 atom in Fig. 4) and the nearest neighbor ions PyH^+ (the point *K* in Fig. 4) are different. The two shortest distances l = 4.46 and 4.66 Å are observed for the PyH^+ and NO_3^- ions linked together by the hydrogen bonds. The remaining six nearest distances between these ions are substantially longer: there exist two distances l ~ 5.05 Å, three distances l ~ 5.15 Å, and one (longest) distance l ~ 5.36 Å. With a decrease in the temperature, the coordination environment formed by the nearest neighbor ions PyH^+ around the NO_3^- ions becomes more symmetric. Among the eight nearest distances between the centers of these ions at normal pressure and T = 16 K, there exist three distances l ~ 4.75 Å, three distances l ~ 5.00 Å, and two distances l ~ 5.25 Å.

In phase **I** of the $PyHNO_3$ pyridine nitrate at room temperature, an increase in the pressure from 0 to 0.3 GPa only weakly affects the lengths and angles of

Table 5. Lengths and angles of the N–H–O_1 and N–H–O_2 hydrogen bonds in the structure of the $PyHNO_3$ compound at different pressures and temperatures

P, GPa	0		0.3	1.6
T, K	290	16	290	290
l_1, Å	2.73(4)	2.77(4)	2.76(4)	2.60(5)
l_2, Å	3.14(5)	3.23(5)	3.13(5)	3.39(6)
N–H–O_1, deg	169.0(2)	175.5(2)	172.5(2)	157.6(6)
N–H–O_2, deg	126.5(2)	127.4(2)	126.9(2)	129.3(6)

the hydrogen bonds (Table 5). Under these conditions, we also observe a tendency toward an increase in symmetry of the nearest environment formed by the PyH^+ ions around the NO_3^- ions. However, in this case, the distances between the centers of the PyH^+ and NO_3^- ions at a pressure $P = 0.3$ GPa include the two shortest distances $l = 4.58$ and 4.69 Å, four distances $l \sim 5.05$ Å, and two distances $l \sim 5.17$ Å.

The orientational phase transition to high-pressure modification **II** of the $PyHNO_3$ compound results in a substantial change in the geometry of the hydrogen bonds between the PyH^+ and NO_3^- ions (Fig. 5). An increase in the pressure from 0.3 to 1.6 GPa leads to a decrease in the length l_1 of the shorter hydrogen bond from 2.76(4) to 2.60(4) Å and an increase in the length l_2 of the second hydrogen bond from 3.13(5) to 3.39(5) Å. The $N–H–O_1$ angle decreases from 172.5° to 157.6°, whereas the $N–H–O_2$ angle increases from 126.9° to 129.3° (Table 5). The nearest distances between the centers of the PyH^+ and NO_3^- ions in high-pressure phase **II** of the $PyHNO_3$ pyridine nitrate at a pressure $P = 1.6$ GPa are approximately 5% shorter than those in phase **I**. The symmetry of the nearest environment formed by the PyH^+ ions around the NO_3^- ions in phase **II** is higher than that in phase **I** at normal pressure and room temperature. Among the nearest distances between the centers of these ions at room temperature and $P = 1.6$ GPa, there exist two distances $l \sim 4.3$ Å, three distances $l \sim 4.85$ Å, and three distances $l \sim 5.07$ Å.

CONCLUSIONS

Thus, the results of the above investigation demonstrated that the structural parameters, the geometry of hydrogen bonds, and symmetry of the nearest environment of the PyH^+ and NO_3^- ions in the deuterated pyridine nitrate $PyHNO_3$ can change significantly under high pressures and low temperatures.

The orientational phase transition induced by a high pressure in the $PyHNO_3$ compound leads to a change in the mutual arrangement of the PyH^+ and NO_3^- ions at $P_{tr} \sim 1$ GPa. However, the monoclinic symmetry of the unit cell in the crystal remains unchanged (space group $P2_1/c$). Compared to phase **I** of the pyridine nitrate at normal pressure, high-pressure phase **II** is characterized by a closer packing and higher symmetry of the nearest environment of the PyH^+ and NO_3^- ions.

REFERENCES

1. P. Czarnecki, W. Nawrocik, Z. Pajak, and J. Wasicki, Phys. Rev. B **49**, 1511 (1994).
2. P. Czarnecki, W. Nawrocik, Z. Pajak, and J. Wasicki, J. Phys.: Condens. Matter **6**, 4955 (1994).
3. J. Wasicki, P. Czarnecki, Z. Pajak, *et al.*, J. Chem. Phys. **107**, 576 (1996).
4. Z. Pajak, P. Czarnecki, J. Wasicki, and W. Nawrocik, J. Chem. Phys. **109**, 4620 (1998).
5. L. Bobrowicz-Sarga, P. Czarnecki, S. Lewicki, *et al.*, Mater. Sci. Forum **321–324**, 1107 (2000).
6. A. I. Kitaĭgorodskiĭ, *Molecular Crystals* (Nauka, Moscow, 1971) [in Russian].
7. M. M. Thiery and J. M. Leger, J. Chem. Phys. **89**, 4255 (1988).
8. A. J. Serewicz, B. K. Robertson, and E. A. Meyers, J. Phys. Chem. **69**, 1915 (1965).
9. S. Lewicki, J. W. Wasicki, L. Bobrowicz-Sarga, *et al.*, Phase Transit. **76**, 261 (2003).
10. V. L. Aksenov, A. M. Balagurov, V. P. Glazkov, *et al.*, Physica B (Amsterdam) **265**, 258 (1999).
11. V. P. Glazkov and I. N. Goncharenko, Fiz. Tekh. Vys. Davleniĭ **1**, 56 (1991).
12. V. B. Zlokazov and V. V. Chernyshev, J. Appl. Crystallogr. **25**, 447 (1992).
13. J. Rodriguez-Carvajal, Physica B (Amsterdam) **192**, 55 (1993).
14. F. Birch, J. Geophys. Res. **83**, 1257 (1978).
15. J. S. Loveday, R. J. Nelmes, W. G. Marshall, *et al.*, Physica B (Amsterdam) **241–243**, 240 (1998).
16. A. M. Balagurov, D. P. Kozlenko, B. N. Savenko, *et al.*, Fiz. Tverd. Tela (St. Petersburg) **40**, 142 (1998) [Phys. Solid State **40**, 127 (1998)].
17. V. P. Glazkov, D. P. Kozlenko, B. N. Savenko, *et al.*, Kristallografiya **44**, 55 (1999) [Crystallogr. Rep. **44**, 50 (1999)].
18. L. D. Landau and E. M. Lifshitz, *Course of Theoretical Physics*, Vol. 1: *Mechanics*, 3rd ed. (Nauka, Moscow, 1973; Pergamon Press, Oxford, 1976).

Translated by O. Borovik-Romanova

Crystallography Reports, Vol. 50, No. 1, 2005, pp. 85–88. Translated from Kristallografiya, Vol. 50, No. 1, 2005, pp. 91–94.

STRUCTURE OF ORGANIC COMPOUNDS

Crystal Structure of *p*-Carboxyphenylhydrazone Benzoylacetone

S. V. Eliseeva*, L. Kh. Minacheva, N. P. Kuz'mina*, and V. S. Sergienko****

** Moscow State University, Vorob'evy gory, Moscow, 119992 Russia*

e-mail: kuzmina@inorg.chem.msu.ru

*** Kurnakov Institute of General and Inorganic Chemistry, Russian Academy of Sciences, Leninskiĭ pr. 31, Moscow, 119991 Russia*

e-mail: min@igic.ras.ru

Received July 15, 2003

Abstract—The crystal structure of *p*-carboxyphenylhydrazone benzoylacetone is determined. The crystals are monoclinic, $a = 13.614(4)$ Å, $b = 11.388(2)$ Å, $c = 20.029(6)$ Å, $\beta = 104.82(2)°$, $V = 2339(9)$ Å^3, $Z = 8$, space group $C2/c$, and $R = 0.038$ for 1622 reflections with $I > 2\sigma(I)$. The crystal is built of $C_{17}H_{14}N_2O_4$ neutral molecules that are linked by O–H···O hydrogen bonds between the carboxyl groups into centrosymmetric pseudodimers. The effect of carboxylation of the phenylhydrazone fragment and the position of the carboxyl group on the molecular packing in the crystal is determined. The N(1)–H(1N)···O(1) intramolecular hydrogen bond (N–H, 0.94 Å; H···O, 1.87 Å; N···O, 2.59 Å; and the N–H···O angle, 133°) is formed in the molecule.

INTRODUCTION

Arylhydrazones, β-diketone derivatives, are of interest due to their ability to combine different functional groups (such as ketonic, carboxyl, amide, amine, and aldehyde groups) in a single molecule [1]. In recent years, much attention has been given to structural studies of these compounds, because they are characterized by the formation of various intramolecular and intermolecular hydrogen bonds. In this paper, we will describe the crystal structure of hydrazone $C_{17}H_{14}N_2O_4$ (**I**), which is a derivative of benzoylacetone and *p*-aminobenzoic acid. For the purpose of revealing the effect of the position of the carboxyl group in the phenyl ring on the molecular packing in the crystal structure, the structure of **I** is compared with those of similar arylhydrazones that are composed of benzoylacetone and *o*-aminobenzoic acid (**II**) [2] or aniline (**III**) [2].

EXPERIMENTAL

Synthesis

Commercial (Merck) *p*-aminobenzoic acid, sodium nitrate, and benzoylacetone were used in this study without additional purification. The C, H, and N contents were determined using elemental microanalysis.

Hydrazone **I** was synthesized according to a modified procedure described in [3, 4]. An $NaNO_2$ aqueous solution (0.1 mol) was added dropwise to a solution of *p*-aminobenzoic acid (0.1 mol) in 1 M HCl (75 ml) in the cold. The resultant solution of the *p*-carboxyphenyldiazonium salt was added dropwise to an alcoholic solution of benzoylacetone (0.1 mol). The reaction mixture was allowed to stand for 24 h and was then treated with a large amount of water. The orange polycrystalline product was dried in air. The yield was 83%.

For $C_{17}H_{14}N_2O_4$ anal. calcd. (%): C, 58.06; H, 4.83; N, 11.29.

Found (%): C, 58.05; H, 4.62; N, 11.34.

The ^{1}H NMR spectrum was recorded on a Bruker AC-600P spectrometer [293 K, $(CD_3)_2SO$, TMS]. δ, ppm: 2.49 (3H, CH_3); 7.26–7.85 (9H, C_6H_5, C_6H_4); 13.64 (1H, COOH); and 14.55 (1H, NHOH).

The IR spectra were measured on a PE-FTIR-1600 spectrometer (Nujol mull, hexachlorobutadiene). ν, cm^{-1}: 1681, 1647 (C=O), 1636 (C=N), 1564 (N=N), 1272–1356 (N–*Ar*), 2552–3090 (N–H + O–H).

The absorption spectra of alcoholic solutions (~10^{-5} M) were recorded on a Specord M40 spectrophotometer.

X-ray Diffraction Analysis

A single crystal ($0.24 \times 0.26 \times 0.49$ mm) of hydrazone **I**, suitable for X-ray diffraction analysis, was chosen from the products prepared through slow crystallization of an alcoholic solution.

The crystal data are as follows: $M = 278$, monoclinic crystal system, space group $C2/c$, $a = 13.614(4)$ Å, $b = 11.388(2)$ Å, $c = 20.029(6)$ Å, $\beta = 104.82(2)°$, $V = 2339(9)$ Å^3, $\rho_{calcd} = 1.373$ g/cm^3, $\mu(MoK_\alpha) = 0.100$ mm^{-1}, $F(000) = 1296$, and $Z = 8$.

The experimental data were obtained on an Enraf–Nonius CAD4 diffractometer ($2° < \theta < 28°$, $\omega/2\theta$ scan

Table 1. Selected bond lengths (*d*, Å) and bond angles (ω, deg) in structure **I**

Bond	*d*	Bond	*d*	Angle	ω	Angle	ω
N(1)–N(2)	1.311(2)	C(3)–C(4)	1.385(3)	N(2)N(1)C(4)	119.0(2)	O(1)C(8)C(7)	119.1(2)
N(1)–C(4)	1.408(2)	C(4)–C(5)	1.384(3)	C(4)N(1)H(1N)	124	O(1)C(8)C(16)	120.0(2)
N(1)–H(1N)	0.94	C(5)–C(6)	1.376(3)	N(2)N(1)H(1N)	114	C(7)C(8)C(16)	120.9(2)
N(2)–C(7)	1.314(2)	C(7)–C(8)	1.491(3)	N(1)N(2)C(7)	121.3(2)	C(7)C(9)C(10)	120.9(2)
O(1)–C(8)	1.221(3)	C(7)–C(9)	1.476(3)	C(17)O(4)H(4O)	109	O(2)C(9)C(7)	120.4(2)
O(2)–C(9)	1.221(3)	C(8)–C(16)	1.495(3)	C(2)C(1)C(6)	119.3(2)	O(2)C(9)C(10)	118.6(2)
O(3)–C(17)	1.230(2)	C(9)–C(10)	1.497(3)	C(2)C(1)C(17)	121.7(2)	C(9)C(10)C(11)	123.1(2)
O(4)–C(17)	1.312(2)	C(10)–C(11)	1.389(3)	C(6)C(1)C(17)	119.0(2)	C(9)C(10)C(15)	118.0(2)
O(4)–H(4O)	0.95	C(10)–C(15)	1.379(3)	C(1)C(2)C(3)	120.5(2)	C(11)C(10)C(15)	118.7(2)
C(1)–C(2)	1.391(3)	C(11)–C(12)	1.384(4)	C(2)C(3)C(4)	119.4(2)	C(10)C(11)C(12)	119.9(2)
C(1)–C(17)	1.473(3)	C(12)–C(13)	1.370(4)	N(1)C(4)C(3)	121.5(2)	C(11)C(12)C(13)	120.5(2)
C(1)–C(6)	1.387(3)	C(13)–C(14)	1.368(4)	N(1)C(4)C(5)	118.0(2)	C(12)C(13)C(14)	120.0(3)
C(2)–C(3)	1.381(3)	C(14)–C(15)	1.384(4)	C(3)C(4)C(5)	120.5(2)	C(13)C(14)C(15)	119.8(3)
				C(4)C(5)C(6)	119.8(2)	C(10)C(15)C(14)	120.9(2)
				C(1)C(6)C(5)	120.5(2)	O(4)C(17)C(1)	122.2(2)
				N(2)C(7)C(8)	124.1(2)	O(3)C(17)O(4)	122.5(2)
				N(2)C(7)C(9)	113.4(2)	O(3)C(17)C(1)	115.3(2)
				C(8)C(7)C(9)	122.3(2)		

mode, MoK_α radiation, λ = 0.7107 Å, T = 293 K). A total of 3991 reflections were collected of which 3606 were unique (R_{int} = 0.0379, $0 \le h \le 17$, $0 \le k \le 15$, $-26 \le l \le 25$).

The structure was solved by direct methods (SHELXS86 [5]) and refined by the least-squares full-matrix procedure (SHELXL97 [6]) in the anisotropic approximation. The positions of the H atoms at the O(4) and N(1) atoms were determined from difference syntheses of the electron density and were not refined. The positions of the remaining hydrogen atoms were calculated geometrically and refined within a riding model. In this refinement, the isotropic thermal parameters U_H of the hydrogen atoms exceeded the equivalent isotropic thermal parameters U_C of the carbon atoms attached to the parent atoms by a factor of 1.2 [1.5 for the hydrogen atoms H(16*A*), H(16*B*), and H(16*C*) of the methyl groups].

The final discrepancy factors are as follows: R_1 = 0.0377, wR_2 = 0.1072, and *GOOF* = 0.997 for 1622 reflections with $I > 2\sigma(I)$; and R_1 = 0.1420 and wR_2 = 0.1378 for all reflections. The total number of the parameters refined is 209, the extinction coefficient is 0.0048(7), and the values of $\Delta\rho_{max}$ and $\Delta\rho_{min}$ are equal to 0.238 and –0.194 e/Å^3, respectively.

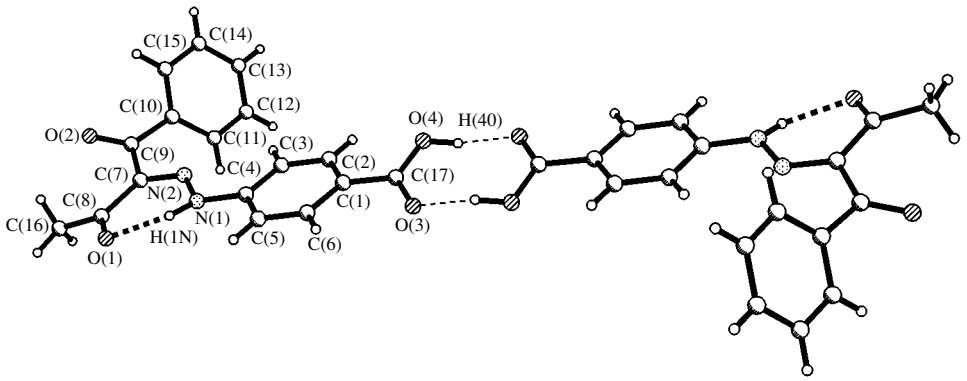

Fig. 1. Pseudodimer in structure **I**.

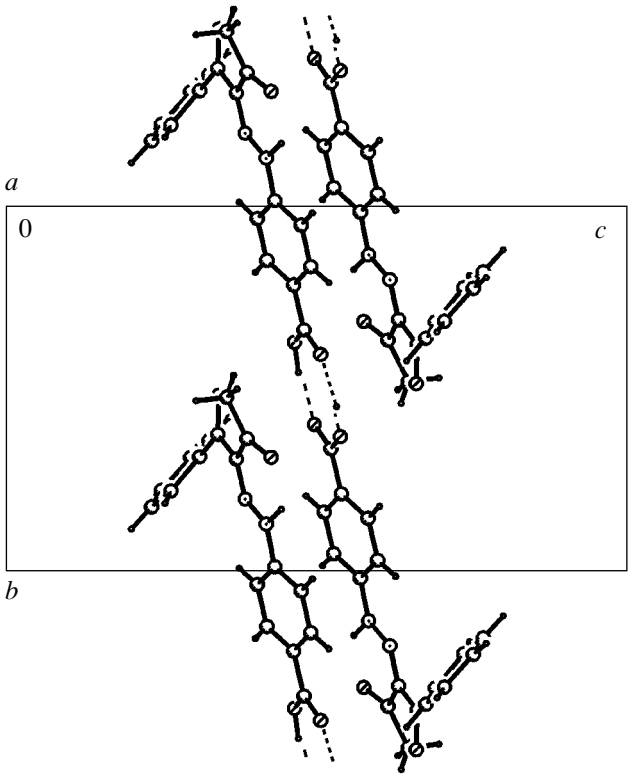

Fig. 2. A fragment of the molecular packing in crystal structure **I**.

The atomic coordinates and thermal parameters have been deposited with the Cambridge Structural Database (no. CCDC 218953). The interatomic distances and bond angles are listed in Table 1.

RESULTS AND DISCUSSION

In the course of the synthesis of hydrazone **I** according to the procedures described in [3, 4], the time of the reaction between the reactants was extended to 24 h. This made it possible to obtain the product with a high yield (83%). The ^{1}H NMR and IR spectra correspond to the composition of the hydrazone thus synthesized. The UV spectrum of compound **I** contains two broad absorption bands in the wavelength ranges 225–275 nm (λ_{max} = 250 nm) and 320–400 nm (λ_{max} = 370 nm). These bands are assigned to the π–π^* and n–π transitions, respectively.

Crystal **I** is built of neutral molecules that are linked by two strong O(4)–H(4O)···O(3) hydrogen bonds between the carboxyl groups into centrosymmetric pseudodimers (Fig. 1).

Compound **I** is a typical representative of β-ketoarylhydrazones. The characteristic features of these compounds are the N–H···O intramolecular hydrogen bonds and the delocalization of the electron density over the NH–N=C central fragment, as can be judged from the equalization of the N–N and N–C bond lengths [2, 7]. In structure **I**, the N(1)–H(1N)···O(1) intramolecular hydrogen bond is formed. Similar intramolecular hydrogen bonds were found in structures **II** and **III** [2]. In structure **II**, the oxygen atom of the carboxyl substituent in the *ortho* position participates in the formation of the second intramolecular hydrogen bond with the H(1N) atom. However, the delocalization of the electron density over the NH–N=C central fragment in structure **I** [N(1)–N(2), 1.311(2) Å; N(2)–C(7), 1.314(2) Å] is more pro-

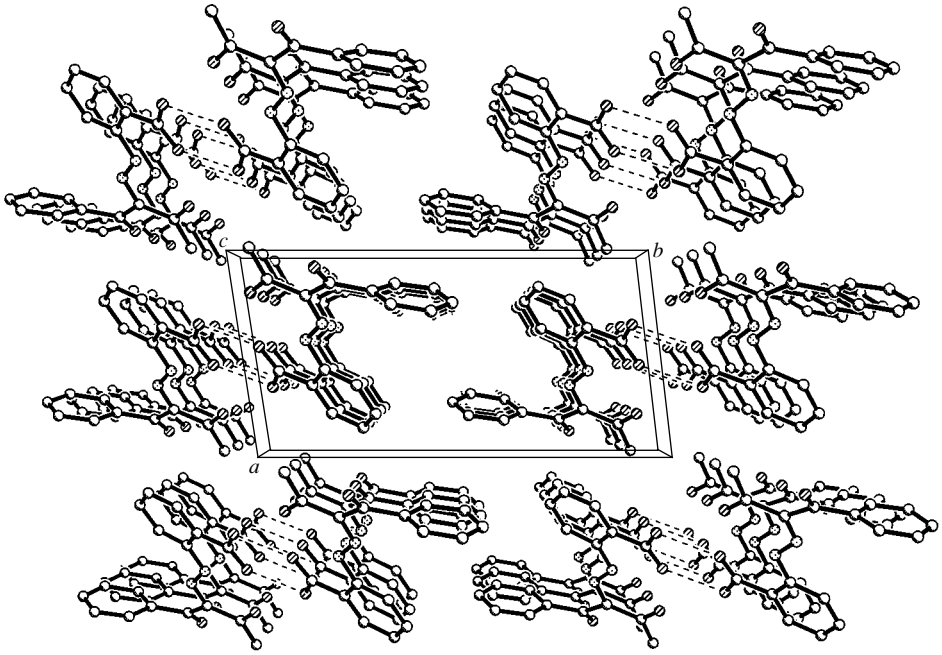

Fig. 3. Molecular packing in structure **II**.

Table 2. Parameters of hydrogen bonds in crystal structures **I**–**III**

Compound	*D*–H··*A*	*D*–H, Å	H··*A*, Å	*D*··*A*, Å	*D*–H··*A* angle, deg	Coordinates of atom *A*
I	N(1)–H(1N)···O(1)	0.94	1.87	2.59	133	*x*, *y*, *z*
	O(4)–H(4O)···O(3A)	0.95	1.73	2.66	169	–*x*, 2 – *y*, 1 – *z*
II	N(1)–H(1N)···O(1)	0.95	1.87	2.60	131	*x*, *y*, *z*
	N(1)–H(1N)···O(4)	0.95	2.05	2.68	122	*x*, *y*, *z*
	O(4)–H(4O)···O(3A)	0.89	1.74	2.62	174	1 – *x*, –*y*, –1 – *z*
	C(2)–H(4)···O(2)	0.91	2.55	3.22	131	–1 –*x*, –*y*, 1 – *z*
III	N(1)–H(1N)···O(1)	0.82	1.93	2.58	135	*x*, *y*, *z*
	C(2)–H(4)···O(2)	0.90	2.56	3.45	167	0.5 +*x*, 1.5 + *y*, *z*

nounced than that in structures **II** (1.317 and 1.303 Å) and **III** (1.300 and 1.322 Å).

The formation of pseudodimers due to the interaction between the carboxyl groups of the neighboring molecules, which was mentioned above for **I**, is also observed in structure **II** [2]. However, the position of the COOH group in the phenyl ring significantly affects the packing of pseudodimers in the crystal structure. For example, in structure **I**, the pseudodimers are shifted relative to each other and are packed into ribbons along the *b* axis (Fig. 2). The planes of the C(1)–C(2)–C(3)–C(4)–C(5)–C(6) rings of two neighboring pseudodimers that are related through an inversion center are situated over one another at a distance of 3.47 Å, which suggests stacking interactions between them. The ribbons are packed into layers aligned parallel to the (001) plane and bounded on both sides by the C(10)–C(11)–C(12)–C(13)–C(14)–C(15) benzene rings. These rings prevent the layers from drawing closer together and, hence, are responsible for the anisometry of the unit cell parameters (the *c* parameter is almost twice as large as the parameter *a* or *b*), which is characteristic of structures **II** and **III** [2]. In structure **II**, unlike structure **I**, the pseudodimers are packed into columns with a parallel arrangement of the planes of the C(1)–C(2)–C(3)–C(4)–C(5)–C(6) and C(10)–C(11)–C(12)–C(13)–C(14)–C(15) rings, as well as the planes of the central fragments of the pseudodimers. However, interactions between the corresponding planes are absent because the molecules in the columns are related by the translation. Molecules in the neighboring columns are linked by the weak C(2)–H(4)···O(2) hydrogen bond (Fig. 3). The molecular packing in crystal structure **III** is similar to that in structure **II**. The parameters of hydrogen bonds in structures **I**–**III** are summarized in Table 2.

Thus, when changing over from structure **III** to structure **II** (upon introduction of the carboxyl group into the *ortho* position of the phenyl ring), the molecular packing remains virtually unchanged, whereas the introduction of the substituent into the *para* position (structure **I**) results in significant changes in the packing of the structural elements.

ACKNOWLEDGMENTS

This study was supported by the Russian Foundation for Basic Research, project no. 02-03-33204.

REFERENCES

1. Yu. P. Kitaev and B. I. Buzykin, *Hydrazones* (Nauka, Moscow, 1970) [in Russian].
2. V. Bertolasi, L. Nanni, P. Gilli, *et al.*, New J. Chem. **18**, 251 (1994).
3. A. Mitchell and D. C. Nonhebel, Tetrahedron **35**, 2013 (1979).
4. H. C. Yao, J. Organomet. Chem. **29**, 2959 (1964).
5. G. M. Sheldrick, Acta Crystallogr., Sect. A: Found. Crystallogr. **46** (6), 467 (1990).
6. G. M. Sheldrick, *SHELXL97: Program for the Refinement of Crystal Structures* (Univ. of Göttingen, Germany, 1997).
7. V. Bertolasi, P. Gilli, V. Ferretti, *et al.*, New J. Chem. **23**, 1261 (1999).

Translated by I. Polyakova

Crystallography Reports, Vol. 50, No. 1, 2005, pp. 89–93. Translated from Kristallografiya, Vol. 50, No. 1, 2005, pp. 95–100.

STRUCTURE OF ORGANIC COMPOUNDS

Molecular and Crystal Structures of Mesomorphic Aromatic Esters: II. The Structure of *p*-Ethoxyphenyl *p*'-Pentylbenzoate

O. V. Noskova*, A. V. Churakov, L. G. Kuz'mina**, J. A. K. Howard***, V. A. Molochko*, and S. M. Pestov***

** Lomonosov Moscow State Academy of Fine Chemical Technology, pr. Vernadskogo 86, Moscow, 117924 Russia*

e-mail: ovnoskova@yandex.ru

*** Kurnakov Institute of General and Inorganic Chemistry, Russian Academy of Sciences, Leninskiĭ pr. 31, Moscow, 119991 Russia*

**** Department of Chemistry, University of Durham, South Road, Durham DH1 3LE, UK*

Received December 29, 2003

Abstract—*p*-Ethoxyphenyl *p*'-pentylbenzoate (**I**), which exhibits a mesophase (*K* 62.6 *N* 63.3 *I*), was studied by X-ray diffraction analysis at 120.0 and 296.0 K. In the molecule **I**, one of the benzene rings is almost coplanar with the carboxy group COO, whereas another benzene ring is twisted with respect to the carboxy group by 65.9°. The geometric parameters of the molecule **I** are indicative of possible conjugation between the carboxy group and the former benzene ring and the absence of conjugation between this group and the second benzene ring. In the crystal packing, extended molecules **I** are oriented along the *bc* diagonal. The mutual orientation of the nearest benzene rings of any two adjacent molecules is T-shaped, which corresponds to a weak C–H…π-type interaction. © *2005 Pleiades Publishing, Inc.*

INTRODUCTION

Previously, we have studied the structures of *p*-butyloxyphenyl *p*'-hexyloxybenzoate and *p*-hexyloxyphenyl *p*'-butyloxybenzoate, which belong to the class of aromatic esters possessing liquid-crystalline properties [1]. In continuation of these studies, we now report the results of X-ray diffraction analysis of a new representative of this class of compounds. Since the final aim of our studies is to construct a model of the structural transition from the crystal state to a nematic phase, it was of particular interest to investigate the structure of this compound not only at low temperatures but also at room temperature. Taking into account that compound **I** has a low melting point (62.6°C), we hoped to reveal which molecular fragments become more labile at high temperature by qualitative comparison of the thermal ellipsoids of the atoms. Presumably, the ordered structure of the compound would be destroyed upon melting predominantly near these fragments.

X-RAY DIFFRACTION STUDY

Colorless single crystals of *p*-ethoxyphenyl *p*'-pentylbenzoate (**I**), which exhibits a nematic mesophase in a narrow temperature range, were grown from an ethyl acetate solution. The transition temperatures (*K* 62.6 *N* 63.3 *I*) determined by DTA [2] are in good agreement with the results obtained previously (*K* 63.0 *N* 63.4 *I*) [3]. The unit-cell parameters, the details of the X-ray diffraction study, and the characteristics of structure solution and refinement at two temperatures are given in Table 1. A planar needlelike single crystal was coated with perfluorinated oil and mounted on a Bruker SMART CCD diffractometer equipped with a coordinate detector (MoK_α radiation). X-ray diffraction data were collected at 120.0(2) and 296.0(2) K. In both cases, reflections were measured using ω-scan technique with a count time of 15 s per step.

The structure was solved by direct methods and refined by the least-squares method against F^2. All hydrogen atoms were revealed from the difference electron density map. The final refinement of the structure was carried out by the full-matrix least-squares method with anisotropic thermal parameters for all non-hydrogen atoms. The hydrogen atoms in the low-temperature structure were refined isotropically. For the room-temperature structure, the hydrogen atoms were refined using the riding model. The experimental data were processed using the SAINT program (Version 6.02A) [4]. The structure solution and refinement were carried out and the graphical representation of the data was created using the SHELXL-Plus program package [5]. The atomic coordinates and other experimental data were deposited with the Cambridge Structural Database (CSD refcodes 231 674 and 231 675 for two temperatures, respectively) and can be obtained from the authors.

1063-7745/05/5001-0089$26.00 © 2005 Pleiades Publishing, Inc.

Table 1. Crystallographic parameters and characteristics of the structure solution and refinement of compound **I**

Molecular formula	$C_{20}H_{24}O_3$	$C_{20}H_{24}O_3$
Molar weight (kg/kmol)	312.39	312.39
Crystal system	Triclinic	Triclinic
Space group	$P\bar{1}$	$P\bar{1}$
a, Å	5.5131(3)	5.5313(8)
b, Å	12.0565(6)	12.0568(18)
c, Å	14.2550(6)	14.521(2)
α, deg	112.000(2)	108.721(7)
β, deg	93.797(2)	93.660(7)
γ, deg	97.094(1)	95.477(6)
V, Å^3	865.25(7)	908.4(2)
Z	2	2
ρ_{calcd}, g/cm^3	1.199	1.142
$\mu(MoK_\alpha)$, mm^{-1}	0.079	0.075
Crystal dimensions, mm	$0.44 \times 0.10 \times 0.06$	$0.44 \times 0.10 \times 0.06$
Temperature, K	120.0(2)	296.0(2)
θ-Scan range, deg	1.55–28.98	1.49–28.99
Ranges of *h*, *k*, *l* indices	$-7 \le h \le 7$, $-16 \le k \le 12$, $-19 \le l \le 19$	$-7 \le h \le 7$, $-16 \le k \le 14$, $-19 \le l \le 15$
Number of measured reflections	6223	5315
Number of independent reflections	4346 [$R_{int} = 0.0241$]	4346 [$R_{int} = 0.0335$]
Number of reflections with $I > 2\sigma(I)$	4034	4136
Parameters in refinement	305	208
R factors based on reflections with $I > 2\sigma(I)$	$R_1 = 0.0549$, $wR_2 = 0.1514$	$R_1 = 0.1207$, $wR_2 = 0.3460$
R factors based of all reflections	$R_1 = 0.0733$, $wR_2 = 0.1660$	$R_1 = 0.1852$, $wR_2 = 0.3811$
GOOF	1.132	1.167
$\Delta\rho_{max}/\Delta\rho_{min}$, e/Å^3	0.414/–0.245	0.509/–0.327

MOLECULAR STRUCTURE

The low-temperature molecular structure and the atomic numbering scheme are shown in Fig. 1. The bond lengths and bond angles in this structure are given in Table 2. The room-temperature molecular structure is shown in Fig. 2. Comparison of Figs. 1 and 2 demonstrates that the sizes of the thermal ellipsoids of all atoms increase, quite naturally, with increasing temperature. However, this effect is most pronounced for the atoms of aliphatic fragments. Moreover, the thermal motion of the terminal atoms of the aliphatic fragments becomes strongly anisotropic, whereas the thermal ellipsoids of the atoms of the benzene rings are close to spheres, which indicates that the aliphatic side chains become more labile upon melting. Hence, it can be sug-

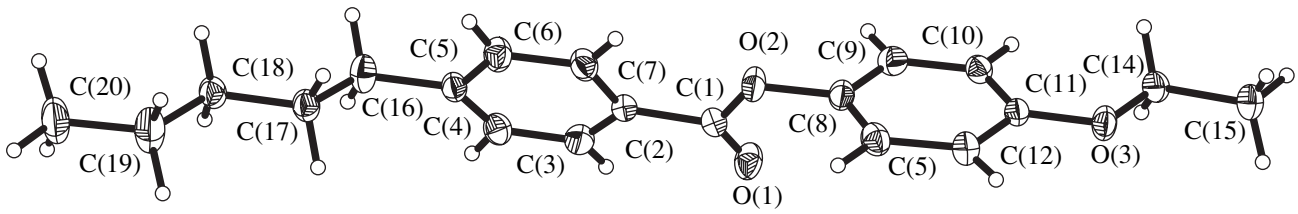

Fig. 1. Molecular structure with thermal ellipsoids at 120 K.

gested that the nematic phase formed upon melting retains ordered regions in the vicinity of the aromatic fragments of the molecules. This assumption is confirmed by analysis of the characteristic features of the crystal packing.

As in the case of two liquid-crystalline aromatic esters studied by us previously [1], one benzene ring in molecule **I** is virtually coplanar with the carboxy group (the dihedral angle is 4°), whereas the plane of the second benzene ring is twisted with the respect to the plane of the carboxy group by 66°.

The coplanar arrangement of the carboxy group and the C(2)···C(7) benzene ring results from the conjugation, which occurs in spite of the steric repulsions between the *ortho*-hydrogen atoms of the benzene ring and the corresponding oxygen atoms. The electronic effect of the ester group also manifests itself in the distribution of the bond lengths in this benzene ring, in which small yet systematic (toward the *para*-quinoid structure) perturbation of the bond lengths is observed. Indeed, the C(3)–C(4) and C(6)–C(7) bonds are shortened (both are 1.392(2) Å), whereas the remaining bond lengths in this ring are in the range 1.396(2)–1.399(2) Å.

In the carboxy group, the length of the formally single C(1)–O(2) bond is 1.364(2) Å, and the length of the formally double C(1)=O(1) bond is 1.203(2) Å. The C(1)–C(2) bond length is 1.491(2) Å. These values are typical of aromatic esters [6]. Distortions of the bond angles at the key C(1) atom of the ester group (O(1)–C(1)–O(2), 123.8(1)°; O(1)–C(1)–C(2), 125.3(1)°; O(2)–C(1)–C(2), 110.9(1)°) are also characteristic of aromatic esters [6, 7].

The fact that the second benzene ring, C(8)···C(13), is significantly twisted with respect to the ester group indicates the absence of conjugation between these fragments. The O(2)–C(8) bond length (1.413(2) Å) is larger than the formally single O(2)–C(1) bond in the ester group, in which the π-electron density is substantially delocalized over the O=C–O fragment.

The C–C bond lengths in the C(8)···C(13) benzene ring vary from 1.383(1) to 1.404(2) Å. The changes are not systematic, which indicates that the geometry of this ring depends only slightly on the electronic effects of the substituents.

Table 2. Bond lengths *d* (Å) and bond angles ω (deg) in molecule **I**

Bond	*d*	Bond	*d*
O(1)–C(1)	1.203(2)	C(6)–C(7)	1.392(2)
O(2)–C(1)	1.364(2)	C(8)–C(9)	1.383(2)
O(2)–C(8)	1.413(2)	C(8)–C(13)	1.389(2)
O(3)–C(11)	1.373(2)	C(9)–C(10)	1.399(2)
O(3)–C(14)	1.440(2)	C(10)–C(11)	1.396(2)
C(1)–C(2)	1.491(2)	C(11)–C(12)	1.404(2)
C(2)–C(3)	1.396(2)	C(12)–C(13)	1.390(2)
C(2)–C(7)	1.397(2)	C(14)–C(15)	1.512(2)
C(3)–C(4)	1.392(2)	C(16)–C(17)	1.528(2)
C(4)–C(5)	1.397(2)	C(17)–C(18)	1.527(2)
C(5)–C(6)	1.399(2)	C(18)–C(19)	1.513(2)
C(5)–C(16)	1.516(2)	C(19)–C(20)	1.520(2)
Angle	ω	Angle	ω
C(1)–O(2)–C(8)	117.7(1)	C(9)–C(8)–C(13)	121.6(1)
C(11)–O(3)–C(14)	117.6(1)	C(9)–C(8)–O(2)	120.7(1)
O(1)–C(1)–O(2)	123.8(1)	C(13)–C(8)–O(2)	117.6(1)
O(1)–C(1)–C(2)	125.3(1)	C(8)–C(9)–C(10)	119.5(1)
O(2)–C(1)–C(2)	110.9(1)	C(11)–C(10)–C(9)	119.5(1)
C(3)–C(2)–C(7)	119.6(1)	O(3)–C(11)–C(10)	124.5(1)
C(3)–C(2)–C(1)	117.7(1)	O(3)–C(11)–C(12)	115.3(1)
C(7)–C(2)–C(1)	122.7(1)	C(10)–C(11)–C(12)	120.2(1)
C(4)–C(3)–C(2)	119.9(1)	C(13)–C(12)–C(11)	119.9(1)
C(3)–C(4)–C(5)	121.2(1)	C(8)–C(13)–C(12)	119.2(1)
C(4)–C(5)–C(6)	118.1(1)	O(3)–C(14)–C(15)	107.3(1)
C(4)–C(5)–C(16)	120.8(1)	C(5)–C(16)–C(17)	115.2(1)
C(6)–C(5)–C(16)	121.0(1)	C(18)–C(17)–C(16)	112.7(1)
C(7)–C(6)–C(5)	121.3(1)	C(19)–C(18)–C(17)	113.7(1)
C(6)–C(7)–C(2)	119.8(1)	C(18)–C(19)–C(20)	114.1(1)

The O(3)–C(14)–C(15) side chain is virtually coplanar with the C(8)···C(13) benzene ring. The C(11)–

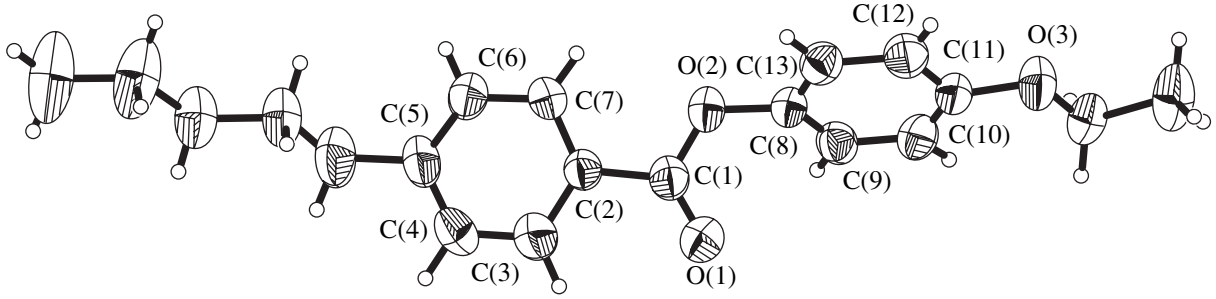

Fig. 2. Molecular structure with thermal ellipsoids at 296 K.

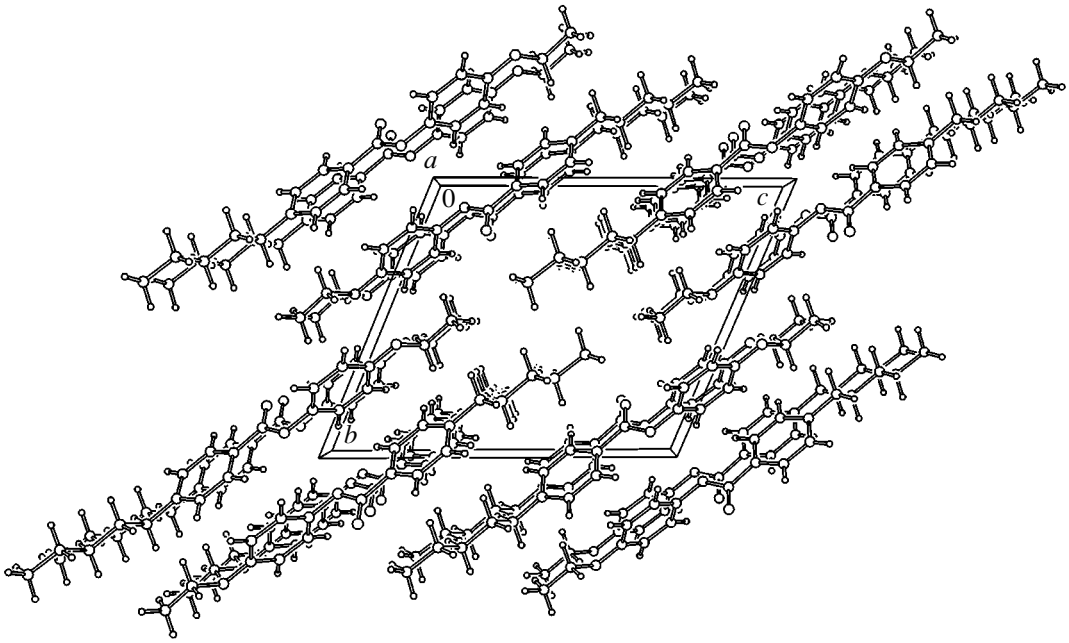

Fig. 3. Overall view of the crystal packing projected along the *a* axis.

O(3)–C(14)–C(15) torsion angle (176.1°) corresponds to the *trans* conformation of this fragment. This orientation is, apparently, due to the fact that the lone electron pair of the O(3) atom localized on the *p* orbital is involved in the interaction with the π* system of the benzene ring. The conclusion about the sp^2-hybridized state of the oxygen atom can be drawn based on the bond angle at this atom (117.6(1)°) and the O(3)–C(11) bond length (1.373(2) Å). The latter is shorter than the O(2)–C(8) bond length, which corresponds to the absence of conjugation between the lone electron pair of the O(2) atom and the C(8)···C(13) benzene ring. The typical angles at sp^3-hybridized oxygen atoms observed in aliphatic ethers, including crown ethers, vary from 111° to 113° [6, 7].

The C(16)···C(20) aliphatic substituent at the C(2)···C(7) benzene ring adopts a planar zigzag conformation. The torsion angles about the C(16)–C(17), C(17)–C(18), and C(18)–C(19) bonds (–178.1°, 176.3°, and –177.5°, respectively) correspond to the *anti* configuration. The angle between this virtually planar fragment and the C(2)···C(7) benzene ring is 58.4°.

CRYSTAL PACKING

The packing of **I** molecules in a crystal projected along the shortest *a* axis is shown in Fig. 3. It can be clearly seen that the long axes of the molecules are oriented along the *bc* diagonal of the unit cell. The benzene rings form contacts with the benzene rings and the aliphatic fragments of the adjacent molecules on opposite sides. The fragment of the crystal packing projected onto the plane of the C(8)···C(13) benzene ring of one of the molecules is shown in Fig. 4. It can be clearly seen that the aromatic fragments are not stacked. The molecules in the series *A*, *B*, and *C*, as those in the series *D*, *E*, and *F*, are related to each other by the translation along the *a* axis. The pairs of the *A* and *D*, *B* and *E*, and *C* and *F* molecules are related to each other by centers of symmetry.

It should be noted that the distances between the O(2) atoms of the molecules related by centers of symmetry [O(2*A*)··O(2*D*), O(2*B*)··O(2*E*), or O(2*C*)··O(2*F*)] are seemingly short. However, the actual distance (3.813 Å) is too large to suggest a weak specific interaction.

The situation is different for the mutual arrangement of the aromatic rings in a pair of the molecules related by a center of symmetry. Due to the above-mentioned symmetry of the mutual arrangement of these molecules, the dihedral angle between the planes of the closely spaced rings of adjacent molecules is exactly equal to the dihedral angle between the benzene rings in the molecule (62.5°). According to the results of *ab initio* quantum-chemical calculations, this nearly T-shaped mutual arrangement of the benzene rings of two adjacent molecules corresponds to the energy minimum [8]. The system is stabilized through a weak C–H··π interaction, which can be considered as a weak hydrogen bond between the C–H group serving as a weak acid and the π system acting as a weak base [9]. This specific interaction is weak. The corresponding intermolecular contacts are consistent with the sums of the van der Waals radii. In particular, the distances from the C(7*A*) atom and the hydrogen atom bound to this C atom to the plane of the C(8*D*)··*C*(13*D*) benzene ring

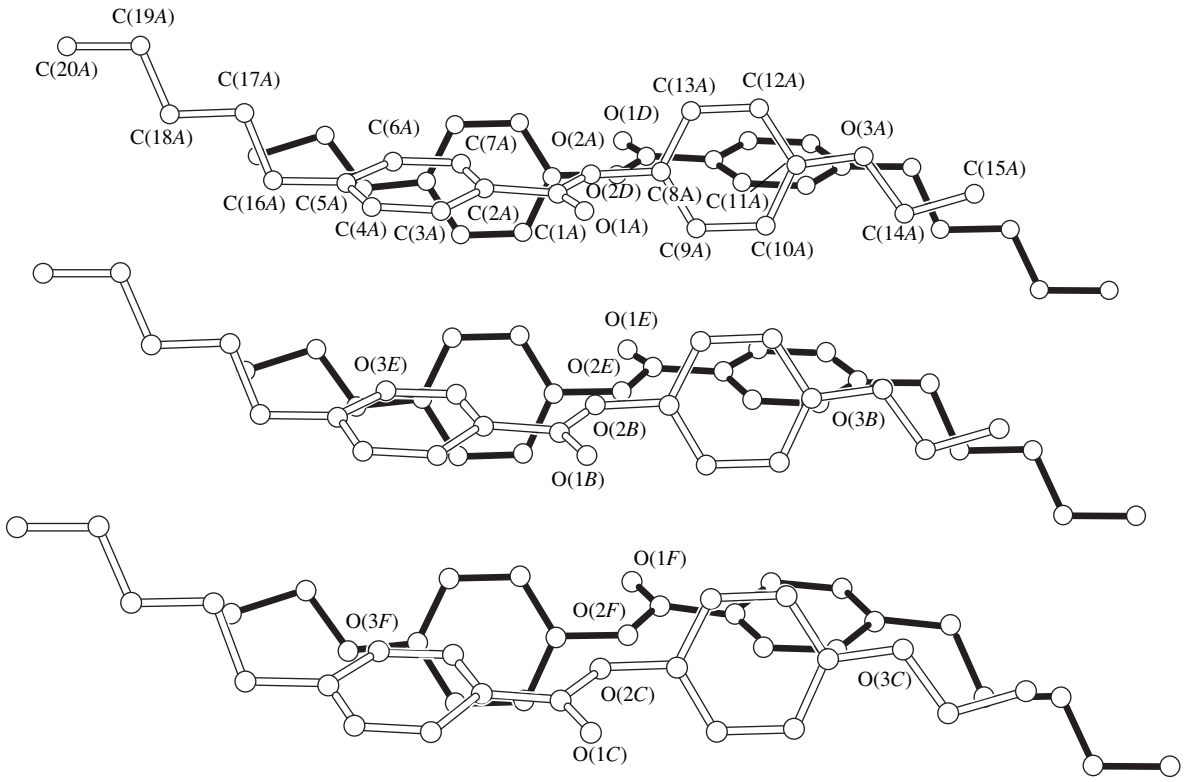

Fig. 4. Fragment of the crystal packing showing the mutual orientation of the adjacent molecules; the atoms belonging to different molecules are denoted by letters (*A*, *B*, …, *F*) in the atom numbers.

(2.88 and 3.57 Å, respectively) are close to the lengths of the van der Waals contacts. However, the cooperative effect of such weak interactions can be sufficiently large to provide the retention (within certain limits) of the mutual orientation of the benzene fragments of adjacent molecules upon melting, i.e., structurization of the melt, which is responsible for the appearance of a liquid-crystalline phase. In the crystal structure, the side aliphatic chains form large loose regions, in which specific weak bonds between the fragments are lacking. Consequently, nothing can prevent the thermal motion of these fragments from increasing with increasing temperature. Presumably, it is these regions in which the ordered structure inherent in the crystal is distorted.

ACKNOWLEDGMENTS

This study was supported by the Russian Foundation for Basic Research, project no. 01-03-32474. L.G. Kuz'mina acknowledges the support of the Royal Society of Chemistry (RSC Journal Grants for International Authors).

REFERENCES

1. O. V. Noskova, A. V. Churakov, L. G. Kuz'mina, *et al.*, Kristallografiya **48** (4), 687 (2003) [Crystallogr. Rep. **48**, 623 (2003)].
2. V. A. Molochko, B. M. Bolotin, and G. M. Kurdyumov, *Liquid Crystals and Their Practical Application* (Ivan. Gos. Univ., Ivanovo, 1976), p. 111 [in Russian].
3. M. E. Neubert, L. T. Carlino, D. L. Fishel, and R. M. D'Sidocky, Mol. Cryst. Liq. Cryst. **59**, 253 (1980).
4. *SAINT. Version 6.02A* (Bruker AXS, Madison, WI, 2001).
5. G. M. Sheldrick, *SHELXTL Plus. Release 5.10* (Bruker AXS, Madison, WI, 1997).
6. F. H. Allen, O. Kennard, D. V. Watson, *et al.*, J. Chem. Soc., Perkin Trans. 2, S1 (1987).
7. F. H. Allen and O. Kennard, Chem. Des. Aut. News **8**, 1 (1993).
8. K. Müller-Dethlefs and P. Hobza, Chem. Rev. **100**, 143 (2000).
9. H. Takahashi, S. Tsuboyama, Y. Umezawa, *et al.*, Tetrahedron **56**, 6185 (2000).

Translated by T. Safonova

Crystallography Reports, Vol. 50, No. 1, 2005, pp. 94–97. Translated from Kristallografiya, Vol. 50, No. 1, 2005, pp. 101–104.

STRUCTURE OF MACROMOLECULAR COMPOUNDS

Structures of Interpolymer Complexes Based on Carboxymethylcellulose and Urea–Formaldehyde Resin

M. M. Khafizov

Tashkent Institute of Irrigation and Agricultural Mechanization Engineers, ul. Qory Niyoziy 39, Tashkent, 700000 Uzbekistan

Received November 21, 2003

Abstract—Interaction of carboxymethylcellulose with polymeric condensation products of urea and formaldehyde was studied. The structure of the final product was found to depend on the nature and structure of the components involved in the interaction. © *2005 Pleiades Publishing, Inc.*

INTRODUCTION

Considerable advances have been made recently in the design of a new class of modified polymeric materials, the so-called interpolymer complexes [1–3]. These advances have stimulated the development of new areas of research in the physics and chemistry of polymers. One of the goals directly associated with the practical application of interpolymer complexes is to synthesize compounds having desired structures and physical-mechanical properties. In this context, it is of interest to study the structures of interpolymer complexes containing rigid-chain polyelectrolytes. The natural polysaccharide carboxymethylcellulose (CMC) belongs to such complexes [4]. The reserves of CMC are large and replenishable. Carboxymethylcellulose-based interpolymer complexes are promising for decreasing water and wind erosion [5], saving irrigation water [6], and constructing composition materials [7, 8]. However, the structures of CMC-containing interpolymer complexes have not been adequately studied.

The aim of this work was to investigate the interactions of CMC with polymeric condensation products of urea and formaldehyde and reveal the dependence of the structure of the final product on the nature and structures of the interacting components.

EXPERIMENTAL

We studied purified CMC with a degree of substitution of 70 and a degree of polymerization P_ω = 450, which was produced at the Namangan Chemical Plant (State Enterprise), and the urea–formaldehyde resin (UFR) with different triazinone-ring contents in the chain (7% in UFR_1, 15% in UFR_2, and 35% in UFR_3) [9]. Samples of the CMC–UFR_1, CMC–UFR_2, and CMC–UFR_3 interpolymer complexes were prepared as films from aqueous solutions according to the procedure described previously [9, 10]. Solutions of mixtures of the polyelectrolytes (pH 2.5) were poured onto the surface of an optical glass, and the solvent was evaporated at room temperature. The films thus prepared were dried *in vacuo*, washed with distilled water to pH 7, and dried in air. Films of the starting CMC were prepared from an aqueous solution using the same procedure.

Electron-microscopic study was carried out on a Hitachi scanning electron microscope (Japan) with a resolution of 60 Å. Samples were prepared by cleaving at liquid nitrogen temperature and treated according to a standard procedure (shading with gold).

X-ray diffraction patterns were obtained on a Dron-2.0 diffractometer (CuK_α radiation, $5° < 2\theta < 4°$). Photographic diffraction patterns of interpolymer complexes samples were obtained on an URS-55 X-ray apparatus (λ = 1.54 Å) with a nickel filter at room temperature using a planar camera.

RESULTS AND DISCUSSION

Studies of the film morphology of CMC and CMC–UFR mixtures by scanning electron microscopy demonstrated that the chemical structure of UFR and the percentage of amino groups, which are responsible for the ability of UFR to be involved in interpolymer Coulomb interactions, significantly affect the structure of the complexes (Fig. 1). The photomicrograph of the CMC–UFR_1 interpolymer complex (Fig. 1b) clearly shows symmetrical particles immersed in CMC serving as a homogeneous matrix. The photomicrograph of the latter is shown in Fig. 1a. Individual symmetrical particles immersed in the matrix form a dispersed phase resulting from three-dimensional (3D) polycondensation of UFR_1. An analogous situation is observed for the CMC–UFR_2 interpolymer complex. Therefore, the CMC–UFR_1 and CMC–UFR_2 interpolymer complexes produced by 3D polycondensation are typical microheterophase systems or composites, in which CMC and UFR serve as continuous and dispersed phases, respectively.

1063-7745/05/5001-0094$26.00

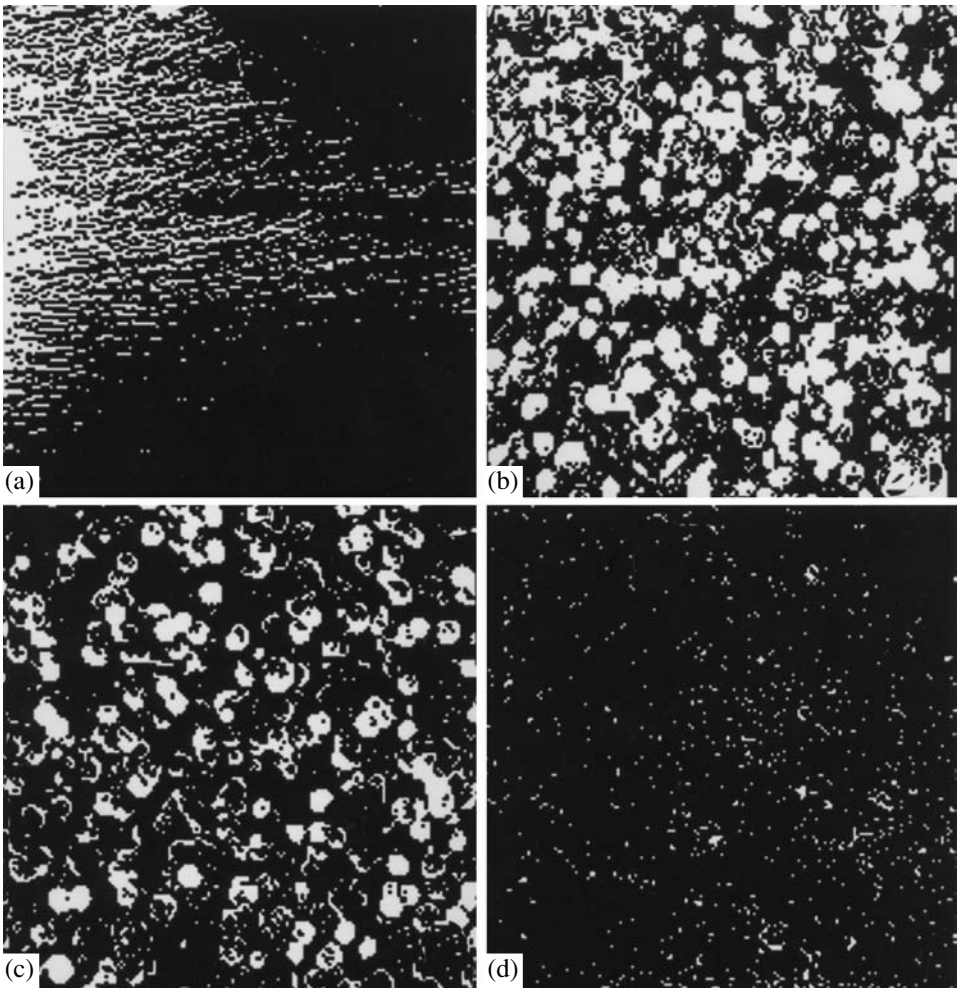

Fig. 1. Scanning electron microscope images of the surfaces of the films of (a) CMC and the interpolymer complexes with equimolar compositions (b) CMC–UFR_1, (c) CMC–UFR_2, and (d) CMC–UFR_3 prepared at pH 2.5 and 25°C.

An increase in the percentage of triazinone fragments in the starting UFR_3 to 35% leads to the formation of a much more homogeneous structure (see Fig. 1d). This accounts for the increase in the affinity of CMC and UFR_3 for each other due to extensive interpolymer Coulomb interactions.

Interpolymer complexes are a special case of polymer mixing [11–13] resulting in the formation of salt bridges and hydrogen bonds between macromolecules of different types. The polymer compatibility can be increased by introducing ionogenic groups capable of interacting. Actually, an increase in the percentage of triazinone fragments in UFR increases the degree of compatibility of segments of a different nature (CMC and UFR), as can be seen from the scanning electron microscope images (Fig. 1). The CMC–UFR_3 interpolymer complex is a more compatible system compared to other interpolymer complexes (Figs. 1b, 1c), which confirms the homogeneity of the structure of the CMC–UFR_3 complex (Fig. 1d).

X-ray diffraction analysis revealed a change in the structure of the interpolymer complexes formed by CMC and UFR (Fig. 2). The X-ray diffraction pattern of CMC obtained at pH 2.5 is shown for comparison (Fig. 2, curve *1*). The X-ray diffraction patterns of H-CMC films have an intense reflection at $2\theta = 20°$ corresponding to intermolecular distance $d = 4.4$ Å, which occurs due to overlap of the [002] and [101] reflections characteristic of *P* cellulose [14]. This reflection indicates a pronounced short-range order along the chain of the rigid-chain polymer. The X-ray diffraction patterns of the interpolymer complexes demonstrate that the structures of these complexes are disordered compared to CMC, as evidenced by the decrease in the intensity of the reflection at $2\theta = 20°$ and broadening of the reflections observed (Fig. 2, curves *2–6*).

Addition of UFR to the system results in the appearance of an additional reflection at $2\theta = 22°$ ($d = 4.5$ Å) with retention of the weak reflection at $2\theta = 20°$ (curve *3*). The maximum at $2\theta = 22°$ corresponds to the [002] reflection for mercerized cellulose [15]. A further

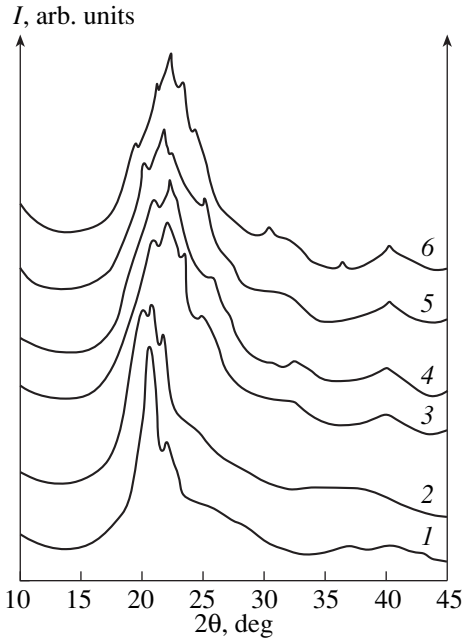

Fig. 2. Wide-angle X-ray diffraction patterns of the films of (*1*) H-CMC and the interpolymer complexes with a CMC : UFR molar ratio of (*2*) 4 : 1, (*3*) 3 : 2, (*4*) 1 : 1, (*5*) 3 : 4, and (*6*) 1 : 2.

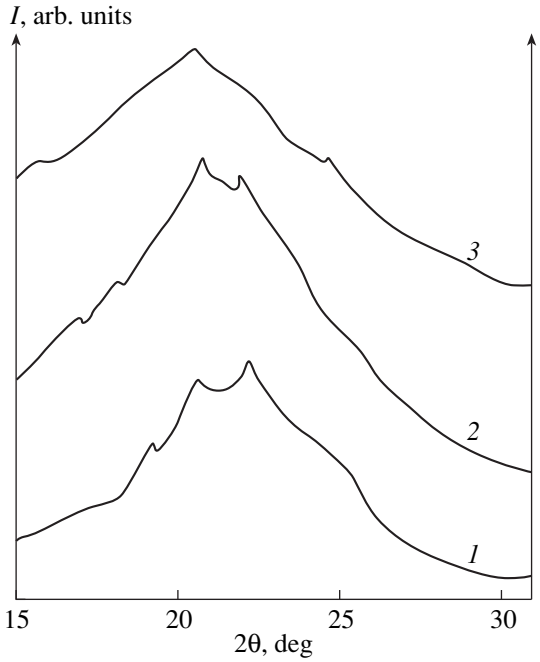

Fig. 3. X-ray diffraction patterns of the films of the (*1*) CMC–UFR_1, (*2*) CMC–UFR_2, and (*3*) CMC–UFR_3 interpolymer complexes prepared at pH 2.5 and 25°C.

increase in the UFR content in the interpolymer complexes is accompanied by the appearance of the diffuse-scattering maximum at 2θ = 25° (curves *5*, *6*), which is indicative of the densification of the amorphous phase in the interpolymer complexes. The broadening of particular reflections in the X-ray diffraction patterns is due to the presence of a highly dispersed UFR phase in the complexes (Figs. 1b, 1c). This indicates that the structure of interpolymer complexes differs radically from that of H-CMC. This difference consists in the radically different packings of the macromolecules, which was clearly demonstrated by high-angle X-ray diffraction measurements.

In contrast to fibrillated H-CMC, the nonstoichiometric interpolymer complexes enriched in either CMC or UFR (H-CMC : UFR = 4 : 1 and 3 : 4, respectively) are amorphous. Their X-ray diffraction patterns are characterized by the presence of diffuse halos. In addition, the X-ray diffraction patterns of the stoichiometric interpolymer complex (H-CMC : UFR = 1 : 1) and the interpolymer complexes enriched in CMC (the component ratio is 3 : 2) or UFR (the component ratio is 1 : 2) have a weak reflection corresponding to the identity period d = 6.6 Å. This reflection is indicative of both the presence of ordered regions in such interpolymer complexes and the occurrence of a short-range order in the arrangement of the fragments of the rigid CMC chains separated by the UFR macromolecules. This order can be substantially impaired as the distance between the adjacent UFR chains increases with increasing the H-CMC content and vice versa. These conclusions are consistent with the 3D molecular models of the fragments of the H-CMC–UFR interpolymer complexes:

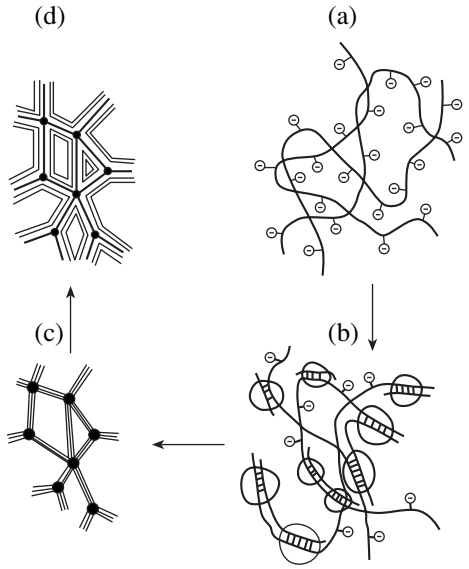

where (a) is CMC, (b) is an interpolymer complex containing an excess of CMC, (c) is a stoichiometric interpolymer complex (H-CMC : UFR = 1 : 1), and (d) is an interpolymer complex containing an excess of UFR.

The X-ray diffraction patterns of the structurally different CMC–UFR interpolymer complexes clearly show changes in the intensities of the [101] and [002] reflections (Fig. 3). In the X-ray diffraction pattern of the CMC–UFR_1 interpolymer complex (curve *1*), these

reflections are clearly observable, whereas a decrease in the intensity of the [002] reflection with a simultaneous increase in the intensity of the [101] reflection is observed in the X-ray diffraction pattern of the CMC–UFR_2 interpolymer complex (curve *2*). In the X-ray diffraction pattern of the CMC–UFR_3 interpolymer complex, the above-mentioned reflections overlap with each other resulting in the appearance of a distinct amorphous halo (curve *3*).

CONCLUSIONS

To summarize, the results of the X-ray diffraction and electron microscopic analysis demonstrate that changes in the composition of the reaction systems and the nature of interpolymer interactions lead to a noticeable change in the structure of interpolymer complexes. In other words, there opens a possibility of preparing CMC–UFR interpolymer complexes with a desired structure controlled by changing the ratio between the interacting components, pH of the reaction medium, and the nature of interpolymer interactions (varying the percentage of triazinone rings). This is of decisive importance for the development of scientific foundations of the synthesis of new polycomplexes based on reactive polymers, which are expected to be widely used in practice.

REFERENCES

1. G. Caroenuto, Polym. News **26** (2), 48 (2001).
2. V. N. Kuleznev, V. Wolf, and N. A. Pozharov, Vysokomol. Soedin., Ser. B **44** (3), 512 (2002).
3. V. A. Kabanov, V. G. Sergeyev, O. A. Pushkina, *et al.*, Macromolecules **33** (26), 9587 (2000).
4. G. A. Petropalovskiĭ, Zh. Prikl. Khim. (Leningrad), No. 2, 241 (1969).
5. M. M. Khafizov, G. I. Mukhamedov, K. U. Kamilov, and Z. Karimov, in *Proceedings of 5th International Congress on Water: Ecology and Technology, EKVATEK-2000* (Moscow, 2002), p. 61.
6. M. M. Khafizov, G. I. Mukhamedov, K. U. Kamilov, and S. I. Iskandarov, in *Proceedings of International Workshop on Cons. Agricult.* (Tashkent, 2002), p. 160.
7. M. M. Khafizov, K. U. Kamilov, G. I. Mukhamedov, and S. I. Iskandarov, Kompoz. Mater., No. 4, 39 (2002).
8. M. M. Khafizov, G. I. Mukhamedov, and Sh. M. Mirzieev, Plast. Massy, No. 3, 33 (2001).
9. G. I. Mukhamedov, M. M. Khafizov, M. N. Khasankhanova, *et al.*, Dokl. Akad. Nauk SSSR **306** (2), 386 (1989).
10. G. I. Mukhamedov, M. M. Khafizov, A. M. Akhmedov, and A. É. Aliev, Vysokomol. Soedin., Ser. B **35** (4), 189 (1993).
11. A. A. Tager and V. S. Blinov, Usp. Khim., No. 6, 1004 (1987).
12. A. A. Tager and T. I. Sholokhovich, Vysokomol. Soedin., Ser. B **14** (6), 1423 (1972).
13. A. A. Tager, *Physics and Chemistry of Polymers* (Khimiya, Moscow, 1978), p. 346 [in Russian].
14. G. A. Petropavlovskiĭ, *Hydrophilic Partly Substituted Ethyls of Cellulose and Their Modification by Chemical Cross Linking* (Nauka, Leningrad, 1988), p. 110 [in Russian].
15. *Methods for Studying Cellulose*, Ed. by V. P. Karlivan (Zinatne, Riga, 1981), p. 44 [in Russian].

Translated by T. Safonova

Crystallography Reports, Vol. 50, No. 1, 2005, pp. 98–101. Translated from Kristallografiya, Vol. 50, No. 1, 2005, pp. 105–108.

REAL STRUCTURE OF CRYSTALS

Growth Dislocations in Zonal Isomorphously Mixed Crystals

M. A. Kuz'mina and S. V. Moshkin

Research Institute of the Earth Crust, St. Petersburg State University, Universitetskaya nab. 7/9, St. Petersburg, 199034 Russia

e-mail: dido@ak2244.spb.edu

Received August 7, 2003

Abstract—The orientation, distribution, and density of dislocations in isomorphously mixed potassium–rubidium biphthalate crystals composed of two zones with different concentrations of isomorphous rubidium impurity are experimentally studied. A model for the formation of growth dislocations in the external zone, which compensate internal heterometry-induced stresses at the interface between the zones, is proposed. © *2005 Pleiades Publishing, Inc.*

The internal heterometry induced stresses, which arise on the intergrowth surfaces of crystal zones with different contents of isomorphous impurity, are reduced to a large extent due to the formation of various defects. The most well known of these defects are inconsistency dislocations [1–3], which were studied in detail in crystalline films. Large faceted isomorphously mixed potassium–rubidium biphthalate crystals (grown as multilayered structures to be used in X-ray technique) are also characterized by a dislocation structure, but with some distinctive features. In this paper, we consider the regularities of the dislocation formation in potassium–rubidium biphthalate crystals composed of two zones with different contents of isomorphous rubidium impurity.

In the 30 potassium–rubidium biphthalate crystals under study, the internal zone was a full-face crystal about $5 \times 2 \times 5$ mm^3 in size and the external zone was a 2–3-mm overgrown layer with a rubidium content differing from that in the internal zone. The latter was either a pure potassium biphthalate crystal (in most cases) or a rubidium-doped crystal (with an overgrown external zone consisting of pure potassium biphthalate). Generally, the difference in the rubidium contents between the zones varied from 0.5 to 10 mol %. The crystals were grown from aqueous solutions with decreasing temperature and constant supersaturation [4–7]. Identical growth conditions ensured only insignificant difference in the growth rates of the faces. The growth of the external zone on the initial crystal was observed by the method of microcrystallization in a thermostated cell [5]. The rubidium content and the lattice distortion were studied by microprobe analysis, flame spectrophotometry, and X-ray diffraction analysis. Dislocations revealed by selective etching (1–2 min in a mixture of ethanol and glycerin (10 : 1) and washing in propanol [5]) of (010) cleavage plates 0.05–0.1 mm thick [5, 7] were investigated by optical microscopy.

The distribution of pyramidal etch pits on (010) cleavages, corresponding to the points of dislocation emergence [5, 8], was typical for all the crystals studied. Microscopic determination of the orientation of dislocations with respect to the faces from the magnitude and direction of the shift of the tips of etch pits from the centers of their orthorhombic bases in the (010) plane showed that dislocations are oriented almost perpendicular to the growing faces in all growth sectors of a zonal crystal (it was difficult to determine the direction of dislocations lines in successive cleavages due to the high density of etch pits). Most dislocations were concentrated in the external zone in the central parts of the sectors of face growth, independent of the sign of interzone stresses. Dislocations lines in zonal crystals form wide beams in the external zone, which are generated near the interface between the zones and emerge on the surfaces of growing faces, leaving free the regions of edge growth.

As the external zone grows, the experimental dislocation density, which is measured as a number of etch pits per unit area with a correction to the angle of inclination of the face with respect to the (010) cleavage, reaches a maximum value at some distance from the interface [7]. For each profile of the change in the dislocation density along the growth direction for a given face, the maximum dislocation density in the external zone of the crystal is directly proportional to the absolute value of the difference in the rubidium contents in the neighboring zones (Fig. 1), i.e., is related to the magnitude of interzone stresses. However, the orienta-

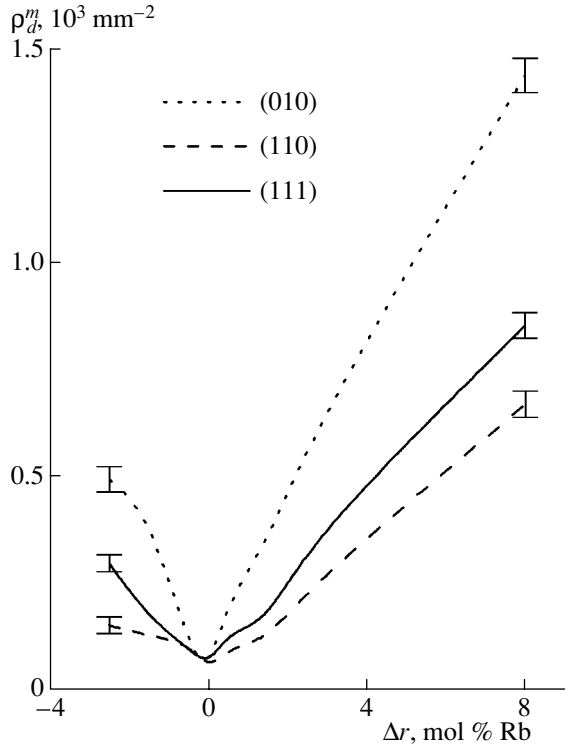

Fig. 1. Dependences of the maximum dislocation density ρ_d^m on the difference Δr in the rubidium contents in the zones of zonal potassium–rubidium biphthalate crystals in the (010), (111), and (110) growth sectors (positive and negative values of Δr correspond to compression and stretching of the external zone, respectively).

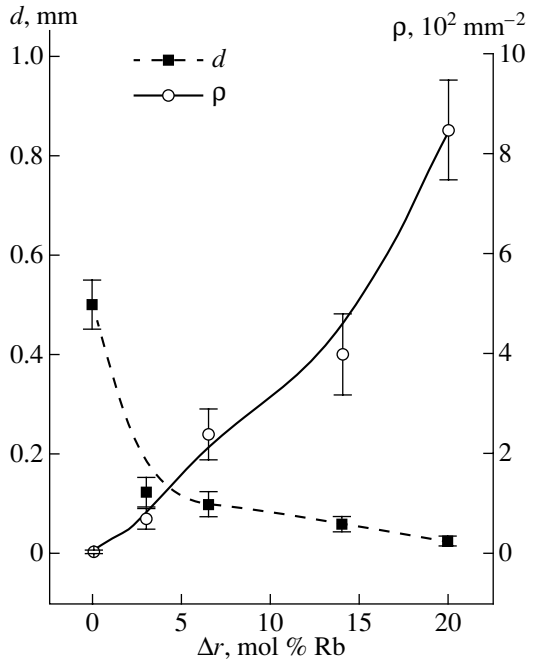

Fig. 2. Dependences of the number of external-zone islands per unit area of the pinacoid face (010) ρ and their average size d (measured as an average distance between the opposite sides of growing hexagonal islands in the plane of the (010) face upon microscopic observation of their growth in a thermostated cell) on the difference Δr in the impurity contents in the zones of zonal potassium–rubidium biphthalate crystals.

tion of the dislocations observed by us does not correspond to the typical orientation of inconsistency dislocations, which are characteristic of heteroepitaxial crystalline films [1, 2], where inconsistency dislocations are oriented, as a rule, parallel to the intergrowth plane of layers of different chemical compositions.

When a crystalline layer containing an isomorphous impurity grows on a face of an initial pure crystal, heterometry stresses arise between this layer and the crystal [6, 7]. Therefore, the higher these stresses, the stronger the deceleration of the motion of the growth layer from the growth centers is [6]. As a result, an island of a new crystalline layer with enhanced relative growth rate along the normal to the face is formed on the face surface. Since the growth of new layer over the initial face is hindered, growth centers with low activity arise on the face, due to which the general number of islands of the growing layer increases. In the course of time, these islands coalesce in the face plane and form a continuous growing crystalline layer [9, 10]. One can observe a direct dependence of the number of islands of the new layer on the increase in the difference in the impurity contents in the neighboring zones (Fig. 2), i.e., on the magnitude of interzone stresses. At a small difference in the zone compositions, these islands gradually increase in size and coalesce into larger ones, forming a smooth external-zone surface on the face. At a large difference in the zone compositions, the tangential growth of the islands that increased in size at the initial moment is decelerated and they are thickened in the normal direction, forming a rough tiled surface of the face of the external zone upon their coalescence.

The lattice of a growing island undergoes stresses and is matched to the lattice corresponding to the initial face, whereas the edges of coalescing islands are elastically deformed to ensure matching to the unstrained lattice of the external zone. At a coalescence of two islands with thicknesses exceeding the critical one, a segment of edge dislocation is formed. The line of this dislocation lies in the intergrowth plane of the layers and is directed along the joint line of the islands (Fig. 3). The formation of this segment of an inconsistency dislocation (insertion of an additional half-plane when the growing layer is stretched or, vice versa, removal of an extraneous half-plane when the layer is compressed (Fig. 3)) makes it possible to reduce the

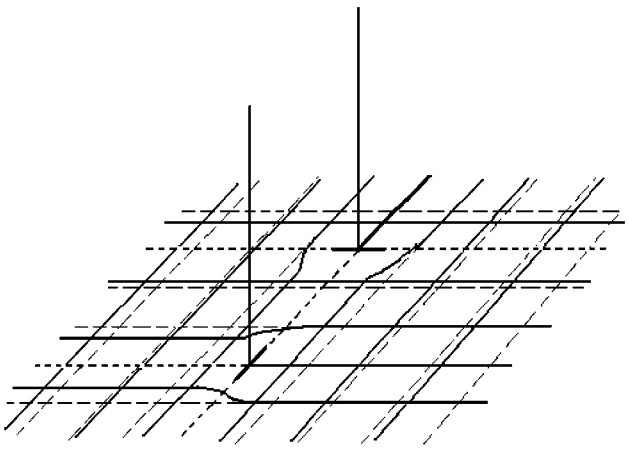

Fig. 3. General scheme of formation of segments of inconsistency dislocations in the plane of the growing face ((010), (110), or (111) for potassium–rubidium biphthalate) and compensating dislocations perpendicular to this plane upon coalescence of the islands of the growing layer in a crystal with orthorhombic lattice under compression of the growing external zone with a large content of isomorphous impurity (planes of the face and growing-zone lattices are shown by dashed and solid lines, respectively; the dislocations lines are shown bold).

heterometry stresses in this region. When several islands coalesce, a grid of closed polygons is formed in the coalescence plane. This grid consists of segments of edge inconsistency dislocations parallel to the coalescence plane of the layers.

At the points where segments of inconsistency dislocations joint or change their direction, additional compensating edge dislocations are inevitably formed in the growing layer (Fig. 3) (independent of the sign of stresses in this layer). The lines of these dislocations emerge on the growth surface and are oriented perpendicular to the face. Their Burgers' vectors lie in the coalescence plane and are equal to the differences of the Burgers' vectors of the adjacent segments of inconsistency dislocations. If coalescing islands are formed on some asperities of the face, there also arises vertical mismatch of their lattices due to the Poisson effect, which leads to the formation of screw dislocations perpendicular to the face. These dislocations serve as additional sources of growth layers. Etching of cleavages of potassium–rubidium biphthalate crystals reveals specifically compensating and screw dislocations, whose lines are perpendicular to the growing face.

In the external growing zones of the crystals under investigation, the region from the interface between the zones to the layers with the highest dislocation densities can be considered as a specific compensation zone, since heterometry stresses relax in it when dislocations are formed. The width of the compensation zone is different for different faces and increases with increasing heterometry stresses independent of their sign. Thus, with an increase in the difference in the rubidium contents in the zones from 0 to 8 mol %, the width of the compensation zone increases from 0.3 to 1.7 mm for a (110) prism and from 0.4 to 2.3 mm for a (111) bipyramid). The experimental growth rates of the crystal faces, the width of the compensation zone, and the data on the maximum dislocation density make it possible to estimate the rates of formation of compensating dislocations in the crystals under study. These rates are also directly proportional to the interzone stresses (for example, in the (111) growth sectors, with an increase in the difference in the rubidium contents in the zones from 0.5 to 8 mol %, the rates of formation of compensating dislocations increase from 95 to 275 mm^{-2} h).

When the islands of the growing layer coalesce and the subsequent growth layers of the external zone joint (since the compensation zone is wider than the zone of the initial island coalescence), there arises a peculiar spatial grid of polygons formed by segments of edge inconsistency dislocations parallel to the face and compensating dislocations perpendicular to the face. During the formation of this grid, the number of compensating dislocations increases and reaches the maximum value. The limited number of growth centers on the initial face determines the relaxation rate of interzone stresses in the growing zone and the width of the compensation zone. After the relaxation of interzone stresses, with a further growth on the face, the formation of dislocations ceases and their general number decreases, which, apparently, is related to the orientation of the dislocations parallel to the face under the action of residual internal stresses.

The proposed model for the formation of a peculiar dislocation system in the growing strained external zone in potassium–rubidium biphthalate crystals explains the characteristic distribution and the orientation of experimentally revealed dislocations by the appearance of compensating dislocations. The unambiguous correspondence of the dislocation density, the width of the compensation zone, and the rate of dislocation formation to the difference in the contents of isomorphous impurity in the neighboring zones of a crystal shows that the character of relaxation of heterometry-induced interzone stresses is determined by the magnitude of these stresses and the features of the growth processes occurring on the crystal face.

REFERENCES

1. G. H. Olson and M. Ettenberg, in *Crystal Growth. Theory and Technique*, Ed. by C. Goodman (Plenum, London, 1974; Mir, Moscow, 1981), Vol. 2.
2. M. G. Mil'vidskiĭ and V. B. Osvenskiĭ, Kristallografiya **22** (2), 431 (1977) [Sov. Phys. Crystallogr. **22**, 246 (1977)].
3. V. I. Vdovin, L. M. Dolginov, L. V. Druzhinina, *et al.*, Kristallografiya **26** (4), 799 (1981) [Sov. Phys. Crystallogr. **26**, 453 (1981)].

4. S. V. Moshkin, O. M. Boldyreva, T. I. Ivanova, *et al.*, J. Cryst. Growth **172**, 226 (1997).
5. M. A. Kuz'mina, S. V. Moshkin, O. M. Boldyreva, and I. P. Shakhverdova, *Physics of Crystallization* (Tver, 1994), p. 103 [in Russian].
6. S. V. Moshkin, M. A. Kuz'mina, O. M. Boldyreva, and T. I. Ivanova, Kristallografiya **45** (6), 1126 (2000) [Crystallogr. Rep. **45**, 1041 (2000)].
7. M. A. Kuz'mina, S. V. Moshkin, and I. P. Shakhverdova, Kristallografiya **46** (6), 1098 (2001) [Crystallogr. Rep. **46**, 1014 (2001)].
8. S. Amelinckx, *The Direct Observation of Dislocations* (Academic, New York, 1964; Mir, Moscow, 1968).
9. N. A. Kiselev, V. Yu. Karasev, and A. L. Vasil'ev, in *Crystal Growth* (Nauka, Moscow, 1990), Vol. 18, p. 43 [in Russian].
10. Yu. B. Bolkhovityanov, in *Crystal Growth* (Nauka, Moscow, 1990), Vol. 18, p. 158 [in Russian].

Translated by Yu. Sin'kov